Doctorate Dissertation

博士論文

Title of Dissertation: Development of input optics for the gravitational wave detector KAGRA

(論文題目: 大型重力波検出器KAGRAにおける入射光学系の開発)

A Dissertation Submitted for Degree of Doctor of Philosophy

Submitted on 12/2017

平成29年12月博士(理学)申請

Department of Physics, Graduate School of Science,

The University of Tokyo

東京大学院理学系研究科物理学専攻

Masayuki Nakano

中野 雅之

Abstract

A gravitational wave (GW) detector called KAGRA is under construction in Japan. KAGRA is the first underground cryogenic GW detector in the world. KAGRA has two arms with the length of 3 km, and KAGRA has a design sensitivity that can detect a GW signal radiated by a coalescence of a pair of 1.4 solar mass neutron stars 140 Mpc away from the earth. Since the first detection of the GW signal by Advanced LIGO (aLIGO) in the U.S., several GW signals have been detected by aLIGO and advanced VIRGO in Italy.

In such a situation, the mission imposed on KAGRA is to achieve a sensitivity good enough to observe a GW signal and to join the GW detector network in the world as soon as possible. The design sensitivity of KAGRA is similar to those of other detectors at the frequencies above 10 Hz, and KAGRA has better sensitivity at the frequencies below 10 Hz. KAGRA has a potential to detect signals that cannot be observed by other detectors. For the GW astronomy, the position determination of the GW source is important. To determine the direction of the GW source, three or more detectors are necessary. When KAGRA joins the GW detector network, the probability that three or more machines are in operation improves to 80% from 50 %. Furthermore, the accuracy of position determination when four detectors are in operation is predicted to be improved to 9.5 deg^2 from 30.25 deg^2 as a result of a simulation. Therefore, the participation of KAGRA in the GW detector network is an urgent matter in the development of the GW astronomy.

To achieve the design sensitivity, several noises in the GW detector have to be reduced properly. One of such noises is the noise included in the laser light, such as the frequency noise, the intensity noise, and the beam jitter noise. We have developed an input optics subsystem, which is a subsystem responsible for the reduction of such laser source noises. The input optics aims to provide low-noise light to the main interferometer. The laser light needs to be stabilized, and the input optics performs the laser frequency stabilization, the laser intensity stabilization, the beam jitter reduction, and spatial mode cleaning.

The author is responsible for the design, the installation, the investigation, and the integration of a pre-stabilized laser (PSL) and an input mode-cleaner (IMC). The PSL is the in-air optics for the beam stabilization, and the IMC is the 50 m round trip length cavity with three suspended mirrors. The PSL and the IMC are the main part of the input optics, and almost all stabilization is done with the PSL and the IMC. The theme of this thesis is the installation and the investigation of the frequency stabilization system (FSS), which is one of the most important systems in the input optics.

The FSS has two requirements; one is the requirement for the duty cycle of 95%, and the other is the requirement for the frequency noise of 1 $\mathrm{Hz}/\sqrt{\mathrm{Hz}}$ at 100 Hz. The frequency noise needs to have a smaller contribution to the GW sensitivity than other fundamental

noises such as the quantum noise, the thermal noise, and the seismic noise. The control of the FSS is automated, and it is possible for the FSS to keep locked for approximately a week. Furthermore, even once the lock gets lost, the FSS can return to the locked state within 1 minute. Therefore, the FSS of KAGRA satisfies the requirement for the duty cycle. Each actuator of the FSS is calibrated by using several transfer function measurements, and a model of the FSS is constructed. The noise budget has been made based on the model, and the noises which limit the frequency stability in almost all bands are identified. The noises included in this noise budget are as follows: the frequency noise of the laser source, the shot noise, the electronics noises in the photodetectors and the control servos, the length fluctuations of the cavities used as the frequency references, the phase noise of the voltage-controlled oscillator(VCO) used as the driver for the acousto-optic modulator(AOM), and the residual amplitude modulation (RAM) noise. We simulate the optimization of the control configuration with the model of the FSS. From this simulation, it is shown that the IMC length fluctuation by the seismic motion is dominant at the frequencies below 100 Hz, and that the RAM noise and the VCO phase noise at the higher frequencies than 100 Hz. Furthermore, the RAM noise and the VCO phase noise don′t satisfy the requirement at the higher frequencies than 2 kHz. However, the noises can meet the requirement in the frequency band below 1 kHz where the GW signals are expected. Moreover, by installation of the pre-mode cleaner (PMC), using the phase noise improved VCO, and adding the faster actuator such as the electro-optic modulator (EOM) to the second loop, those noises can be improved and satisfy the requirement in the whole frequency band.

The most recent task of KAGRA is to participate in the third observation run (O3) as the fourth GW detector in the GW detector network. The O3 is scheduled in 2019, and for that purpose, it is necessary to reach a sensitivity to detect a GW signal from a binary neutron stars coalescence located within at least 10 to 20 Mpc away.

The FSS, for which the author is responsible, gets ready to participate in the O3. From now on, the author continues to work on the installation of the input optics such as the intensity stabilization system, the pre-mode cleaner which is the cavity for the beam jitter reduction and the spacial mode cleaning.

Contents

Glossaries

AdV Advanced Virgo.
AOM Acousto-Optic Modulator.
AS Anti-Symmetric.

bKAGRA Baseline KAGRA.
BS Beam Splitter.

CMRR Common Mode Reduction Ratio.

DRMI Dual-Recycling Michelson Interferometer.

EOM Electro-Optic Modulator.
ETM End Test Mass.

FPMI Fabry-Perot Michelson Interferometer.
FSR Free Spectral Range.
FSS Frequency Stabilization System.

GAS Geometric Anti-Spring.
GRB Gamma Ray Burst.
GW Gravitational Wave.

IFI Input Faraday Isolator.
iKAGRA Initial KAGRA.
IMC Input Mode Cleaner.
IMMT Input Mode Matching Telescope.
ISS Intensity Stabilization System.
ITM Input Test Mass.

LIGO Large Interferometer Gravitational wave Observatory.

MZI Mach-Zehnder Interferometer.

NPRO NonPlanar Ring Oscillator.

OLG Open Loop Gain.
OMC Output Mode Cleaner.

PD Photo Detector.
PDH Pound Drever Hall.
PMC Pre-Mode Cleaner.
PRC Power Recycling Cavity.
PRFPMI Power Recycling Fabry-Perot Michelson Interferometer.

PRM Power Recycling Mirror.
PSL Pre-Stabilized Laser.
PZT PieZoelectric Transducer.

RAM Residual Amplitude Modulation.
RC Reference Cavity.
REFL REFLection.
RF Radio Frequency.
RIN Relative Intensity Noise.
RSE Resonant Sideband Extraction.

SRC Signal Recycling Cavity.
SRM Signal Recycling Mirror.

TT gauge Transverse Traceless gauge.

UGF Unity Gain Frequency.
ULE Ultra Low Expansion.

VCO Voltage-Controlled Oscillator.

1 Introduction

The gravitational wave (GW) is a physical phenomenon predicted by Einstein's general theory of relativity in 1916 [1], which is a distortion of space-time propagating at the speed of light. In 1989, Taylor and Weisberg indirectly proved the existence of the GW from the observation of a binary pulsar [2]. Assuming that the attenuation of the revolution period of the binary pulsar called PSR 1913 is due to the radiation of the GW, the attenuation almost agrees with the observation. Subsequently in 2015, 100 years after the prediction, direct detection of the GW signal from a black hole binary was achieved by Large Interferometer Gravitational wave Observatory (LIGO), which is a large interferometric GW detector in the U.S. [3]. The first detection of the GW signal was a very significant scientific event. Since the gravitational interaction is much weaker than the electromagnetic interaction, GWs carry information that electromagnetic waves cannot provide. Therefore, GW signals provide a new brunch of astronomy different from the current astronomy using electromagnetic waves and neutrinos. Furthermore, by analyzing many GW events, experimental verification of the general theory of relativity becomes possible.

In this chapter, we first describe the theoretical background of GWs in Section 1.1, and the principle of GW detectors and several optical configurations are described in Section 1.2. After that, we describe the new astronomy by means of GWs in Section 1.3. In the same section, the GW detectors in the world and the significance of KAGRA, which is the GW detector under construction in Japan, are described. Then, we describe the input optics of KAGRA, which is the main theme of this thesis, and the outline of this thesis briefly in Section 1.4

1.1 Gravitational wave

1.1.1 Metric tensor and geodesic equation

In the general theory of relativity, the nature of space-time is described by a metric tensor $g_{\mu\nu}$. A proper length between two points x^μ and $x^\mu + dx^\mu$ is denoted as

$$ds^2 = g_{\mu\nu} dx^\mu dx^\nu, \tag{1.1}$$

where the Einstein summation is used to shorten the equation. In the Einstein summation, the summation is taken over all the values of the indices, when the same index appears in superscript and subscript. Hereafter, the coordinates are defined as $x^0 = ct, x^1 = x, x^2 = y$, and $x^3 = z$. Subscripts and superscripts of Roman letters represent 1, 2, or 3, and those of Greek letters represent 0, 1, 2, or 3. This ds shows the geometric properties of

space-time.

A motion of a free falling particle, to which no force other than gravity is applied, depends only on geometric properties of space-time. The particle satisfies the geodesic equations,

$$\frac{d^2x^\lambda}{d\tau^2} = -\Gamma^\lambda{}_{\mu\nu}\frac{dx^\mu}{d\tau}\frac{dx^\nu}{d\tau}, \tag{1.2}$$

where $\Gamma^\lambda{}_{\mu\nu}$ is called the Christoffel symbol and is a function only of the metric tensor. It can be written as

$$\Gamma^\lambda{}_{\mu\nu} = \frac{1}{2}g^{\lambda\alpha}\left(\frac{\partial g_{\alpha\mu}}{\partial x^\nu} + \frac{\partial g_{\alpha\nu}}{\partial x^\mu} - \frac{\partial g_{\mu\nu}}{\partial x^\alpha}\right). \tag{1.3}$$

A geodesic equation multiplied by the mass of the particle can be regarded as an equation of motion. Therefore, the Christoffel symbol represents the strength of a gravitational field. Also, since the Christoffel symbol is represented by a derivative of a metric tensor, a metric tensor is regarded as a gravitational potential.

Curvature of space is described by the Ricci curvature tensor $R_{\mu\nu}$, and the Ricci curvature tensor $R_{\mu\nu}$ is described by the Riemann curvature tensor $R^\mu{}_{\nu\alpha\beta}$, which is a function of Christoffel symbols, and they are written as

$$R^\mu_{\nu\alpha\beta} = \frac{\partial\Gamma^\mu{}_{\nu\beta}}{\partial x^\alpha} - \frac{\partial\Gamma^\mu{}_{\nu\alpha}}{\partial x^\beta} + \Gamma^\mu{}_{\gamma\alpha}\Gamma^\gamma{}_{\nu\beta} - \Gamma^\mu{}_{\gamma\beta}\Gamma^\gamma{}_{\nu\alpha}, \tag{1.4}$$

$$R_{\mu\nu} = R^\alpha{}_{\mu\alpha\nu}. \tag{1.5}$$

The Ricci scalar R is a scalar derived from the Ricci tensor as

$$R = R^\alpha{}_\alpha. \tag{1.6}$$

1.1.2 Einstein equation

A metric tensor $g_{\mu\nu}$ with mass follows the Einstein equation,

$$G_{\mu\nu} \equiv R_{\mu\nu} - \frac{1}{2}g_{\mu\nu}R = \frac{8\pi G}{c^4}T_{\mu\nu}, \tag{1.7}$$

where G is a Newtonian constant of gravitation, and c is the speed of light, $G_{\mu\nu}$ is called the Einstein tensor, $T_{\mu\nu}$ is called the energy-momentum tensor which represents a mass distribution.

A metric tensor in flat space-time is called as the Minkowski metric and it is expressed as $\eta_{\mu\nu} = \mathrm{diag}(-1, 1, 1, 1)$. Now a metric tensor in general space-time $g_{\mu\nu}$ can be written as $g_{\mu\nu} = \eta_{\mu\nu} + h_{\mu\nu}$, where $h_{\mu\nu}$ is the difference from the Minkowski space-time. Here, $h_{\mu\nu}$

is assumed to be small. The following quantities are defined for later.

$$h \equiv h^{\alpha}{}_{\alpha}, \tag{1.8}$$

$$\bar{h}_{\mu\nu} \equiv h_{\mu\nu} - \frac{1}{2}\eta_{\mu\nu}h. \tag{1.9}$$

A Christoffel symbol can be written as

$$\Gamma^{\lambda}{}_{\mu\nu} = \frac{1}{2}\left(\frac{\partial \bar{h}^{\lambda}{}_{\mu}}{\partial x^{\nu}} + \frac{\partial \bar{h}^{\lambda}{}_{\nu}}{\partial x^{\mu}} - \frac{\partial \bar{h}_{\mu\nu}}{\partial x^{\lambda}}\right). \tag{1.10}$$

Now an approximation of the Einstein equation, taking the first-order of $h_{\mu\nu}$ by perturbation expansion, is effective. Such an approximation is called a linear approximation. In the linear approximation of the Einstein equation, the Lorentz gauge is taken. In the Lorentz gauge,

$$\frac{\partial \bar{h}^{\mu\nu}}{\partial x^{\nu}} = 0. \tag{1.11}$$

By using the Lorentz gauge, the Einstein tensor can be derived as

$$G_{\mu\nu} = -\frac{1}{2}\Box \bar{h}_{\mu\nu}, \tag{1.12}$$

where

$$\Box = \eta^{\mu\nu}\frac{\partial}{\partial x^{\mu}}\frac{\partial}{\partial x^{\nu}}. \tag{1.13}$$

From the above, the linearized Einstein equation can be written as

$$\Box \bar{h}_{\mu\nu} = -\frac{16\pi G}{c^4}T_{\mu\nu}. \tag{1.14}$$

1.1.3 Gravitational wave

In the vacuum, since there is no mass, $T_{\mu\nu} = 0$. Therefore, the linearized Einstein equation (1.14) can be written as

$$\Box \bar{h}_{\mu\nu} = 0. \tag{1.15}$$

This is the wave equation for $\bar{h}_{\mu\nu}$. In other words, $\bar{h}_{\mu\nu}$, which represents the distortion from the Minkowski space, is transmitted in space-time as a wave. This wave of the distortion of space-time is called a gravitational wave (GW).

A monochromatic plane wave solution of Eq. (1.15) can be derived as

$$\bar{h}_{\mu\nu} = A_{\mu\nu}\exp(ik_{\alpha}x^{\alpha}), \tag{1.16}$$

where $A_{\mu\nu}$ is the amplitude and k_{α} is the wave number for each axis of the GW. For $\bar{h}_{\mu\nu}$

to satisfy the Einstein equation (1.14) and the Lorentz gauge condition (1.11),

$$A_{\mu\nu}k^{\nu} = 0, \tag{1.17}$$

$$k_{\mu}k^{\mu} = 0. \tag{1.18}$$

Since this solution has the degrees of freedom in selecting coordinates, we take the Transverse Traceless gauge (TT gauge), as a gauge condition together with the Lorentz gauge condition,

$$A^{\alpha}{}_{\alpha} = 0, \tag{1.19}$$

$$A_{\mu\nu}U^{\nu} = 0, \tag{1.20}$$

where U^{ν} is an arbitrary time-like unit vector.

In Eq. (1.20), if $U^{\nu} = \delta^{\nu}{}_{0}$ (time base of the Minkowski space), a time component of $\bar{h}_{\mu\nu}$ is zero from Eq. (1.20) and the trace of $\bar{h}_{\mu\nu}$ is also zero from Eq. (1.19).

Taking the traveling direction of the GW along with the z-axis, a plane wave solution is derived as

$$\bar{h}^{TT}_{\mu\nu} = A_{\mu\nu}e^{i\omega(t-z/c)}, \tag{1.21}$$

$$A_{\mu\nu} = \begin{pmatrix} 0 & 0 & 0 & 0 \\ 0 & \bar{h}_{+} & \bar{h}_{\times} & 0 \\ 0 & \bar{h}_{\times} & -\bar{h}_{+} & 0 \\ 0 & 0 & 0 & 0 \end{pmatrix}, \tag{1.22}$$

where $\bar{h}_{+}$ and $\bar{h}_{\times}$ are amplitudes of each polarization of the GW described later. From Eq. (1.21), we can see that the GW travels at the speed of light. Furthermore, Eq. (1.22) shows the GW is a transverse wave with two degrees of freedom.

Equation (1.21) can be generalized as

$$\bar{h}^{TT}_{\mu\nu} = \sum_{A=+,\times} h_A(\hat{n})e^{A}_{\mu\nu}e^{i\omega(t-\boldsymbol{x}\hat{\boldsymbol{n}}/c)}, \tag{1.23}$$

where $\boldsymbol{x}$ is a position vector of an observation point, $\hat{\boldsymbol{n}}$ is a unit vector in the direction of the GW propagation, and $e^{+}_{\mu\nu}, e^{\times}_{\mu\nu}$ are polarization tensors. $e^{+}_{\mu\nu}$ and $e^{\times}_{\mu\nu}$ can be written as

$$e^{+}_{\mu\nu} \equiv \hat{u}_{\mu}\hat{u}_{\nu} - \hat{v}_{\mu}\hat{v}_{\nu}, \tag{1.24}$$

$$e^{\times}_{\mu\nu} \equiv \hat{u}_{\mu}\hat{u}_{\nu} + \hat{v}_{\mu}\hat{v}_{\nu}, \tag{1.25}$$

where $\hat{\boldsymbol{u}}$ and $\hat{\boldsymbol{v}}$ are unit vectors orthogonal to $\hat{\boldsymbol{n}}$. Since superposition of all directions and

frequencies is an actually observed GW, the GW strength can be written as

$$\bar{h}^{TT}_{\mu\nu} = \sum_{A=+,\times} \int_{-\infty}^{\infty} d\omega \int d^3\hat{\boldsymbol{n}} h_A(\omega, \hat{n}) e^A_{\mu\nu} e^{i\omega(t-\boldsymbol{x}\hat{\boldsymbol{n}}/c)}. \tag{1.26}$$

1.1.4 Gravitational wave radiation

Next, we think about GW radiation. By solving the linearized Einstein equation (1.14), we can discuss the radiation of a GW. Equation (1.14) can be solved by using a retarded potential as

$$\bar{h}_{\mu\nu}(x^0, \boldsymbol{x}) = \frac{4}{G} \int \frac{T_{\mu\nu}(x^0 - \frac{|\boldsymbol{x}-\boldsymbol{x'}|}{c}, \boldsymbol{x'})}{|\boldsymbol{x}-\boldsymbol{x'}|} d^3x'. \tag{1.27}$$

If we assume that a mass distribution of a GW source is sufficiently compact and the source is sufficiently far from an observer, Eq. (1.27) can be approximated by using the quadrupole moment Q_{ij} of the mass distribution as

$$\bar{h}_{\mu\nu} = \frac{2G}{c^4 r} \ddot{Q}_{ij}(t'), \tag{1.28}$$

where $r = |\boldsymbol{x} - \boldsymbol{x'}|$ and $t' = t - r/c$. Q_{ij} can be written by using the mass distribution $\rho(\boldsymbol{x'}, t')$ as

$$Q_{ij}(t') = \int \rho(\boldsymbol{x'}, t') \left(x'_i x'_j - \frac{1}{3}\delta_{ij} x'^i x'^j \right). \tag{1.29}$$

Unlike electromagnetic waves, GWs are not radiated from dipoles. This is because the dipole moment is always zero when we employe the coordinate system which takes the center of mass as the origin. Therefore, GWs are not radiated from an axial symmetrical motion of an object with an axial symmetrical mass distribution.

1.1.5 Interaction between gravitational wave and space-time

To detect GW signals, we need to know how GWs interact with space-time. To think about the interaction of the GW and space-time, we first consider an effect of a GW on a free particle on the Minkowski space-time. In this case,

$$\frac{dx^\mu}{d\tau} = (1, 0, 0, 0). \tag{1.30}$$

From the geodesic equation (1.2) and Eq. (1.10), acceleration of the particle is derived as

$$\begin{aligned} \frac{d^2x^\lambda}{d\tau^2} &= -\Gamma^\lambda{}_{00} \\ &= \frac{1}{2}\left(\frac{\partial \bar{h}^\lambda{}_0}{\partial x^0} + \frac{\partial \bar{h}^\lambda_0}{\partial x^0} - \frac{\partial \bar{h}_{00}}{\partial x^\lambda} \right) \\ &= 0. \end{aligned} \tag{1.31}$$

Therefore, the GW does not give any acceleration to the free particle. The TT gauge can be regarded as a gauge whose coordinates change so that the particle's coordinates do not change due to GWs and remain stationary. However, since this is a characteristic inherent to the TT gauge, it is necessary to introduce proper distances among free particles so as not to depend on the coordinates, in order to consider general interactions.

Consider that a GW traveling in the z direction is incident on two adjacent free particles $P_1(0,0,0,0), P_2(0,\xi_1,0,0)$. If the proper distance hlbetween these particles changes by $\delta\xi$, $\delta\xi$ can be written as

$$\begin{aligned}
\xi + \delta\xi &= \int_{P_1}^{P_2} \left|ds^2\right|^{\frac{1}{2}} \\
&= \int_{P_1}^{P_2} |g_{\mu\nu} dx^\mu dx^\nu|^{\frac{1}{2}} \\
&= \int_0^{\xi} |g_{11}|^{\frac{1}{2}}\, dx \\
&= \left(1 + \frac{1}{2}\bar{h}_{11}\right)\xi, \qquad (1.32) \\
\Rightarrow \delta\xi &= \frac{1}{2}\bar{h}_{11}\xi. \qquad (1.33)
\end{aligned}$$

Equation (1.32) shows that the GW changes the proper distance between the free particles.

Next, let us consider a case where two free falling masses P_1 and P_2 are separated by a tiny distance ξ^i, and a GW traveling in the z-axis direction enters there. The distance between P_1 and P_2 changes by

$$\begin{aligned}
\begin{pmatrix} \delta\xi^1 \\ \delta\xi^2 \end{pmatrix} &= \frac{1}{2}\begin{pmatrix} \bar{h}_+ & \bar{h}_\times \\ \bar{h}_\times & \bar{h}_+ \end{pmatrix}\begin{pmatrix} \xi^1 \\ \xi^2 \end{pmatrix} e^{ik(ct-z)} \\
&= \frac{1}{2}\bar{h}_+ \begin{pmatrix} \xi^1 \\ -\xi^2 \end{pmatrix} e^{ik(ct-z)} + \frac{1}{2}\bar{h}_\times \begin{pmatrix} \xi^2 \\ \xi^1 \end{pmatrix} e^{ik(ct-z)}. \qquad (1.34)
\end{aligned}$$

Therefore, the two degrees of freedom of a GW correspond to the two modes: one in which the y-axis contracts as the x-axis extend (+ mode) and the other in which the + mode is inclined by 45° ($\times$ mode). GWs have the action of extending and contracting the space in this way. Figure 1.1 shows how each polarization of the GW changes the distance between particles.

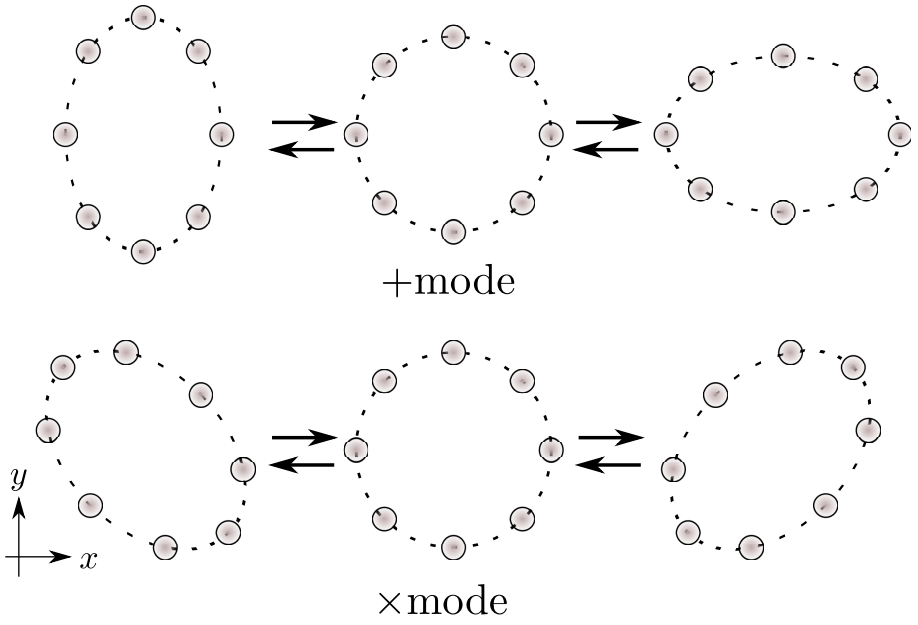

Figure 1.1: Schematic view of polarization modes of the GW. The circles in the pictures represent the movement of free falling masses when the GW in each mode propagates.

1.2 Gravitational wave detector

1.2.1 Principle of the gravitational wave detector

For direct detection of GW signals, it is necessary to observe minute changes in the proper length between free falling masses. Since this change is tiny, we need a detector with high sensitivity. The first attempt to directly detect the GW signal was made by Weber in the 1960's with a resonant GW detector [4]. This type of detector detects the GW signal by measuring a change in length of an elastic body of the detector, which is caused by an elastic vibration mode excited by a tidal force of the GW.

In recent years, the development of a large GW detector using a laser interferometer has been the mainstream. An interferometric type of a GW detector uses an interferometer to observe a differential motion in two arms.

A conceptual diagram of the laser interferometer is shown in Fig. 1.2. A light emitted from a laser source is divided into two arms by a beam splitter (BS). The light reflected by a mirror placed at the end of each arm is recombined on the BS, and the power of the interference light is measured with a photodetector (PD). There are two output ports of the light in the Michelson interferometer. They are called an anti-symmetric (AS) port and a reflection (REFL) port as shown in Fig. 1.2. The interference fringe changes due to the difference in phase change caused during the light travel in each arm. When the difference between two arm lengths fluctuates, the phase difference changes. Then, it causes the change in the fringe. The BS and mirrors are suspended and can be regarded as free

falling masses at the frequencies higher than the resonance frequency of the suspension. When a GW comes in the interferometer, the proper distance between the mirrors and the BS fluctuates differentially as can be seen in Fig. 1.1, so that the interference fringes change. The interferometric detector measures this change and detects a GW signal.

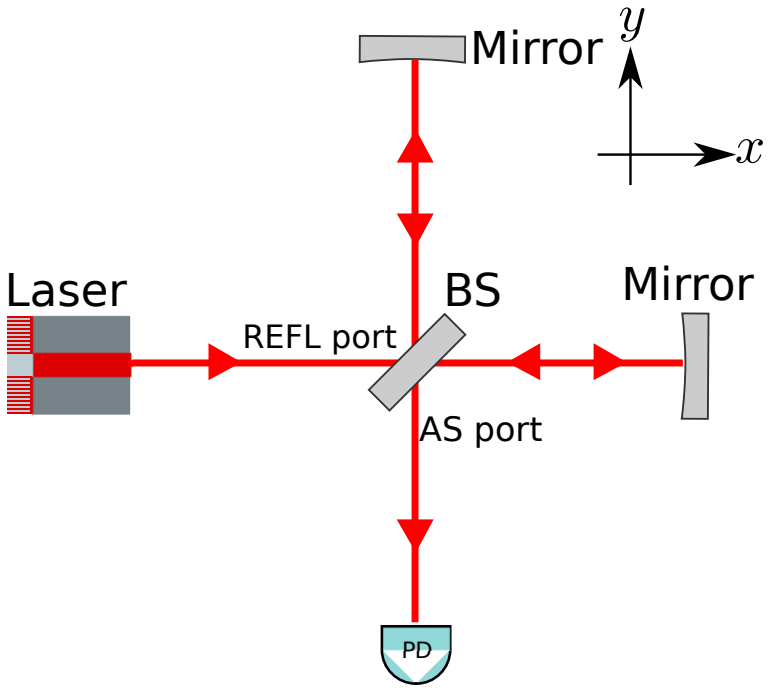

Figure 1.2: Schematic view of a Michelson interferometer

Let us consider the response to the GW in the Michelson interferometer. An electric field of the incident light can be written as

$$E(t) = E_0 e^{i\Omega t}, \tag{1.35}$$

where Ω is an angular frequency of the incoming light and E_0 is an amplitude of the electric field of the light. This light is split into two by the BS. It is reflected by the mirror and the reflected light is recombined on the BS. Then, the power of the recombined light is detected by a PD on the AS port. The electric field of the light detected by the PD can be written as

$$E_{\mathrm{PD}} = E_x e^{i(\Omega t - \phi_x)} + E_y e^{i(\Omega t - \phi_y)}, \tag{1.36}$$

where ϕ_x and ϕ_y are the phase changes of the light in each arm, respectively, and E_x and E_y are the amplitudes of the two divided lights. Therefore, the power of the recombined

light can be derived as

$$\begin{aligned} P_{\mathrm{PD}} &= |E_{\mathrm{PD}}|^2 \\ &= E_x^2 + E_y^2 + 2E_xE_y\cos(\phi_x - \phi_y) \\ &= \frac{P_{\max} + P_{\min}}{2} + \frac{P_{\max} - P_{\min}}{2}\cos(\phi_x - \phi_y), \end{aligned} \tag{1.37}$$

where

$$P_{\max} = (E_x + E_y)^2, \tag{1.38}$$

$$P_{\min} = (E_x - E_y)^2. \tag{1.39}$$

From $P_{\max}$ and $P_{\min}$, a contrast of an interferometer can be defined as

$$c = \frac{P_{\max} - P_{\min}}{P_{\max} + P_{\min}}. \tag{1.40}$$

From Eq. (1.37), an interferometer whose contrast is closer to 1 is more sensitive to the phase difference.

Let the proper distances from the BS to each mirror be ξ_x and ξ_y, respectively. Assuming that each arm is on the xy axis and the GW of the + polarization is incident in the z-axis direction. The phase rotations ϕ_x and ϕ_y can be written as

$$\phi_x(t) = \frac{2\xi_x\Omega}{c} + \frac{\Omega}{2}\int_{t-2\xi_x/c}^{t} dt' h(t'), \tag{1.41}$$

$$\phi_y(t) = \frac{2\xi_y\Omega}{c} - \frac{\Omega}{2}\int_{t-2\xi_y/c}^{t} dt' h(t'), \tag{1.42}$$

where $h(t)$ is an amplitude of the GW. Note that signs of the interactions of the GW in the x direction and the y direction are opposite. Then, if we assume that $\xi_x \sim \xi_y \sim \xi$, the difference between the phase rotations ϕ_x and ϕ_y can be derived as

$$\phi_x - \phi_y = \frac{2(\xi_x - \xi_y)\Omega}{c} + \delta\phi_{\mathrm{GW}}, \tag{1.43}$$

where

$$\begin{aligned} \delta\phi_{\mathrm{GW}} &= \Omega\int_{t-2\xi_x/c}^{t} h(t')dt' \\ &= \Omega\int_{t-2\xi_x/c}^{t} dt\int_{-\infty}^{\infty} d\omega h(\omega) \\ &= \int_{-\infty}^{\infty} d\omega\frac{2\Omega}{\omega}\sin\left(\frac{\xi\omega}{c}\right)e^{-i\xi\omega/c}h(\omega)e^{i\omega t} \\ &\equiv \int_{-\infty}^{\infty} d\omega H_{\mathrm{MI}}(\omega)h(\omega)e^{i\omega t}, \end{aligned} \tag{1.44}$$

where $\delta\phi_{\rm GW}$ is the difference in the phase rotations caused by a GW, and $H_{\rm MI}(\omega)$ is the sensitivity of the interferometer to the GW. Equation (1.44) shows the information on the GW is included in the phase of the light. From Eq. (1.37), the power of the light on the PD can be written as

$$\begin{aligned} P_{\rm PD} &\simeq \frac{P_{\rm max}+P_{\rm min}}{2} + \frac{P_{\rm max}-P_{\rm min}}{2}\left\{\cos\left(\frac{2(\xi_x-\xi_y)\Omega}{c}\right) + \delta\phi_{\rm GW}\sin\left(\frac{2(\xi_x-\xi_y)\Omega}{c}\right)\right\} \\ &= A\delta\phi_{\rm GW} + (\text{DC term}), \end{aligned} \tag{1.45}$$

where A is the coefficient of the signal to the phase rotation caused by the GW. Therefore, the power on the PD changes by the GW, and we can detect the GW signal by using the signal from the PD.

The frequency responses of the Michelson interferometers with some arm lengths are shown in Fig. 1.3. At the low frequencies, the sensitivity increases as the arm length becomes longer, whereas at high frequencies, the sensitivity cannot be improved by changing the arm length. That is because the GW, which has a shorter period than a storage time of the light in the interferometer, is canceled during a round trip in the arm. The angular frequency ω_c at which the sensitivity gets maximum can be derived as

$$\omega_c = \frac{\pi c}{2\xi}. \tag{1.46}$$

Above ω_c the sensitivity decreases because of the cancellation.

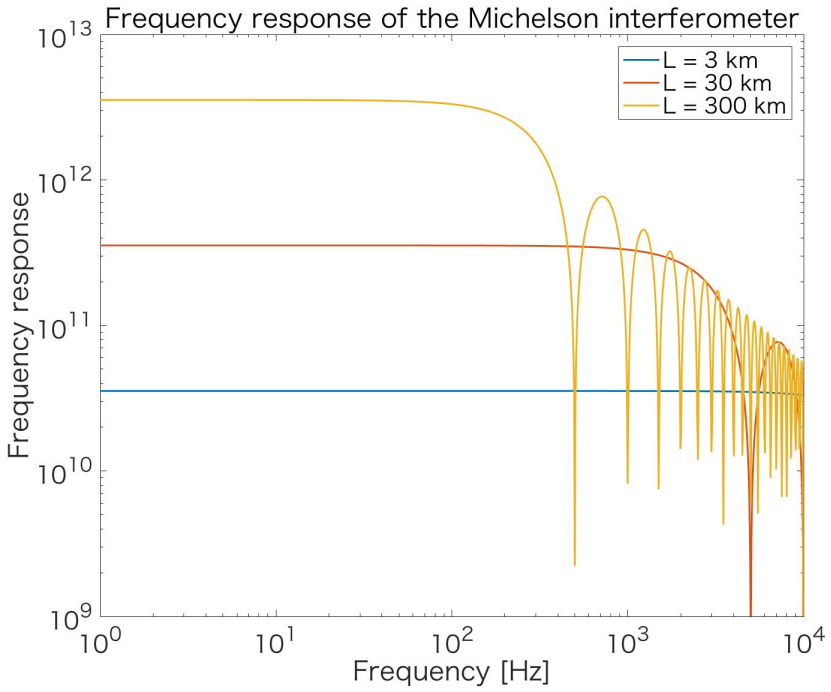

Figure 1.3: Sensitivities of Michelson interferometers with the arm length of 3 km, 30 km, and 300 km, respectively.

1.2.2 Optical configuration of GW detectors

The optical configuration of GW detectors currently being operated or constructed is not a simple Michelson interferometer, but the one combining several optical cavities to improve the sensitivities. Several optical configurations are listed below:

Fabry-Perot Michelson interferometer

The sensitivity of a GW detector becomes best when it detects the GW signal of the frequency satisfying Eq. (1.46). The arm length with the maximum sensitivity to the 1-kHz GW signal is about 75 km. However, it is impossible to construct an interferometer with such a long arm. Therefore, in the GW detector, the sensitivity is improved by using Fabry-Perot cavities (described in Appendix A) as the arms and extending the effective arm lengths. This interferometer configuration is called a Fabry-Perot Michelson interferometer (FPMI). Two mirrors constituting the Fabry-Perot cavity are called an input test mass[1] (ITM) and an end test mass (ETM). The schematic diagram of the FPMI is shown in Fig. 1.4.

The sensitivity $H_{\rm FPMI}(\omega)$ of the FPMI [5] can be written as

$$H_{\rm FPMI}(\omega) = \frac{2\alpha\Omega}{\omega}\frac{\sin\gamma}{1 - r_F r_E e^{-2i\gamma}}e^{-i\gamma}, \tag{1.47}$$

where r_F and r_E are the values of reflectivitiy of the ITM and the ETM, respectively, γ and α are written as

$$\alpha = \frac{t_F^2 r_E}{-r_F + (r_F^2 + t_F^2)r_E}, \tag{1.48}$$

$$\gamma = \frac{\xi\omega}{c}, \tag{1.49}$$

where t_F is the transmittance of the ITM. The absolute value of the sensitivity $H_{\rm FPMI}(\omega)$ can be derived as

$$|H_{\rm FPMI}(\omega)| = \frac{2\alpha\Omega}{\omega(1 - r_F r_E)}\frac{|\sin\gamma|}{\sqrt{1 + (2\mathcal{F}\pi)^2\sin^2\gamma}}, \tag{1.50}$$

where $\mathcal{F}$ is the finesse (described in Appendix A.2.1) of the arm cavity. The sensitivities of FPMIs with several values of finesse are shown in Fig. 1.5. The arm length is assumed to be 3 km in all the cases. The FPMI with high finesse cavities has the low cut-off frequency above which the sensitivity starts to get worse, and the low cut-off frequency leads to the high sensitivity at low frequencies. This is because the average bounce number is proportional to the finesse, and the higher finesse cavity has a longer effective length

[1] In GW detectors, the main mirrors are often called test masses.

and a longer storage time. The average bounce number N_{FPMI} can be derived as

$$N_{\mathrm{FPMI}} = \frac{2\mathcal{F}}{\pi}. \tag{1.51}$$

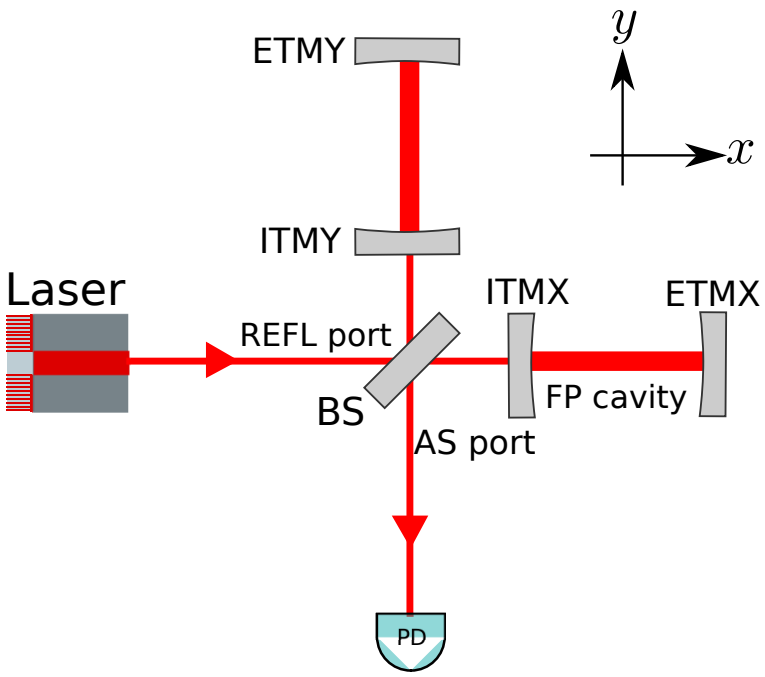

Figure 1.4: Schematic view of an FPMI. Fabry-Perot cavities are used to extending the effective arm lengths. An ITMX(Y) and an ETMX(Y) represent the input test mass and the end test mass of the $x(y)$-arm.

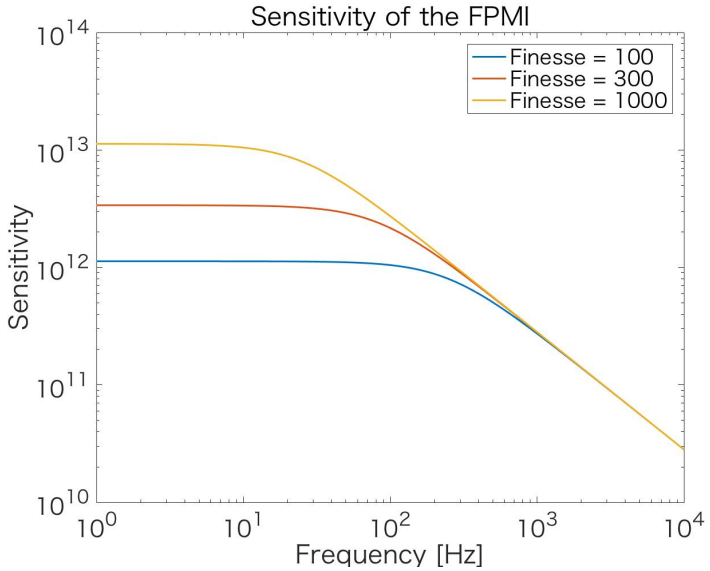

Figure 1.5: Sensitivities of FPMIs with the arm length of 3 km and finesse of 100, 300, and 1000, respectively.

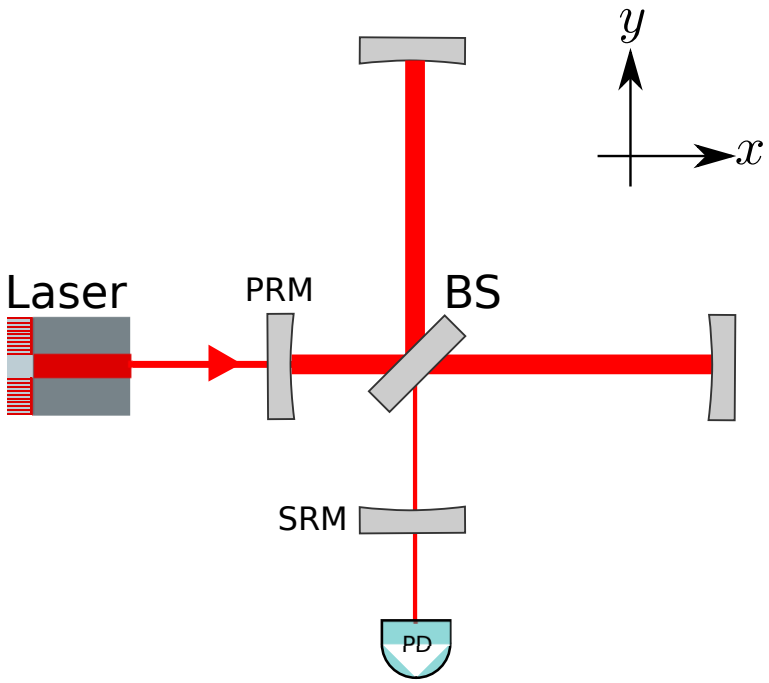

Figure 1.6: Schematic view of a DRMI. A PRM increases the effective power in the interferometer, and an SRM amplifies the GW signal.

Dual recycling Michelson interferometer

Another configuration to improve the GW sensitivity of the interferometer is a dual recycling Michelson interferometer (DRMI). A schematic diagram of the DRMI is shown in Fig. 1.6.

Normally, in a GW detector, the mirror is controlled at a position, where the light does not come out to AS port, to reduce the shot noise. We call this control a dark fringe lock. In this case, all the power of the light returns to the REFL port. Here, by reflecting the returned light in phase with the incident light, the effective power in the interferometer can be increased. The cavity formed by the Michelson interferometer and the power recycling mirror (PRM) installed at the REFL port is called a power recycling cavity (PRC). The PRC reduces the shot noise by increasing the effective power in the interferometer. The ratio of the laser power on the BS with the PRM to that without the PRM is called a power recycling gain.

In the case of the dark fringe lock, all GW signals are transmitted to the AS port. By reflecting this signal to the interferometer, it is possible to amplify the signal. The mirror installed at the AS port is called a signal recycling mirror (SRM), and the cavity composes of the SRM and the Michelson interferometer is called a signal recycling cavity (SRC).

As shown in Eq. (1.44), the length of the arm that gives the maximum sensitivity is determined by the GW frequency. This is because the GW whose period is shorter than a storage time of the light in the interferometer is canceled during a round trip in

the arm. Since the GW signal is transmitted to the AS port, the PRC does nothing for the GW signal. Therefore, the cut-off frequency of the GW signal is not affected. On the other hand, the SRC changes the cut-off frequency since the SRM reflects the GW signal and extends the storage time. Therefore, even if the FPMI and the SRC are used in combination, there is not a significant merit. However, by combining the PRC and the SRC, the sensitivity can be improved. Such a configuration is called a dual-recycling Michelson interferometer (DRMI).

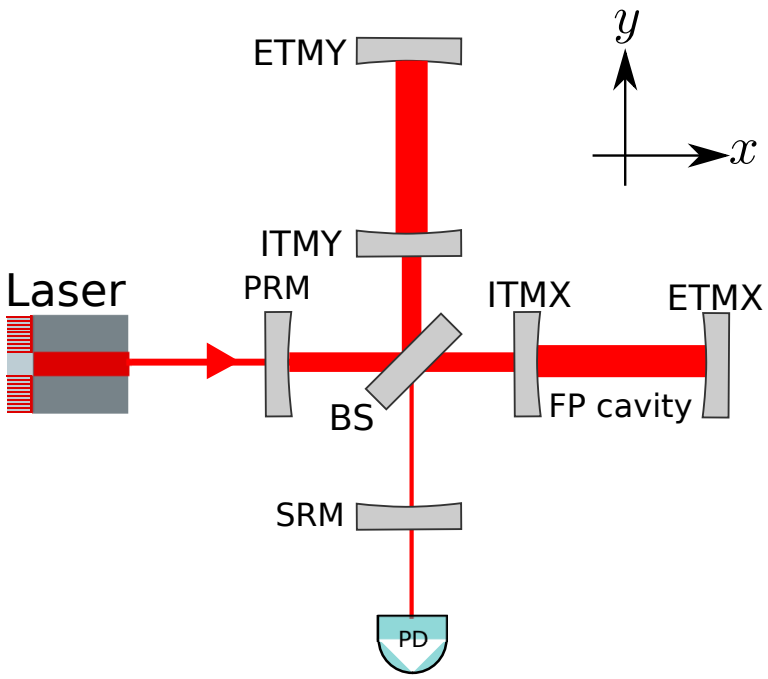

Figure 1.7: Schematic view of an RSE interferometer. The configuration itself seems to be the combination of an FPMI and a DRMI, though the role of SRC is opposite to that in the DRMI interferometer.

Resonant sideband extraction interferometer

The optical configuration of a resonant sideband extraction (RSE) interferometer is a combination of an FPMI and a DRMI [6]. The schematic view of the RSE interferometer is shown in Fig. 1.7. Although the arm cavity and the PRC play the same role as in the FPMI and the DRMI, the role of the SRC is exactly opposite to the DRMI in the RSE interferometer. The length of the SRC in the DRMI and that in the RSE are shifted by a half wavelength of the laser. As a result, the SRC works to lower the effective finesse of the arm cavities with respect to the GW signal. Therefore, the cut-off frequency of the frequency response gets higher, which means that the sensitivity gets better up to higher frequencies. On the other hand, since the finesse of the arm cavity with respect to the incident light is not changed by the SRM, a large power is accumulated in the arm cavity, and the GW signal itself is enhanced. In the RSE interferometer, the arm cavity is

designed to have high finesse, so that the signal strength is increased. At the same time, high sensitivity can be achieved up to higher frequencies by the SRM.

1.2.3 Noise of the gravitational wave detector

In a GW detector, it is necessary to detect a tiny distance change, so that various disturbances must be identified as noise. All the noises have to be sufficiently suppressed to detect the GW signal. Furthermore, most efforts are devoted to noise reductions. This subsection explains the main noise sources in the GW detector.

Seismic noise

The seismic motion shakes mirrors of a GW detector, and this mirror motion is the displacement noise in the GW detector. The mirrors are isolated from a seismic motion by being suspended.

Assuming that the movement of the suspended mass, as shown in Fig. 1.8, is sufficiently small, the equation of motion can be derived as

$$m\ddot{x} = -\frac{mg}{l}(x - x_g) - \gamma\dot{x}, \tag{1.52}$$

where m is the mass, g is the acceleration of gravity, x_g is the ground motion, l is the length of the suspension, and γ is the viscous damping coefficient. Here, the third term on the right side represents the damping force proportional to the velocity of the mass. Equation (1.52) can be solved by Fourier transformation as

$$\tilde{x}(\omega) = \frac{\omega_0^2}{-\omega^2 + iQ\omega_0\omega + \omega_0^2}\tilde{x_g}(\omega), \tag{1.53}$$

where ω_0 is the resonance angular frequency of the suspension, and Q is the quality factor. They can be derived as

$$w_0 = \sqrt{\frac{g}{l}}, \tag{1.54}$$

$$Q = m\frac{\omega_0}{\gamma}. \tag{1.55}$$

As the quality factor represents the magnitude of energy dissipation, the oscillation is damped faster in a larger quality factor system.

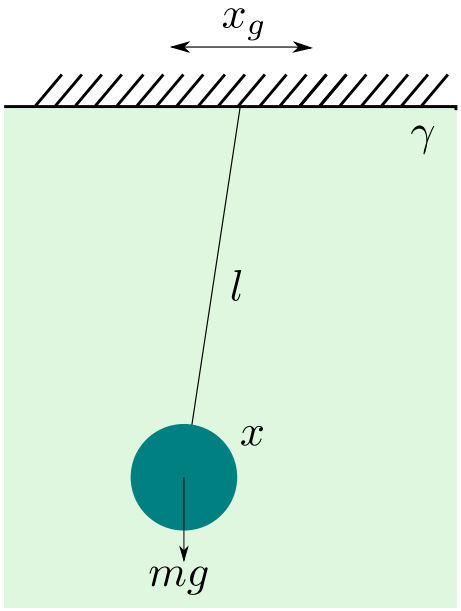

Figure 1.8: Schematic view of the pendulum in a viscous medium, where m is the mass, g is the acceleration of gravity, x_g is the ground motion, l is the length of the suspension, and γ is the viscous damping coefficient.

As shown in Eq. (1.53), the transfer function of the suspension from the ground motion to the mass motion is inversely proportional to the square of the frequency in the frequency region satisfying $\omega \gg \omega_0$. Therefore, the longer suspension, which has the lower resonance frequency, can attenuate the seismic motion more efficiently at high frequencies. Furthermore, in the case of the multi-stage suspension, each stage has the seismic isolation as represented by Eq. (1.53), and the whole suspension works as the cascading seismic isolation filters.

The mirrors of the GW detector are suspended by long suspensions which have several stages to reduce the seismic motion. However, since there is a limit to lowering the resonance frequency, it is difficult to provide sufficient vibration isolation in the low-frequency region as $\omega \ll \omega_0$. Therefore, the seismic noise becomes a problem at low frequencies (typically below several tens of Hz).

Thermal noise

A thermal noise limits the sensitivity at the frequency range around 100 Hz. Since the mirrors of an interferometer are in contact with a heat bath of a finite temperature, the contact causes thermal vibration, and this vibration also induces a displacement noise. Besides, since the suspension suspending the mirror is also in contact with the heat bath, the vibration mode is excited and causes the displacement of the mirror. It is known that the dissipation of the system determines the thermal noise by the fluctuation-dissipation theorem [7, 8]. This noise can be reduced by using a mirror with a substrate of a high quality factor or by using a suspension with a fiber of a high quality factor. Therefore,

fused silica which has a high quality factor at room temperature is used as a substrate material in mirrors of current GW detectors [9].

The thermal noise can be reduced by cooling mirrors and suspensions. In the next generation GW detectors, the thermal noise will be suppressed by cooling mirrors to a cryogenic temperature. However, since the quality factor of fused silica is low at cryogenic temperatures, fused silica cannot be used in cryogenic detectors. On the other hand, sapphire and silicon have high quality factors at cryogenic temperatures and high thermal conductivities. Therefore, they are used as a mirror substrate material for cryogenic interferometers [10, 11].

Quantum noise

A quantum fluctuation of light causes a quantum noise. It is one of the noises limiting the sensitivity of a GW detector. The quantum noise includes a shot noise and a radiation pressure noise. The shot noise is caused when the power of light is measured on a PD due to a fluctuation of the number of photons reaching the detector by the uncertainty principle. Furthermore, since photons have momenta, they apply forces to the mirror when the mirror reflects them, and this force also fluctuates due to the fluctuation of the number of photons. As a result, the mirror of the interferometer is shaken, and the displacement noise is induced. This is called the radiation pressure noise.

Although the shot noise can be reduced by increasing the laser power, the radiation pressure noise is simultaneously increased. Due to this trade-off relationship, there is a sensitivity limit which cannot be overcome only by changing the power, and this limit is called a standard quantum limit [12]. To surpass the standard quantum limit, techniques such as squeezing of light have been developed [13].

Noise of laser source

The fluctuations of the laser frequency and the laser intensity can cause the noises in a GW detector.

First, consider the frequency noise. The frequency noise can be regarded as equivalent to the phase noise, since the differentiation of the phase noise is the frequency noise. Therefore, we consider the phase noise here. Let a phase fluctuation be $\delta\phi(t)$, then Eq. (1.37) can be rewritten as

$$\begin{aligned} P_{\mathrm{PD}} =& \frac{P_{\max} + P_{\min}}{2} \\ &+ \frac{P_{\max} - P_{\min}}{2} \cos[\phi_x - \phi_y + \{\delta\phi(t - \xi_x/c) - \delta\phi(t - \xi_y/c)\}]. \end{aligned} \tag{1.56}$$

When the lengths of the arms are equal, the phase fluctuation is not a problem. However, if there is asymmetry in the lengths of the arms, the phase fluctuation becomes noise on the GW signal. In the FPMI or the RSE interferometer, the asymmetry in finesse of each arm cavity also causes the phase noise. The ratio at which the phase noise is suppressed

by the symmetry of the interferometer is called a common mode reduction ratio (CMRR). In a GW detector, the frequency noise is reduced by controlling the frequency of the laser using an optical cavity as a reference.

Next, consider the intensity noise. Let $E_x = E_y = E_0/2$, $\phi_x - \phi_y = (2n+1)/2\pi + \phi_- + \delta\phi_{\rm GW}$, where n is an integer, and the intensity noise be δP. Equation (1.37) can be rewritten as

$$\begin{aligned} P_{\rm PD} &= \frac{P_0 + \delta P}{2} + \frac{P_0 + \delta P}{2}\cos(\phi_x - \phi_y) \\ &\simeq \frac{P_0 + \delta P}{2}(\delta\phi_{\rm GW} + \phi_-) \\ &\simeq \frac{P_0}{2}\delta\phi_{\rm GW} + \frac{\delta P}{2}\phi_-. \end{aligned} \tag{1.57}$$

Therefore, by controlling the arm length such as $\phi_x - \phi_y = (2n+1)/2\pi$, the intensity noise can be suppressed. However, the arm lengths cannot be controlled perfectly, so the intensity noise becomes a problem. The intensity noise can be reduced by measuring the laser power with a PD and feeding back the signal to an amplitude actuator.

When higher-order spatial modes are mixed in the laser, the contrast of the interferometer decreases and the performance of the interferometer deteriorates. Also, if the propagation direction of the beam spatially fluctuates, this beam motion, which is called the beam jitter, couples with the cavity to become noise. As will be described in Appendix A.4.3, these noises can be reduced by using optical cavities.

1.3 Gravitational wave astronomy

1.3.1 Gravitational wave astronomy

GWs are radiated from any motion of a mass involving a change in a quadrupole moment of a mass distribution. For example, a strength of a GW from an object that moves at velocity v with mass M, can be roughly estimated from Eq. (1.28) as

$$\begin{aligned} h &\sim \frac{G}{c^4}\frac{Mv^2}{r} \\ &= 10^{-16}\left(\frac{M}{M_\odot}\right)\left(\frac{10\ {\rm kpc}}{r}\right)\left(\frac{v}{c}\right)^2. \end{aligned} \tag{1.58}$$

As seen in Eq. (1.58), the amplitude of the generated GW is tiny, and it is impossible with current technologies to observe the GW signal generated from motions of objects on the earth. Since the strength of the GW depends on the mass and the velocity of the source, an astronomical event in which a massive object moves at high speed can be a detectable GW source.

The reason why the GW signal is difficult to be detected is the weakness of the grav-

itational interaction. The strength of the electromagnetic interaction is characterized by the fine-structure constant $\alpha = e^2/\hbar c = 1/137$, where e is the elementary charge, and the corresponding constant representing the strength of the gravitational interaction is as small as $\alpha_G = Gm_p^2/\hbar c = 7 \times 10^{-37}$, where m_p is the mass of a proton. This tiny interaction of gravity is a disadvantage in the sense of detection of GW signals.

On the other hand, the weakness of the gravitational interaction can be an advantage from the astronomical and the astrophysical viewpoints. For example, when considering a formation process of a neutron star in a supernova explosion, the information obtained by light is at most about the surface of the star. Photons carrying information about the inside of the neutron star is scattered and absorbed by many electrons and atoms. On the other hand, since the interaction of the GW is weak, a GW generated in the central region of the neutron star is hardly scattered and absorbed. Therefore, it is possible to observe the GW signal carrying the information on the central region of the neutron star. The advantage and the significance of the GW astronomy is that the GW allows us to explore astrophysics and universe beyond reach of conventional astronomical probes using the electromagnetic waves.

1.3.2 Sources of gravitational waves

As mentioned above, astronomical events are the detectable GW source. Several types of gravitational wave sources are listed in this subsection.

Compact binary coalescence

There are many binary systems in the universe formed of compact stars with huge mass like neutron stars and black holes. In these binary systems, two stars rotate around each other, and this rotational motion generates a GW. Since the generation of the GW involves energy dissipation, the distance between the two stars gradually decreases, and the rotation frequency increases accordingly. This stage is called an in-spiral phase, and a frequency of a GW generated in this phase increases with time. This frequency sweeps from 10 Hz up to about 1 kHz in the binary neutron stars, and hundreds of Hz′s in the binary black holes.

The frequency and strength evolution of the GW in the in-spiral phase can be written approximately as [14]

$$f_{\mathrm{GW}}(\tau) \sim 1.9 \text{ Hz} \left(\frac{1.4M_\odot}{M_c}\right)^{\frac{5}{8}} \left(\frac{1 \text{ day}}{\tau}\right)^{\frac{3}{8}}, \tag{1.59}$$

$$h(\tau) \sim 1.7 \times 10^{-23} \left(\frac{M_c}{1.4M_\odot}\right)^{\frac{5}{4}} \left(\frac{\tau}{1 \text{ day}}\right)^{-\frac{1}{4}} \left(\frac{15 \text{ Mpc}}{r}\right), \tag{1.60}$$

where τ is the time to coalescence, r is the distance between the source and the observer,

and M_c is the chirp mass. The chirp mass is defined as $M_c = (m_1 m_2)^{3/5}(m_1 + m_2)^{-1/5}$, where m_1 and m_2 are the mass of each compact object.

After the in-spiral phase, the two compact objects collide and coalesce. In this coalescence phase, the waveform of the GW generated from the binary black holes can be accurately predicted by the general theory of relativity. Therefore, if the waveform of the GW radiated by the coalescence of the binary black holes is analyzed, the general theory of relativity is verified.

The waveform of the GW generated by the coalescence of the binary neutron stars depends on the mass and the state equation of inside of each neutron star. The mass of each neutron star can be determined by the waveform in the in-spiral phase. Therefore, it is expected that we can know the state equations of neutron stars by observing and analyzing GW signals from the coalescence of binary neutron stars.

As we will describe later, the first detection of the GW signal was from the coalescence of the binary black holes in 2015. Since the binary black holes had not been found until this first GW detection, this detection was not only the first detection of the GW signal, but also the first evidence for the binary black holes. Therefore, this historical event opened a new window of the astronomy, i.e. the GW astronomy.

Rotation of compact stars

A rotating compact star like a neutron star can be a GW source, when it has axial asymmetry in its mass distribution. Such a rotating star is called a pulsar. An amplitude of a GW from a pulsar depends on the magnitude of the asymmetry and it can be written as [15]

$$h \sim 1.1 \times 10^{-25} \left(\frac{\epsilon}{10^{-6}}\right) \left(\frac{I}{10^{38}\ \mathrm{kg\ m^2}}\right) \left(\frac{10\ \mathrm{kpc}}{r}\right) \left(\frac{f_{\mathrm{GW}}}{1\ \mathrm{kHz}}\right), \tag{1.61}$$

where I is the moment of inertia around the axis of rotation and ϵ is the asymmetry of the pulsar. The asymmetry is defined as $\epsilon = (I_1 - I_2)/I$, where I_1 and I_2 are the moments of inertia around the axes orthogonal to the rotation axis.

The magnitude of asymmetry of the neutron star depends on the state equation of the neutron star. Therefore, by analyzing the amplitude of GW signals radiated from pulsars, there is a possibility that some knowledges about the mechanism of the asymmetry and the state equation of the neutron star can be obtained.

Supernova

A supernova explosion is a major explosion that occurs when a massive star ends its lifetime. The supernova explosion mechanism has not been fully understood. Therefore, the magnitude and the waveform of the radiated GW is not well predicted. Along with recent improvements in supercomputer performance and numerical simulation techniques, quantitative understanding is expected to further advance in the near future. The GW

strength from the supernova explosion at 20 Mpc far from the earth is estimated as $h = 10^{-21} - 10^{-22}$ and the frequency of the GW is predicted as widespread around 1 kHz [16].

Stochastic background

A stochastic background of the GW includes GWs from numerous unresolved astrophysical sources, cosmological origins in the early universe, and cosmic strings. In particular, GWs from the early universe are interesting. As the universe has been filled with plasma for 380,000 years since the universe was born, electromagnetic waves could not travel freely in this period. On the other hand, GWs could travel freely even in plasma because the gravitational interaction is weak. Therefore, by observing GW signals generated immediately after the universe creation, it is possible to directly observe the early universe. The prediction of the strength and frequency of these GWs varies widely according to the theoretical models.

One example of the stochastic GW background is a GW generated in the inflation [17]. It is predicted that GWs were generated by the quantum fluctuation of space-time during the inflation, and the GWs generated at that time still remain as background. If we can detect the GWs derived from the inflation, we will have evidence for the inflation model in the early universe.

1.3.3 Detection of gravitational wave signals

The first detection of GW signals was one of the most important scientific events in the last several decades. With the detection of a GW signal from a coalescence of binary black holes [3] as a start, two more GW signals from binary black holes coalescences were detected [18, 19] by Advanced LIGO. In 2017, the first detection with three detectors, two detectors of Advanced LIGO and Advanced Virgo was achieved [20]. Moreover, a GW signal from a coalescence of binary neutron stars was detected [21].

The first event observed in 2015 is named GW150914. This event was not only the first detection of the GW signal but also the first evidence for the binary black holes and their coalescence. According to the analysis, this GW source is the binary black holes located about 410 Mpc away from the earth and their masses were $36M_{\odot}$ and $29M_{\odot}$, respectively. The GW signal frequency was swept from 35 Hz to 150 Hz during 0.2 seconds. After the coalescence, the waveform called a ring down, which occurs for a short period after the coalescence, appeared around 250 Hz. This waveform of the GW was in accordance with the one expected by the general theory of relativity. Figure 1.9 shows the waveform of this event.

What is surprising in GW150914 was that the GW source was not binary neutron stars but binary black holes. Until the first observation, many scientists expected to observe

GW signals from coalescences of binary neutron stars first. This observation gave us an important suggestion on the event rate of coalescences of binary black holes, namely, 9-240 events per year within the range of 1 Gpc, which is far more than the predicted value of 0.1-1 events per year. It was also a surprise that their masses were about $30M_{\odot}$. The mass of a celestial compact object that had been a candidate for a black hole by the X-ray observations so far was approximately $10M_{\odot}$.

Since the first observation, the GW signals from three coalescences of binary black holes have been observed by two detectors of Advanced LIGO. In August 2017, Advanced Virgo in Italy participated in the observation, and GW signals from a coalescence of the binary black holes and a coalescence of the binary neutron stars were detected simultaneously by the three detectors of Advanced LIGO and Advanced Virgo. These events are named GW170814 and GW170817, respectively. The source position determination accuracy of GW150914 was 600 deg^2, as the position was determined by the two detectors. On the other hand, in the case of GW170814, the source position determination accuracy was improved to be 60 deg^2, as the position was determined by the three detectors. From the above, one sees that simultaneous observations by three or more detectors are indispensable, when determining the position of the GW source. In addition, We emphasize that GW170817 was also an important event in the multi-messenger astronomy described in the next section.

The masses and the distances of the compact objects of each event are summarized in Table 1.1.

Event	Source	Primary mass $[M_{\odot}]$	Secondary mass $[M_{\odot}]$	Final mass $[M_{\odot}]$	Distance [Mpc]
GW150914 [3]	BH-BH	36^{+5}_{-4}	29^{+4}_{-4}	62^{+5}_{-4}	410^{+160}_{-180}
GW151226 [18]	BH-BH	$14^{+8.3}_{-3.7}$	$7.5^{+2.3}_{-2.3}$	$20.8^{+6.1}_{-1.7}$	440^{+180}_{-190}
GW170104 [19]	BH-BH	$31.2^{+8.4}_{-6.0}$	$19.4^{+5.3}_{-5.9}$	$48.7^{+5.7}_{-4.6}$	880^{+450}_{-390}
GW170608 [22]	BH-BH	12^{+7}_{-2}	7^{+2}_{-2}	$18.0^{+4.8}_{-0.9}$	340^{+140}_{-140}
GW170814 [20]	BH-BH	$30.5^{+5.7}_{-3.0}$	$25.3^{+2.8}_{-4.2}$	$53.2^{+3.2}_{-2.5}$	540^{+130}_{-210}
GW170817 [21]					
(Low-spin priors)	NS-NS	$1.36 - 1.60$	$1.17 - 1.36$	$2.74^{+0.04}_{-0.01}$	40^{+8}_{-14}
(High-spin priors)	NS-NS	$1.36 - 2.26$	$0.86 - 1.36$	$2.82^{+0.47}_{-0.09}$	40^{+8}_{-14}

Table 1.1: Parameters of the GW source for each event. BH represents a black hole and NS represents a neutron star.

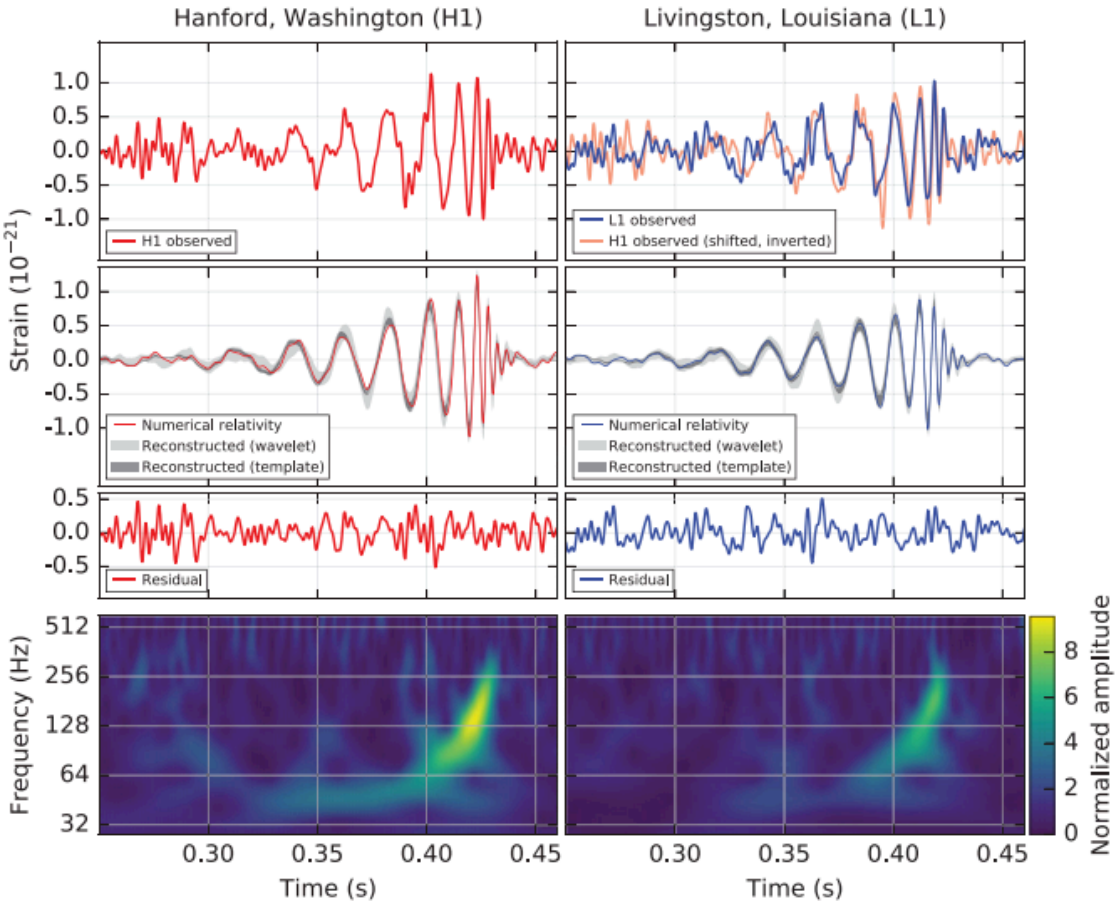

Figure 1.9: Waveform of GW150914 [3].

1.3.4 Multi messenger astronomy

Some GW sources have mechanisms that radiate electromagnetic waves and neutrinos. In the case of such a GW source, the simultaneous observations of GW signals, electromagnetic waves, and neutrinos can provide more information than the individual observation can. The astronomy based on coordinated observations in such a way is called the multi-messenger astronomy.

For the multi-messenger astronomy, the quick communication among the relevant observations is essential. A particularly important thing for the GW observation is to determine the arrival direction of GWs accurately and to communicate it to the other observations. There is a big difference in angular resolution between a GW detector and other detectors. For example, typical optical telescopes can determine the arrival direction of light with one telescope, while the GW detector cannot precisely determine the arrival direction of a GW with one detector. In order to determine the arrival direction, it is necessary to use the difference in the arrival time of the GW by using several GW detectors. For this purpose, three or more GW detectors are necessary.

By the multi-messenger astronomy that includes GWs, research on γ-ray burst (GRB)

is expected to make progress. A GRB is a phenomenon in which γ-rays are observed like a flash. A GRB with a short duration of about 2 seconds are called a short GRB. Although it was assumed that the source of the short GRB was a coalescence of binary neutron stars, there was no experimental verification. However, in August 2017 when the GW signal from the coalescence of the binary neutron stars was detected by Advanced LIGO and Advanced Virgo, the GRB was also observed with a delay of 1.7 seconds [23]. This event demonstrated that short GRBs originated from coalescences of the binary neutron stars. The γ-ray intensity emitted from GRB170817A was lower than those emitted from any other short GRBs ever observed. It is an open question whether such dark short GRBs have just been overlooked or GRB170817A is special. In any case, if similar GRBs are observed with multi-messenger observations with GWs, it is expected that they will provide new knowledge on astrophysics.

1.3.5 Gravitational wave detectors in the world

LIGO

Large Interferometer Gravitational wave Observatory (LIGO) is a GW observatory composed of two sites in the U.S. One is located in Hanford, Washington State, and the other in Livingstone, Louisiana State. LIGO is divided into three phases.

The first phase is called initial LIGO (iLIGO) [24]. In this phase, there were one detector with 4 km arm length and another with 2 km arm length in the Hanford site, and another with 4 km arm length in the Livingstone site. The optical configuration was a Power recycled Fabry-Perot Michelson interferometer (PRFPMI) which combines an FPMI and a PRC. The laser source was a 10 W Nd:YAG laser. To isolate the test masses from the seismic vibration, they are suspended by single-stage pendulums which are mounted on four-layer passive vibration isolation platforms. iLIGO was sensitive to detect the GW signal from a coalescence of a pair of 1.4-solar mass neutron stars at about 15 Mpc far from the earth. Figure 1.10 shows the iLIGO sensitivity curves during the fifth science run of iLIGO.

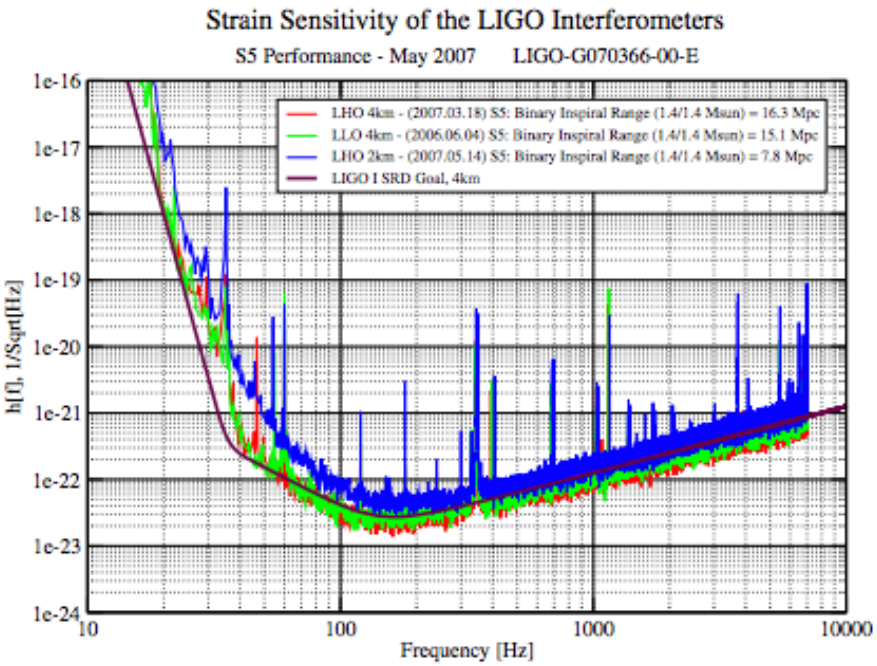

Figure 1.10: Designed sensitivity of iLIGO (magenta), together with measured sensitivity curves of the iLIGO during the final science run (red, green, and blue) in strain amplitude spectral density [24].

After iLIGO, LIGO shifted to the second phase called Enhanced LIGO (eLIGO) [25]. In this phase, the laser power was increased to 35 W, and a signal acquisition method was changed from the RF demodulation method (developed from the Pound-Drever-Hall (PDH) method described in Appendix A.3) to what is called the DC readout method [26]. In the RF demodulation method, the interferometer is locked on a dark fringe, and the signal of differential motion of the arm lengths, which includes GW information, is acquired by the beat signal between the RF sideband and the carrier light. Even in the case of dark fringe lock, junk lights such as RF sidebands and higher-order spatial mode lights leak out to the AS port. Since junk lights increase the shot noise, they should be reduced somehow. The junk lights can be filtered by a cavity, however, it will also filter out the RF sideband including the GW signal. On the other hand, in the DC readout method, the control point in the mirrors is microscopically shifted from the dark fringe, so that the weak DC light leaks to the AS port. In this case, the intensity of the DC light leaking to the AS port varies in proportion to the GW signal, so the RF sideband is unnecessary. Therefore, the cavity to filter the junk lights at the AS port can be used to reduce the shot noise. This cavity is called an output mode cleaner (OMC) and installed in eLIGO.

After eLIGO, a major improvement was made. This third phase is called Advanced LIGO (aLIGO) [27]. aLIGO has a design sensitivity 10 times better than that of iLIGO. aLIGO can observe GW signals from a coalescence of binary neutron stars at 190 Mpc far away, and it is expected to detect about 10 coalescences of binary neutron stars per year.

In fact, aLIGO has successfully observed GW signals from five coalescences of binary black holes and from one coalescence of binary neutron stars. aLIGO uses the iLIGO building and the vacuum tanks, but the detector part is completely new. aLIGO composes of two detectors with 4-km arm length, one in each site. The laser power is increased up to 125 W, and the optical configuration is an RSE interferometer. As with eLIGO, the signal acquisition method is the DC readout method, and the OMC is also used.

Compared to eLIGO, the vibration isolation system has been greatly improved in aLIGO, and the test masses are isolated by three-stage vibration isolation systems. In the first step, a basic system chamber (BSC), in which a test mass is stored, is isolated by an active seismic isolation platform called a hydraulic external pre-isolator (HEPI). In the BSC, an internal seismic isolator (BSC-ISI), which is an in-vacuum two-stage seismic isolator, is mounted as the second stage of the seismic isolation system. The BSC-ISI is a system that combines the active seismic isolation with the passive one. Figure 1.11 shows the schematic view and the CAD diagram of the HEPI and the BSC-ISI. As the final stage, the test mass is suspended from the BSC-ISI platform by a quadruple suspension. The CAD diagram of the quadruple suspension is shown in Fig. 1.12.

aLIGO completed the construction of the equipment in mid 2014 and the first observation as aLIGO was done for 4 months from September 2015. During that observation, aLIGO succeeded in the first detection of the GW signal from the coalescence of the binary black holes, GW150914. At that time, the observation range for GW signals from the coalescence of binary neutron stars was 60 Mpc.

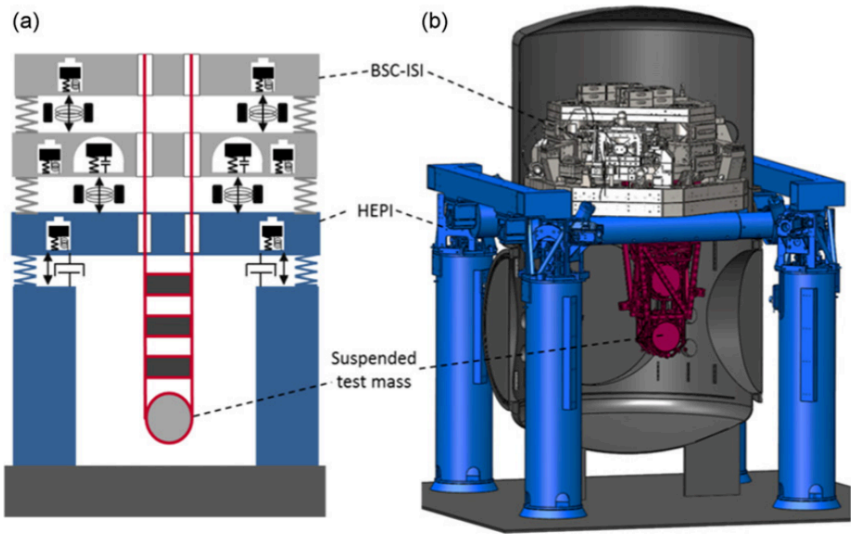

Figure 1.11: (a) Schematic and (b) CAD diagram of the isolation system supporting the core optics in the BSC chambers [28].

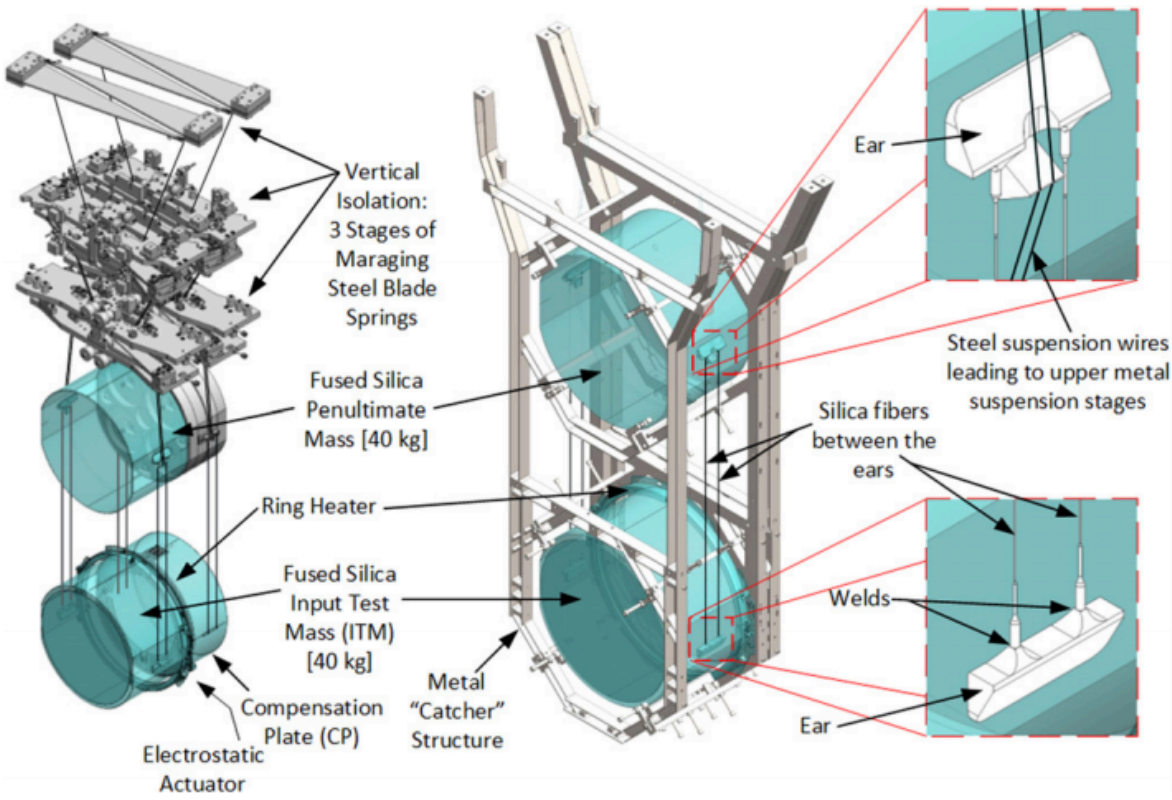

Figure 1.12: CAD diagram of the quadruple pendulum suspension for the core optics of the interferometer [27].

Virgo

Virgo is a GW detector with arm length of 3 km built near Pisa, Italy. The Virgo project can be divided into two phases, Virgo [29] and Advanced Virgo (AdV) [30].

Virgo′s interferometer configuration was a PRFPMI like iLIGO. It is noteworthy that test masses are suspended by using a seismic isolation system called a superattenuator. The superattenuator is effective above 10 Hz and it is a prototype of what is now used in AdV. Figure 1.13 shows the CAD diagram of the superattenuator. The superattenuator is a vibration isolation system similar to that in KAGRA described in Chapter 2, consisting of inverted pendulums, seismic filters, and a mirror payload. The inverted pendulum is a horizontal mechanical oscillator with an ultralow resonance frequency by balancing a restoring force of a metal elastic rod and an anti-spring force due to the weight of a mass. Figure 1.14 shows the schematic view of the inverted pendulum. Each pendulum chain has the seismic isolation system in the vertical direction using cantilever blade springs. The seismic filter incorporates a mechanism that reduces the spring constant of the cantilever blade spring by using the anti-spring effect of the magnet to lower the resonance frequency.

The detection range for the GW signal from coalescence of binary neutron stars of Virgo was 7 Mpc. Since 2007, Virgo and LIGO have fully cooperated in the data analysis. They actually took 5-month data simultaneously and the data analysis was made in cooperation.

This was the beginning of the current GW detector network.

After that, Virgo started the AdV project that uses the infrastructure of Virgo and updates detectors from Virgo. AdV will achieve the sensitivity 10 times higher than Virgo′s design sensitivity using technologies such as a high power laser, an RSE interferometer configuration, a DC readout, and an OMC. When the design sensitivity is achieved, the detection range for a GW signal from a coalescence of binary neutron stars will reach 140 Mpc. AdV completed the construction of the equipment in mid 2016. After improving its sensitivity, AdV joined the simultaneous observation with LIGO in August 2017. During that observation, AdV detected the GW signals from the coalescences of the binary black holes [20] and of the binary neutron stars [21].

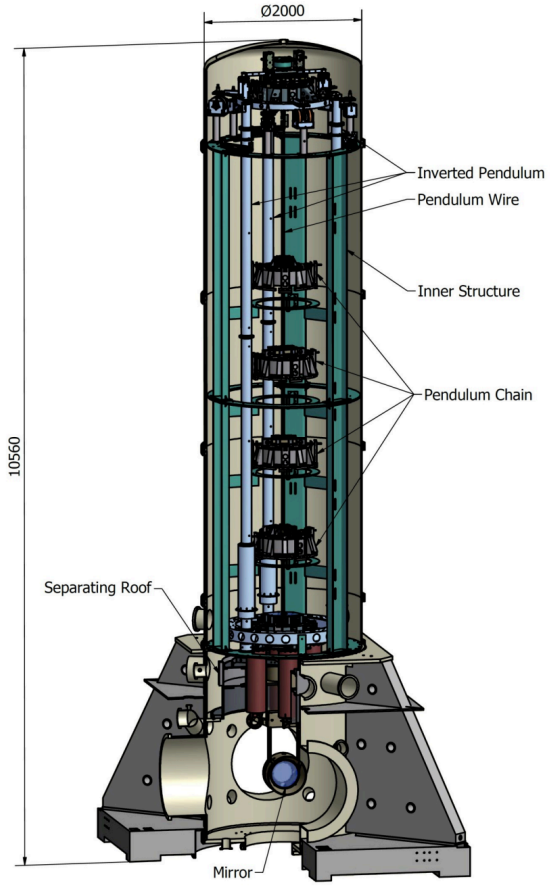

Figure 1.13: CAD diagram of the Virgo superattenuator [29].

KAGRA

KAGRA is a GW detector with arm length of 3 km under construction in the mine of Kamioka, Hida City, Gifu Prefecture, Japan. iLIGO and Virgo is called the first generation detectors, and aLIGO and AdV are called the second generation detectors. On the other hand, KAGRA is called the 2.5th generation detector. This is because the KAGRA incorporates several more advanced features. KAGRA is constructed underground for a

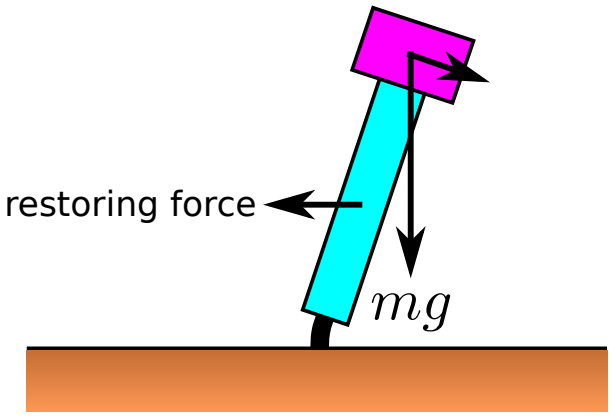

Figure 1.14: Schematic view of the inverted pendulum. The gravity acts as the anti-spring force. The effective spring constant gets small when anti-spring force and restoring force get balanced, which means the resonance frequency gets low.

quiet seismic motion and a stable environment, and the mirrors and suspensions will be cooled down to cryogenic temperatures to suppress thermal noises in them. Furthermore, the test masses are isolated from the seismic motion by a large seismic isolation system similar to the Virgo superattenuator. The detail of each feature will be described in Chapter 2.

KAGRA has a design sensitivity that can detect a GW from a coalescence of binary neutron stars at the distance of 140 Mpc. In the case of the coalescence of a pair of 30-solar mass black holes, the detection range reaches 1.27 Gpc, corresponding to the expected event rate of 24-440 events per year [31]. Figure 1.15 shows the design sensitivity of KAGRA. The sensitivity of KAGRA is limited by the seismic noise at low frequencies, the quantum noise at high frequencies, and the thermal noise in the middle. A comparison of the sensitivities among aLIGO, AdV, and KAGRA is shown in Fig. 1.16. At the frequencies around 100 Hz, where GWs from coalescences of binary neutron stars and binary black holes sweep, all detectors have the design sensitivity at a similar level. On the other hand, KAGRA shows the best sensitivity in the band below 10 Hz, thanks both to the quiet seismic motion level at the Kamioka mine where KAGRA is located and to the mirrors isolated from the seismic motion with huge seismic isolation systems. In addition, the sensitivity of KAGRA is slightly better than that of the other detectors around 100 Hz. This is because the thermal noise in the mirrors is reduced by cooling them.

Other detectors

Prototype detectors such as GEO600 [32] in Germany, 40-m prototype [33] in the U.S., TAMA300 [34], and CLIO [35] in Japan, were in operation before, and they mostly serve as technology development sites for the current large GW detectors.

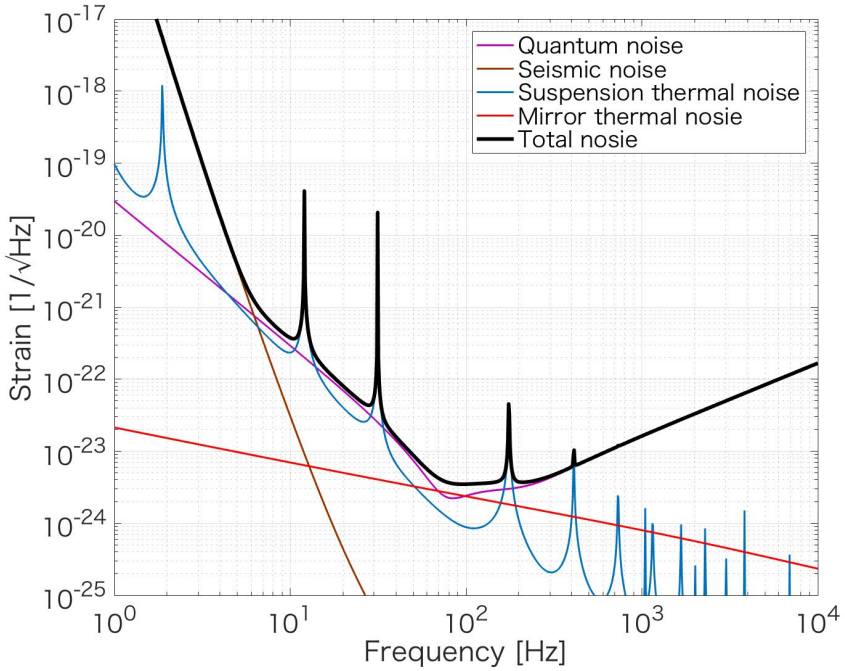

Figure 1.15: Sensitivity curve of KAGRA (black). The sensitivity is limited by the seismic noise (brown), the suspension and the mirror thermal noise (cyan and red), and the quantum noise (magenta).

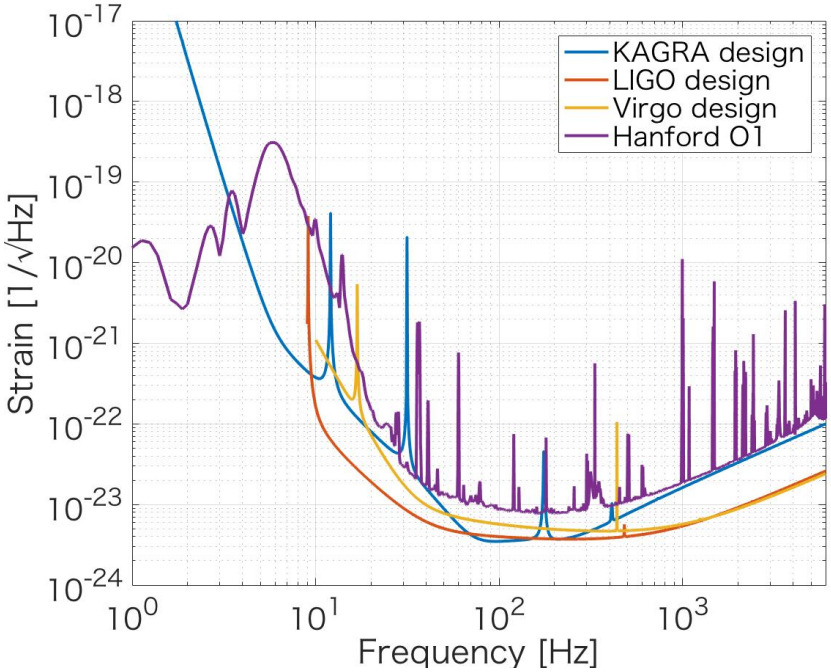

Figure 1.16: Sensitivity curves of each detector. The designed sensitivity curves of KAGRA (blue), LIGO (red), and Virgo (yellow) are shown, together with the measured sensitivity of the Hanford site (magenta) in the first observation run (O1) of aLIGO in 2015.

1.3.6 Significance of KAGRA

Before the first GW detection in 2015, GW150914, the GW detectors in the world were trying to observe the first GW event. However, the situation has changed completely. aLIGO and AdV have already succeeded in detecting the GW signals from the several events. In this situation, we would like to confirm the significance of KAGRA once again.

As shown in Fig. 1.16, the sensitivity at lower frequencies than 10 Hz is better than other detectors. Figure 1.17 shows the spectra of the GW150917 and the typical neutron star binary coalescence with the designed sensitivity curves of KAGRA and aLIGO [36]. As shown in Fig. 1.17, KAGRA can measure the GW signal at the frequencies where aLIGO cannot measure. This means that KAGRA can measure GW signals in the in-spiral phase for a longer time than the other detectors. As mentioned in Subsection 1.3.2, the mass of each star is determined by the waveform in the in-spiral phase. Therefore, the longer measurement of the GW signal in the in-spiral phase by KAGRA can determine the mass more accurately. Furthermore, the predicted GW signal of the known spinning pulsars are shown in Fig. 1.18 [37]. The amplitude is calculated under the assumption that the observed spin-down rate is fully dominated by the gravitational wave emission. As shown in Fig. 1.18, the frequencies of many of the GWs from the pulsars are below 10 Hz, where only KAGRA has the sensitivity for the GW signal, and actually only KAGRA can detect the GW signals from some of such pulsars with the designed sensitivity.

The second significant contribution of KAGRA as the fourth detector is the improvement of the duty cycle of the GW detector network. It is necessary for the interferometer to control the distance between the mirrors and lock it to the operating point. The interferometers easily lose lock, and until it gets re-locked, the observation stops. If we assume each detector has the 80 % duty cycle, the duty cycle, when all detectors in a three-detector network are operated in coincidence, is approximately 50 %. If the fourth detector join to the detector network, the duty cycle, when more than three detectors are in operation, is approximately 80 %.

The third significant contribution is the improvement of the ability to localize the GW sources. By using the Monte Carlo simulation, the sky localization accuracy with three detectors as well as with four detectors are calculated [38]. By this simulation, with the three detectors of aLIGO and AdV assumed, the average accuracy of the sky localization of a GW from a coalescence of binary neutron stars is 30.25 deg^2. On the other hand, with the four detectors including KAGRA assumed, the sky localization accuracy improves to 9.5 deg^2.

Position determination accuracy, which is important in the future development of the GW astronomy, will be greatly improved by KAGRA joining the GW detector network. Therefore, the task currently required to KAGRA is to achieve the sensitivity necessary to the GW observation as soon as possible and to participate in the GW detector network.

The most recent task is to participate in the third observation (O3) by aLIGO and AdV planned in 2019. For this purpose, it is necessary to reach the sensitivity corresponding to the observation range of at least 10 to 20 Mpc for a coalescence of the binary neutron stars. It is urgent to construct every subsystem in KAGRA to achieve such a sensitivity.

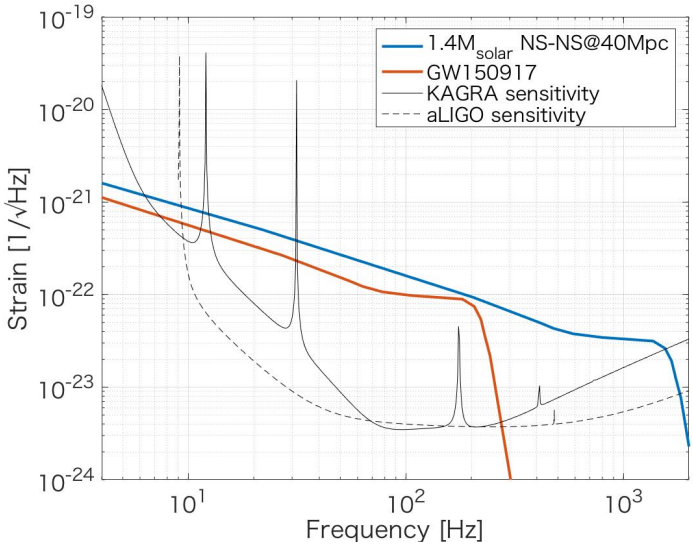

Figure 1.17: Strain spectra of the GW150917 and a typical coalescence of a neutron star binary with the designed sensitivities of KAGRA and aLIGO. A neutron star binary with the chirp mass of $1.4M_{\odot}$ is assumed as the typical neutron star binary. Black solid and dashed curves are the designed sensitivity of KAGRA and aLIGO, respectively.

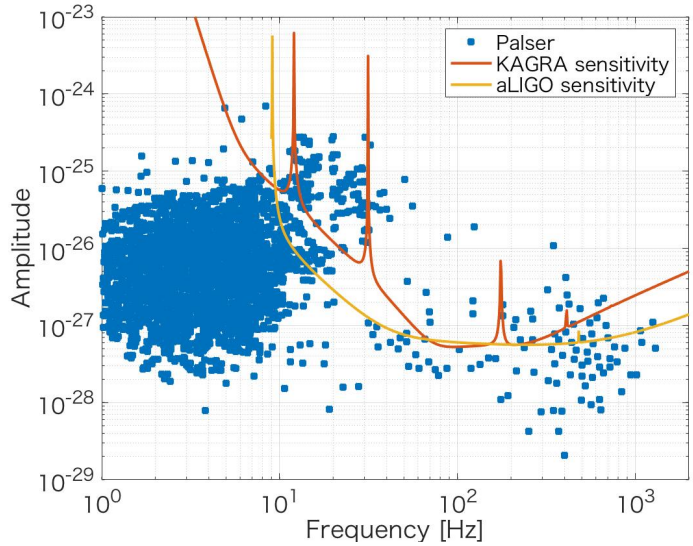

Figure 1.18: Predicted GW signals from pulsars with the KAGRA and aLIGO designed sensitivities with 1 year observation.

1.4 Research target and outline of this thesis

As mentioned above, KAGRA has to join the GW detector network in the world as soon as possible, and for that, the reduction of noises is an essential task. The GW detectors consist of various components such as a laser system, suspensions, mirrors, cryogenic systems, vacuum systems, a data management system, a data analyzing system, an environmental monitoring system, and so on. In the GW detector project, various subsystems work on each subsystem to reduce each noise.

Among them, a subsystem for reducing the noise of the laser and supplying low-noise light to the interferometer is called an input optics subsystem. The roles required for the input optics are as follows:

- Reduction of the frequency noise and the intensity noise.
- Reduction of the beam jitter.
- Mode matching to the main interferometer

Another requirement is for the duty cycle. The input optics has the several optical cavities through which the laser passes. If the cavities are not locked on the resonance, no light is provided into the main interferometer. The input optics must not disturb the main interferometer operation. During the first observation run of aLIGO, the percentage of time, when the interferometer is in the state of observing or locking, was about 80 % [39]. KAGRA should aim at a duty cycle equal to or higher than that. Therefore, the requirement for the duty cycle of the input optics was set to 95%.

The stabilization of the incident light to the main interferometer is one of the essential tasks in order to participate in the GW detector network. Installation of the input optics is ongoing in KAGRA, and up to now the installation of the in-air optics which are called pre-stabilized laser (PSL) and the triangular optical cavity called input mode cleaner (IMC) has been completed.

The requirements at 100 Hz for each noise are as follows:

- Frequency noise at the IMC output: $\delta f < 1\ \mathrm{Hz}/\sqrt{\mathrm{Hz}}$
- Relative intensity noise at the IMC output: $\delta p < 10^{-8}\ /\sqrt{\mathrm{Hz}}$
- Beam jitter at the output of the PSL: $\sqrt{(\delta x/w_0)^2 + (\delta\theta/\alpha_0)^2} < 3 \times 10^{-10}\ /\sqrt{\mathrm{Hz}}$

Here, δf is the frequency noise, δp is the relative intensity noise, δx is the transverse motion of the beam, $\delta\theta$ is the angular motion of the beam, w_0 is the waist size of the beam, and the α_0 is the divergence angle of the beam (see Appendix A.4.1).

The frequency stabilization system is one of the most important systems in the input optics subsystem. The frequency stabilization system uses optical cavities as the frequency reference. The linear cavity, called the reference cavity (RC), located on the PSL table

and the IMC are the optical cavities used as the frequency reference in KAGRA. In the frequency stabilization, if the length of the frequency reference cavity fluctuates due to seismic vibration, the frequency stability gets worse. Therefore, the cavities for the frequency references need to be isolated from the seismic motion. For example, a schematic view of seismic isolation system of the input mode cleaner which is one of the reference cavities of aLIGO is shown in Fig. 1.19. The input mode cleaner is isolated from seismic motion by using the HEPI, which is also used for vibration isolation of the test mass, and the HAM (Horizontal Access Module chamber)-ISI, which is the seismic isolated chamber simplified from BSC-ISI, and the mirrors are further suspended with a 3-stage suspension. Also in AdV, the vibration isolation of the input mode cleaner is performed by a suspension called a short superattenuator which reduces the six-stage seismic filter of a supperattenuator to the three-stage one. On the other hand, as mentioned in Subsection 3.2.3, KAGRA has a very simple seismic isolation system with a passive vibration isolation by stacks and a two-stage suspensions for the input mode cleaner. This is thanks to the fact that the seismic motion of the KAGRA site is quiet. However, it is necessary to confirm that such a simplified system can actually satisfy the requirement for the frequency stability.

The author is responsible for the design, the installation, the investigation, and the integration of the pre-stabilized laser table and the input mode cleaner in KAGRA. The frequency stabilization system which is one of the main role of the PSL and the IMC is the main theme of this thesis. In this thesis we describe the modeling based on actual measurements and performance evaluation of the frequency stabilization system. Furthermore, the simulation of the improved frequency stabilization system necessary to achieve the requirement is described. The main target of my research written in this thesis is to construct the frequency stabilization system which satisfies the requirement for the frequency noise and the duty cycle.

The outline of this thesis is as follows. Chapter 2 explains the KAGRA overview. Firstly each feature of the KAGRA such as the optical configuration, the suspensions, and the cryogenic systems is described. Then, we move to the input optics and describe the component and the stabilization system. In Chapter 3, we describe installation works of the input optics. As described in Chapter 2, the KAGRA project is divided into two phases: initial KAGRA (iKAGRA) and baseline KAGRA (bKAGRA). The input optics also has two phases, and the installation works in both phases are described. In Chapter 4, we explain the frequency stabilization system. The frequency stabilization system was investigated and modeled by the several measurements, and we estimated the frequency noise based on this model. Then, we compare this estimated noise with the requirement, and evaluate the performance of the frequency stabilization system. Chapter 5 summarizes this thesis and describes future works.

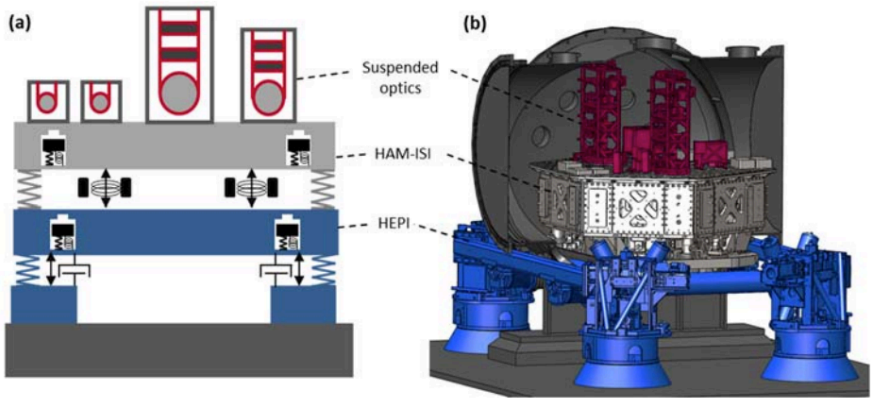

Figure 1.19: (a) Schematic view and (b) CAD diagram of the isolation systems supporting the input mode cleaner in the HAM chambers in aLIGO [27].

2 Gravitational wave detector KAGRA

KAGRA is a gravitational wave (GW) detector currently under construction in Japan. KAGRA is built underground to suppress the noise due to the seismic motion. Furthermore, by cooling mirrors and suspensions to a cryogenic temperature, the thermal noise is suppressed and the improvement in sensitivity is expected. These two features are not employed in other GW detectors such as aLIGO and AdV constructed so far.

A low-noise light source is indispensable for the GW detector. It is the role of input optics to provide the low-noise light to the main interferometer. In this chapter, we will first describe the features of KAGRA in Section 2.1. Then, we focus on the input optics in Section 2.2.

2.1 Overview of KAGRA

KAGRA is the GW detector constructed under the Ikenoyama of Kamioka, Hida city, Gifu prefecture (36°24′43″N in latitude, 137°18′21″E in longitude). An excavation of a tunnel with a total length of 6 km took over 1 year and 10 months. Figure 2.1 shows a top view of KAGRA. A control room is located at the Mozumi office in the upper left corner of the figure. It takes about 10 minutes by car from the Mozumi office to the Atotsu entrance which is the entrance to the KAGRA tunnel. Facilities such as Super-Kamiokande (SK) and CLIO are also built under Ikenoyama.

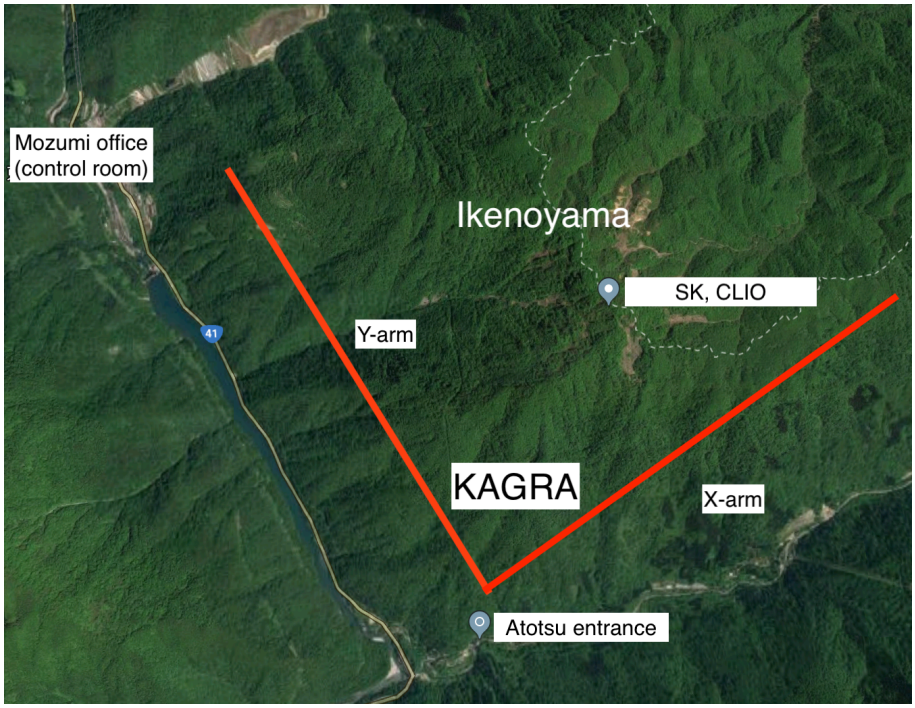

Figure 2.1: Top view of KAGRA. The control room is located at the Mozumi office, and the Atotsu entrance is the entrance of the KAGRA tunnel.

KAGRA has three features: the location of the underground, cryogenic mirrors and suspensions, and an RSE interferometer. In general, the sensitivity of the GW detector is limited by the seismic noise at the low frequencies below 10 Hz, by the thermal noise at the intermediate frequencies between 10 Hz and 200 Hz, and by the shot noise at the high frequencies above 200 Hz. By constructing the interferometer in the underground of Kamioka, where the seismic motion is small, the seismic noise is smaller than in other detectors. Also by cooling the mirrors and the suspensions, the thermal noise can be suppressed. Furthermore, by using the RSE interferometer, the shot noise can be reduced. Therefore, by these techniques, it is possible to improve the sensitivity at the whole frequency range to the level which allows us to detect GW signals. In this section, each feature will be explained in detail.

2.1.1 Optical configuration of KAGRA

The configuration of KAGRA is an RSE interferometer with an arm length of 3 km. In Fig. 2.2, the overview of KAGRA is shown. In KAGRA, we cannot inject the high power laser light so as to keep the mirrors at the cryogenic temperature. If the power transmitted through the ITMs is too high, the input test masses will be heated by absorption of the laser power in the substrate. Therefore, high finesse arm cavities are used to amplify the GW signal by raising the power accumulated in the cavities, and then the cut off frequency of the GW signal is brought up to 100 Hz by utilizing the effect of the signal extraction of the RSE interferometer. In this configuration, the injection power and the power recycling gain don′t need to be so high. The design finesse of the KAGRA′s arm cavities is 1530, while the design finesse of the LIGO′s arm cavities is 450. As a result, the incident laser power to achieve the design sensitivity in KAGRA is 78 W which is about 60% of that of aLIGO.

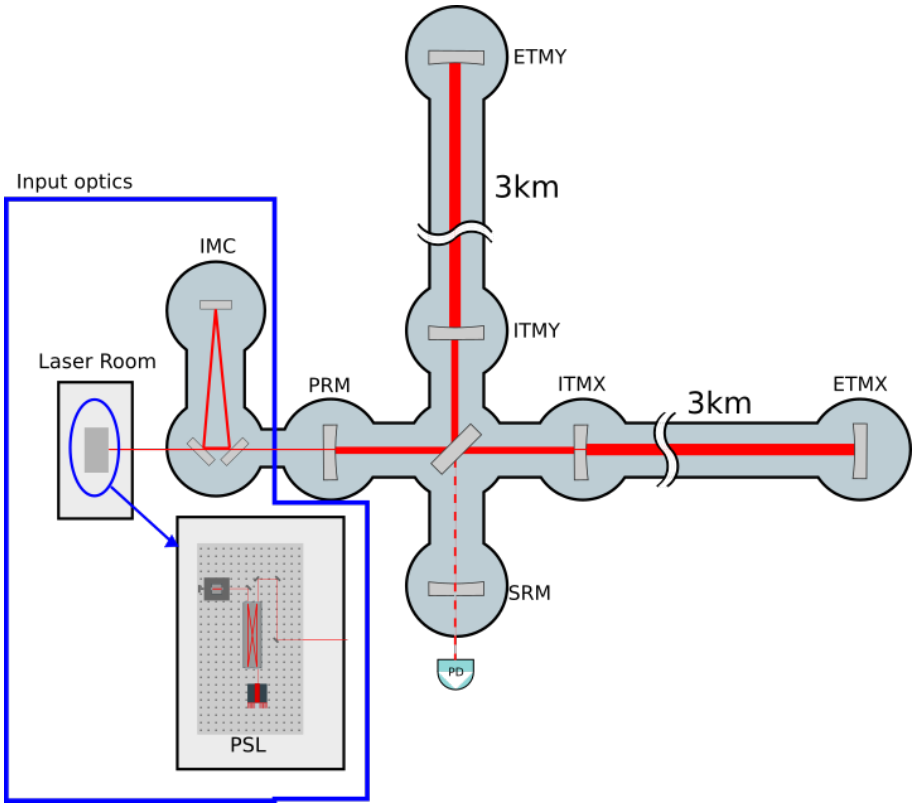

Figure 2.2: Overview of the KAGRA interferometer. The input test masses (ITMX and ITMY) and the end test masses (ETMX and ETMY) compose the arm cavities. The power recycling mirror (PRM) and the signal recycling mirror (SRM) compose the power recycling cavity (PRC) and the signal recycling cavity (SRC), respectively.

2.1.2 Underground detector

KAGRA is built underground. By excavating a L-shaped tunnel horizontally, we built an interferometer underground at a depth of 200 m. A primary purpose is to reduce the seismic noise described in Subsection 1.2.3. The seismic motion level at the interferometer is 1/100 lower than that in Chiba prefecture which is located in the suburb of Tokyo, by setting up the interferometer in the tunnel on the hard rock ground. The plot in Fig. 2.3 shows a spectrum of the seismic motion around the KAGRA site. Since CLIO is located underground of the same mountain as KAGRA, the CLIO seismic spectrum is equivalent to that of KAGRA. The seismic motion level of KAGRA is hundred times lower than that in Kashiwa City, Chiba Prefecture [40].

Another advantage of the underground site is an environmental stability. The temperature and the humidity in the tunnel are constant throughout the year, which makes it possible to keep the environment inside the tunnel optimal for the experiment. Changes in the environment cause changes in the interferometer conditions such as an alignment of the beam, suspension lengths, and so on. These changes in the interferometer conditions prevent a stable operation. Therefore, the underground environment has a significant

advantage in operating the GW detector.

The gravity gradient causes another noise limiting the sensitivity of the GW detector. The gravitational field fluctuates due to a change in a density distribution caused by the seismic motion, and the gravitational fluctuation shakes the mirrors in the GW detector. This noise is called the gravity gradient noise. In KAGRA, the calculation shows that the gravity gradient noise is about ten times lower than that in aLIGO [41].

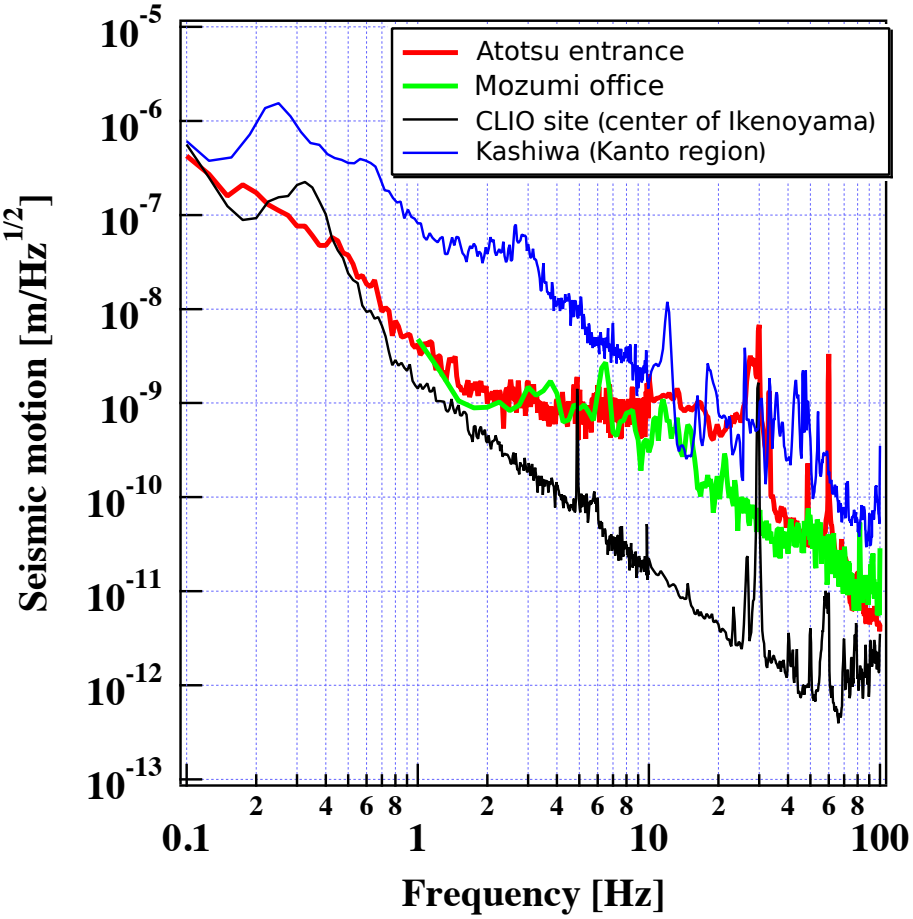

Figure 2.3: Spectrum of the seismic motion. The Atotsu entrance and the Mozumi office are shown in Fig. 2.1. Although the Atotsu entrance and the Mozumi office are located on the ground surface, the seismic motions at these places are quieter than that in Kashiwa which is in the suburb of Tokyo. This is because the Kamioka area is on the hard rock. Furthermore, the seismic motion around CLIO is quieter than that at Atotsu and Mozumi in the higher frequency rage than 2 Hz, because CLIO is located underground. As KAGRA is located underground inside the same mine as CLIO, the seismic motion at the KAGRA site is expected to have the same level as at the CLIO site [40].

2.1.3 Type-A suspension

In a GW detector, mirrors are suspended to be isolated from the seismic motion. A vibration isolation performance of a suspension is determined by the resonance frequency and the number of stages of the suspension as described in Subsection 1.2.3. Therefore, the longer suspension has the better isolation performance due to the lower resonance frequency. In KAGRA, the seismic isolation is done by suspending the test mass with a eight-stage suspension with a total length of 13.5 m. This suspension is called type-A, and it is divided into a room temperature part and a cryogenic temperature part. The room temperature part is called a type-A tower, and the cryogenic temperature part is called a cryogenic payload. We describe the cryogenic payload in the next subsection. Figure 2.4 shows the schematic view of the type-A suspension and the CAD diagram of the type-A suspension chamber.

The type-A tower is similar to the Virgo′s superattenuator. At the first stage, inverted pendulums (IPs) are used to isolate the seismic motion at low frequencies. The IP can adjust the resonance frequency by the load weight, and it can realize the resonance frequency of 0.1 Hz or less. Therefore, the IP can isolate the mirror from the seismic motion in the frequency band from 0.2 Hz to 0.5 Hz called a micro seismic motion. The micro seismic motion is the ground motion excited by the waves in the sea. A stage called a top filter, which has a vertical vibration isolation system, is mounted on the IP. Then, four vertical vibration isolation stages are suspended from the top filter. The top three among the four stages are called standard filters, and the bottom one is called a bottom filter. Those stages have the vertical isolation filters called geometric anti-spring (GAS) filters [42]. The GAS filter is a vibration isolator using cantilever blades. By balancing the upward restoring force of the cantilever and the gravitational force, the effective spring constant can be reduced and the resonance frequency can be lowered. Figure 2.5 shows the schematic view of the GAS filter. From the bottom filter, the cryogenic payload is suspended.

The difference between the Type-A suspension and the Virgo superattenuator is the length of the IP. Since the IP is mounted on the ground in AdV, it is necessary to lengthen the IP to construct the long suspension. For this reason, the IP with the height of about 10 m is used in AdV. However, mechanical resonances exist in the low frequency region due to its length, and it may cause the seismic noise and the difficulty in control of the interferometer. On the other hand, the IP with the length of about 2 m is enough for KAGRA, since we can excavate a tunnel of 2 floors and hang the suspension from the second floor.

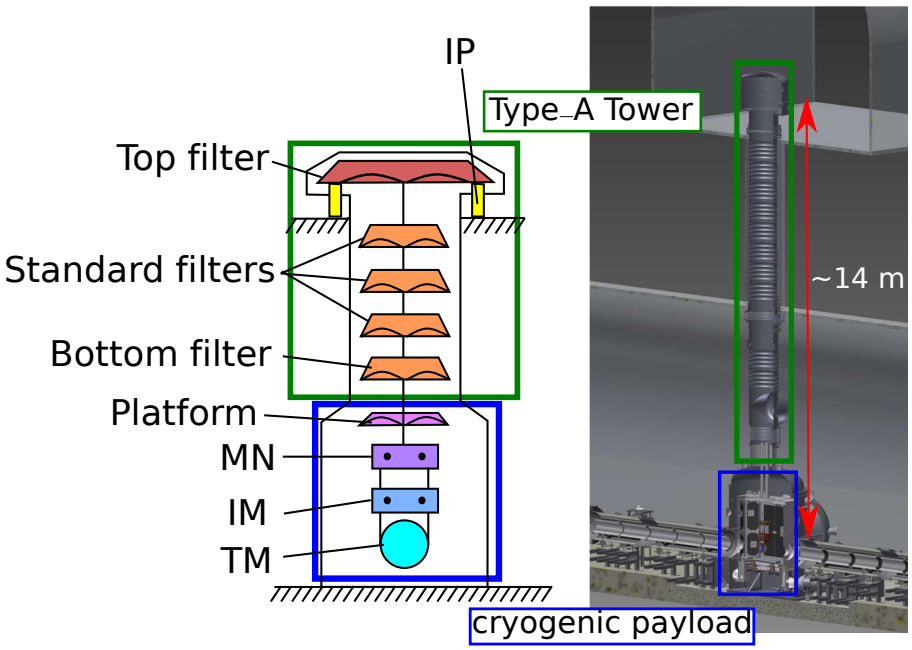

Figure 2.4: Schematic view of the Type-A suspension (left) and the CAD drawing of the Type-A suspension chamber (right). The top filter is isolated by the inverted pendulum (IP). Four vertical vibration isolation stages are suspended from the top filter, and the top three stages are called standard filters. The forth stage is called the bottom filter, and the cryogenic payload is suspended from the bottom filter. The cryogenic payload has four stages, and these stages are called the platform, the marionette (MN), the intermediate mass (IM), and the test mass (TM) from the top.

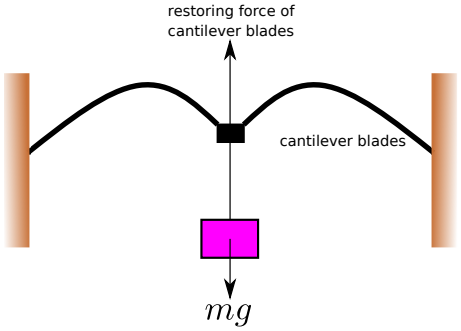

Figure 2.5: Schematic view of the GAS filter. The cantilever blade has the restoring upward force. The effective spring constant gets small when the gravitational force and restoring force get balanced, which means the resonance frequency gets low.

2.1.4 Cryogenic Payload

To reduce the thermal noise, the test masses are cooled down to the cryogenic temperatures in KAGRA. As mentioned in Subsection 1.2.3, the thermal noise is one of the noises limiting the sensitivity of a GW detector, and it is the noise caused by the thermal vibration of mirrors and suspensions. Therefore, the thermal noise can be reduced by cooling them at cryogenic temperature. In KAGRA, the thermal noise is reduced by cooling the mirrors and the suspensions to 20 K. Reduction of the thermal noise is demonstrated by CLIO, which is a prototype detector with a cryogenic interferometer built in the same mine [35].

According to the fluctuation-dissipation theorem, the thermal noise is caused by the dissipation of the system. Therefore, mirrors and suspensions need to have high quality factors. Fused silica which is usually used for a mirror substrate has a low quality factor at cryogenic temperatures. Therefore, KAGRA uses sapphire, which has a high quality factor even at the cryogenic temperature, as the substrate material of the mirror.

The suspension thermal noise is also caused by the dissipation of the suspension. Therefore, the suspension with a high quality factor is needed to reduce the suspension thermal noise. The quality factor of the suspension is determined by the quality factor of the material and the mechanical loss of the suspension. To achieve the high quality factor, the cryogenic payload consists of sapphire fibers, sapphire ears, and sapphire blade springs [43]. The CAD diagram of the cryogenic payload is shown in Fig. 2.6. The bonding method of the sapphire test mass, the sapphire fibers, and the sapphire blade springs determine how much the mechanical loss of cryogenic payload can be reduced. In KAGRA, a hydroxide catalysis bonding technique [44] is used to attach a sapphire ear to a sapphire mirror. The sapphire ear has slits, while the sapphire fiber has nail heads at both ends. The sapphire fiber hooks the sapphire ear. The upper part of the sapphire fiber is hooked up by the sapphire blade spring. By using the Hydroxide catalysis bonding technique, the test mass and the sapphire ears can be bonded with very thin bonds, so the mechanical loss can be reduced.

The cryogenic payload consists of 4 vertical stages, as shown in Fig. 2.6. Located at the top is the part called platform which has a vertical vibration isolation filter using a blade spring. Next, there is a stage called a marionette (MN) which is a stage mainly for aligning the test mass in the angular direction. The third stage, a bottom intermediate mass (IM), is suspended by the MN. The fourth stage, a sapphire mirror, is suspended by the bottom IM with the sapphire fibers. There is another chain suspended from the platform stage to actuate each stage of the main chain, consisting of an MN recoil mass, an IM recoil mass, and a TM (test mass) recoil mass.

The sapphire mirror is cooled by heat conduction through heat links. The heat links are connected from the bottom IM to the cryogenic shield via the MN, the platform, and

the MN recoil mass. Heat exchange between the test mass and the bottom IM is done through the sapphire fibers. The cryogenic shield is connected to the cryogenic cooler, and it cools down the test mass to 20 K.

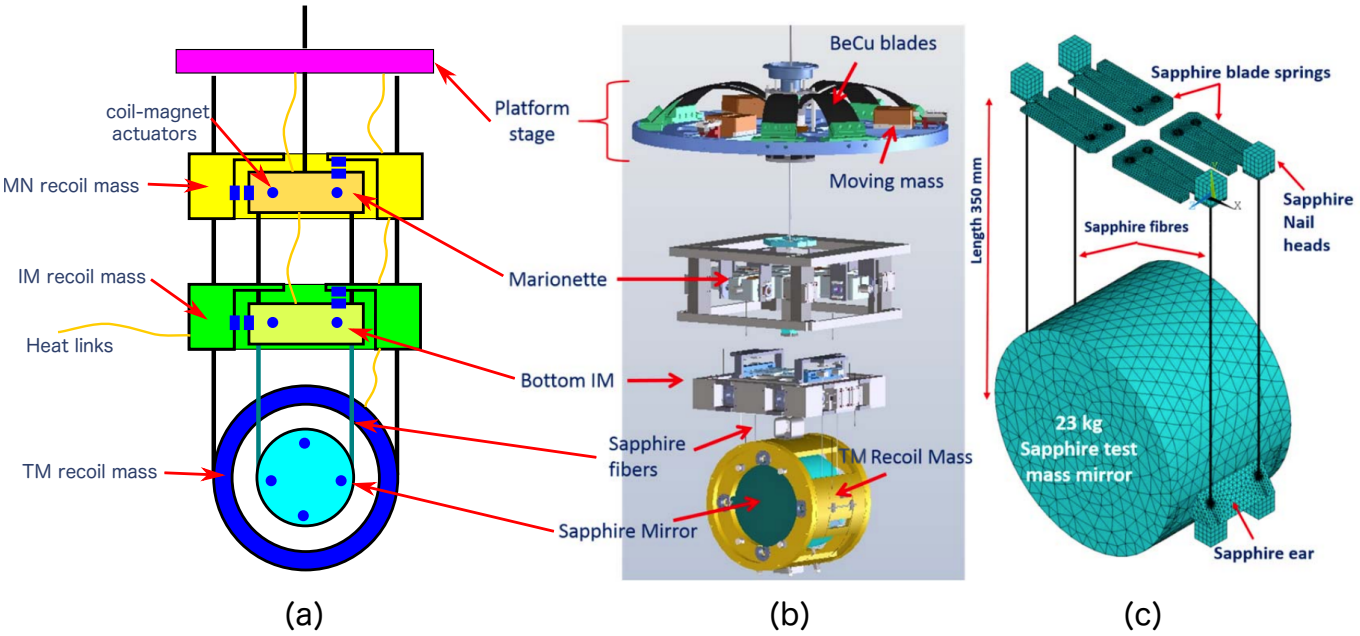

Figure 2.6: (a) Schematic view of the cross-section, and (b) CAD drawing of the cryogenic payload and (c) the CAD drawing of the TM part.

2.1.5 Installation schedule

KAGRA is under construction and the installation is underway in each subsystem. The installation schedule is divided into two phases, the first phase is called iKAGRA (initial KAGRA) and the second phase is called bKAGRA (baseline KAGRA) [41]. iKAGRA refers to the period of the test operation conducted in May 2016, and the purposes are to confirm alignment of the entire facility, to prepare for the final configuration, and to demonstrate the operation of the GW detector by actually controlling a large interferometer. Therefore, the configuration is simple. The optical configuration was a Michelson interferometer with an arm length of 3 km without arm cavities, a PRC and an SRC. Mirrors were suspended with double pendulums of about 1 m in height and the interferometer was operated at room temperature.

After the iKAGRA test run, KAGRA started to work on the next phase, bKAGRA. While the goal of iKAGRA was an operation of a large interferometer, bKAGRA aims to detect a GW signal with an RSE interferometer. As the first stage of bKAGRA, we had a test operation at cryogenic temperature for the first time from April to May 2018. In this test operation, the optical configuration is a Michelson interferometer like iKAGRA, but the end mirror is suspended by a Type-A suspension as described in Subsection 2.1.3

and the interferometer is operated at the cryogenic temperature. After that, we will sequentially install arm cavities, the PRC, and the SRC. On the way to the designed sensitivity, we will achieve the same level of sensitivity as the current aLIGO and AdV to participate in the 3rd observation run (O3) by aLIGO and AdV planned in 2019.

2.2 KAGRA input optics

For GW detectors using interferometers, a low-noise light source is indispensable. The light emitted from the laser light source contains the intensity noise and the frequency noise, and they degrade the sensitivity of the detector. Moreover, the beam jitter causes a noise, and higher-order spatial modes worsen the performance of the interferometer as shown in Subsection 1.2.3. Therefore, it is necessary to stabilize the light before entering the interferometer. The input optics subsystem is responsible for the stabilization of the laser light. The overview of the input optics is shown in Fig. 2.7 and the place where the input optics is located in the whole KAGRA is shown in Fig. 2.2. The input optics has components as below; A pre-mode cleaner (PMC), a modulation system, a reference cavity (RC), an input mode cleaner (IMC), an input Faraday isolator (IFI), and an input mode matching telescope (IMMT). In the following subsections, each component is described.

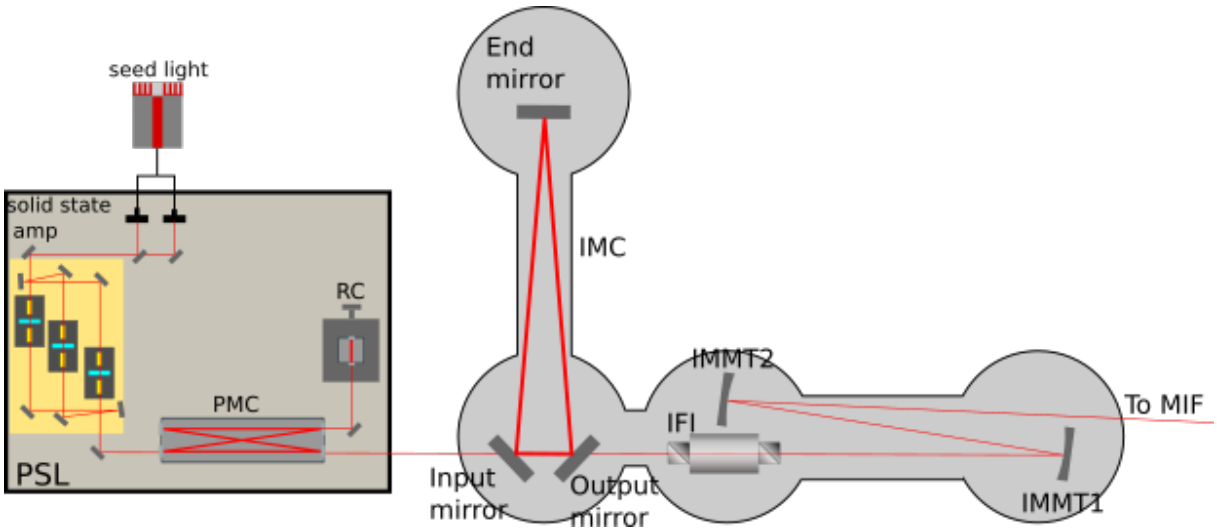

Figure 2.7: Overview of the bKAGRA input optics. There are the PMC, the RC and the laser source on the pre-stabilized laser (PSL) table. The modulation system is also located on the PSL table, but it was omitted in the figure. Then, the IMC, the IFI, and the IMMTs are set up following the PSL table, and they are inside the vacuum chamber.

2.2.1 Components of input optics

Laser source

The contribution of the shot noise decreases in proportion to the square root of the laser power. Therefore, to increase the sensitivity, it is necessary to use a high power laser. KAGRA will use a laser with an output of 180 W. A nonplanar ring oscillator (NPRO) [45] with the output power of 400 mW is used as the seed laser source. The seed laser injected to a fiber amplifier is split into two paths, and the laser power in each path is increased up to 40 W. Then, they are added coherently and pass through the solid-state amplifier to be amplified up to 180 W [46].

Pre-mode cleaner

A pre-mode cleaner (PMC) is an optical cavity located at the most upstream in the input optics. The primary role of the PMC is the reduction of the intensity noise in the radio frequency (RF) band, the reduction of the beam jitter, and the spatial mode cleaning. The parameters of the PMC used in KAGRA are shown in Table 2.1, while the principle of the optical cavity and the meaning of each parameter are described in Appendix A.

A piezoelectric transducer (PZT) is attached to one mirror of the PMC. The cavity length is controlled so that a resonance frequency of the PMC follows the laser frequency. A slow signal below 0.1 Hz is fed back to a heater attached to the spacer, and the thermal expansion is used to control the cavity length.

Since the noise with periods shorter than the storage time of an optical cavity is averaged in the cavity, the optical cavity acts as a first-order low-pass filter for the intensity noise and the frequency noise (see Appendix A.2.3). The cut-off frequency of this low-pass filter is called the cavity pole. In the case of the PMC, the cavity pole is 600 kHz. Therefore, the intensity noise and the frequency noise are filtered out at the higher frequencies than 600 kHz.

The PMC is designed so that a round trip gouy phase rotation ζ_0 (see Appendix.A.4.1) is not the integer multiple of π for the mode cleaning performance and the beam jitter reduction (see Appendix A.4.3). The designed power transmittance of the fundamental mode and the higher-order modes are shown in Fig. 2.8. As shown in Fig. 2.8, the PMC is designed such that the lower-order mode has low transmittance. The lowest-order mode whose amplitude transmittance exceeds 0.1 is the 18th-order mode. The beam jitter noise reduction ratio expressed by the ratio between the transmitted amplitude of the fundamental mode and that of the first-order mode is 0.0164. The phase of the laser light is modulated to obtain the control signal by the Pound-Drever-Hall (PDH) method (described in Appendix A.3.2). This modulation frequency is chosen such that the phase modulation frequency does not coincide with the resonance frequency of the higher-order

modes.

Shape	Bow-tie
Round trip length	$L_{\mathrm{PMC}} = 2$ m
ROC of input and output mirrors	$R_{\mathrm{PMC}} = 3$ m
ROC of monitor mirrors	∞
FSR	$f_{\mathrm{PMC}}^{\mathrm{FSR}} = 149$ MHz
Finesse	$\mathcal{F}_{\mathrm{PMC}} = 125$
Cavity pole	$f_{\mathrm{PMC}}^{\mathrm{c}} = 600$ kHz

Table 2.1: Parameters of the PMC

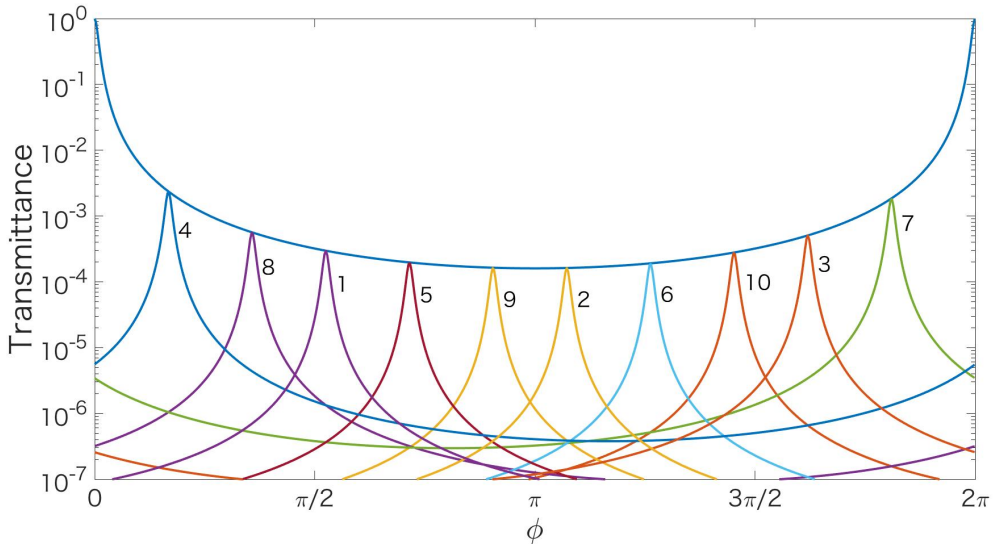

Figure 2.8: Calculation plots of the power transmittance of the PMC for higher-order modes. The upper blue line is the transmittance of TEM_{00}, and each peak represents the transmittance of the nth-order mode, respectively. The horizontal axis shows the phase rotation ϕ during the round trip in the cavity. Here, $\phi = \arg(\exp(i\Omega L/c))$, where Ω is the angular frequency of the laser light and L is the cavity length. The PMC is designed such that the lower-order mode has low transmittance.

Reference cavity

To reduce the frequency noise of a laser, an optical cavity, which has a resonance frequency more stable than the frequency fluctuation of the laser, is used as a frequency reference. One of the cavities used for this purpose is a reference cavity (RC). Since the stability of the cavity length is essential for the frequency stabilization, a spacer made of ultralow expansion (ULE) glass which has little thermal expansion is placed in a vacuum chamber. A heater and a thermometer are attached to the vacuum chamber, and the local temperature is controled. The parameters of the RC are shown in Table 2.2. The details of the RC will be described in Subsection 3.2.2.

Shape	Linear
Round trip length	$L_{\mathrm{RC}} = 10$ cm
ROC of the input mirror	$R_{\mathrm{RC}} = 50$ cm
ROC of the output mirror	∞
FSR	$f_{\mathrm{RC}}^{\mathrm{FSR}} = 1.5$ GHz
Finesse	$\mathcal{F}_{\mathrm{RC}} = 11100$
Cavity pole	$f_{\mathrm{RC}}^{\mathrm{c}} = 67.6$ kHz

Table 2.2: Parameters of the RC

Modulation system

Control signals of the IMC (described later) and the main interferometer are obtained by the PDH method. For that, it is necessary to apply modulations, which is one of the input optics' roles. The modulation required to use PDH method is the phase modulation, and the phase modulation is usually applied to the light by using an electro-optic modulator (EOM). The EOM is an optical device which can modulate the phase of the light. The EOM crystal can change the optical path length by changing the refractive index with applying a voltage to the crystal exhibiting an electro-optic effect. The change in the optical path lengh causes the phase difference in the outcoming light. The KAGRA input optics uses EOMs to apply phase modulations. At the same time, the tunable amplitude modulation is also applied by using a Mach-Zehnder interferometer (MZI) together with EOMs [47]. In an RSE interferometer, the frequency of the extracting GW signal can be adjusted by tuning the SRC length microscopically [6]. The tunable amplitude modulation is used for the SRC length tuning.

Pre-stabilized laser table

The in-air optical table and the components on it are called the pre-stabilized laser (PSL) table. The PMC, the RC, and the modulation system are located on the PSL table. Figure 2.9 shows the bKAGRA PSL layout.

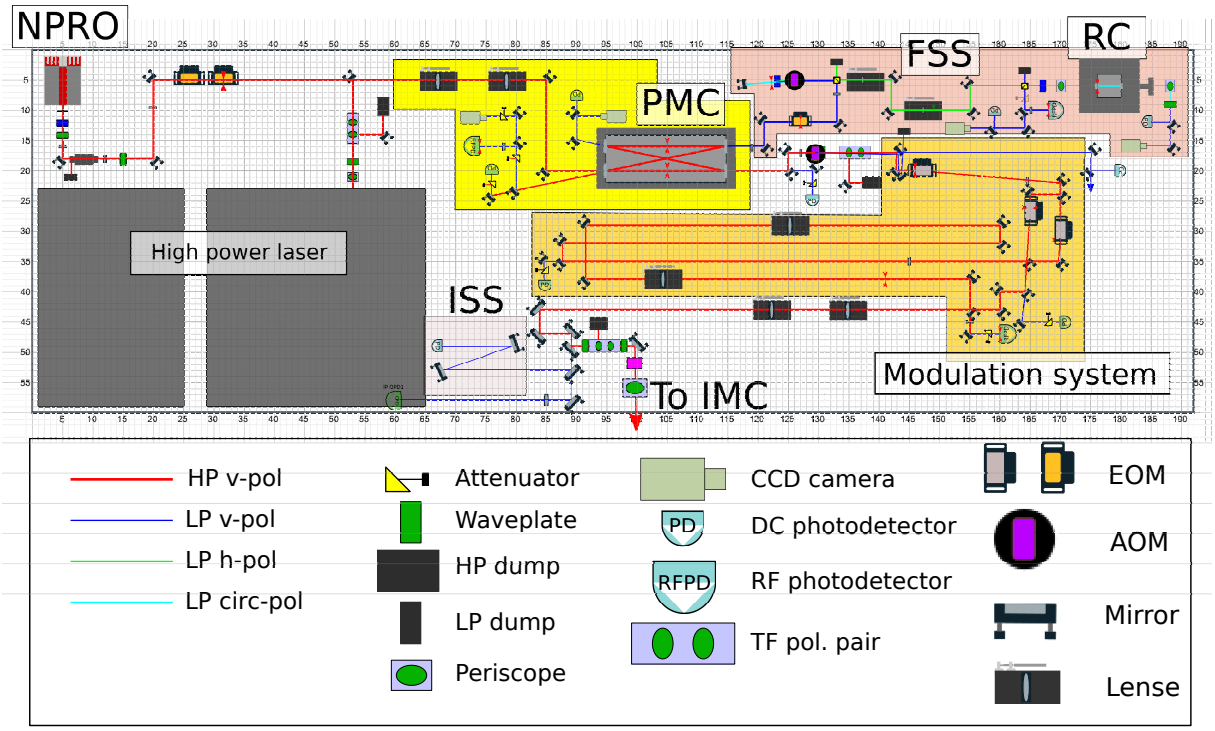

Figure 2.9: Layout of the bKAGRA PSL. The PMC area has the PMC, mode matching lenses, and an RF PD for the PDH method. The light outcoming from one mirror of the PMC goes into the FSS path. There are the double path acousto-optic modulator (AOM) (described in Subsection 3.2.5), mode matching lenses, the RC, and an RF PD in the FSS path. In the modulation system, one EOM modulates the phase of the laser, and two EOMs constitute the MZI for tunable amplitude modulation.

Input mode cleaner

An input mode cleaner (IMC) is an optical cavity through which the light stabilized on the PSL table passes before entering the main interferometer. The cavity axis is on the horizontal plane. It is one of the largest and the most important components in the input optics. The main roles of the IMC are the frequency stabilization and the spatial mode cleaning. The IMC is the triangular cavity with a cavity length of 53.3 m in a round trip. Since the mirrors constituting the IMC are isolated from the seismic motion with a double pendulum, it works as a reference cavity more stable than the RC in the frequency band above the resonance frequency of the pendulum. As we will see later, the frequency stabilization is done in two loops using the RC and the IMC. The IMC parameters are shown in Table 2.3. The details of the IMC are described in Subsection 3.2.3

Since the resonance frequency of the IMC is stable at high frequencies, the laser frequency is controlled to be kept at the resonance frequency of the IMC. On the other hand, since the RC is a more stable cavity than the IMC at low frequencies, the cavity length of the IMC is controlled for the resonance frequency to follow the laser frequency. The cavity length is controlled by using the coil-magnet actuator attached to each mirror.

Shape	Triangular
Round trip length	$L_{\mathrm{IMC}} = 53.3$ m
ROC of the end mirror	$R_{\mathrm{IMC}} = 37.33$ m
ROC of the input and output mirrors	∞
FSR	$f_{\mathrm{IMC}}^{\mathrm{FSR}} = 5.62$ MHz
Finesse	$\mathcal{F}_{\mathrm{IMC}} = 540$
Cavity pole	$f_{\mathrm{IMC}}^{\mathrm{c}} = 6.13$ kHz

Table 2.3: Parameters of the IMC

Input Faraday isolator

A light incident on the main interferometer is reflected by the interferometer and returns to the REFL port. The reflected light includes the control signal of the main interferometer. Therefore, it is necessary to separate the reflected light from the incident light. Moreover, if the light comes back to the laser source by chance, the operation of the laser source becomes unstable. For this purpose, an optical element called a Faraday isolator is used. The Faraday isolator is an optical element to isolate going and returning light using the Faraday effect. The Faraday effect refers to a phenomenon by which the polarization direction rotates during light passes through a material to which a magnetic field is applied. The Faraday isolator separates the reflected light with a polarizer by changing the polarization directions of incident light and reflected light by 90 degrees using the Faraday effect.

KAGRA uses a large Faraday isolator after the IMC to separate the reflected light. This is called an input Faraday isolator (IFI). The IFI is made with the cooperation of the University of Florida [48]. The IFI is compatible with ultrahigh vacuum and high input laser power.

Input mode matching telescope

For a light cleaned by the IMC, it is necessary to match the spatial mode to the resonance mode of the main interferometer. For this purpose, we use two curved mirrors after the IFI and call this an input mode-matching telescope (IMMT). The two mirrors of the IMMT are seismically isolated by double pendulums of the same type as the one used for the mirror of the IMC. Also, since the mirrors of the IMMT can be rotated by using the coil-magnet actuator, they are also used to align the incident light to the main

interferometer.

2.2.2 Stabilization system

The input optics has an active stabilization system as follows.

Frequency stabilization

As mentioned above, a frequency stabilization system (FSS) at KAGRA is an active stabilization system with a hierarchical control using several optical cavities as frequency references. The schematic diagram of the FSS control loop is shown in Fig. 2.10. The laser frequency is stabilized by using the RC in the first loop, and achieves the further stability by using the IMC in the second loop. Figure 2.11 shows the designed frequency noises suppressed by each FSS loop. As is shown in Fig. 2.11, the designed frequency stability meets the requirement for the frequency noise.

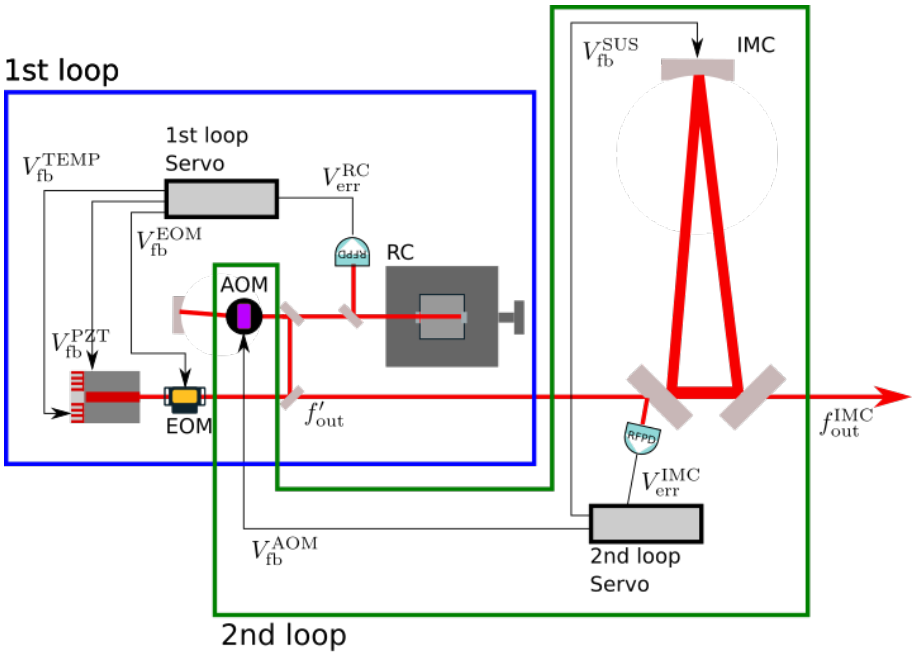

Figure 2.10: Schematic diagram of the FSS loop. The symbols employed in this diagram correspond to those in the block diagrams shown in Fig. 4.2 and Fig. 4.3.

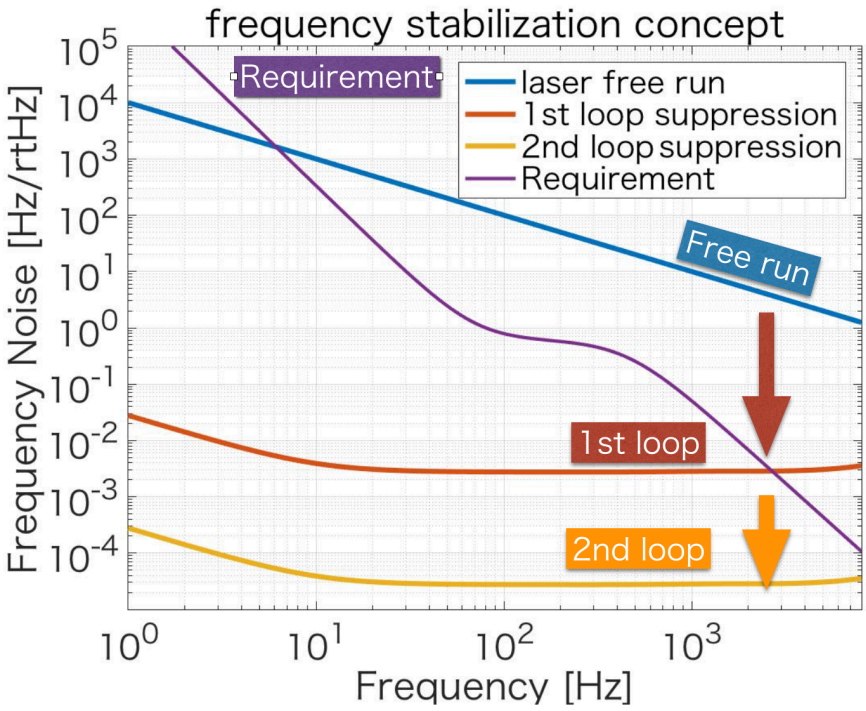

Figure 2.11: Frequency stabilization by the FSS. The first loop controls the RC as a frequency reference, and the second loop refers to the IMC.

Intensity stabilization

The intensity of the laser should also be stabilized in the input optics. The reduction of the intensity noise is performed by measuring a power of the light using a PD and controlling the power of the light by the PD signal. Ideally, the intensity stabilization is limited by the shot noise. Therefore, the higher power of the light is incident on the PD, and the intensity stability gets the better.

The intensity stabilization system (ISS) is also a hierarchical stabilization system similar to the FSS. The sensor in the first loop is a PD placed on the PSL, and the second loop uses another PD that receives the transmitted light of the IMMT in the vacuum. Higher power is injected to the PD in the second loop than the one in the first loop to achieve the lower shot noise. The requirement for the intensity noise is calculated from the design sensitivity and the coupling transfer function from the intensity noise to the output signal of the main interferometer. In the lower frequency band than 2 Hz, the seismic noise limits the GW sensitivity, and it increases rapidly as the frequency decreases. Therefore, the requirement for the intensity noise gets relaxed in this frequency band. Above 2 Hz, the quantum noise limits the sensitivity and the quantum noise starts to get larger at 50 Hz. This is the reason why the noise requirement above 50 Hz gets relaxed. The requirement becomes tighter again at the frequencies above 1 kHz. This is because the intensity fluctuation shakes the mirror by the radiation pressure, and this mirror motion becomes the dominant noise at this frequency band. The requirement for a relative intensity noise (RIN) is shown in Fig. 2.12.

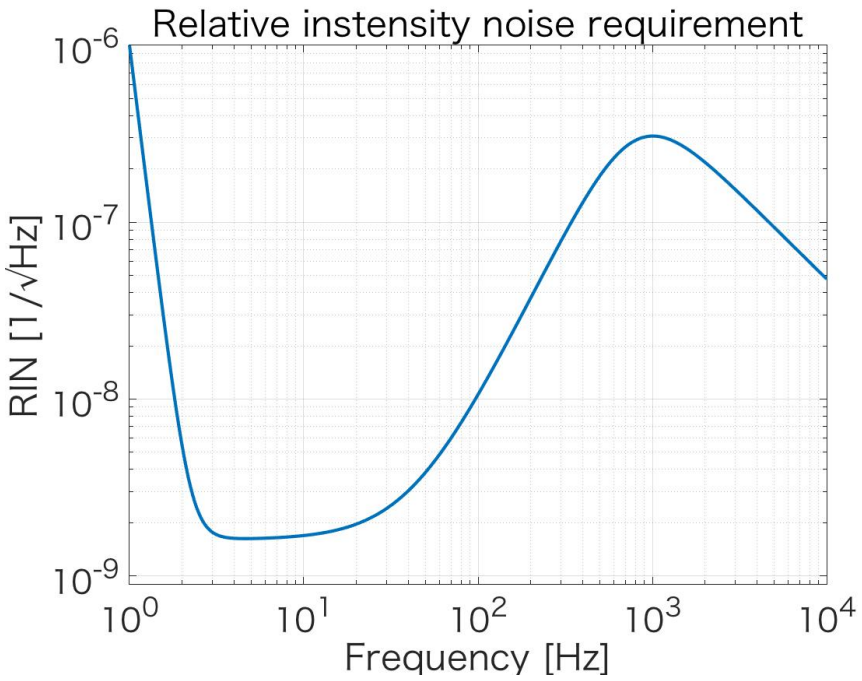

Figure 2.12: Requirement for the RIN

3 Installation of KAGRA input optics

As mentioned in Section 2.1.5, KAGRA is currently in the phase of bKAGRA. In iKAGRA, the interferometer was simplified, and the input optics was also simplified. Especially, the stabilization system was simplified. For the frequency stabilization, only the IMC worked as a frequency reference, and the IMC control signal was fed back directly to the laser frequency. Also, the intensity stabilization was not installed. This is because iKAGRA has no requirement for sensitivity and there was no need for stabilization of an intensity noise and a frequency noise. So we focused on demonstrating the input optics with as simple a system as possible.

On the other hand, the role of bKAGRA input optics is to provide the laser light stable enough to observe GWs. As seen in Subsection 1.2.3, the intensity noise, the frequency noise, the beam jitter noise, and mixing of higher-order spatial modes are the noises in the GW detector. The input optics reduces these noises so that they do not limit the sensitivity of the GW detector.

We installed the PSL table and the IMC in iKAGRA, and the input optics successfully provided the main interferometer with the laser light. After that, We also installed the FSS and evaluated its performance. Then, We finished designing the control loop which satisfies the requirement. The intensity stabilization is being installed by collaborators from Toyama Univ.

In this chapter, first, we show the installation works of iKAGRA input optics briefly in Section 3.1. Then, we move on to the bKAGRA input optics installation in Section 3.2.

3.1 iKAGRA input optics

An overview of the iKAGRA input optics is shown in Fig. 3.1. As mentioned above, the iKAGRA input optics was rather simple, compared with the bKAGRA configuration. The main goal of iKAGRA was to gain the experience in the operation of the large scale interferometer, and the main purpose of the iKAGRA input optics is a test of remote operation of each component. Therefore, iKAGRA did not have any requirement for the detector sensitivity. That means there was no frequency or intensity stability requirements for iKAGRA, and iKAGRA input optics did not need any stabilization system. The iKAGRA input optics had only the PMC and the IMC and no frequency and intensity stabilization systems. Also, the PMC was different from the one which will be used in bKAGRA. The cavity pole was high and the filtering performance of the RF intensity noise was not as good as the bKAGRA PMC.

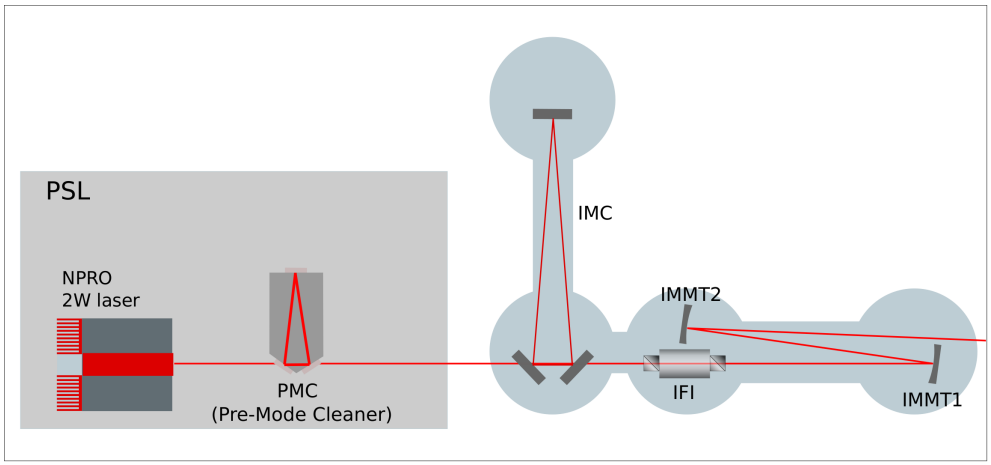

Figure 3.1: Overview of the iKAGRA input optics.

In such a simplified system, only the IMC was the same as the bKAGRA IMC. The main interferometer does not receive any laser light without the IMC being locked. Therefore, the duty cycle of the IMC is one of the essential factors determining the duty cycle of iKAGRA itself. The IMC control loop was connected to the digital control system, and the script called Guardian [49] was used to monitor the IMC's states and re-locked the IMC, when the IMC lost lock. In addition to the robustness of the IMC control loop itself, the Guardian script significantly improved the IMC duty cycle. Figure 3.2 is the plot of the duty cycle of the IMC and the main interferometer during the iKAGRA test run. The duty cycle through the second half run was 98.2% [41], and it satisfied the requirement of 95%. Actually, the IMC duty cycle is much higher than the main interferometer. Therefore, the IMC did not disturb the main interferometer, and we can say that the iKAGRA input optics achieved sufficient performance in the iKAGRA test observation.

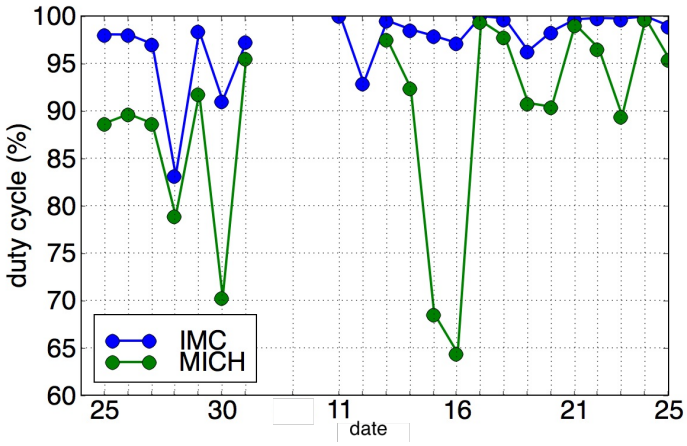

Figure 3.2: Duty cycle of the IMC and the main Michelson interferometer (MICH) during the iKAGRA test run. The test run started on 25th March and ended on 25th April in 2016. The blank between 31st March and 11th April was the maintenance term of the interferometer when the test run was stopped.

3.2 bKAGRA input optics

3.2.1 Pre-stabilized laser

Figure 3.3 shows a photo of the current status of the bKAGRA PSL table. Currently, a 2-W NPRO laser is used as a laser light source. The main path up to the IMC has been already installed. The PMC is being installed now. The RC, which is a frequency reference of the FSS first loop, has been installed.

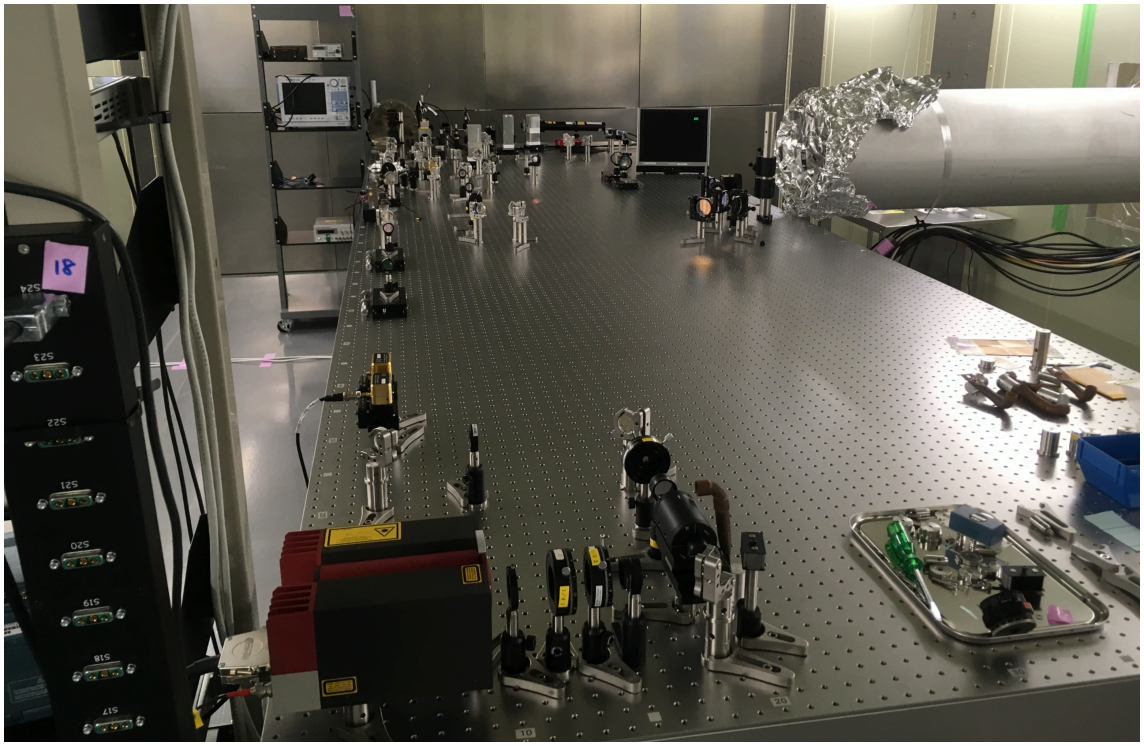

Figure 3.3: Photo of the current bKAGRA PSL.

3.2.2 Reference cavity

The RC on the PSL table is used as the frequency reference in the first loop of the FSS. The RC is a rigid linear cavity. The spacer is made of ULE (ultralow expansion) glass with dimensions of 100-mm diameter and 100-mm width. A flat mirror and a curved mirror with an ROC of 50 cm are optically contacted to the spacer. Figure 3.4 is a photo of the RC spacer.

The RC must be isolated from external fluctuations such as the thermal extension, the seismic motion, and optical length fluctuations due to residual gas. Therefore, the RC should be housed in a proper container with an appropriate support. The cavity is mounted on a Zerodur support with a radiation shield inside. Zerodur is a glass-ceramics composite material composed of an amorphous base material and a crystalline dispersion

material. Materials with different expansion coefficients are mixed to reduce the expansion coefficient near the room temperature. Viton balls are inserted between the support and the spacer for the vibration isolation. The RC is housed inside a vacuum chamber, and a heater is attached to the can. The vacuum chamber is wrapped with a thermal insulator and put into an aluminum shell. Figure 3.5 shows a photo of the inside of the aluminum shell and the vacuum chamber.

The ULE glass has a zero-crossing temperature of 29.5 °C according to the data sheet, at which the coefficient of thermal expansion is zero. Therefore, the local temperature will be maintained at this temperature.

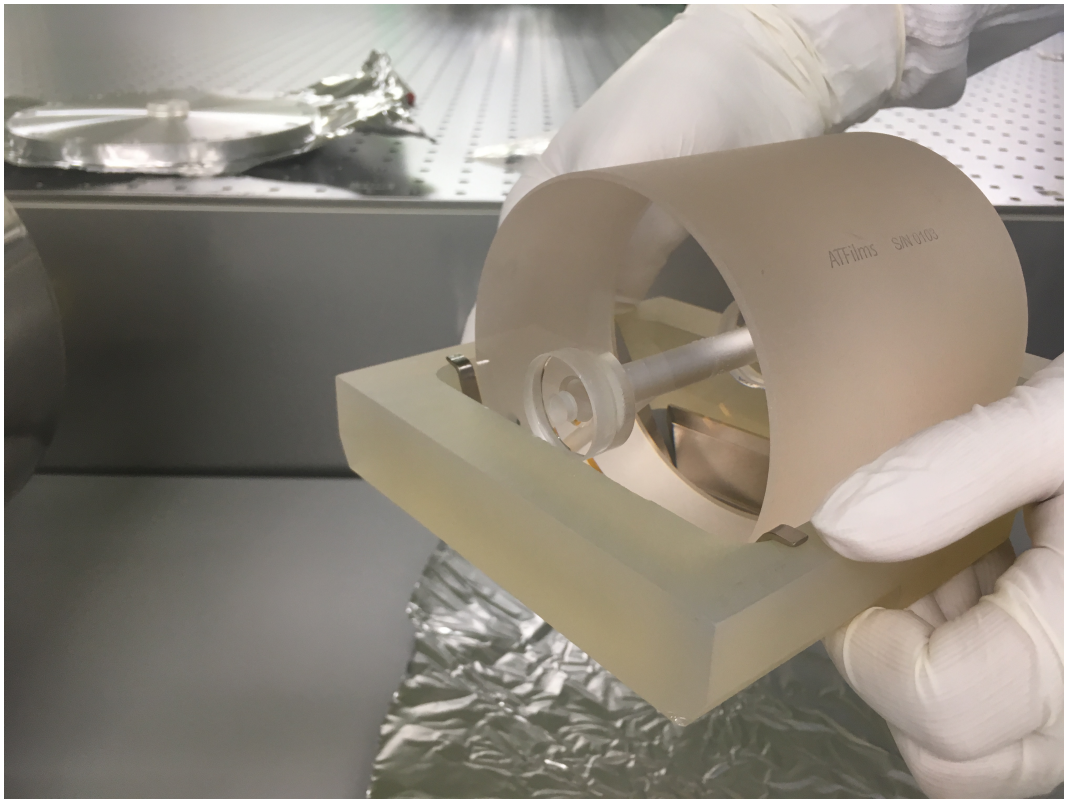

Figure 3.4: Photo of the RC spacer.

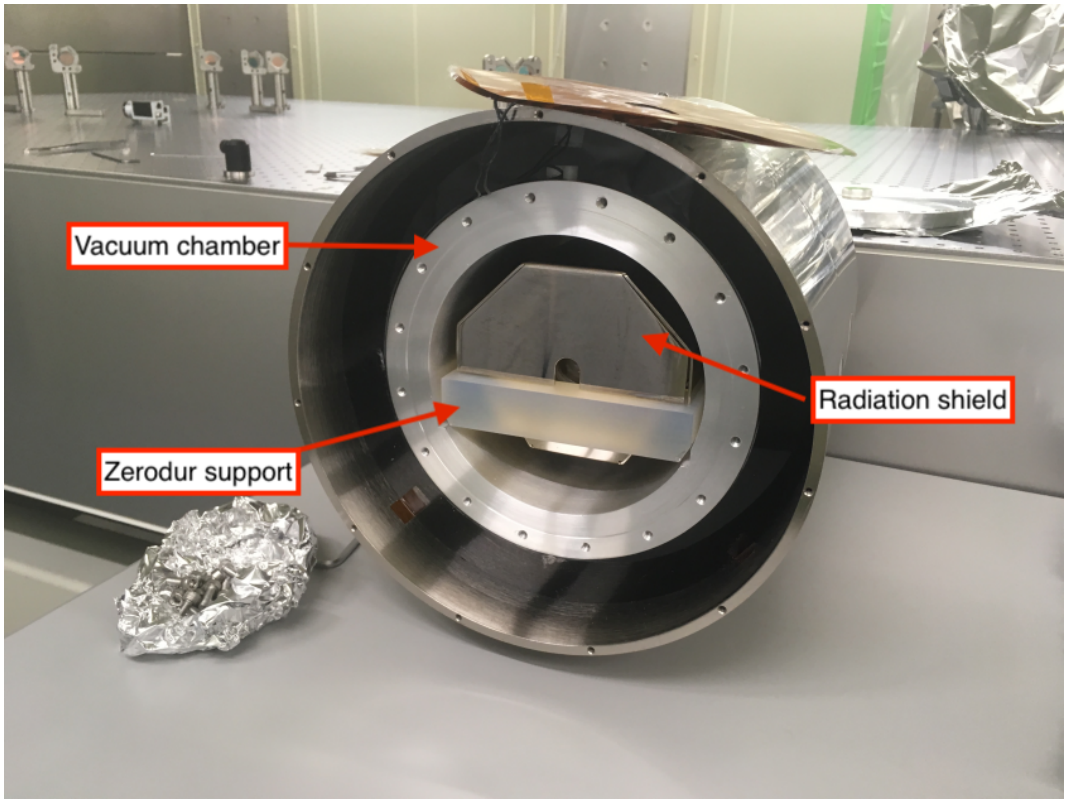

Figure 3.5: A vacuum chamber is located inside an aluminum shield. A semitransparent plate is a Zerodur support, on top of which a cavity as well as a radiation shield are mounted. After closing the vacuum chamber, a heater is attached on a vacuum flange. The cavity is not seen in the photo. A thermal insulator is installed between the vacuum chamber and the aluminum shield.

3.2.3 Input mode cleaner

The stabilized laser frequency by the RC is further stabilized by the second loop by using the IMC as the frequency reference. The IMC performs the beam jitter reduction and the spatial mode cleaning. Since the intracavity power of the IMC reaches more than 10 kW, if there is a dust on the mirror, it will burn and damage the coating of the mirror. Therefore, the IMC is installed in a vacuum. Careful attention was paid to eliminate the contamination during the installation work.

The IMC mirrors are made of synthetic quartz glass with dimensions of 100-mm diameter and 30-mm thickness. The input and the output mirrors are flat mirrors, and the end mirror is a curved mirror with an ROC of 37.3 mm. (The definition of each mirror is shown in Fig. 2.7.) The transmittances of the input and the output mirrors are around 6000 ppm, and that of the end mirror is 5 ppm.

As we have seen, when using a cavity as a frequency reference, the fluctuation of the cavity length deteriorates the frequency stability of the laser. Thus, the IMC mirrors have to be isolated from the seismic motion. The IMC has two seismic isolation systems,

one is a vacuum-compatible vibration isolation stack [50], and the other is a two-stage suspension called Type-C [51]. Figure 3.6 shows a schematic view of the IMC seismic isolation systems.

The stacks isolate a breadboard on which the IMC suspension is located from the seismic motion of the baseplate which is fixed on the ground. Each of the three legs of the breadboard has 3-layer stacks. The isolation bandwidth is above 10 Hz.

Figure 3.7 shows an overview of a Type-C suspension. Type-C suspensions were developed to suspend the test masses of the TAMA300 detector [51]. Four tungsten wires suspend an intermediate mass from an upper stage, and the IMC mirror is suspended by four tungsten wires from the intermediate mass. The intermediate mass has eddy current dumping, and the IMC mirror mass has coil-magnet actuators. Picomotors are installed on the upper stage to move the whole suspension horizontally.

Figure 3.8 shows a modeled transfer function from the ground motion to the IMC mirror motion of the Type-C suspension. As described in Section 4.3.1, the first resonance frequency of the longitudinal motion is estimated to be around 0.95 Hz, and the Q value is 4-5. The second resonance is calculated by rigid-body modeling described in the reference [42]. The second resonance frequency and the Q value were calculated as around 4 Hz and 2-3, respectively. Figure 3.9 shows a spectrum of the seismic motion of the IMC mirrors. The spectrum is estimated using a ground motion spectrum based on a 1.5-year-long measurement.

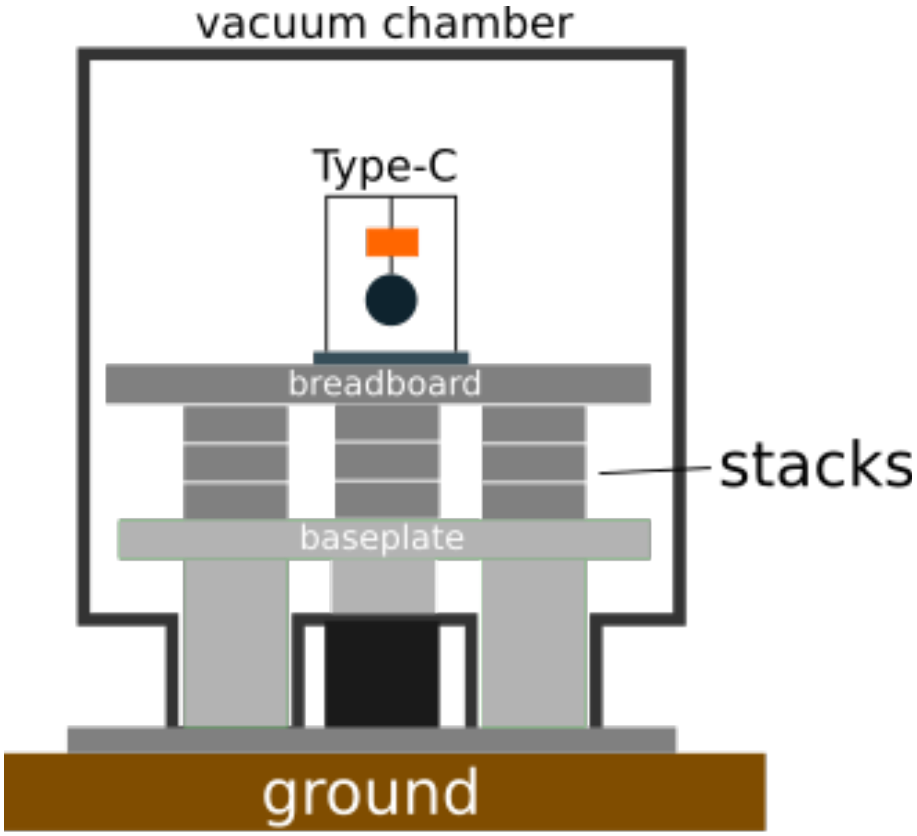

Figure 3.6: Schematic view of the seismic isolation systems of the IMC. The vacuum-compatible stacks are located between a breadboard and a baseplate.

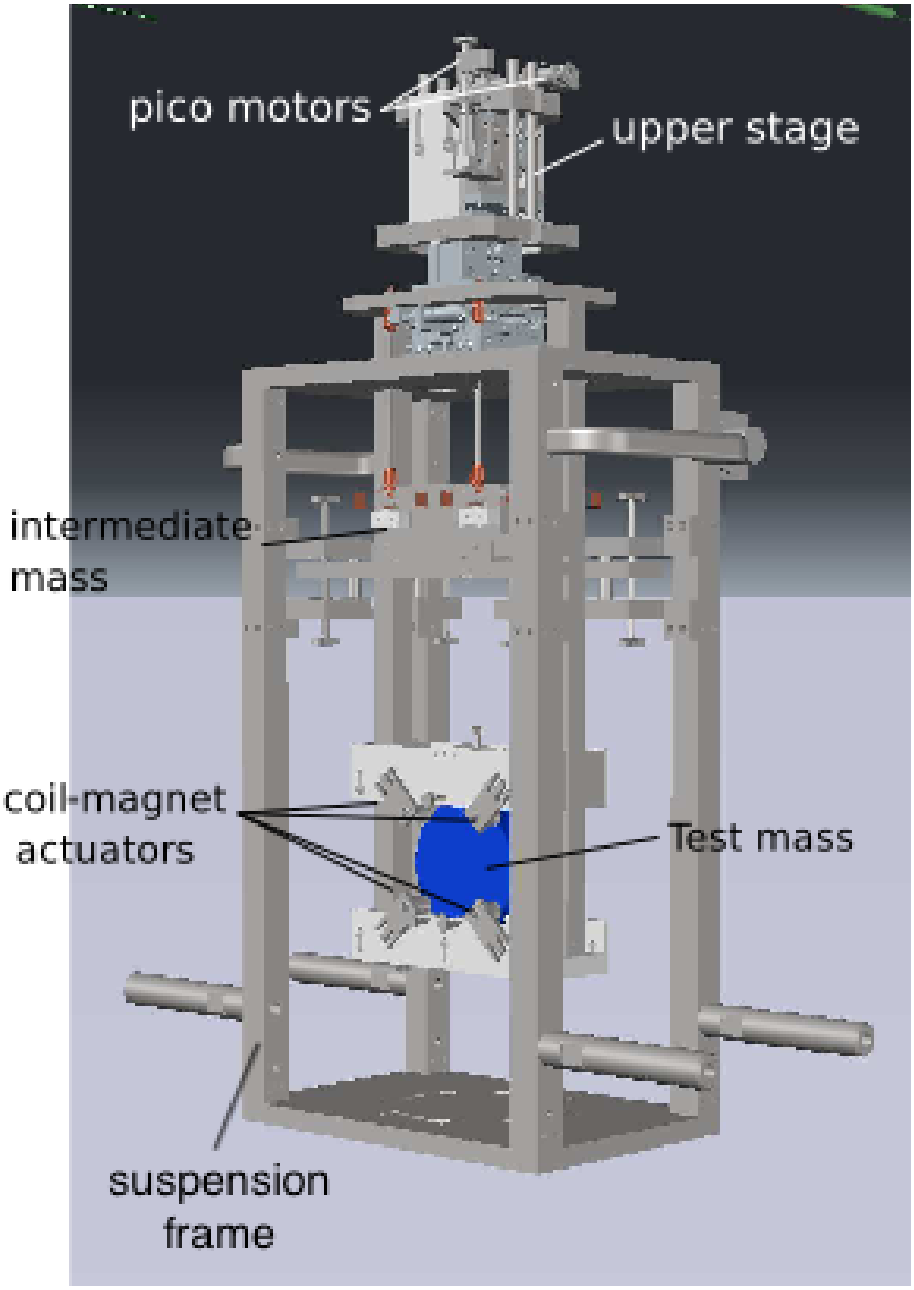

Figure 3.7: Picture of a Type-C suspension.

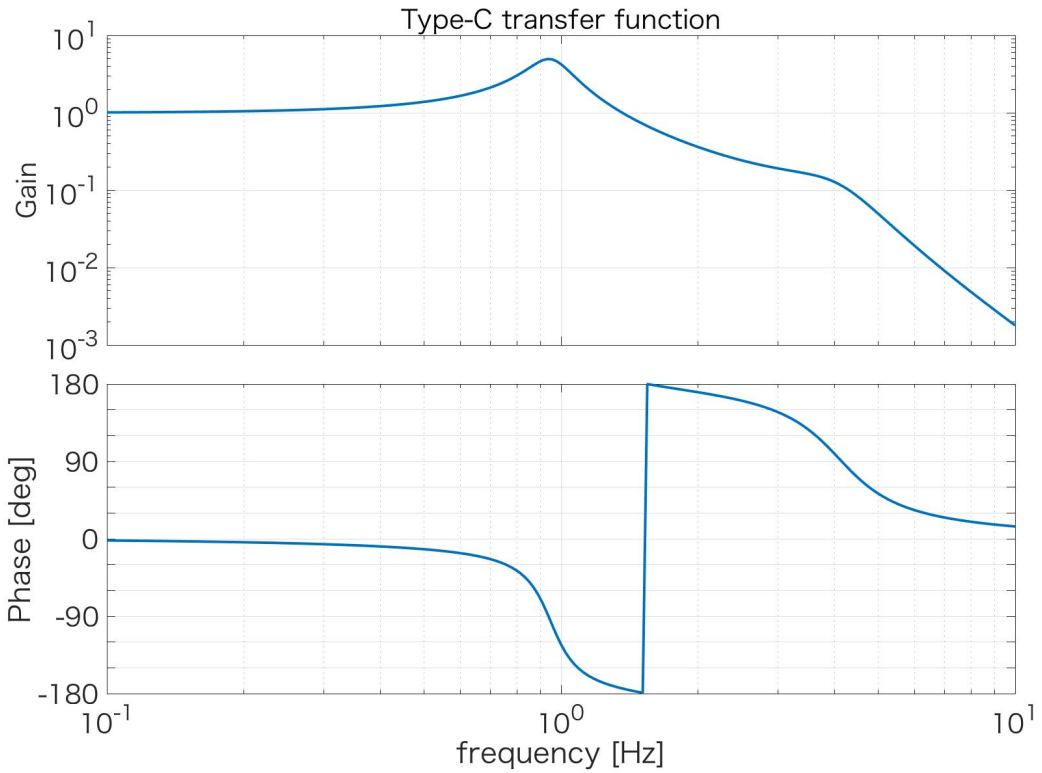

Figure 3.8: Transfer function from the ground motion to a test mass motion of Type-C suspension.

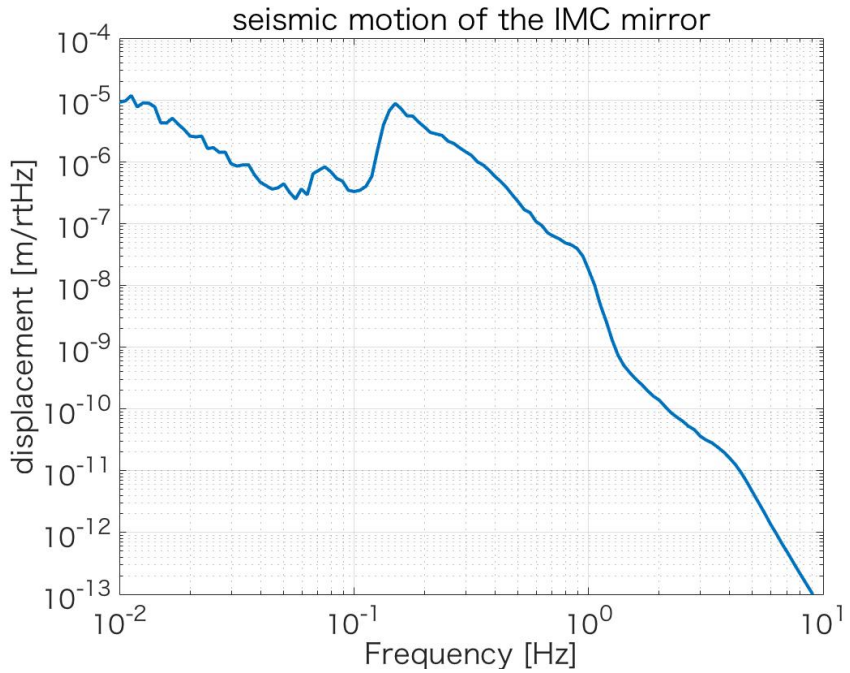

Figure 3.9: Estimated seismic motion of a test mass of the Type-C suspension based on a 1.5-year-long measurement of the ground motion.

3.2.4 First loop of the frequency stabilization

As shown in the Fig. 2.10, the first loop of the FSS stabilizes the laser frequency by using the RC as a frequency reference.

Actuators

The first loop has three different bandwidth actuators; a heater for temperature tuning of laser crystal as a slow actuator, a laser PZT as a middle speed actuator, and a broadband EOM as a fast actuator. The FSS servo circuit has the two analog filters for the broadband EOM and the PZT. The servo circuit is connected to the digital control system, which can control the gains of the servo filters, turn the control loop on and off, inject an excitation signal, and make a servo filter for the temperature control remotely.

Open loop gain

As shown in Appendix B, an open loop gain (OLG) determines the stability of the feedback system. To increase the OLG and suppress noises more efficiently, it is necessary to make the unity gain frequency (UGF) as high as possible. On the other hand, if it is too high, the phase margin disappears, and the system becomes unstable. Therefore, it is necessary to adjust the servo gains, in order to set the UGF that can obtain a sufficient OLG while securing the enough phase margin. Besides, it is necessary to adjust the servo gain of the PZT loop and that of the EOM loop by considering the phase difference of the OLG at the crossover frequency. If the crossover frequency is too high, the phase difference gets close to 180° due to the phase delay of the PZT. In contrast, if it is too low, the control signal to the EOM gets saturated.

The servo circuit, which is installed in the first loop of the FSS, has two variable gain stages. One of them can change the overall gain of the first loop, while the other can change only the gain of the PZT loop. The UGF is determined by the OLG of the EOM loop and the crossover frequency is determined by the relative gain between the PZT loop and the EOM loop. Therefore, it is possible to adjust the UGF and the crossover frequency independently with these two gains.

Figure 3.10 shows the OLG of the current first loop. From Fig. 3.10, the UGF f_{UGF}, the phase margin θ_{PM}, the crossover frequency f_{co}, and the phase difference θ_{co} at the crossover frequency can be read off as follows:

$$
\begin{aligned}
& f_{\mathrm{UGF}} = 500 \text{ kHz}, \\
& f_{\mathrm{co}} = 18 \text{ kHz}, \\
& \theta_{\mathrm{PM}} = \theta_{\mathrm{UGF}} + 180 = 26^\circ, \\
\text{and} \quad & \theta_{\mathrm{co}} = \theta_{\mathrm{co}}^{\mathrm{EOM}} - \theta_{\mathrm{co}}^{\mathrm{PZT}} = 108^\circ.
\end{aligned}
$$

The phase in a Bode diagram is often written in the range of $-180°$ to $180°$. When the phase is delayed by more than -180°, the curve is not continuous and jumps from -180° to 180°. However, an actual phase delay is continuous. In Fig. 3.10, the phase of the OLG of the PZT loop can be read off as $\theta_{\rm co}^{\rm PZT} = 158°$, but in fact $\theta_{\rm co}^{\rm PZT} = 158° - 360° = -202°$.

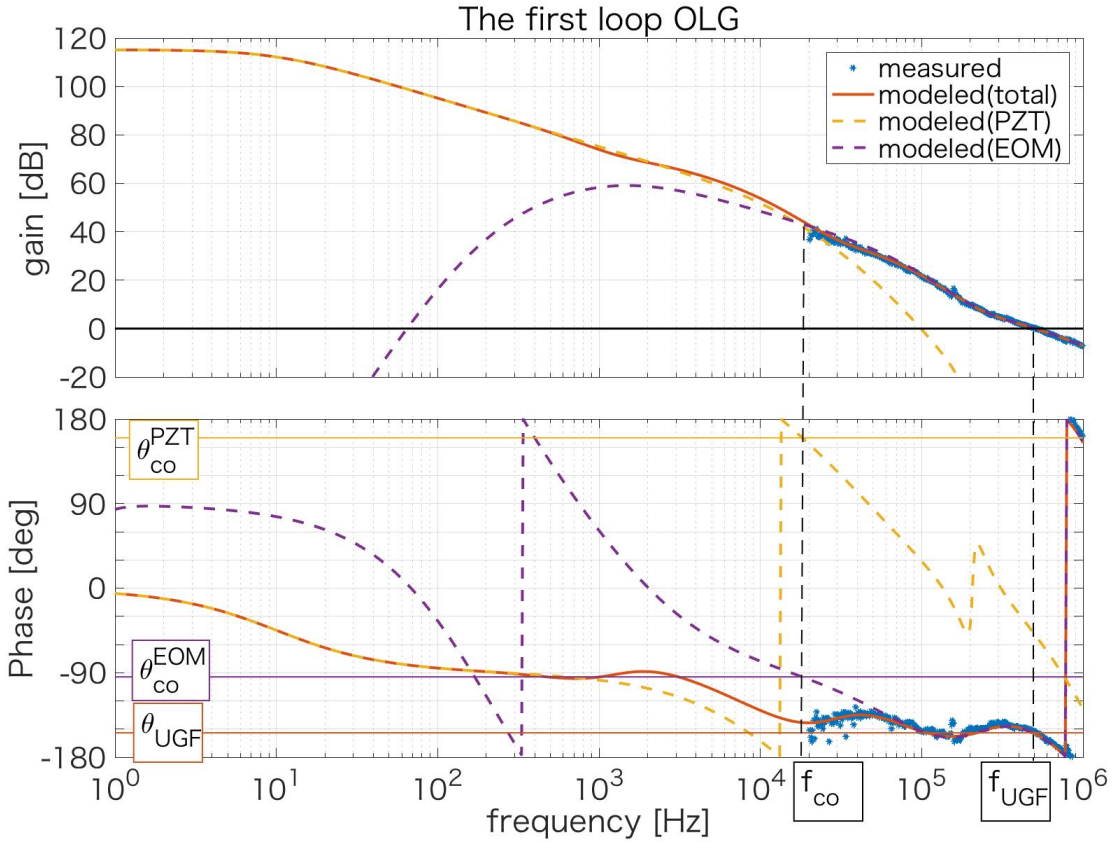

Figure 3.10: Bode diagram of the OLGs of the first loop. The orange line is the estimated OLG of the entire loop, and yellow and purple dashed lines are the OLG of the PZT loop and the EOM loop, respectively. These plots are estimated by the parameters described in Section 4.3. The UGF $f_{\rm UGF}$ is 500 kHz, and the phase margin $\theta_{\rm PM}$ is $\theta_{\rm UGF} + 180 = 26°$. The crossover frequency $f_{\rm co}$ is 18 kHz, and the phase difference between the PZT loop and the EOM loop is $\theta_{\rm co}^{\rm EOM} - \theta_{\rm co}^{\rm PZT} = -94° - (-202°) = 108°$.

3.2.5 Second loop of the frequency stabilization

The second loop of the FSS stabilizes the laser frequency by using the IMC as a frequency reference.

Actuator

The second loop of the FSS uses an AOM as an actuator to control the laser frequency [52]. A PZT is attached to the AOM crystal, and this PZT generates a sound wave in the crystal. The frequency of this sound wave is determined by the frequency of the input signal to the PZT. When the laser light is incident on the AOM crystal where the sound wave is generated as described above, the emitted light from the AOM has a

diffraction angle θ, since the density gradient in the AOM crystal caused by the sound wave acts as a diffraction grating. This diffraction angle can be written from the Bragg's condition as

$$\theta = \frac{\lambda\Omega}{v}, \tag{3.1}$$

where Ω is the RF angular frequency of the sound wave and v is the sound speed in the crystal. In addition to this, since the light exchanges the energy with the sound wave, the frequency of the outgoing light shifts as

$$\omega_{\mathrm{out}} = \omega_{\mathrm{in}} \pm \Omega, \tag{3.2}$$

where ω_{in} and ω_{out} are the incoming and the outgoing light angular frequencies. As described above, when we change the angular frequency of the RF signal Ω, not only the outgoing light frequency ω_{out} but also the diffraction angle θ changes. Therefore, if the light emitted from the AOM is incident on the RC directly, the change in the diffraction angle misaligns the cavity axis and the laser light. To avoid this misalignment, a curved mirror with an ROC of R is put at a place away from the AOM by the distance of R, as shown in Fig. 3.11. In this case, since the light is perpendicularly incident on the curved mirror, it returns to the AOM again through the same path regardless of the diffraction angle. The AOM diffracts the light again, but the incident light and the reflected light on the AOM follow the same path, because the diffraction angle is the same as the first diffraction angle. If this light is incident on the RC, the alignment is kept. Such a configuration is called a double path configuration.

An AOM driver consists a voltage-controlled oscillator (VCO), a mixer, and an amplifier. The VCO is an electric element whose frequency of the output signal varies depending on the input voltage. By using the VCO, we control the amount of the frequency shift Ω by the AOM. Here, in the case of the double path configuration, since the laser frequency is shifted twice, it is shifted by twice the frequency of the output signal from the VCO.

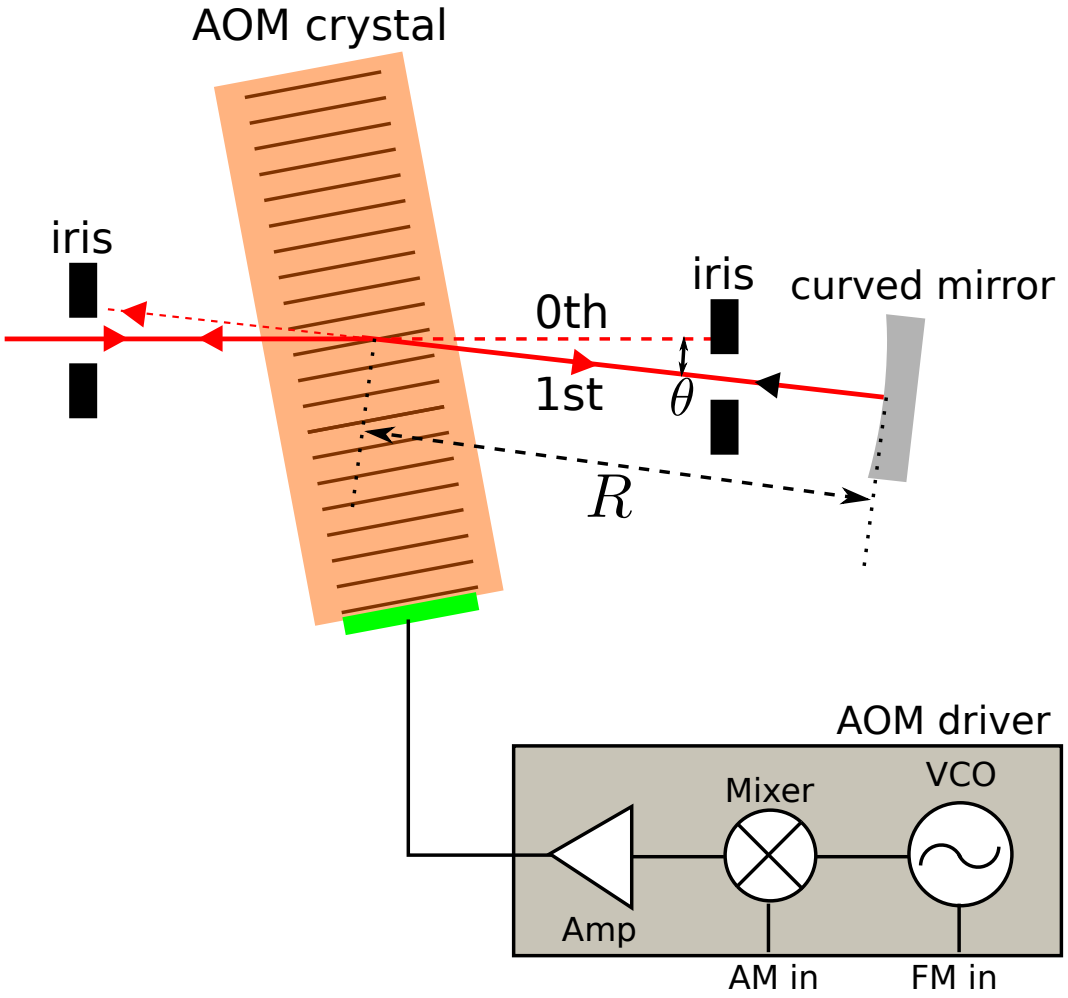

Figure 3.11: The configuration of a double path AOM.

Open loop gain

Figure 3.12 shows the OLG of the current second loop. From Fig. 3.12, the UGF f_{UGF}, the phase margin θ_{PM}, the crossover frequency f_{co}, and the phase difference at the crossover frequency θ_{co} can be read off as follows:

$$
\begin{aligned}
& f_{\mathrm{UGF}} = 39 \text{ kHz}, \\
& f_{\mathrm{co}} = 4 \text{ Hz}, \\
& \theta_{\mathrm{PM}} = \theta_{\mathrm{UGF}} + 180^\circ = 30^\circ, \\
\text{and} \quad & \theta_{\mathrm{co}} = \theta_{\mathrm{co}}^{\mathrm{SUS}} - \theta_{\mathrm{co}}^{\mathrm{AOM}} = 56^\circ.
\end{aligned}
$$

The phase margins at the UGF and the crossover frequency are larger than 30 degrees. Therefore, these margins can be considered to be sufficient.

The IMC has been locked for more than six days in bKAGRA and this confirms this system is sufficiently robust. Figure 3.13 is a plot of transmitted light power from the IMC. The transmitted light power is normalized to 1 as the locked state on 28th December in 2017. This plot demonstrates that the IMC was kept locked for more than six days.

Furthermore, in case the IMC loses lock, it takes less than one minute for the IMC to be re-locked owing to the Guardian script. Therefore, under the assumption that the IMC loses lock once a week, the duty cycle will be 99.99%. This obviously means that the FSS satisfied the requirement of the duty cycle to be better than 95%.

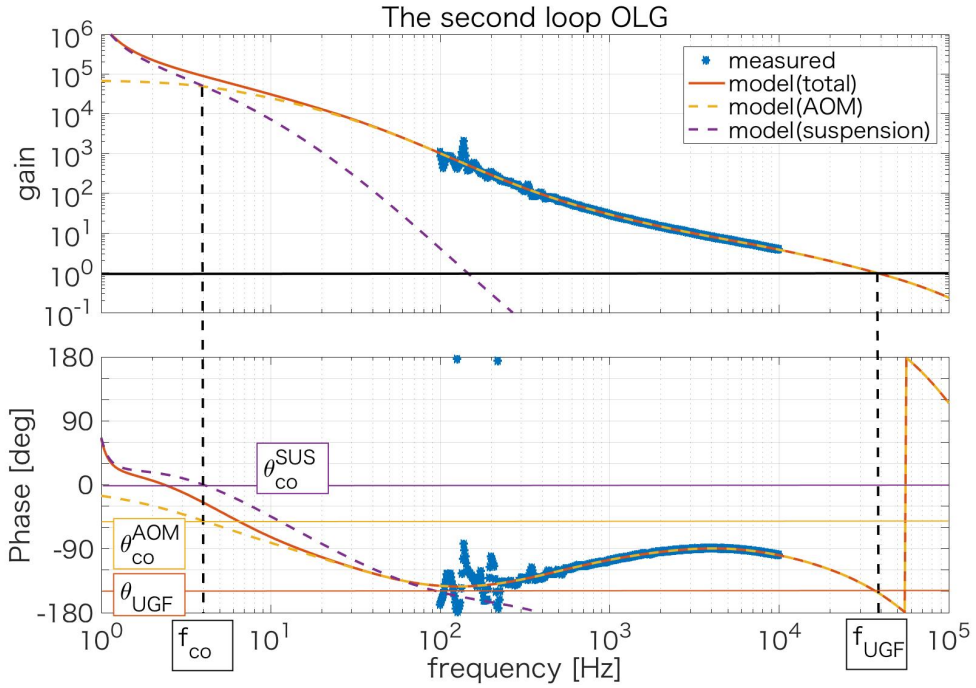

Figure 3.12: Bode diagram of the OLGs of the second loop. The solid orange line is the estimated OLG of the second loop, and yellow and purple dashed lines are the OLG of the AOM loop and the suspension loop, respectively. These plots are estimated by the parameters described in Section 4.3. The UGF f_{UGF} is 39 kHz, and the phase margin θ_{PM} is $\theta_{\mathrm{UGF}} + 180^\circ = 30^\circ$. The crossover frequency f_{co} is 4 Hz, and the phase difference between the AOM loop and the suspension loop is $\theta_{\mathrm{co}}^{\mathrm{SUS}} - \theta_{\mathrm{co}}^{\mathrm{AOM}} = 56^\circ$.

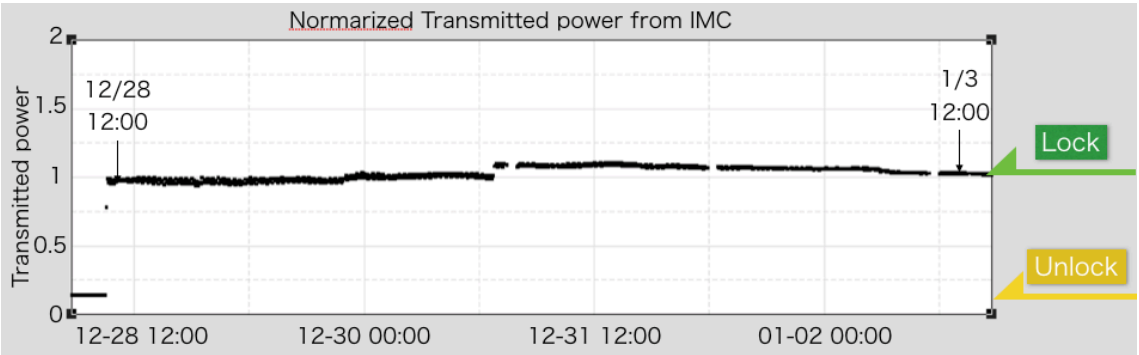

Figure 3.13: Plot of the transmitted power from the IMC. The vertical axis is the transmitted power normalized to 1, when it is locked. The IMC is kept locked for more than six days. There was a power drift however, this was caused by the change of the alignment of the IMC. The lack of the data is due to the trouble in the data acquisition system.

4 Frequency stabilization

As we have seen, the frequency stabilization is done by using optical cavities. A reference cavity (RC) and an input mode cleaner (IMC) are used as the frequency references in bKAGRA. Although we have not mentioned so far, the arm cavity of the main interferometer is also used as a frequency reference, and the frequency stabilization system (FSS) has hierarchical control of three stages in total. The schematic diagram of the first loop and the second loop, which use the RC and the IMC as the frequency reference, is shown in Fig. 2.10.

This chapter describes the detail of the frequency stabilization system, which is the main theme of this thesis. First, we show the requirement for the frequency noise in Section 4.1. Then, the modeling of the control loop is described in Section 4.2. After that, the calibration of the parameters in the model is described in Section 4.3. In Section 4.4, the simulation about the optimization of the control loop necessary for the frequency stablization to meet the requirement is described. Finally, the noise budget with the optimized configuration is described in Section 4.5.

4.1 Requirement for the frequency noise

The requirement for the frequency noise is set under the condition that it becomes smaller than fundamental noises such as the quantum noise or the thermal noise. The requirement includes the safety margin of 10. As described in Subsection 1.2.3, when considering the frequency noise, it is necessary to consider a common mode reduction ratio (CMRR). In the case of an RSE interferometer, CMRR can be derived as

$$\mathrm{CMRR} = \frac{\delta L}{L} + \frac{\delta \mathcal{F}}{\mathcal{F}}, \tag{4.1}$$

where δL and $\delta \mathcal{F}$ are the differences in the arm lengths and in the finesse values between the two arms. The arm lengths have a designed asymmetry as $\delta L/L = 1/1000$. For the finesse, we assume that the asymmetry of the cavity loss is 10 ppm corresponding to $\delta \mathcal{F}/\mathcal{F} = 1/200$ as shown in Eq. (A.61). In the GW detectors, typically the cavity loss is the order of 100 ppm and 10 % asymmetry is reasonable. Therefore, the CMRR is calculated as 1/200. The requirement for the frequency noise in the IMC output is shown in Fig. 4.1.

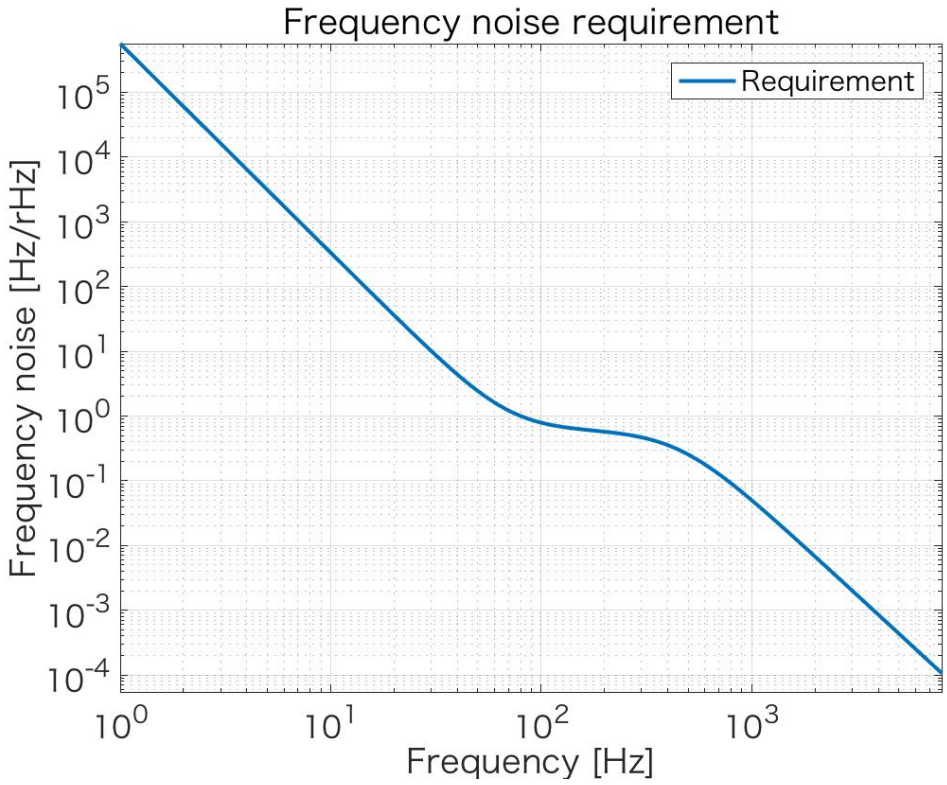

Figure 4.1: Frequency noise requirement for the IMC output. CMRR is assumed as 1/200.

.

4.2 Modeling of the frequency stabilization

4.2.1 First loop with the reference cavity

In the first loop of the FSS, the RC is used as a frequency reference, and a laser frequency is controlled to a resonance frequency of the RC. In the first loop, the control is performed by actuators with three different speeds to take the control band as wide as possible and secure a large control range. The slowest and the largest range actuator is a heater tuning the temperature (TEMP) of the nonplanar ring oscillator (NPRO) laser crystal. It can actuate the laser frequency in a range of several GHz/s with a bandwidth of 0.1 Hz. The second actuator is a piezoelectric transducer (PZT) actuator attached to the laser crystal. It can actuate the laser frequency, by changing the effective length of the laser crystal, in a range of about 200 MHz with a bandwidth of 100 kHz. The fastest actuator is a broadband electro-optic modulator (EOM). The EOM controls the phase of the laser light with a bandwidth of 1 MHz. The error signal to control the laser frequency is generated by the Pound-Drever-Hall (PDH) method.

Figure 4.2 shows a block diagram of the FSS first loop. We can evaluate the transfer function from the free-run laser frequency fluctuation f_{laser} to the stabilized output laser

frequency fluctuation $f_{\rm out}^{\rm RC}$ by this block diagram. Blocks in the figure stand for actuator responses A_x, servo transfer functions F_x, and cavity transfer functions $D_{\rm RC}$ and $C_{\rm RC}$, where subscript x is an indicator of the actuator corresponding to either TEMP, PZT or EOM, $C_{\rm RC}$ is the transfer function of a low-pass filter due to the cavity pole of the RC described in Eq. (A.78), and $D_{\rm RC}$ is called an optical gain which is the coefficient of the error signal proportional to the frequency variation. There are two kinds of measurable signals, the error signal $V_{\rm err}^{\rm RC}$ and the feedback signal $V_{\rm fb}^{x}$ to each actuator.

In addition to the laser frequency fluctuation, four noise sources are shown in the block diagram, the servo electrical noise $\delta v_{\rm F}^{\rm RC}$, the shot noise $\delta f_{\rm shot}^{\rm RC}$, the resonance frequency fluctuation of the RC $\delta f_{\rm res}^{\rm RC}$, and the sensor noise $\delta v_{\rm sen}^{\rm RC}$.

The output frequency fluctuation $f_{\rm out}^{\rm RC}$ can be derived as

$$f_{\rm out}^{\rm RC} = \frac{1}{1+G_{\rm RC}}(f_{\rm laser} + AF_{\rm tot}(\delta v_{\rm sen}^{\rm RC} + \delta v_{\rm F}^{\rm RC}) + AF_{\rm tot}D_{\rm RC}\delta f_{\rm shot}^{\rm RC} + G_{\rm RC}\delta f_{\rm res}^{\rm RC}), \tag{4.2}$$

where $AF_{\rm tot} = \sum_x A_x F_x$ is the sum of the product of each actuator response and servo filter, and $G_{\rm RC} = C_{\rm RC}D_{\rm RC}AF_{\rm tot}$ is the open loop gain (OLG). The error signal and the feedback signal can be calculated as

$$V_{\rm err}^{\rm RC} = \frac{1}{1+G_{\rm RC}}(H_{\rm RC}(f_{\rm laser} + \delta f_{\rm res}^{\rm RC} + \frac{\delta f_{\rm shot}^{\rm RC}}{C_{\rm RC}}) + \delta v_{\rm sen}^{\rm RC} + G_{\rm RC}\delta v_{\rm F}^{\rm RC}), \tag{4.3}$$

$$V_{\rm fb}^{x} = \frac{1}{1+G_{\rm RC}}(H_{\rm RC}F_x(f_{\rm laser} + \delta f_{\rm res}^{\rm RC} + \frac{\delta f_{\rm shot}^{\rm RC}}{C_{\rm RC}}) + F_x(\delta v_{\rm sen}^{\rm RC} + \delta v_{\rm F}^{\rm RC})), \tag{4.4}$$

where $H_{\rm RC} = D_{\rm RC}C_{\rm RC}$. If the OLG $G_{\rm RC}$ is much larger than one, Eqs. (4.2), (4.3), and (4.4) can be written as

$$f_{\rm out}^{\rm RC} \simeq \frac{f_{\rm laser}}{G_{\rm RC}} + \delta f_{\rm res}^{\rm RC} + \frac{\delta f_{\rm shot}^{\rm RC}}{C_{\rm RC}} + \frac{\delta v_{\rm sen}^{\rm RC}}{H_{\rm RC}} + \frac{\delta v_{\rm F}^{\rm RC}}{H_{\rm RC}}, \tag{4.5}$$

$$V_{\rm err}^{\rm RC} \simeq \frac{H_{\rm RC}}{G_{\rm RC}}(f_{\rm laser} + \delta f_{\rm res}^{\rm RC} + \frac{\delta f_{\rm shot}^{\rm RC}}{C_{\rm RC}} + \frac{\delta v_{\rm sen}^{\rm RC}}{H_{\rm RC}} + G_{\rm RC}\frac{\delta v_{\rm F}^{\rm RC}}{H_{\rm RC}}), \tag{4.6}$$

$$\text{and} \quad V_{\rm fb}^{x} \simeq \frac{1}{A_x}(f_{\rm laser} + \delta f_{\rm res}^{\rm RC} + \frac{\delta f_{\rm shot}^{\rm RC}}{C_{\rm RC}} + \frac{\delta v_{\rm sen}^{\rm RC}}{H_{\rm RC}} + \frac{\delta v_{\rm F}^{\rm RC}}{H_{\rm RC}}). \tag{4.7}$$

Therefore, the laser frequency fluctuation is suppressed by the OLG $G_{\rm RC}$. However, the resonance frequency fluctuation of the RC is not suppressed in the output frequency. This means that the stability of the laser frequency is determined by the stability of the cavity length of the RC, when the other noises are sufficiently small. This is because the PDH method cannot distinguish between the cavity length fluctuation and the frequency fluctuation, as can be seen from Eq. (A.86). The servo electrical noise and the sensor noise can be reduced by increasing the optical gain $D_{\rm RC}$ by increasing either the laser power on a photodetector (PD) or the modulation depth of RF sidebands as shown in Eq. (A.86).

Note that the error signal or the feedback signal does not carry any information to

distinguish the sensor noise from the resonance frequency fluctuation of the cavity because generally, $\delta v_{\rm sen}^{\rm RC}/H_{\rm RC}, \delta f_{\rm res}^{\rm RC}$, and $\delta f_{\rm shot}^{\rm RC}$ are smaller than $f_{\rm laser}$. From the signal inside the loop, we can only derive the free-running laser frequency fluctuation $f_{\rm laser}$ as $A_x V_{\rm fb}^x$.

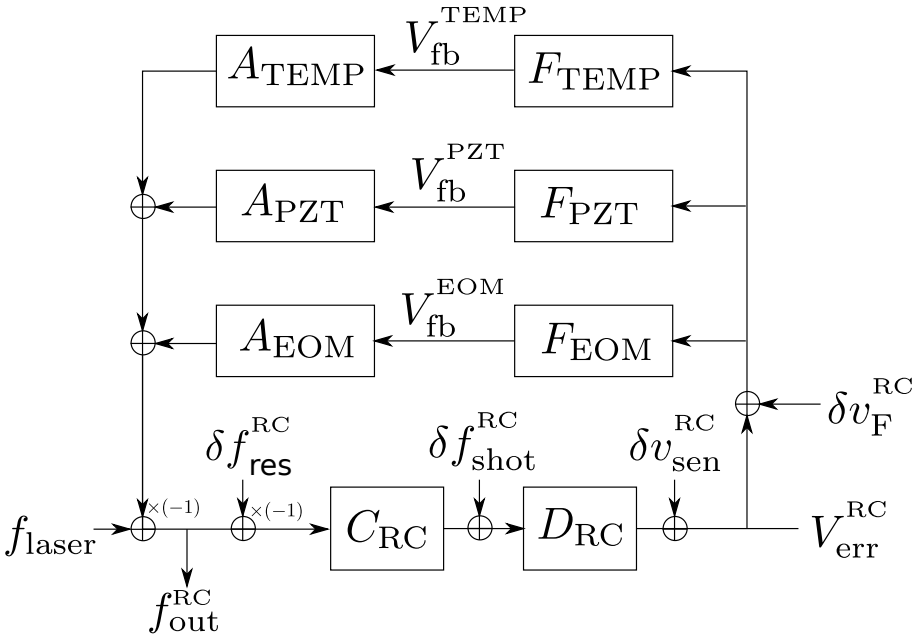

Figure 4.2: Block diagram of the first loop of the FSS. The schematic diagram of the whole FSS is shown in Fig. 2.10. $f_{\rm laser}$ is the free-run frequency fluctuation of the laser source, $f_{\rm out}^{\rm RC}$ is the stabilized laser frequency fluctuation. We have three actuators, the heater tuning the temperature of the laser crystal, the PZT attached to the laser crystal, and the broadband EOM. $A_{\rm TEMP}, A_{\rm PZT}$, and $A_{\rm EOM}$ are the corresponding actuator responses. The error signal $V_{\rm err}^{\rm RC}$ and feedback signals $V_{\rm fb}^{\rm TEMP}, V_{\rm fb}^{\rm PZT}$, and $V_{\rm fb}^{\rm EOM}$ are the signals which we can measure. Four noises, the resonance frequency fluctuation of the RC $\delta f_{\rm res}^{\rm RC}$, the shot noise $\delta f_{\rm shot}^{\rm RC}$, the sensor noise $\delta v_{\rm sen}^{\rm RC}$, and the servo electrical noise $\delta v_{\rm F}^{\rm RC}$ are included in the diagram.

4.2.2 Second loop with the input mode cleaner

In the second loop of the FSS, the laser frequency is locked to the resonance frequency of the IMC. The IMC is much more stable in the high-frequency band than the RC, since the IMC mirrors are suspended. On the other hand, the resonance frequency of the RC is more stable than that of the IMC in the lower-frequency band, as the IMC suspensions move more than the RC spacer. Therefore, the laser frequency is controlled to follow the IMC resonance frequency in the high-frequency band, and the IMC length is controlled to follow the laser frequency, which is stabilized by the RC, in the lower-frequency band. For this control, two actuators are used in the IMC loop. The first one is a coil-magnet actuator attached to one of the IMC mirrors. It controls the cavity length of the IMC with a bandwidth of about 10 Hz. The other is an acousto-optic modulator (AOM) used in a double pass configuration. As shown in Fig. 2.10, the AOM is placed in the path

towards the RC and shifts the frequency of the incident laser light to the RC. As a result, the laser frequency in the main path to the IMC and the resonance frequency of the RC are shifted, so that the RC and the IMC can resonate at the same time. The AOM has the several tens of MHz range with a bandwidth of more than 100 kHz.

Figure 4.3 shows the block diagram of the second loop of the FSS. The first loop part is wrapped into G_{RC}. Blocks in Fig. 4.3 represent IMC loop actuators, servos, and an optical response of the IMC. A_{AOM} and A_{SUS} are the actuator responses of the double pass AOM and the coil-magnet actuator of the IMC mirror suspension, respectively. $F_{\mathrm{AOM}}^{\mathrm{IMC}}$ and $F_{\mathrm{SUS}}^{\mathrm{IMC}}$ are the transfer function of each servo filter, respectively. C_{IMC} is a low-pass filter due to the cavity pole of the IMC, and D_{IMC} is the optical gain of the IMC.

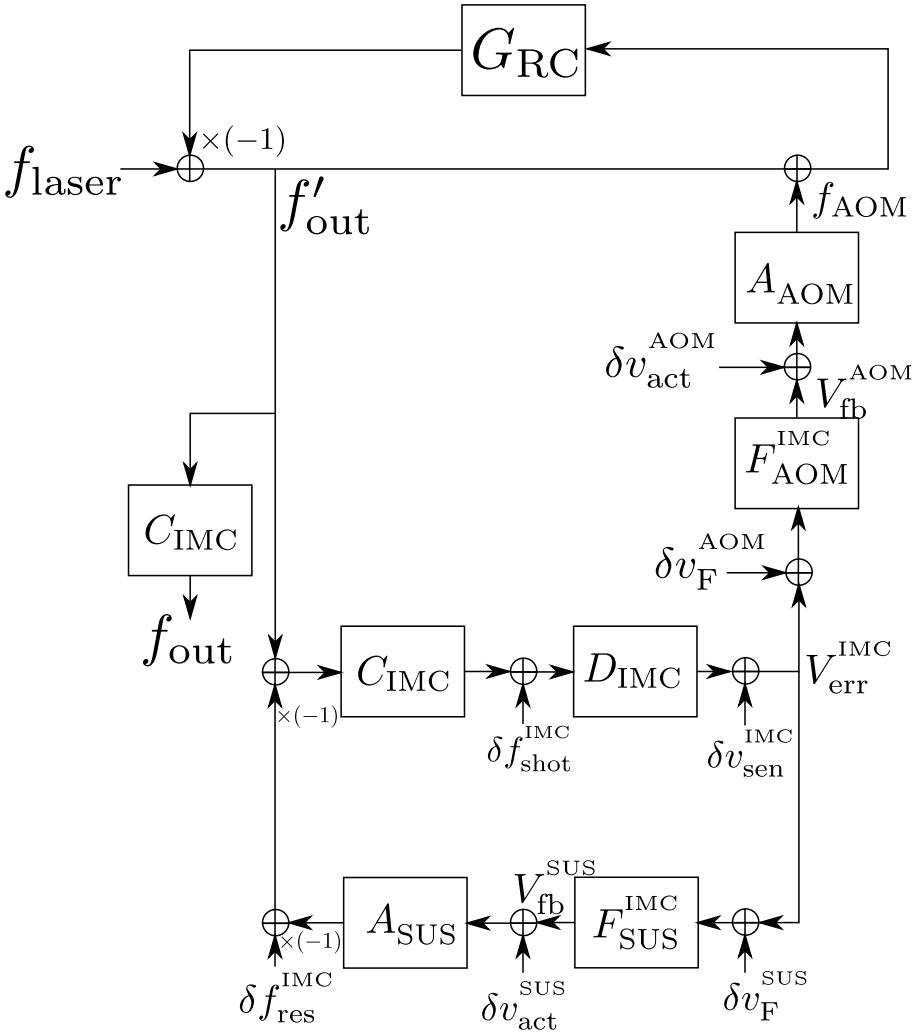

Figure 4.3: Block diagram of the FSS second loop. The schematic diagram of the whole FSS is shown in Fig. 2.10. We have two actuators, a double pass AOM and a coil-magnet actuator on the IMC mirror. A_{AOM} and A_{SUS} are the corresponding actuator responses. The error signal $V_{\mathrm{err}}^{\mathrm{IMC}}$ and feedback signals $V_{\mathrm{fb}}^{\mathrm{AOM}}$ and $V_{\mathrm{fb}}^{\mathrm{SUS}}$ are signals which we can measure. Resonance frequency fluctuation of the IMC $\delta f_{\mathrm{res}}^{\mathrm{IMC}}$, shot noise $\delta f_{\mathrm{shot}}^{\mathrm{IMC}}$, sensor noise $\delta v_{\mathrm{sen}}^{\mathrm{IMC}}$, servo electrical noises $\delta v_{\mathrm{F}}^{\mathrm{AOM}}$ and $\delta v_{\mathrm{F}}^{\mathrm{SUS}}$, and electrical noises of actuator drivers $\delta v_{\mathrm{act}}^{\mathrm{AOM}}$ and $\delta v_{\mathrm{act}}^{\mathrm{SUS}}$ are included as new noises in the second loop.

The noise sources included in the diagram are the servo electrical noises $\delta v_{\mathrm{F}}^{\mathrm{SUS}}$ and $\delta v_{\mathrm{F}}^{\mathrm{AOM}}$, the shot noise $\delta f_{\mathrm{shot}}^{\mathrm{IMC}}$, the resonance frequency fluctuation of the IMC $\delta f_{\mathrm{res}}^{\mathrm{IMC}}$, and the sensor noise $\delta v_{\mathrm{sen}}^{\mathrm{IMC}}$. $\delta v_{\mathrm{act}}^{\mathrm{AOM}}$ and $\delta v_{\mathrm{act}}^{\mathrm{SUS}}$ are the actuator noises of the AOM and the coil-magnet actuator. Since the AOM and the coil-magnet actuator of the suspension are controlled by using the driver with the electric circuit, the electric circuit noise has to be taken into account. On the other hand, the PZT and the EOM, which are the actuators in the first loop, are controlled by directly applying the voltage of the control signal, so no such a noise is included.

The transfer function from f_{AOM} to ${f_{\mathrm{out}}}'$ can be derived as

$$ {f_{\mathrm{out}}}' = \frac{-G_{\mathrm{RC}}}{1+G_{\mathrm{RC}}} f_{\mathrm{AOM}}. \tag{4.8} $$

The unity gain frequency (UGF) of the second loop is lower than that of the first loop. Therefore, the OLG of the first loop G_{RC} is much larger than 1 at all frequencies in the second loop bandwidth and Eq. (4.8) can be rewritten as ${f_{\mathrm{out}}}' = -f_{\mathrm{AOM}}$. Therefore, the stabilized output frequency from the IMC $f_{\mathrm{out}}^{\mathrm{IMC}}$ can be derived as

$$ \begin{aligned} f_{\mathrm{out}}^{\mathrm{IMC}} = \frac{C_{\mathrm{IMC}}}{1+G_{\mathrm{IMC}}}((1+G_{\mathrm{SUS}}^{\mathrm{IMC}})(f_{\mathrm{out}}^{\mathrm{RC}} + A_{\mathrm{AOM}}(\delta v_{\mathrm{act}}^{\mathrm{AOM}} + F_{\mathrm{AOM}}\delta v_{\mathrm{F}}^{\mathrm{AOM}})) \\ + F_{\mathrm{AOM}}A_{\mathrm{AOM}}(\delta v_{\mathrm{sen}}^{\mathrm{IMC}} + D_{\mathrm{IMC}}\delta f_{\mathrm{shot}}^{\mathrm{IMC}}) + G_{\mathrm{AOM}}^{\mathrm{IMC}}(\delta f_{\mathrm{res}}^{\mathrm{IMC}} + A_{\mathrm{SUS}}(\delta v_{\mathrm{act}}^{\mathrm{SUS}} + F_{\mathrm{SUS}}^{\mathrm{IMC}}\delta v_{\mathrm{F}}^{\mathrm{SUS}}))), \end{aligned} \tag{4.9} $$

where $G_{\mathrm{SUS}}^{\mathrm{IMC}} = C_{\mathrm{IMC}}D_{\mathrm{IMC}}F_{\mathrm{SUS}}^{\mathrm{IMC}}A_{\mathrm{SUS}}$ and $G_{\mathrm{AOM}}^{\mathrm{IMC}} = C_{\mathrm{IMC}}D_{\mathrm{IMC}}F_{\mathrm{AOM}}^{\mathrm{IMC}}A_{\mathrm{AOM}}$ are the OLGs of each actuator loop, and $G_{\mathrm{IMC}} = G_{\mathrm{SUS}}^{\mathrm{IMC}} + G_{\mathrm{AOM}}^{\mathrm{IMC}}$ is the total OLG of the second loop. Then, the error signal and feedback signals can be calculated as

$$ \begin{aligned} V_{\mathrm{err}}^{\mathrm{IMC}} = \frac{1}{1+G_{\mathrm{IMC}}}(H_{\mathrm{IMC}}(f_{\mathrm{out}}^{\mathrm{RC}} + A_{\mathrm{AOM}}(\delta v_{\mathrm{act}}^{\mathrm{AOM}} + F_{\mathrm{AOM}}\delta v_{\mathrm{F}}^{\mathrm{AOM}})) \\ + (\delta v_{\mathrm{sen}}^{\mathrm{IMC}} + D_{\mathrm{IMC}}\delta f_{\mathrm{shot}}^{\mathrm{IMC}}) + H_{\mathrm{IMC}}(\delta f_{\mathrm{res}}^{\mathrm{IMC}} + A_{\mathrm{SUS}}(\delta v_{\mathrm{act}}^{\mathrm{SUS}} + F_{\mathrm{SUS}}^{\mathrm{IMC}}\delta v_{\mathrm{F}}^{\mathrm{SUS}}))), \end{aligned} \tag{4.10} $$

$$ \begin{aligned} V_{\mathrm{fb}}^{\mathrm{AOM}} = \frac{F_{\mathrm{AOM}}^{\mathrm{IMC}}}{1+G_{\mathrm{IMC}}}((H_{\mathrm{IMC}}(f_{\mathrm{out}}^{\mathrm{RC}} + A_{\mathrm{AOM}}\delta v_{\mathrm{act}}^{\mathrm{AOM}}) + v_{\mathrm{F}}^{\mathrm{AOM}}) \\ + (\delta v_{\mathrm{sen}}^{\mathrm{IMC}} + D_{\mathrm{IMC}}\delta f_{\mathrm{shot}}^{\mathrm{IMC}}) + H_{\mathrm{IMC}}(\delta f_{\mathrm{res}}^{\mathrm{IMC}} + A_{\mathrm{SUS}}(\delta v_{\mathrm{act}}^{\mathrm{SUS}} + F_{\mathrm{SUS}}^{\mathrm{IMC}}\delta v_{\mathrm{F}}^{\mathrm{SUS}}))), \end{aligned} \tag{4.11} $$

and

$$ \begin{aligned} V_{\mathrm{fb}}^{\mathrm{SUS}} = \frac{F_{\mathrm{SUS}}^{\mathrm{IMC}}}{1+G_{\mathrm{IMC}}}(H_{\mathrm{IMC}}(f_{\mathrm{out}}^{\mathrm{RC}} + A_{\mathrm{AOM}}(\delta v_{\mathrm{act}}^{\mathrm{AOM}} + F_{\mathrm{AOM}}\delta v_{\mathrm{F}}^{\mathrm{AOM}})) \\ + (\delta v_{\mathrm{sen}}^{\mathrm{IMC}} + D_{\mathrm{IMC}}\delta f_{\mathrm{shot}}^{\mathrm{IMC}}) + H_{\mathrm{IMC}}(\delta f_{\mathrm{res}}^{\mathrm{IMC}} + A_{\mathrm{SUS}}\delta v_{\mathrm{act}}^{\mathrm{SUS}}) + \delta v_{\mathrm{F}}^{\mathrm{SUS}}), \end{aligned} \tag{4.12} $$

where $H_{\mathrm{IMC}} = D_{\mathrm{IMC}}C_{\mathrm{IMC}}$.

Here, the control band of the second loop is divided into two, and the frequency fluctuation of the outgoing light in each frequency band is discussed.

First, think about the lower frequency band where the suspension control is stronger

than the AOM control, that is $G_{\rm SUS}^{\rm IMC} \gg G_{\rm AOM}^{\rm IMC}$. This is a lower frequency band than the resonance frequency of the IMC suspension, and since the cavity length of the RC is more stable, the cavity length of the IMC is controlled in this frequency band. The output frequency fluctuation can be derived as

$$f_{\rm out}^{\rm IMC} \simeq f_{\rm out}^{\rm RC} + \frac{G_{\rm AOM}^{\rm IMC}}{G_{\rm SUS}^{\rm IMC}}(\delta f_{\rm res}^{\rm IMC} + \frac{\delta f_{\rm shot}^{\rm IMC}}{C_{\rm IMC}} + \frac{\delta v_{\rm sen}^{\rm IMC}}{H_{\rm IMC}}) + (\frac{\delta v_{\rm F}^{\rm AOM}}{H_{\rm IMC}} + \frac{A_{\rm AOM}}{G_{\rm IMC}}\delta v_{\rm act}^{\rm AOM}) + G_{\rm AOM}^{\rm IMC}(\frac{\delta v_{\rm F}^{\rm SUS}}{H_{\rm IMC}} + \frac{A_{\rm SUS}}{G_{\rm IMC}}\delta v_{\rm act}^{\rm SUS}). \tag{4.13}$$

Next, consider the higher frequency band where the AOM control is stronger than the suspension control, that is $G_{\rm SUS}^{\rm IMC} \ll G_{\rm AOM}^{\rm IMC}$. Since the IMC is a stable frequency reference in this band, the frequency of the laser is controlled to follow the IMC resonance frequency. In this band, the output frequency fluctuation can be derived as

$$f_{\rm out}^{\rm IMC} \simeq \frac{1+G_{\rm SUS}^{\rm IMC}}{G_{\rm AOM}^{\rm IMC}} f_{\rm out}^{\rm RC} + \delta f_{\rm res}^{\rm IMC} + \frac{\delta f_{\rm shot}^{\rm IMC}}{C_{\rm IMC}} + \frac{\delta v_{\rm sen}^{\rm IMC}}{H_{\rm IMC}} + (1+G_{\rm SUS}^{\rm IMC})(\frac{\delta v_{\rm F}^{\rm AOM}}{H_{\rm IMC}} + \frac{A_{\rm AOM}}{G_{\rm IMC}}\delta v_{\rm act}^{\rm AOM}) + G_{\rm SUS}^{\rm IMC}(\frac{\delta v_{\rm F}^{\rm SUS}}{H_{\rm IMC}} + \frac{A_{\rm SUS}}{G_{\rm IMC}}\delta v_{\rm act}^{\rm SUS}). \tag{4.14}$$

As seen from Eq. (4.13), the frequency stability of the outgoing light is determined by the residual frequency fluctuation $f_{\rm out}^{\rm RC}$ of the first loop in the band where $G_{\rm SUS}^{\rm IMC} \gg G_{\rm AOM}^{\rm IMC}$. In this frequency band, since the cavity length of the IMC follows the frequency of the laser, it does not work as a frequency reference, and it is natural that the RC determines the frequency stability. On the other hand, the resonance frequency fluctuation of the IMC $\delta f_{\rm res}^{\rm IMC}$ determines the frequency stability of the laser in the band where $G_{\rm SUS}^{\rm IMC} \ll G_{\rm AOM}^{\rm IMC}$. However, as you can see from the first term of Eq. (4.14), the resonance frequency fluctuation of the RC will shake the IMC, if $G_{\rm SUS}^{\rm IMC} > 1$. As a result, the frequency of the outgoing light also fluctuates. Therefore, it is necessary to suppress the gain of the suspension loop at as low frequency as possible. Similarly from the second term of Eq. (4.13), if the OLG of the suspension loop $G_{\rm SUS}^{\rm IMC}$ is larger than 1, the residual frequency fluctuation $f_{\rm out}^{\rm RC}$ makes the output frequency stability worse by shaking the IMC via the IMC suspension loop.

In the intermediate frequency band where $G_{\rm SUS}^{\rm IMC} \sim G_{\rm AOM}^{\rm IMC}$, the residual frequency fluctuation $f_{\rm out}^{\rm RC}$ and the resonance frequency fluctuation of the IMC $\delta f_{\rm res}^{\rm IMC}$ are not suppressed in the second loop. However, the crossover frequency, at which $G_{\rm SUS}^{\rm IMC} = G_{\rm AOM}^{\rm IMC}$, is around 1 Hz in the second loop, and the IMC resonance frequency fluctuation $\delta f_{\rm res}^{\rm IMC}$ is much larger than the residual frequency fluctuation $f_{\rm out}^{\rm RC}$ at the frequency around 1 Hz. Therefore, in this intermediate frequency band, the frequency stability of the outgoing light is determined by $\delta f_{\rm res}^{\rm IMC}$.

The servo noises $\delta v_{\rm F}^{\rm AOM}$ and $\delta v_{\rm F}^{\rm SUS}$ can be suppressed by increasing the optical gain

D_{IMC}. However, we cannot suppress the actuator noises $\delta v_{\mathrm{act}}^{\mathrm{AOM}}$ and $\delta v_{\mathrm{act}}^{\mathrm{SUS}}$ without decreasing each loop gain.

4.2.3 Third loop with arm cavities

Error signals from the arm cavities are fed back to the end test massed (ETMs) in the lower-frequency band below 10 Hz and fed back to the IMC suspension in the higher-frequency band. Therefore, in the fast frequency band, the resonance frequency of the IMC follows the resonance frequency of the arm cavities. The arm cavities are more stable than the IMC, and the stability of the laser frequency is ideally determined by the frequency stability of the arm cavities. The formulation of the third loop is a repetition of the second loop. Therefore, we will skip it.

4.3 Calibration of the frequency stabilization system

4.3.1 Actuators

For an investigation of the FSS performance, the FSS must be modeled accurately. In general, to model the feedback loop system, we need to know a plant transfer function, an actuator response, and a servo filter transfer function. The transfer function of the servo filter can be easily measured. In the FSS case, the plant is the optical cavity and the measurement the optical gain is difficult since there are no good out-of-loop sensors which can measure the frequency fluctuation of the laser light. However, if the actuator response can be calibrated, the optical gain can be estimated from the OLG, the transfer function of the servo filter, and the actuator response. Therefore, the calibration of the actuator response is the critical issue for the modeling of the FSS.

The basic idea of calibration is to set one absolute reference and to take a ratio to the reference. Let us think of the simple feedback system with two actuators as shown in Fig. 4.4. Inject the excitation signal $V_{\rm exc}$ between one servo and actuator pair. The transfer function, V_2/V_1 can be derived as

$$\frac{V_2}{V_1} = \frac{G_1}{1+G_2}, \tag{4.15}$$

where $G_1 = HF_1A_1$ and $G_2 = HF_2A_2$ are the OLGs of each loop. If G_2 is much greater than than 1,

$$\frac{V_2}{V_1} \simeq \frac{F_2A_2}{F_1A_1}. \tag{4.16}$$

Therefore, if A_1, F_1, and F_2 are known, A_2 can be derived from V_2/V_1 without H which is the optical response of the cavity in the FSS case. In this calibration, the AOM is chosen as the absolute reference, based on which we calibrate the other actuators.

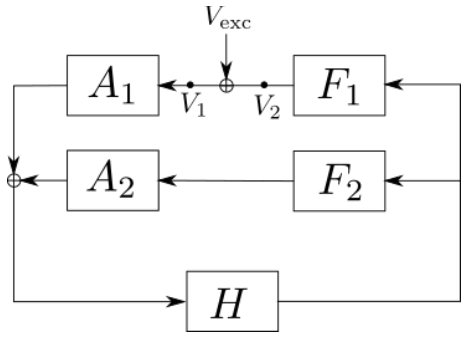

Figure 4.4: Block diagram with two actuators. A, F, and H are transfer functions of an actuator, a servo filter, and a plant respectively.

- AOM calibration

  The amount of a shift frequency in the laser light by an AOM is the same as the

frequency of a sound wave in the AOM crystal, as is shown in Eq. (3.2). It is easy to know the frequency by measuring an output RF signal frequency from a voltage-controlled oscillator (VCO). Therefore, the AOM is the most appropriate actuator as the absolute reference for the FSS calibration. Figure 4.5 shows the measured frequency of the output RF signal from the AOM driver as a function of an input voltage to the VCO. The output frequency was measured with a network analyzer. The slope of the plot is 5.01 MHz/V. Therefore, the actuator efficiency of the AOM a_{AOM} is calibrated as

$$a_{\mathrm{AOM}} = 10.02 \pm 0.01\,\mathrm{MHz/V}. \tag{4.17}$$

Here, note that the actuator efficiency becomes twice as large as the slope due to the double path configuration.

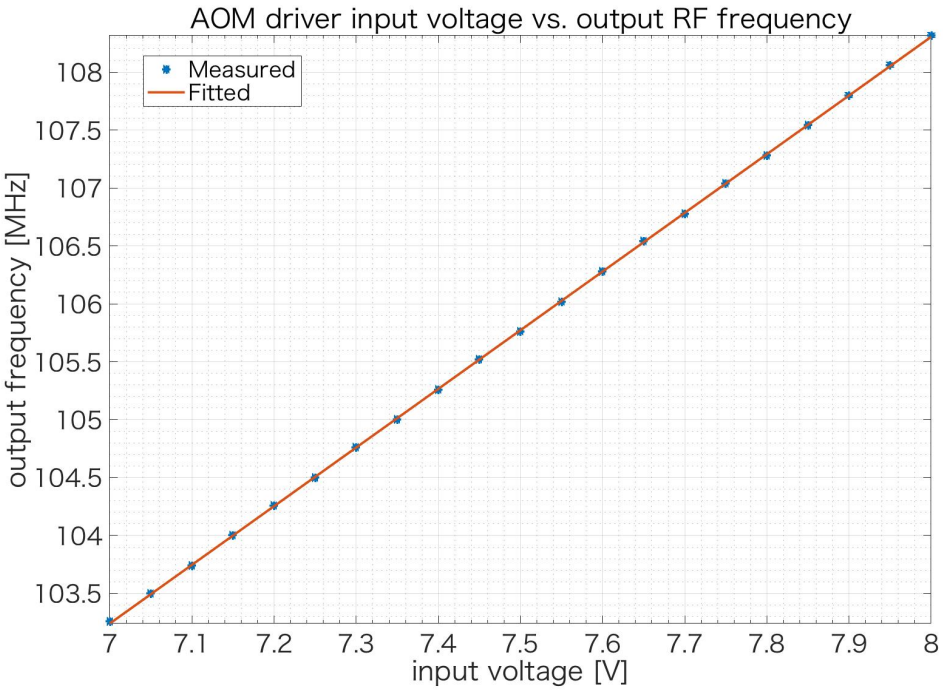

Figure 4.5: Plot of output signal frequency from the AOM driver as a function of the FM input voltage. Blue points are the measured data and red line is a fitted curve.

The bandwidth of the AOM is important to design the second loop. Therefore, the actuator response of the AOM was measured in addition to the actuator efficiency. The first loop was locked with the PZT, and the OLG was measured. Then, the excitation signal was injected into the AOM driver. The transfer function from the excitation signal V_{exc} to the error signal V_{err} can be derived as

$$\frac{V_{\mathrm{err}}}{V_{\mathrm{exc}}} = \frac{H_{\mathrm{RC}} A_{\mathrm{AOM}}}{1 + G_{\mathrm{PZT}}}. \tag{4.18}$$

The OLG G_{PZT} was measured, and the cavity pole of the RC is obtained by an-

other measurement described in Subsection 4.3.2. Therefore, the actuator response is derived as

$$A_{\mathrm{AOM}} = \frac{V_{\mathrm{err}}}{V_{\mathrm{exc}}} \frac{1 + G_{\mathrm{PZT}}}{H_{\mathrm{RC}}}. \tag{4.19}$$

Figure 4.6 shows the calculated actuator response A_{AOM} by using the measured transfer function $V_{\mathrm{err}}/V_{\mathrm{exc}}$, H_{RC}, and G_{PZT}. Since we are not interested in the overall gain, the calculated actuator response A_{AOM} is normalized by the DC gain. From Fig. 4.6, the actuator response can be assumed as the first-order low-pass filter. The gain of a first-order low-pass filter at pole frequency is -3 dB. Therefore, the pole frequency of the AOM response can be read off as

$$f_{p-\mathrm{AOM}} = 167 \pm 4\,\mathrm{kHz}, \tag{4.20}$$

where this measured value and its error are based on five measurements.

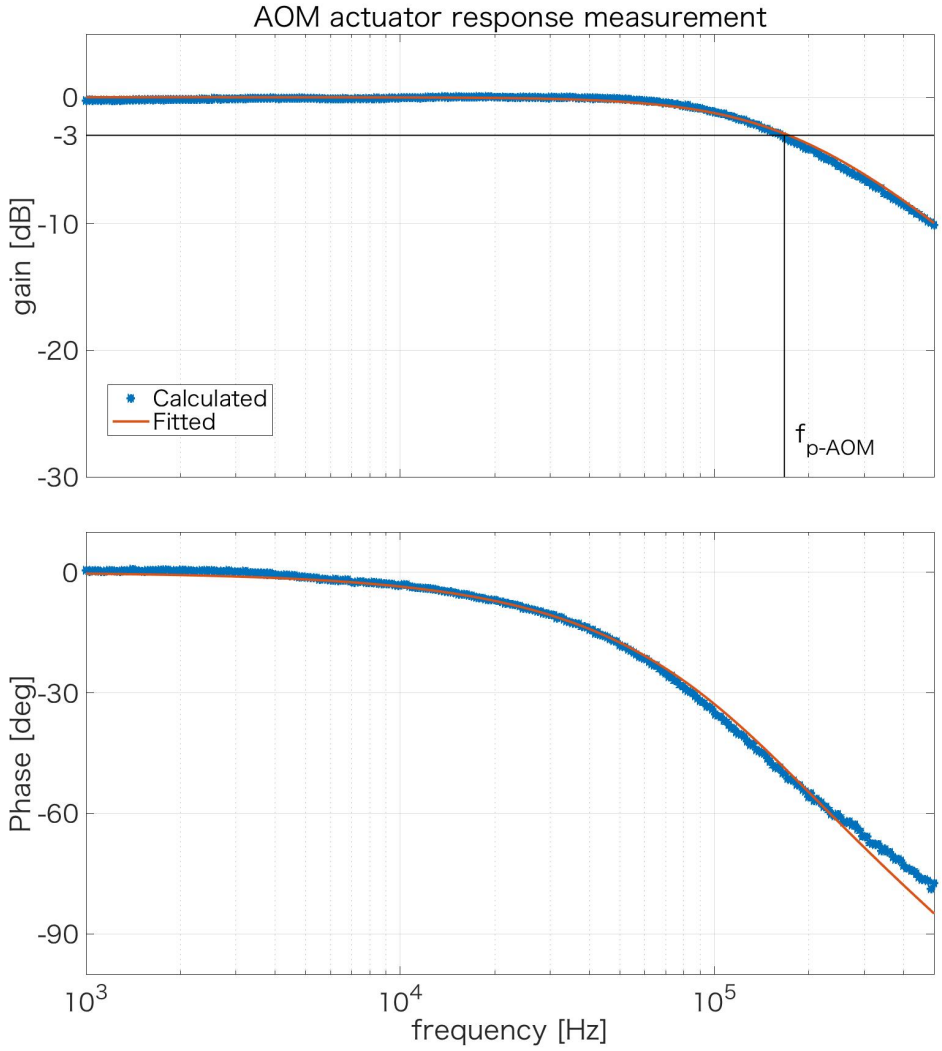

Figure 4.6: Calculated actuator response of the AOM A_{AOM}. It is the first-order low-pass filter and it has one pole at 167 kHz.

- NPRO PZT calibration

  For the calibration of the NPRO PZT, the FSS first loop was locked only with the PZT. Then, the control signal to the PZT was divided into two, of which one was injected into the AOM. In this case, A_1 and A_2 in Eq. (4.16) are the actuator response of the PZT and that of the AOM, respectively. Moreover, as $F_1 = F_2$ holds, the transfer function can be written as $V_2/V_1 = A_{\mathrm{PZT}}/A_{\mathrm{AOM}}$ at frequencies below the UGF. The measured transfer function of $V_2/V_1 = 0.127$ below the UGF. The actuator efficiency of the NPRO PZT is obtained as

$$A_{\mathrm{PZT}} = 1.27 \pm 0.05\,\mathrm{MHz/V}. \tag{4.21}$$

- Broadband EOM calibration

  For the calibration of the broadband EOM, the FSS first loop was locked with the PZT and the broadband EOM. The measurement was done in the PZT loop. Since the transfer function is measured in the frequency band of $G_{\mathrm{EOM}} \gg 1$, from Eq. (4.16),

$$\frac{V_2}{V_1} = \frac{F_{\mathrm{PZT}} A_{\mathrm{PZT}}}{F_{\mathrm{EOM}} A_{\mathrm{EOM}}}. \tag{4.22}$$

  Therefore, the frequency response of the EOM can be derived as

$$A_{\mathrm{EOM}} = \frac{F_{\mathrm{PZT}} A_{\mathrm{PZT}}}{F_{\mathrm{EOM}}} \frac{V_1}{V_2}. \tag{4.23}$$

  The frequency response calculated by using the obtained data is shown in Fig. 4.7. The obtained actuator response is

$$A_{\mathrm{EOM}}(f) = (160 \pm 10) \left(\frac{f}{10\,\mathrm{kHz}} \right) \mathrm{Hz/V}. \tag{4.24}$$

  Note here that the EOM does not modulate a frequency but a phase. Therefore, the actuator response is proportional to the Fourier frequency f.

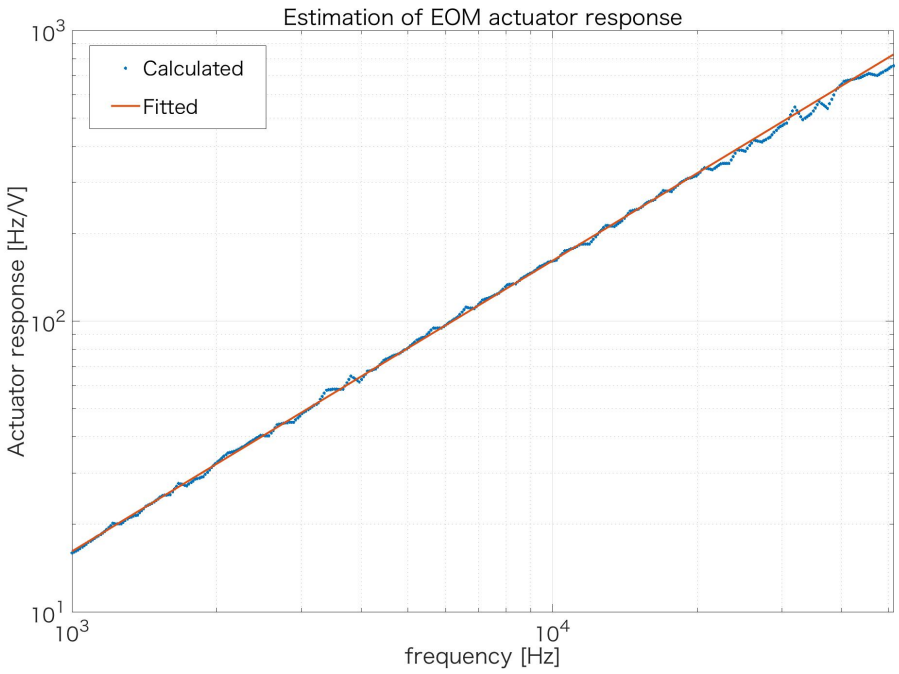

Figure 4.7: Frequency response of the broadband EOM. Blue dots are the calculated data with the measured value by Eq. (4.23) and red line is a fitted curve.

- IMC suspension calibration

  The actuator response of the suspension can be derived from the equation of motion. The equation of motion can be written as

$$m\ddot{x} = -\frac{mg}{l}x - \gamma\dot{x} + F, \tag{4.25}$$

  where m is the mass of the test mass, g is the gravitational acceleration, l is the length of the suspension, F is the external force, and γ is the viscous damping coefficient. Equation (4.25) can be solved in the same manner as Eq. (1.52). The external force can be written as $F = AV$, where A is the actuator efficiency of the actuator, and V is the input voltage. Therefore, the frequency response from the input voltage to the displacement of the IMC mirror can be derived as

$$\tilde{x}(f) = \frac{A_{\mathrm{SUS}} f_0^2}{-f^2 + if f_0/Q + f_0^2}\tilde{V}(f), \tag{4.26}$$

  where $\tilde{x}(f)$ and $\tilde{V}(f)$ are the Fourier components of the displacement and the input voltage to the actuator, f_0 is the resonance frequency, Q is a quality factor, and A_{SUS} is an actuator efficiency at low frequencies.

  For the IMC suspension calibration, the second loop was locked with the AOM and the IMC suspension. The transfer function V_2/V_1 was measured in the suspension loop. From a similar calculation to that for the broadband EOM calibration, the

suspension response can be derived as

$$A_{\mathrm{SUS}} = \frac{F_{\mathrm{AOM}} A_{\mathrm{AOM}}}{F_{\mathrm{SUS}}} \frac{V_2}{V_1}. \tag{4.27}$$

The calculated frequency response by using the measured data is shown in Fig. 4.8. The resonance frequency f_0 can be obtained by reading off the peak frequency. By using the frequency f_1, f_2 at which the gain is $\sqrt{2}$ times lower than the peak height, the quality factor Q can be obtained as

$$Q = \frac{f_0}{f_2 - f_1}. \tag{4.28}$$

The obtained parameters of the suspension actuator response are as follows:

$$f_0 = 0.95 \pm 0.05\,\mathrm{Hz}, \tag{4.29}$$

$$Q = 4.8 \pm 0.7, \tag{4.30}$$

$$\text{and} \quad A_{\mathrm{SUS}} = 42 \pm 3\,\mathrm{MHz/V}, \tag{4.31}$$

where each measured value and its error are based on ten measurements.

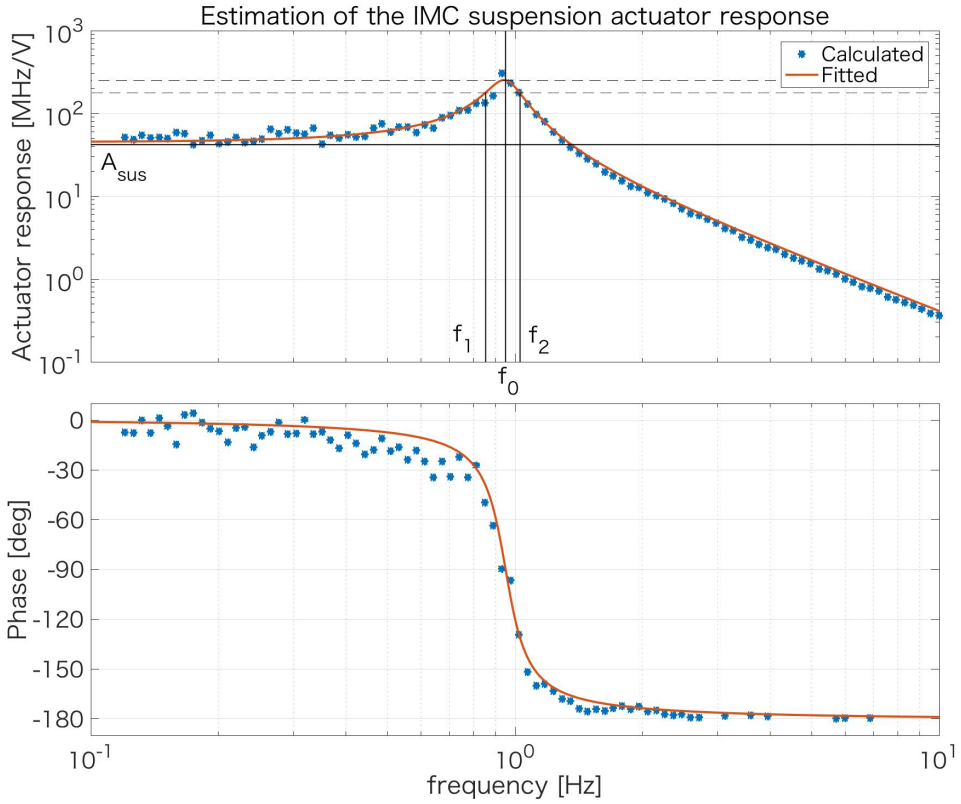

Figure 4.8: Frequency response of the IMC suspension. Blue dots are the calculated data with measured value by Eq. (4.27) and red line is a fitted curve. f_0 is the resonance frequency, and Q can be derived as $Q = f_0/(f_2 - f_1)$.

.

4.3.2 Cavity parameters

Cavity pole

As described in Appendix A.2.3, an optical cavity works as a low-pass filter for noises with a cutoff frequency of a cavity pole. The cavity pole is another important parameter to investigate the system. Cavity poles of the RC and the IMC were estimated by different methods

- Reference cavity

  To measure the cavity pole of the RC, an excitation signal was injected into an amplitude modulation port of the AOM driver. This means that the amplitude modulation (AM) was applied to the injection light. Then, the transfer function $P_{\mathrm{trans}}/P_{\mathrm{refl}}$ was measured, where P_{trans} and P_{refl} are the transmitted and reflected power, respectively. The AM is reduced by the low-pass filter of the cavity as shown in Appendix A.2.3, and the high-frequency component is cut in the outgoing light. Therefore, the cavity pole can be obtained from the transfer function $P_{\mathrm{trans}}/P_{\mathrm{refl}}$. Figure 4.9 shows the measured transfer function $P_{\mathrm{trans}}/P_{\mathrm{refl}}$ and the fitted curve. The estimated cavity pole $f_{\mathrm{cp}}^{\mathrm{RC}}$ is

$$f_{\mathrm{cp}}^{\mathrm{RC}} = 67 \pm 2\,\mathrm{kHz}. \tag{4.32}$$

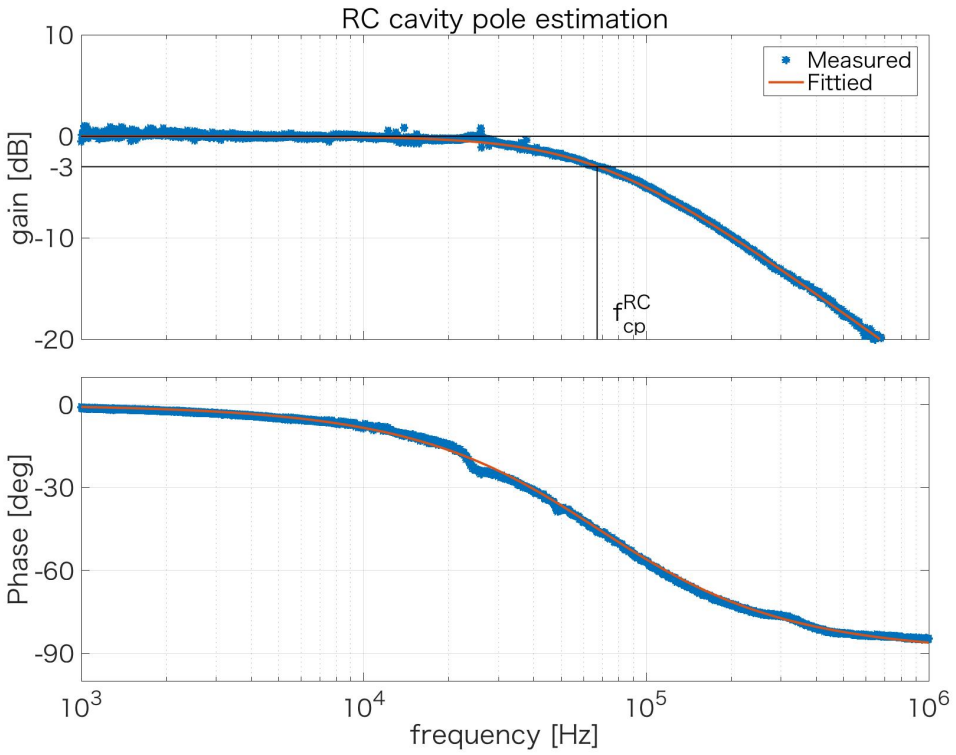

Figure 4.9: Transfer function $P_{\mathrm{trans}}/P_{\mathrm{refl}}$. Blue dots are measured data, and red curve is fitted with the low-pass filter with the cutoff frequency of 67 kHz.

- IMC

  The IMC cavity pole was measured by the transfer function from a control signal of the AOM to an error signal. The measured transfer function corresponds to $A_{\mathrm{AOM}}H_{\mathrm{IMC}}$, where A_{AOM} is almost flat below 100 kHz as shown in Fig. 4.6. Therefore, the shape of this transfer function is the same as that of the cavity low-pass filter. The measured transfer function is shown in Fig. 4.10. The estimated cavity pole $f_{\mathrm{cp}}^{\mathrm{IMC}}$ is

$$f_{\mathrm{cp}}^{\mathrm{IMC}} = 6.1 \pm 0.3\,\mathrm{kHz}. \tag{4.33}$$

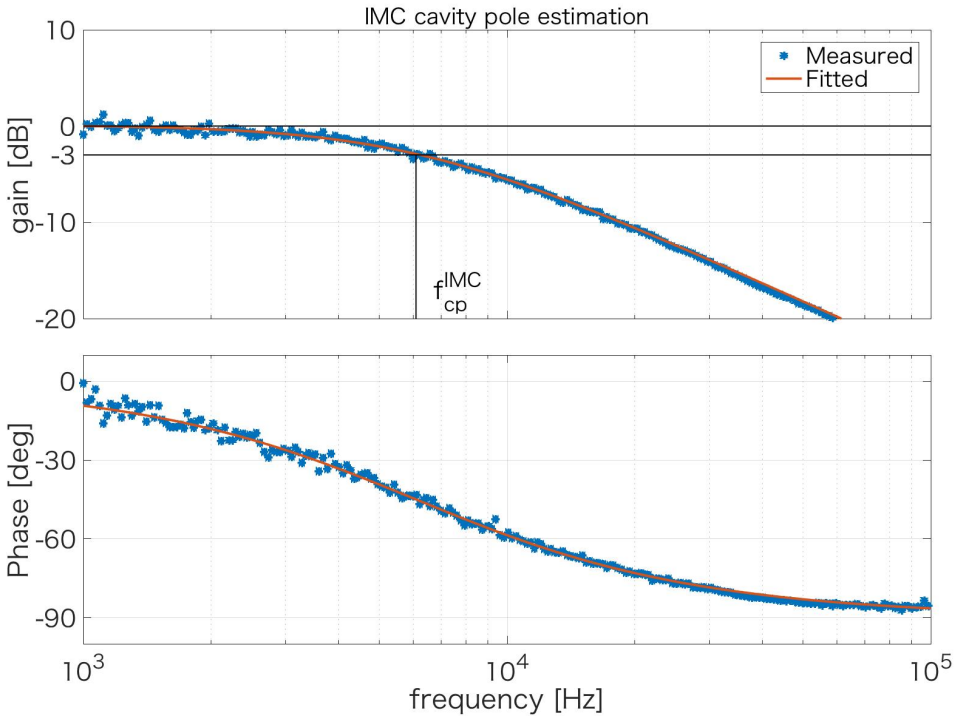

Figure 4.10: Transfer function $P_{\mathrm{trans}}/P_{\mathrm{refl}}$. Blue dots are measured data and red curve is fitted with the low-pass filter with the cutoff frequency of 6.1 kHz.

Free spectral range

- Reference cavity

  A free spectral range (FSR) is equivalent information to a cavity length. The RC cavity length of 10 cm was employed from the designed value. Then, the FSR of the RC is calculated as

$$\nu_{\mathrm{FSR}}^{\mathrm{RC}} = 1.5\,\mathrm{GHz}. \tag{4.34}$$

- IMC

  To control the IMC, the incident light to the IMC is modulated in phase. The PDH signal cannot be obtained, when the modulation frequency and the FSR of the IMC become equal. This is because the sideband for obtaining the beat signal also

resonates with the IMC. Namely, the relative phase between the sideband and the carrier remains unchanged in the reflected light and the phase modulation of the reflected light is kept. The obtained FSR is

$$\nu_{\mathrm{FSR}}^{\mathrm{IMC}} = 5.6242 \pm 0.0003\,\mathrm{MHz}. \tag{4.35}$$

Finesse

From the FSR and the cavity pole, finesse can be calculated. The values of finess of each cavity are as follows:

$$\mathcal{F}_{\mathrm{RC}} = 11100 \pm 300, \tag{4.36}$$

$$\mathcal{F}_{\mathrm{IMC}} = 458 \pm 20. \tag{4.37}$$

Optical gain

As mentioned above, an optical gain of a cavity can be estimated from an OLG. The OLG of the first loop and the second loop can be written as

$$G_{\mathrm{RC}} = D_{\mathrm{RC}} C_{\mathrm{RC}} (A_{\mathrm{PZT}} F_{\mathrm{PZT}} + A_{\mathrm{EOM}} F_{\mathrm{EOM}}), \tag{4.38}$$

$$G_{\mathrm{IMC}} = D_{\mathrm{IMC}} C_{\mathrm{IMC}} (A_{\mathrm{SUS}} F_{\mathrm{SUS}} + A_{\mathrm{AOM}} F_{\mathrm{AOM}}), \tag{4.39}$$

where C is the transfer function of low-pass filter and D is the optical gain of each cavity, and C, A, and F are already obtained. Therefore, from OLGs, the optical gain can be obtained as

$$D_{\mathrm{RC}} = 7.6 \pm 0.5\,\mathrm{V/MHz}, \tag{4.40}$$

$$D_{\mathrm{IMC}} = 7.8 \pm 0.7\,\mathrm{V/MHz}. \tag{4.41}$$

$$\tag{4.42}$$

In Figs.3.10 and 3.12, the modeled OLGs with the obtained parameters are shown with measured OLGs.

4.3.3 Error estimation

Each parameter is estimated by the fitting of each transfer function. We took ten measurements for each transfer function and fitting was performed for each measured data to estimate the parameters. The error of the parameter was estimated by taking the standard error of the ten estimated values for each parameter.

When we make the noise budget, these errors propagate to the error of the noise calculation. For instance, the error in an optical gain propagates in the whole frequency range, and a cavity pole error propagates in the frequency range higher than the cavity pole. However, almost all errors are less than 10 % of each parameter, and the requirement includes the safety margin of 10. Therefore, these errors are small enough to make the noise budget.

4.3.4 Parameter list in the frequency stabilization system model

As a summary of this section, the parameter list obtained above is shown in Table 4.1.

Actuator parameters	
Actuator efficiencies	$A_{\mathrm{AOM}} = 10.02$ MHz/V
	$A_{\mathrm{PZT}} = 1.27$ MHz/V
	$A_{\mathrm{EOM}} = 160$ Hz/V @ 10kHz
suspension	$A_{\mathrm{IMC}} = 40$ MHz/V @ DC
pole of the AOM	$f_{p-\mathrm{AOM}}$= 167 kHz
resonance frequency of the IMC suspension	$f_0 = 0.955$ Hz
Q-factor of the IMC suspension	Q =4.8
Cavity parameters	
Optical gain	D_{RC}=7.6 V/MHz
	D_{IMC}=7.8 V/MHz
FSR	$f_{\mathrm{FSR}}^{\mathrm{RC}} = 1.5$ GHz
	$f_{\mathrm{FSR}}^{\mathrm{IMC}} = 5.6242$ MHz
cavity pole	$\nu_{\mathrm{cp}}^{\mathrm{RC}} = 67$ kHz
	$\nu_{\mathrm{cp}}^{\mathrm{IMC}} = 6.1$ kHz
Finesse	$\mathcal{F}_{\mathrm{RC}} = 11100$
	$\mathcal{F}_{\mathrm{IMC}} = 460$

Table 4.1: Parameters of the FSS.

4.4 Optimization of the control configuration

We simulated the OLGs of the FSS loops with an optimal configuration. Figures 4.11 and 4.12 show the optimal OLGs. The improvements in the simulated model of each loop are as follows:

First loop

- The servo gain of the PZT path is increased by 16 dB.

  The original laser frequency noise does not meet the requirement at higher frequencies than 6 kHz. Therefore, the PZT path gain is increased by 16 dB to suppress the laser frequency noise. In Fig. 4.11, the optimized OLG is the orange line, and it is larger than that before the optimization by 16 dB in the frequency band below 10 kHz where the PZT loop is dominant.

- The servo gain of the EOM path is decreased by 3 dB.

  To optimize the UGF and earn the phase margin as much as possible, the servo gain of the EOM path is decreased by 3 dB. As a result, the phase margin is 32°. Typically, the phase margin of 30° is enough for the robust control of the cavity, and the system will not oscillate. In Fig. 4.11, the optimized OLG is the orange line, and it is larger than that before the optimization by 3 dB in the frequency band higher than 300 kHz where the EOM loop is dominant.

Second loop

- The laser power on the PD is increased up to 2.5 mW from 50 μW.

  The servo noise of the second loop does not meet the requirement above 2 kHz, and the shot noise does not meet the requirement above 6 kHz as well. From Eq. (A.118) the shot noise is inversely proportional to the square root of the laser power. Also from Eq. (4.14), the higher optical gain suppresses the servo noise contribution. This is because the servo gain necessary for realizing the same OLG becomes small, if the optical gain is high. The contribution of the servo noise becomes small as a result. Therefore, higher laser power is required to be injected into the PD in order to improve the contribution of the shot noise and the servo noise in the second loop.

  In the simulation, the laser power on the PD is increased from the current power of 50 μW to 2.5 mW. This assumption is feasible, because the main laser power is increased up to 40 W from 2 W.

- The mode matching ratio of the IMC is improved up to 80 % from 20 %

  The mode matching ratio is also important to increase the optical gain of the cavity. The more laser power couples with the cavity of the higher mode matching ratio,

which increases the optical gain of the cavity. The mode matching ratio is improved from 20% up to 80 %. The mode matching ratio of the IMC in the test operation of iKAGRA was above 85%. Therefore, this assumption is feasible.

The optical gain is assumed to get higher by factor of 200 than current value by the improvement of the mode matching ratio and the power increasing.

- A second-order high-pass filter with the cutoff frequency of 0.5 Hz is added to the AOM loop.

  At the lower frequencies below 1 Hz, the cavity length of the RC is more stable than that of the IMC. Therefore, the control signal should not be fed back to the AOM, since the IMC length fluctuation propagates to the laser frequency. The high-pass filter cuts off the control signal to the AOM at the lower frequencies.

- A boost filter to earn the servo gain in the band from 10 Hz to 10 kHz is added to the AOM loop.

  The residual amplitude modulation (RAM) noise in the first loop limits the performance of the frequency stabilization in the frequency band from 10 Hz to 10 kHz. Since the RAM noise can be suppressed by the second loop, the boost filter was added in order to increase the OLG of the second loop.

  Because of this boost filter, the phase difference between two OLGs of each actuator loop gets slightly closer to 180°. Therefore, the total OLG at the frequencies around 2 Hz gets smaller by this optimization. That means the suppression ratio becomes worse and several noises increase at these frequencies. However, the noises at these frequencies satisfy the requirements by huge margins, and the differences are small enough compared to these margins.

Open loop gains

The UGF and phase margin are as follows:

$$
\begin{aligned}
f_{\mathrm{UGF}}^{\mathrm{1st}} &= 390\ \mathrm{kHz}, & f_{\mathrm{UGF}}^{\mathrm{2nd}} &= 34\ \mathrm{kHz},\\
f_{\mathrm{co}}^{\mathrm{1st}} &= 61\ \mathrm{kHz}, & f_{\mathrm{co}}^{\mathrm{2nd}} &= 2\ \mathrm{Hz},\\
\theta_{\mathrm{PM}}^{\mathrm{1st}} &= 32^\circ, & \theta_{\mathrm{PM}}^{\mathrm{2nd}} &= 64^\circ,\\
\text{and}\quad \theta_{\mathrm{co}}^{\mathrm{1st}} &= 158^\circ, & \theta_{\mathrm{co}}^{\mathrm{2nd}} &= 212.6^\circ.
\end{aligned}
$$

The phase margins are enough for the both loops. $\theta_{co}^{\mathrm{1st}}$ is close to 180° and actually the OLG of the total first loop has a dip at the crossover frequency. Nonetheless, this optimized system is a stable system, as the gain of the OLG is more than 20 dB at the crossover frequency.

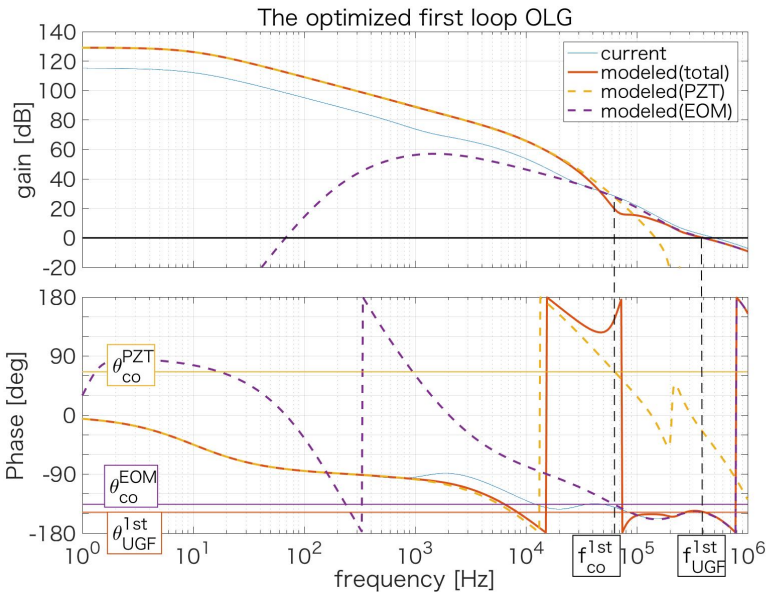

Figure 4.11: Bode diagram of the simulated OLGs of the first loop. The solid orange line is the estimated OLG of the first loop, and yellow and purple dashed lines are the OLGs of the PZT loop and the EOM loop, respectively. Blue thin line is the current OLG. The optimized UGF f_{UGF} is 390 kHz, and the phase margin θ_{PM} is $\theta_{\mathrm{UGF}} + 180° = 32°$. The crossover frequency f_{co} is 61 kHz, and the phase difference between the PZT loop and the EOM loop is $\theta_{\mathrm{co}}^{\mathrm{EOM}} - \theta_{\mathrm{co}}^{\mathrm{PZT}} = -136° - (-294°) = 158°$.

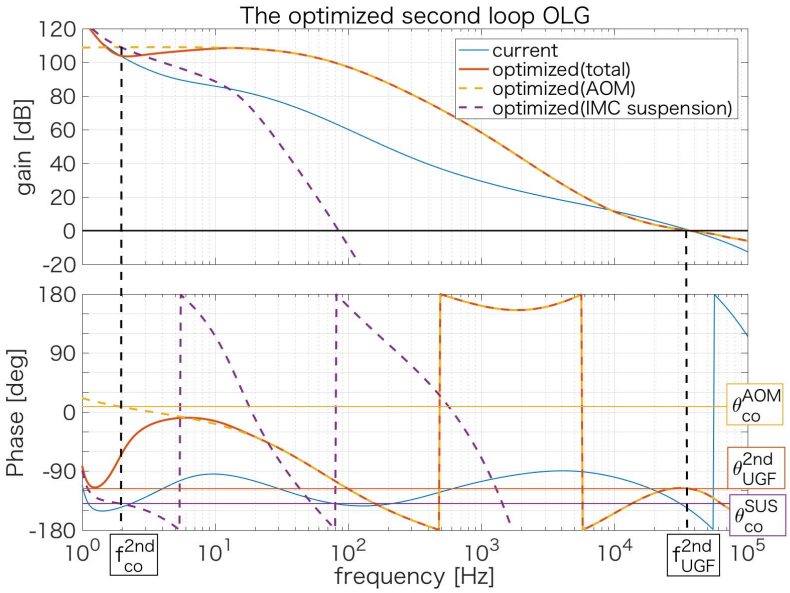

Figure 4.12: Bode diagram of the OLGs of the second loop. The solid orange line is the estimated OLG of the second loop, yellow and purple dashed lines are the OLG of the AOM loop and the suspension loop, respectively. Blue thin line is the current OLG. The UGF $f_{\mathrm{UGF}}^{\mathrm{2nd}}$ is 34 kHz, and the phase margin $\theta_{\mathrm{PM}}^{\mathrm{2nd}}$ is $\theta_{\mathrm{UGF}}^{\mathrm{2nd}} + 180° = 64°$. The crossover frequency $f_{\mathrm{co}}^{\mathrm{2nd}}$ is 4 Hz, and the phase difference between the AOM loop and the suspension loop is $\theta_{\mathrm{co}}^{\mathrm{SUS}} - \theta_{\mathrm{co}}^{\mathrm{AOM}} = 212.6°$.

4.5 Noise budget of the frequency stabilization system

With the parameters estimated in the previous section, we can make a model of the whole FSS loop. Then, as described in Section 4.2, the contributions of each noise in the FSS have been estimated. By using this noise budget, the control loop is designed so that all the noises satisfy the requirements. In this section, first of all, the simulated results of the optimized OLGs are shown. Then, the contributions of measured or estimated noises in the FSS with the current and the optimized configurations are shown and compared with the requirement.

4.5.1 Laser frequency noise

The original laser noise is suppressed by the first and the second loops. The current laser source is the NPRO laser, and it is not the same as the final laser of bKAGRA. However, it is worth checking the contribution of the original noise of the NPRO laser, since the final laser of bKAGRA also uses an NPRO laser as a seed laser [53]. The laser frequency noise is assumed as

$$f_{\mathrm{laser}}(f) = 100 \left(\frac{100\,\mathrm{Hz}}{f} \right) \mathrm{Hz}/\sqrt{\mathrm{Hz}}. \tag{4.43}$$

Figure 4.13 is the contribution of the NPRO laser frequency noise. The laser frequency noise has a larger suppression after the optimization by increasing the OLG of the first loop and the second loop. By increasing the servo gain of the PZT loop in the first loop, the noise is suppressed by 16 dB up to 10 kHz. Furthermore, the boost filter in the second loop suppresses the noise at the frequencies from 10 Hz to 1 kHz.

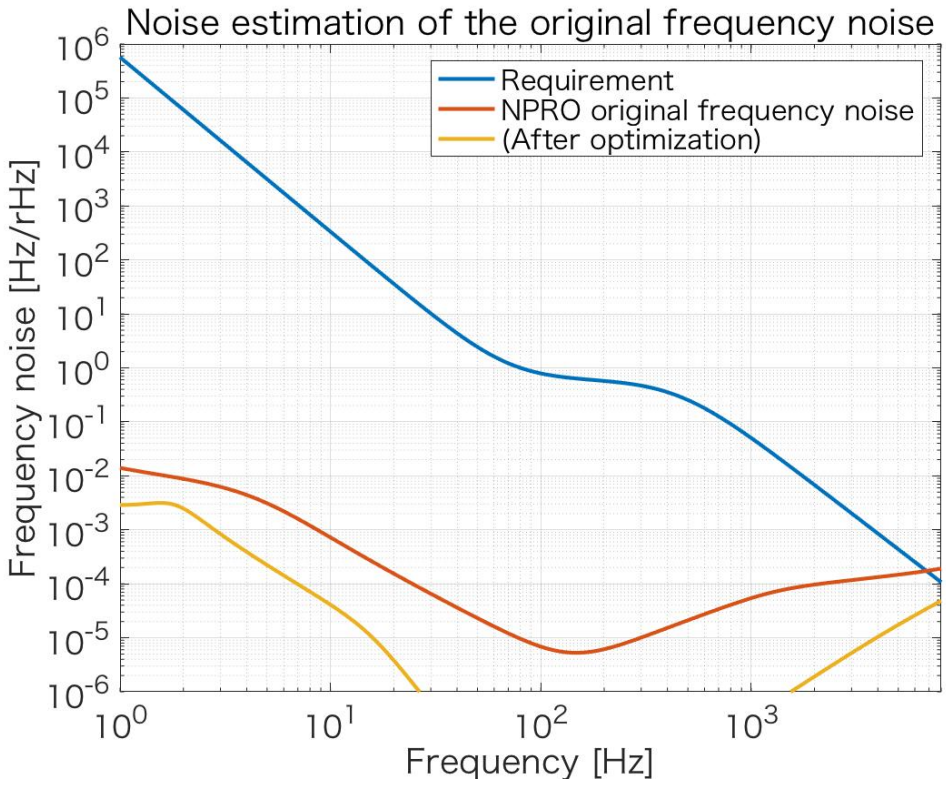

Figure 4.13: Contributions of the NPRO laser frequency noise to the frequency noise in the outgoing light from the IMC. The red curve is the contribution with the current configuration, and the yellow curve is that with the simulated optimal configuration. By increasing the OLG of the first loop and the second loop, the noise meets the requirement.

4.5.2 Noise from resonance frequency fluctuation of the reference cavity

The resonance frequency fluctuation due to residual gas and a seismic motion is estimated. From Eq. (A.125), the resonance frequency fluctuation due to residual gas can be derived as

$$\delta\nu_{\rm gas} = \delta l_{\rm gas}\frac{\Omega_{\rm FSR}}{\lambda} = \frac{1}{4\pi}\frac{8\sqrt{2}}{\sqrt{\pi}}\frac{(n_0-1)^2}{(A_0/V_0)u_0\sqrt{l\lambda}}\left(\frac{p}{p_0}\right)\left(\frac{T_0}{T}\right)\frac{\Omega_{\rm FSR}}{\lambda}, \tag{4.44}$$

where $\Omega_{\rm FSR}$ is the FSR of the RC, λ is the laser wavelength, n_0 is the refractive index of gas, $A_0 = 6.02 \times 10^{23}$ is the Avogadro's number, u_0 is the average speed of the molecule. $V_0 = 2.24 \times 10^{-2}$ m^3 is the volume of gas for the amount of 1 mol under standard state in which the pressure is the standard pressure of $p_0 = 1$ atm and the temperature is the standard temperature of $T_0 = 273.15$ K. The pressure p is assumed as 1 Pa and the temperature T is assumed as 300 K. Molecules of the gas are assumed as mixture of O_2 and N_2 with a ratio of 1:4. Average speed u_0 can be derived as

$$u_0 = \sqrt{\frac{3k_bT}{2m_0}}, \tag{4.45}$$

where k_b is the Boltzmann constant and m_0 is the average mass of the molecule. Then, $\delta\nu_{\rm gas}$ can be obtained as

$$\delta\nu_{\rm gas} = 2.0 \times 10^{-4} \ \mathrm{Hz}/\sqrt{\mathrm{Hz}}. \tag{4.46}$$

Molecular masses of O_2 and N_2 and their refractive indices at the wavelength of 1064 nm are listed in Table 4.2.

The cavity length fluctuation due to the seismic motion can be derived from Eq. (A.126). The coupling constant A between the cavity length fluctuation and the acceleration of the seismic vibration is assumed as

$$A = 10^{-10} \ (\mathrm{m/s^2})^{-1}. \tag{4.47}$$

The coupling constant A assumed above is the product of that obtained by the experiment using the same type of a cavity with the safety factor 10 [54]. The measured seismic motion spectrum in Kamioka is used to derive the seismic acceleration spectrum, as shown in Fig. 2.3.

The contributions of these noises are summarized in Fig. 4.14. All the noise levels satisfy the requirement even before the optimization.

The molecular mass	$m_{\rm O_2} = 5.3\times10^{-23}$ g
	$m_{\rm N_2} = 4.7\times10^{-23}$ g
Refractive index	$n_{\rm O_2} = 1 + 2.97 \times 10^{-4}$
	$n_{\rm N_2} = 1 + 2.72 \times 10^{-4}$

Table 4.2: Molecular masses and refractive indices for the residual gas noise estimation under the standard state.

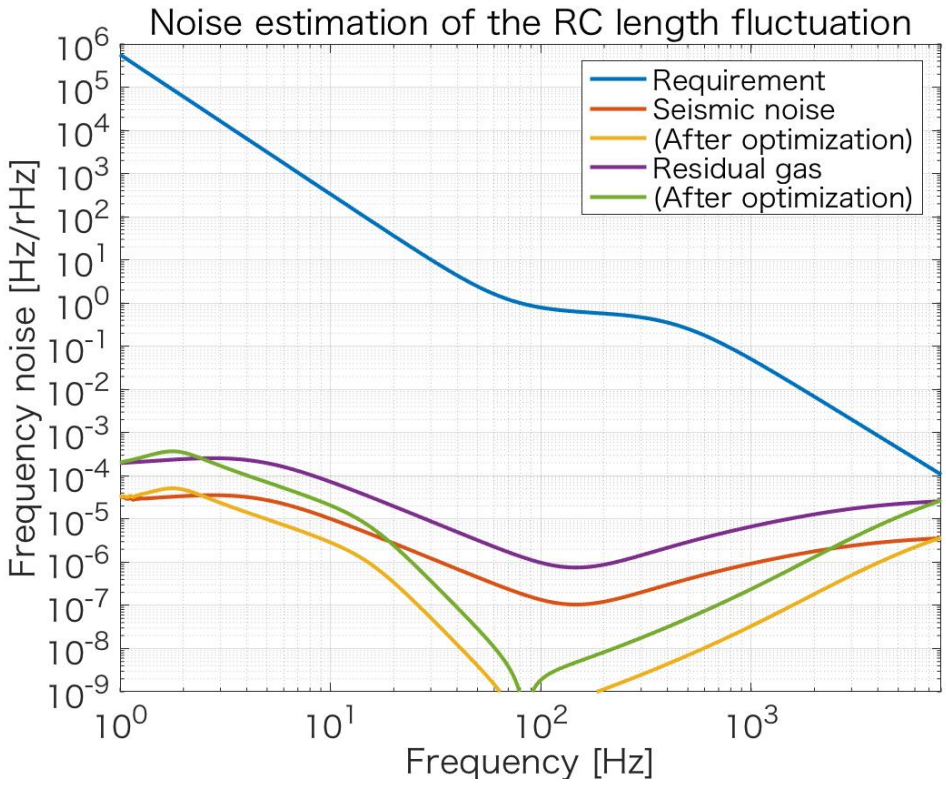

Figure 4.14: Contributions of resonance frequency fluctuation of the RC to the frequency noise in the outgoing light from the IMC. Red and yellow curves are the contributions of the RC length fluctuation due to the seismic motion with the current configuration and with the simulated optimal configuration, respectively. Magenta and green curves are the contributions of residual gas noise with the current configuration and the simulated optimal configuration, respectively. All of the noises meet the requirement, and the boost filter in the second loop suppresses these noises at the frequencies from 10 Hz to 1 kHz. At the frequencies around 2 Hz, the noises increase because of the new boost filter in the AOM loop as mentioned in Section 4.4.

4.5.3 Noise from the IMC length fluctuation

The seismic motion of the IMC mirrors is estimated as shown in Fig. 3.9. Since the OLG of the second loop around 1 Hz is lowered, the suppression of the seismic noise gets small at the frequencies around 1 Hz. On the other hand, the contribution of the seismic noise is suppressed at the frequencies below 0.1 Hz. That is because the propagation of the IMC length fluctuation to the laser frequency was reduced by the high-pass filter added to the AOM loop. At the frequencies higher than 10 Hz the suspension loop has no difference in the optimization. Therefore, we cannot see any difference.

Here, the IMC length fluctuation was determined with an assumption that all three mirrors move independently. However, when all three mirrors move in the same direction, the cavity length does not change. If the seismic motion is correlated with each mirror, actual cavity length fluctuation is smaller than our expectation due to this corre-

lation mainly in the low-frequency band. Therefore, note that the IMC length fluctuation estimated here is an overestimation, and even so it meets the requirement.

The contributions of these noises are shown in Fig. 4.15. All the noise levels satisfy the requirement.

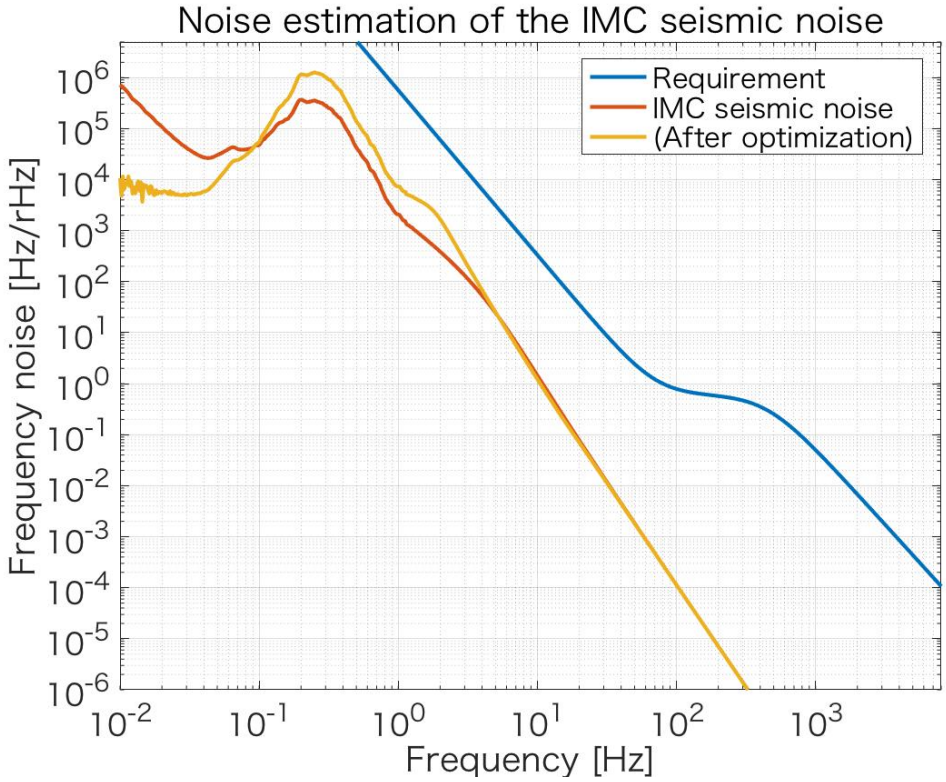

Figure 4.15: Contributions of the IMC length fluctuation to the frequency stability in the outgoing light from the IMC. The red curve is the contribution with the current servo filter, and the yellow curve is that with the simulated optimal servo filter. All noises meet the requirement.

4.5.4 Servo noise

The servo noise spectra were measured at the output port of each servo filter with the input port terminated. Then, those are divided by transfer functions of each servo filter and converted to input equivalent noise spectra. Figure 4.16 shows the contributions of servo noises of each servo filter.

The second loop servo noise does not satisfy the requirement with the current control configuration. By increasing the optical gain of the IMC, the contribution of the servo noise in the second loop is expected to be suppressed by a factor of 200. In the system with the increased optical gain, that noise will meet the requirement.

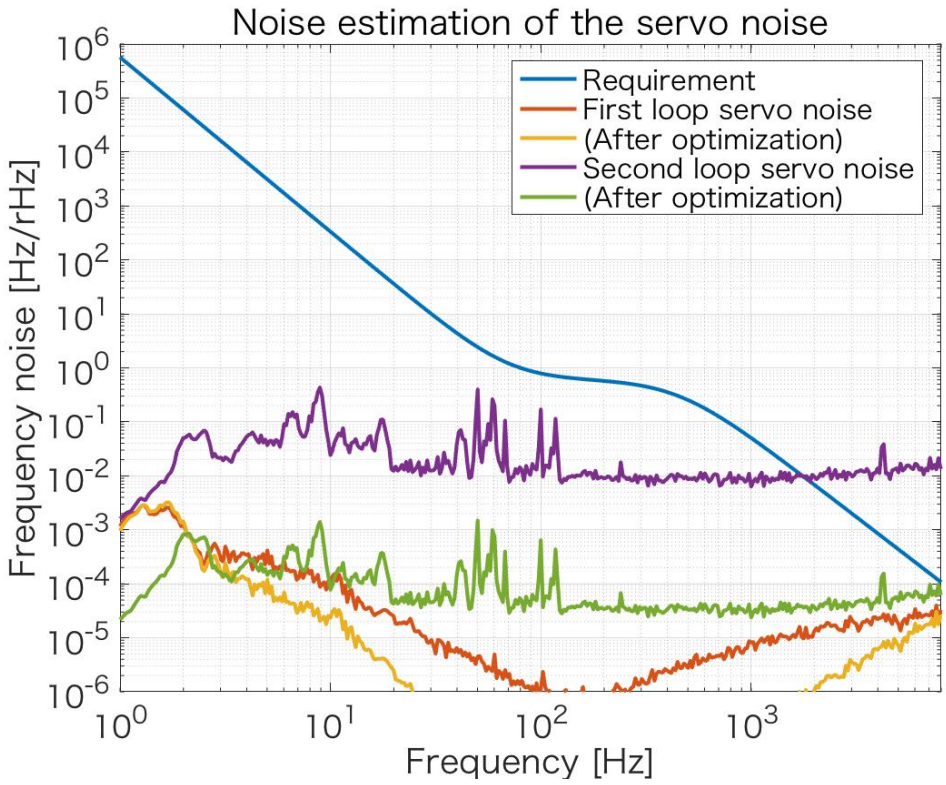

Figure 4.16: Contributions of the servo noise to the frequency noise in the outgoing light from the IMC. Orange and yellow curves are the contributions of the first loop servo noise with the current configuration and with the simulated optimal configuration, respectively. The servo noise of the first loop is suppressed by the boost filter added to the second loop. Magenta and green curves are the contributions of the second loop servo noise with the current optical gain and with the simulated higher optical gain, respectively. By increasing the optical gain of the IMC, all of the noises meet the requirement.

4.5.5 Shot noise

From Eq. (A.118), the shot noise can be estimated. The RC and the IMC are cavities designed as $R_f = R_e$, where R_f and R_e are the reflectance of input and output mirrors. Therefore, the reflectance of the cavity can be derived as 0, as shown in Eq. (A.63). If we assume the quantum efficiency of the PD as a typical value of 0.8, the shot noise can be obtained as

$$\delta\nu_{\mathrm{shot}} = 1.2 \times 10^{-4} \frac{10^4}{\mathcal{F}} \frac{10\ \mathrm{cm}}{L} \sqrt{\frac{1064\ \mathrm{nm}}{\lambda}} \sqrt{\frac{2\ \mathrm{mW}}{P_c}}\ \mathrm{Hz}/\sqrt{\mathrm{Hz}}, \tag{4.48}$$

where $\mathcal{F}$ is the finesse of the cavity, L is the cavity length, and P_c is the carrier power on the PD. Figure 4.17 shows the shot noise contributions. Originally, they almost fulfill the requirement, and they satisfy the requirement with further margin by increasing the carrier power on the PD.

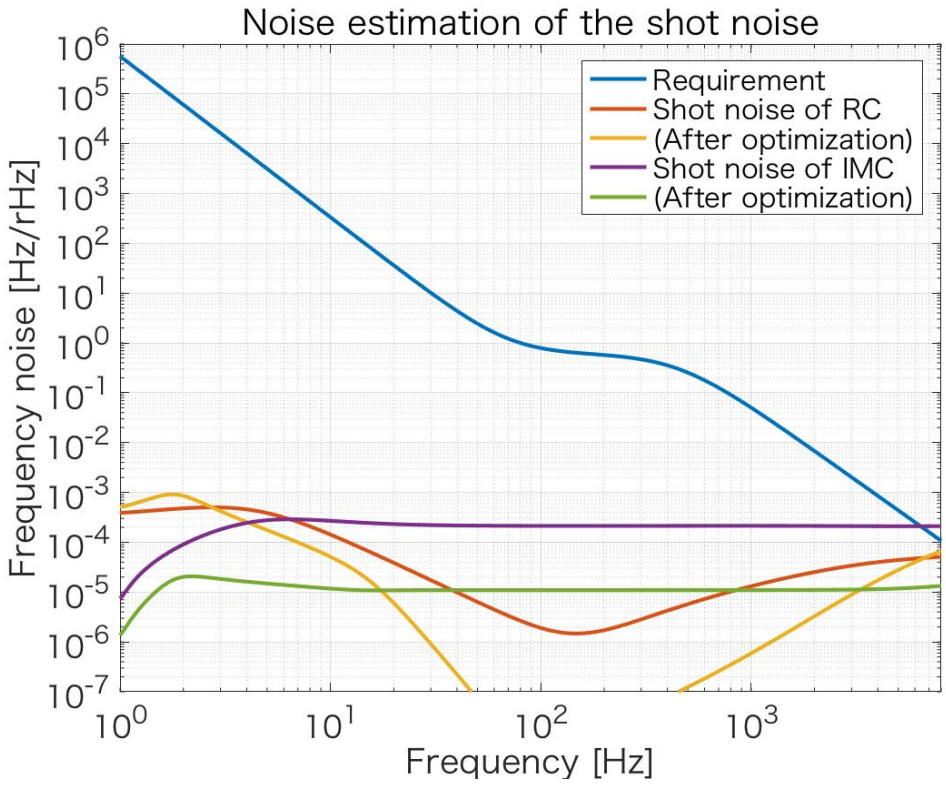

Figure 4.17: Contributions of the shot noise on the IMC and the RC control signals to the frequency noise in the outgoing light from the IMC. Orange and yellow curves are the contributions of the first loop shot noise with the current servo filter and with the simulated servo filter, respectively. The shot noise of the first loop is suppressed by the boost filter added to the second loop. Magenta and green curves are the contributions of the second loop servo noise with the current laser power and with the increased laser power, respectively. Due to increasing the laser power, all of the noises meet the requirement. At the frequencies around 2 Hz, the noises increase because of the new boost filter in the AOM loop as mentioned in Section 4.4.

4.5.6 Dark noise of the second loop RF PD

A dark noise of an RF PD to obtain the error signal of the second loop was measured. The dark noise was measured at the output of a demodulator, in other words, the error point of the second loop. The noise was measured with and without laser injection. The noise level with the laser was the same as that without the laser. Therefore, this noise is supposed to be the electric noise of the PD. Figure 4.18 shows the contributions of the IMC PD dark noise. The PD dark noise is also suppressed by increasing the optical gain of the IMC. This is because the cavity with the higher optical gain generates the larger signal, and the signal to noise ratio is improved as a result.

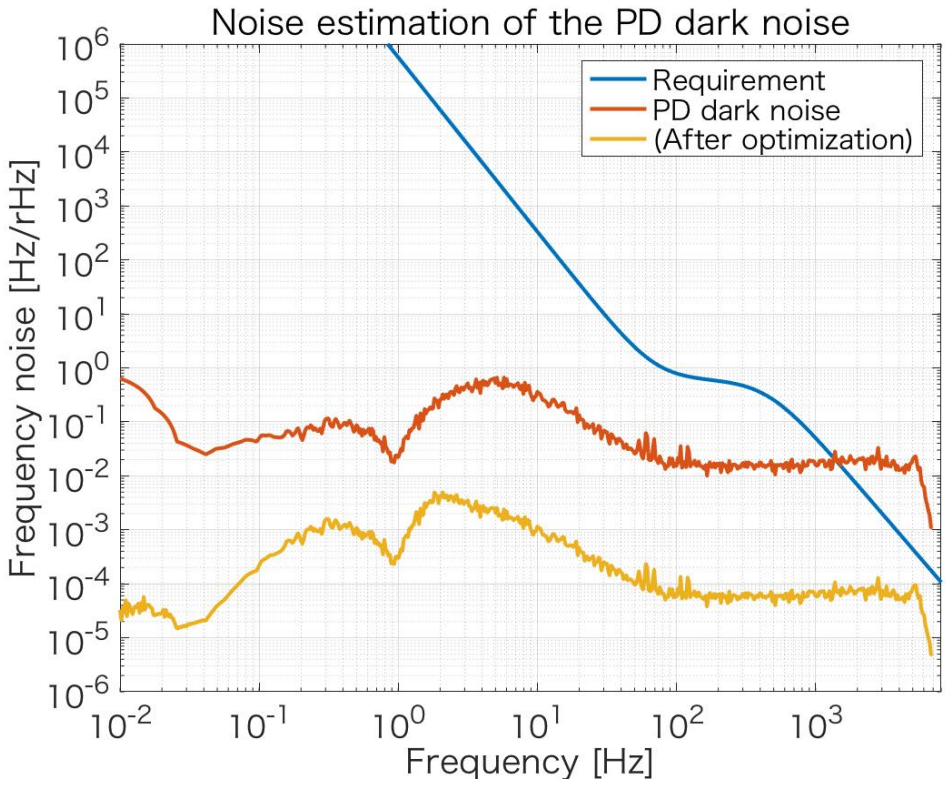

Figure 4.18: Contributions of the RF PD dark noise of the second loop to the frequency noise in the outgoing light from the IMC. The orange curve is the contribution with the current optical gain, and the yellow curve is that with the higher optical gain. By increasing the optical gain and improving the signal to noise ratio, the noise is suppressed and meets the requirement.

4.5.7 Residual amplitude modulation noise

An RAM noise, as shown in Appendix A.5.2, is one of the noises which are inherent in the PDH method. As mentioned above, the RF PD dark noise level of the second loop does not show any difference between with and without the laser injection. This means that the RAM noise of the second loop has not been measured so far, since the injected power on the second loop PD is too small to detect the RAM noise. Therefore, the RAM index $\tilde{\epsilon}_m(\omega)$ in Eq. (A.124) is assumed to be 10^{-5} by referring to the RAM obtained in a similar experiment [55, 56]. Then, from Eq. (A.124), the contribution of the RAM noise can be derived as $\delta\nu(f) = 2 \times 10^{-4}$ Hz/$\sqrt{\text{Hz}}$ with the designed phase modulation index $\delta_m = 0.01$ in the first loop of the FSS. It almost meets the requirement.

The first loop has a large RAM noise compared with the second loop between 10 Hz to 1 kHz. The RAM noise was measured by demodulating the signal from the RF PD on which the injection light to the RC was directly incident. The modulation index of the RAM was measured as $\epsilon_m \sim 10^{-3}$ at 100 Hz. Figure 4.19 shows the contribution of the measured RAM noise to the frequency noise calculated from Eq. (A.124) with the

designed modulation index $\delta_m = 0.2$. After the optimization, it satisfies the requirement in the frequency band below 2 kHz, where gravitational wave (GW) signals are expected from compact objects.

To reduce the RAM noise above 2 kHz, we have to align the polarization direction and the crystal axis of the EOM to generate the sideband for the PDH method. If they are misaligned, the EOM modulates not only the phase but also the amplitude of the laser. Moreover, the linearity of the polarization of the laser light is also important. An elliptically polarized light is represented by a linear combination of linearly polarized lights in two directions having different phases. Therefore, the EOM modulates the amplitude of the elliptically polarized light. The polarization ratio of the laser was measured as about 1/50. The thin film polarizer used in LIGO can isolate linearly polarized lights in two directions with the polarization ratio of 1/100. By using such a polarizer and aligning more precisely, the RAM noise can be reduced. Furthermore, the pre-mode cleaner (PMC) works as a passive filter of the RAM. The cavity pole of the PMC is 600 kHz, and the modulation frequency for the PDH method in the first loop is 51 MHz. As shown in Appendix A.2.3, the RAM is expected to be reduced by a factor of (51 MHz)/(600 kHz) = 85. Therefore, after the installation of the PMC, the RAM noise introduced before the PMC is expected to be suppressed. By reduction of the RAM by the PMC and the fine alignment of the polarization, the RAM noise is expected to meet the requirement even above 2 kHz.

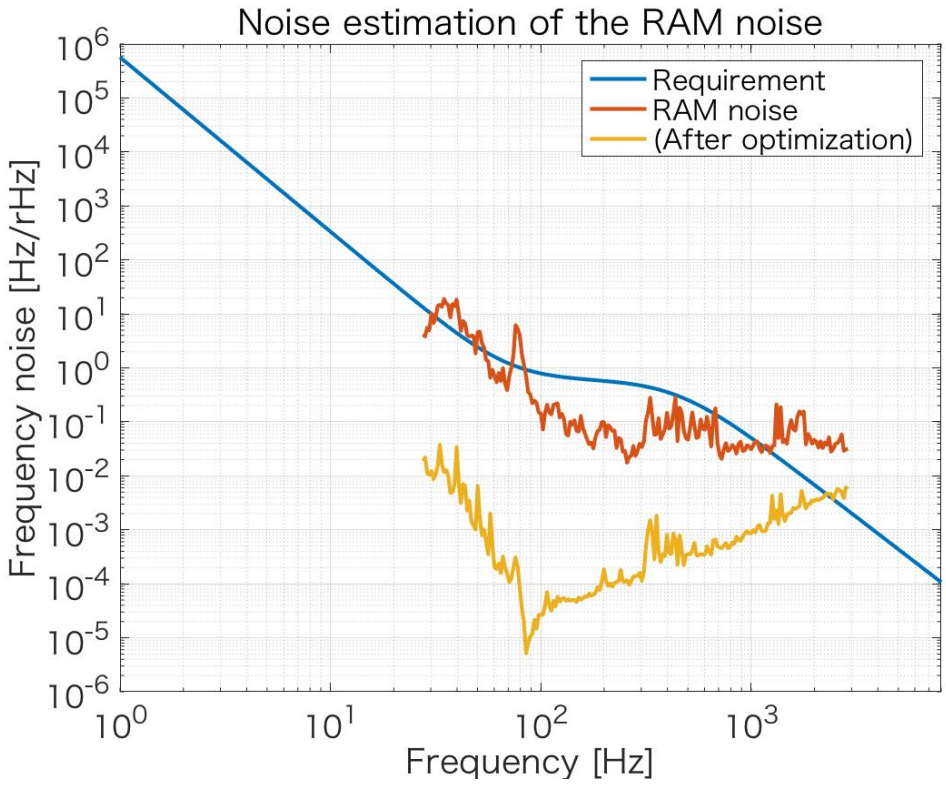

Figure 4.19: Contribution of the RAM noise of the first loop to the frequency noise of the outgoing light from the IMC. The orange curve is the contribution with the current configuration, and the yellow curve is that with the simulated configuration. Even after increasing the OLG of the second loop, the noise does not meet the requirement above 2 kHz.

4.5.8 VCO phase noise

The VCO has the phase noise which causes the frequency noise of the laser. To estimate the VCO noise, the IMC was used as an out-of-loop sensor to measure the frequency noise. At first, the first loop was locked, and the IMC was locked only with the IMC suspension. Then, we measured and calibrated the feedback signal to the suspension. The AOM driver was turned on, and a DC signal was injected into an input port of the VCO during one measurement and turned off during the other measurement. Figure 4.20 shows the calibrated feedback signal to the AOM. When the VCO was turned on, the frequency noise increased above 3 kHz. This means that the frequency noise above 3 kHz is due to the phase noise of the VCO. From this measurement, the VCO noise was determined as

$$\delta\nu_{\mathrm{VCO}} = 0.3\,\mathrm{Hz}/\sqrt{\mathrm{Hz}} \tag{4.49}$$

From the experience, the noise was assumed to be flat for all frequencies.

The contribution of the VCO noise is shown in Fig. 4.21. After the optimization, the VCO noise satisfies the requirement in the frequency band below 2 kHz

To reduce the VCO phase noise, one possibility is to use the lower phase noise VCO. Actually, the VCO used in aLIGO has the better phase noise by a factor of 20 than the VCO of KAGRA. Even with such a high performance VCO, the phase noise does not satisfy the requirements above 4 kHz. Another possibility is to add a broadband EOM to the second loop as a fast actuator. If the crossover frequency between the AOM loop and the EOM loop is assumed as 20 kHz, the OLG of the second loop at 8 kHz will be increased by more than 20 dB. Therefore, it is possible to satisfy the requirements by the improvement of the VCO and adding the EOM as the fast actuator.

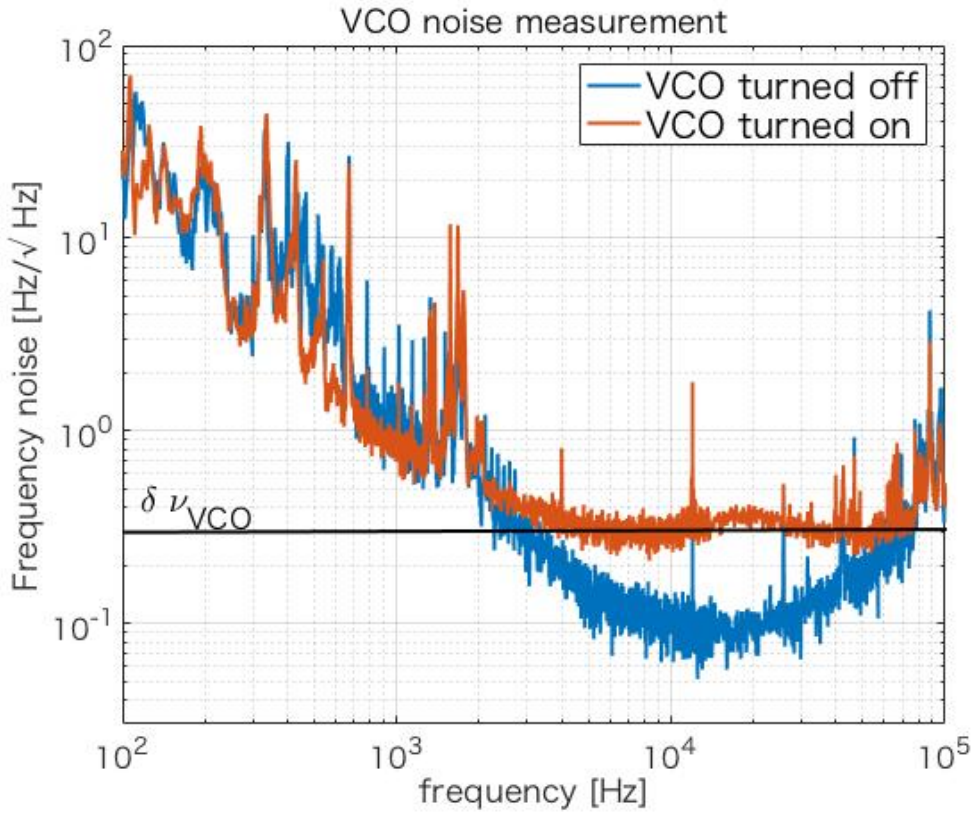

Figure 4.20: Calibrated feedback signals for the VCO noise measurement into the frequency noise. The VCO phase noise appears above 3 kHz.

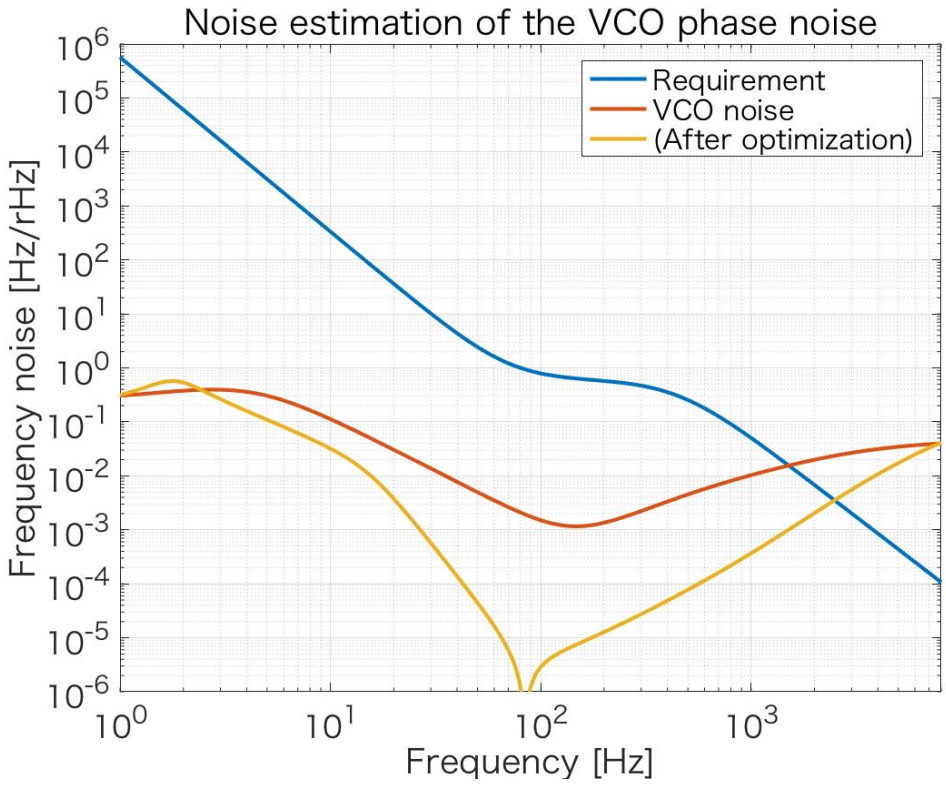

Figure 4.21: Contributions of the VCO phase noise to the frequency noise in outgoing light from the IMC. The red curve is the contribution with current configuration and the yellow curve is with the optimized configuration. At the frequencies around 2 Hz, the noises get worse because of the new boost filter in the AOM loop as mentioned in Section 4.4.

4.5.9 Confirmation of the noise budget

Figure 4.22 is the noise budget curve of the feedback signal to the AOM. This is equivalent to the out-of-loop measurement of the first loop, since the IMC can be regarded as the frequency sensor of the outgoing light from the pre-stabilized laser (PSL) table. The RAM noise and the VCO noise limit the first loop. The feedback signal can be explained by the noises which have been discussed so far in almost all bands. If we had other unknown noises in the first loop, the feedback signal would be larger than our expectation. Therefore, we conclude that the correct estimation of the noise is performed in the first loop.

The actual performance of the second loop cannot be measured at this point. After locking the arm cavity of the main interferometer, the out-of-loop measurement of the second loop can be done. Then, the actual frequency stability will be measured.

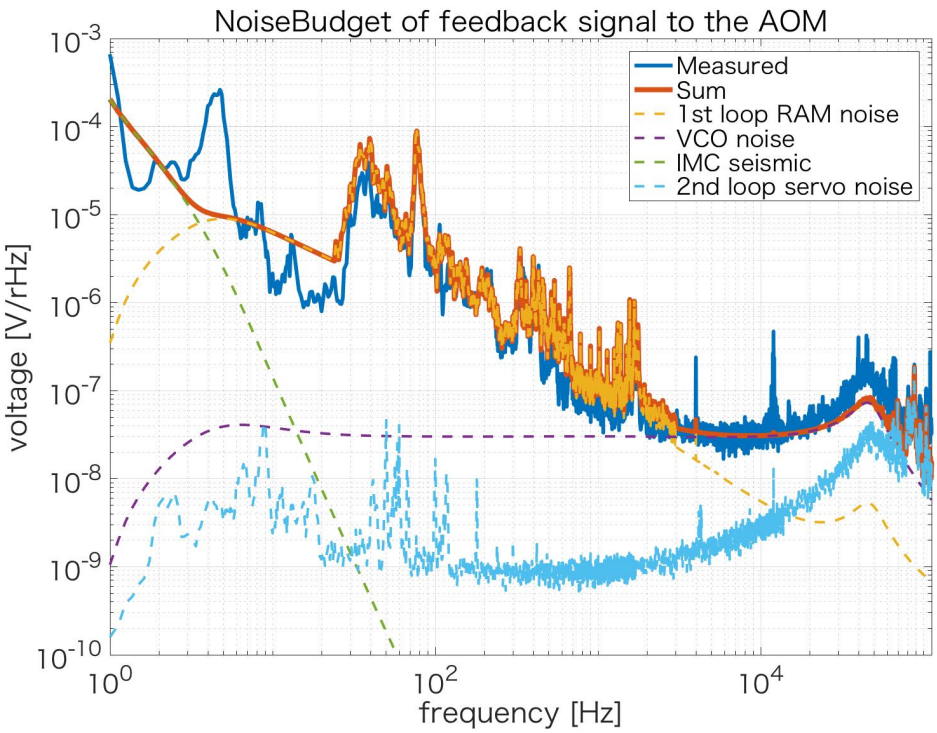

Figure 4.22: Noise budget of the feedback signal. The blue line is the measured signal and the orange line is the sum of the estimated noises. The other noises such as the NPRO laser noise, the resonance frequency fluctuation noise of the RC, the first loop servo noise, the shot noise, and the PD dark noise on the second loop are omitted in this plot, because these noises are lower than the other noises at all of the frequencies.

4.5.10 Summary of the noise budget

As we have seen, by the optimization of the control configuration, it is possible to suppress all the noises to satisfy the requirements at the frequency band below 2 kHz which is the frequency band of the target gravitational wave signals such as the coalescence of the binary compact objects . Figure 4.23 shows the noises currently limiting the frequency stability. In the frequency band lower than 100 Hz, the stability is limited by the resonance frequency fluctuation of the IMC. That means the stability of the laser frequency is determined by the stability of the resonance frequency of the IMC.

There are two noises which do not meet the requirement in the band higher than 2 kHz. Our data acquisition system can acquire the signal with the frequency of up to 8 kHz. Therefore, it is preferable to stabilize it so that the frequency noise do not deteriorate the sensitivity up to 8 kHz. As for the RAM noise, one of the reasons why RAM noise can be caused is that the crystal axis of the EOM for the PDH method and the polarization direction of the light are not correctly aligned. Therefore, after the alignment of the polarization direction, the RAM noise is expected to be improved. Also, the PMC will filter the RAM noise above its cavity pole frequency, and the expected suppression ratio

of the RAM is 1/85. After installation of the PMC and fine alignment between the polarization and the EOM crystal axis, this noise is expected to meet the requirement.

Another one is the noise due to the VCO. Currently, the VCO used in bKAGRA is not a VCO with the low noise. Therefore, the lower noise VCO can help to suppress the noise contribution. For instance, in aLIGO, a VCO with a phase noise lower by about ten times than our VCO has been developed and used. Another way to suppress the VCO phase noise is to add a new fast actuator to the second loop like a broadband EOM. If that actuator can control the laser frequency up to 160 kHz, the frequency stabilization can gain the factor of about 20 at the frequency of 8 kHz. Since the broadband EOM can control at the frequencies up to 500 kHz in the first loop, this control loop is feasible enough. Then, it is possible that the VCO phase noise is reduced and satisfy the requirement.

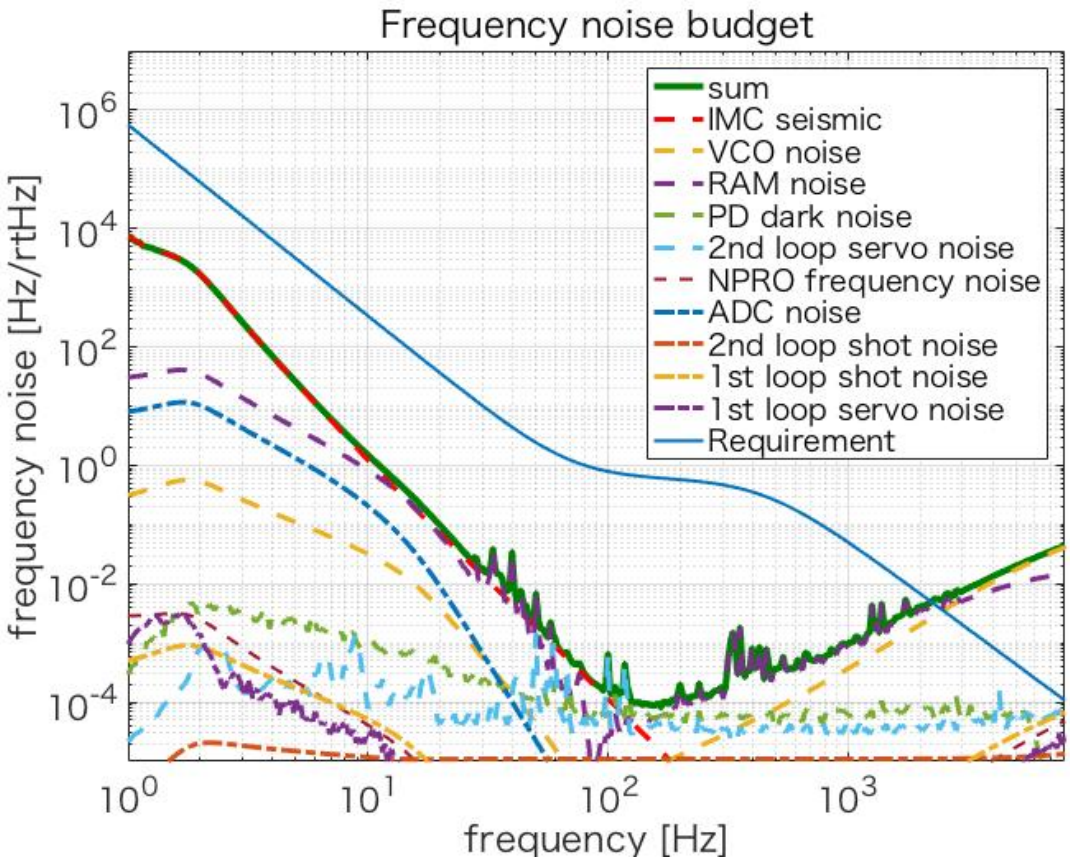

Figure 4.23: Noise budget of the frequency noise. The IMC seismic noise and the RAM noise are dominant at the frequencies below 100 Hz. In contrast, above 100 Hz, the RAM noise and the VCO noise are dominant, and they meet requirement below 2kHz, where GW signals are expected from compact objects. The seismic noise of the RC and the residual gas noise of the RC are not included in this plot because those noises are much lower than other noises.

5 Conclusion

5.1 Summary

A gravitational wave (GW) detector called KAGRA is under construction in Japan. KAGRA is the first underground cryogenic GW detector in the world. KAGRA has two arms with the length of 3 km, and KAGRA has a design sensitivity that can detect GW signals radiated by a coalescence of the pair of 1.4 solar mass neutron stars 140 Mpc away from the earth. Since the first detection of the GW signal by Advanced LIGO (aLIGO) in the U.S., several GW signals have been detected by aLIGO and advanced VIRGO (AdV) in Italy.

In such a situation, the mission imposed on KAGRA is to achieve a sensitivity good enough to observe a GW signal and to join the GW detector network in the world as soon as possible. The design sensitivity of KAGRA is similar to those of the other detectors at frequencies above 10 Hz, and KAGRA has better sensitivity at the frequencies below 10 Hz. KAGRA has the potential to detect signals that cannot be observed by the other detectors. For the GW astronomy, the position determination of the GW source is important. To determine the direction of the GW source, three or more detectors are necessary. When KAGRA joins the GW detector network, the probability that three or more machines are in operation improves to 80% from 50 %. Furthermore, the accuracy of position determination when four detectors are in operation is predicted to be improved up to 9.5 deg^2 as a result of a simulation. Therefore, a participation of KAGRA in the GW detector network is an urgent matter in the development of the GW astronomy.

For this purpose, each subsystem in the KAGRA project has to reduce noises so that these noises do not deteriorate the performance of the GW detector. The input optics is one of these subsystems, and the role of the input optics is to provide the stabilized laser light to the main interferometer. The author is responsible for the design, the installation, the investigation, and the integration of a pre-stabilized laser (PSL) and an input mode-cleaner (IMC). The PSL is the in-air optics for the beam stabilization, and the IMC is the 50-m round trip length cavity with three suspended mirrors. The PSL and the IMC are the main part of the input optics, and almost all stabilization is done with the PSL and the IMC. Development of the input optics for bKAGRA began in April 2016 when the test operation of iKAGRA was completed, and almost all optical elements of the PSL and the IMC have been installed. Regarding the frequency stabilization system (FSS), the installation has been done, and performance evaluation is completed.

Control of the FSS is robust, and it has been demonstrated that it can continue to be locked for a week without any adjustment. Furthermore, even if they lost lock, it takes less than one minute to be re-locked, and therefore the requirement for the duty cycle of 95% can be said to be satisfied.

Regarding the frequency stability, the requirement was decided so that the contribution of the frequency noise to the GW sensitivity gets smaller than the contribution of other fundamental noise such as the quantum noise and the thermal noise. We evaluated the performance and confirmed whether the frequency noise meets the requirement. Although some are not satisfied at present, almost all the noises meet the requirement when the control configuration is optimized in the frequency band of the target GW signals.

A noise due to a residual amplitude modulation (RAM) and a noise due to the phase noise of the voltage-controlled oscillator (VCO) do not satisfy the requirement at frequencies above 2 kHz, and it is preferable for those noises to satisfy in all frequency band where the data can be acquired. As for the RAM, the fine alignment of the polarization of the light and the crystal axis of the electro-optic modulator (EOM), and the PMC installation are expected to reduce the RAM, and it is possible for the RAM noise to satisfy the requirement. As for the VCO phase noise, if we use an existing high performance one, we can expect a performance improvement roughly by a factor of ten. And a new faster actuator like a broadband EOM will help to increase the open loop gain (OLG) up to 10 kHz. If these measures are taken, the requirement is expected to be satisfied.

The KAGRA FSS is a similar system to those of aLIGO and AdV. The reference cavity (RC) and the IMC are also used as frequency references in aLIGO and AdV. What is noteworthy in KAGRA′s FSS is the simplicity of the vibration isolation system. The KAGRA's IMC has a vibration isolation system that suspends a mirror with a two-stage pendulum and places it on a vibration-isolated breadboard with three-layer stacks, and the RC has no vibration isolation system. Moreover, we don′t have any active local control for seismic isolation in the FSS. On the other hand, the RC has an active seismic isolation system in aLIGO. Besides, the mirror of the IMC is suspended with the complex system described in Section 1.4. We confirm that KAGRA does not need such an elaborate vibration-isolation system thanks to a quiet seismic motion. KAGRA's FSS achieves the frequency stability required for the GW detection with the simplest configuration in the world.

5.2 Future work

As mentioned several times in this thesis, the most recent task is to participate in the third observation run, the O3, which is planned in 2019.

By the O3, the input optics is required to increase the laser power to 40 W, to install the PMC and intensity stabilization system, and to provide the light to the main interferometer stably. On the current schedule, the commissioning of the main interferometer toward the O3 is scheduled from September 2018. Therefore, by August 2018 it is required to finish these upgrades. The PMC has already been assembled, and it is now being installed. As for the intensity stabilization, a prototype experiment and the

hardware installation have already been completed by the author and the collaborators from Toyama Univ. We will develop the control design and evaluate its performance.

As for the FSS, the performance evaluation with current configuration has been completed, and there are some noises which do not achieve the required value. Therefore, it is necessary to optimize the control configuration as discussed in this thesis. After optimization and installation of the PMC and the high power laser, the frequency stability have to be investigated again, and be confirmed to satisfy the requirement. One concern about the high power laser installation is that some new noises might limit the frequency stability. For example, the fluctuation of the cavity length of the IMC due to the classical radiation pressure could be a problem. If the laser power fluctuates, the radiation pressure of the laser will also fluctuate and shake the IMC mirrors. Since the radiation pressure is proportional to the power of the laser, even if it is not a problem at the current laser power, there is a possibility that it becomes a problem, when the laser power is increased. Reduction of the intensity noise is indispensable to reduce this noise. The intensity stabilization system is being installed and it is expected to reduce this noise to satisfy the requirement.

Although only the IMC length is controlled so far, the alignment control of the IMC is also required. The signal for the alignment control is acquired by a method called wave front sensing. In this method, an alignment control signal is obtained by the beat signal between TEM_{00} component of the phase modulation sideband and TEM_{10} mode of the carrier light. The preparation of hardware devices such as a photodetector (PD) for signal acquisition and circuits for demodulation is completed. By the time when the O3 starts, we need to install them and stabilize the control loop.

With respect to the beam jitter noise, it is also necessary to check whether this noise will limit the sensitivity or not. We will evaluate the current jitter noise using the IMC, and reduce it if it is necessary.

A Fabry-Perot Cavity

A Fabry-Perot cavity is an optical element composed of two or more mirrors. Light incident on the Fabry-Perot cavity circulates many times inside the cavity to cause multiple interferences. When internal light and newly incident light are aligned in phase, the light power accumulates inside the cavity. This state is called resonance of the cavity, and keeping the cavity on the resonance is called locking the cavity. A cavity resonates when a round-trip phase rotation is an integral multiple of 2π, i.e., the newly incident light is in phase with the circulating light, and this is called a resonance condition.

The Fabry-Perot cavity has frequency selectivity. By using this characteristic, it is possible to stabilize the frequency by controlling the frequency of the laser as locking it to the cavity resonance frequency. Also, due to the relatively long storage time of light in the cavity, the cavity has the property of a passive filter, reducing a frequency noise and an intensity noise in the high-frequency band. Furthermore, it has selectivity to the spatial mode of the incident light, and the light can be mode-cleaned by passing through the cavity.

In most of the GW detectors in the world, we use several Fabry-Perot cavities to stabilize the laser light and to increase the sensitivity of the detector. In this chapter, we show the properties of a Fabry-Perot cavity.

A.1 Expression of the light

A.1.1 Parameters for the light expressions

To understand the principle of a Fabry-Perot cavity, first, consider how to express light in equations. Here, to simplify, light is treated as an ideal plane wave with linear polarization. Consider light propagating in the positive direction of the x axis. This light can be expressed by the strength of the electric field. The strength of this electric field $E(t-x/c)$ is a sinusoidal function with respect to $\zeta = t - x/c$. $E(\zeta)$ can be expressed as follows:

$$E(\zeta) = \mathcal{E}_0 \cos(\Omega_0 \zeta - \phi_0), \tag{A.1}$$

$$= \mathcal{E}_c \cos \Omega_0 \zeta + \mathcal{E}_s \sin \Omega_0 \zeta, \tag{A.2}$$

$$= \frac{\mathcal{E} e^{i\Omega_0 \zeta} + \mathcal{E}^* e^{-i\Omega_0 \zeta}}{\sqrt{2}}, \tag{A.3}$$

where Ω_0 is the angular frequency of the light. In this chapter we refer to angular frequencies when the term frequency is used. These three equations all represent the electric field of the light with either two complex or two real parameters. Equation (A.1) is a simple representation of a wave and $\mathcal{E}_0$ and ϕ_0 are called an amplitude and a phase, respectively.

Equation (A.2) is a representation using real parameters $\mathcal{E}_c$ and $\mathcal{E}_s$, called quadrature amplitudes and Eq. (A.3) uses a complex amplitude, $\mathcal{E}$. The relationship between the parameters can be written as

$$\begin{aligned}
&\mathcal{E}_0 = \sqrt{\mathcal{E}_c^2 + \mathcal{E}_s^2} = \sqrt{2}|\mathcal{E}|, && \tan\phi_0 = \mathcal{E}_s/\mathcal{E}_c = \arg\mathcal{E}, \\
&\mathcal{E}_c = \frac{\mathcal{E} + \mathcal{E}^*}{\sqrt{2}} = \sqrt{2}\mathrm{Re}[\mathcal{E}] = \mathcal{E}_0\cos\phi_0, && \mathcal{E}_s = \frac{\mathcal{E} - \mathcal{E}^*}{i\sqrt{2}} = \sqrt{2}\mathrm{Im}[\mathcal{E}] = \mathcal{E}_0\sin\phi_0, \\
&\mathcal{E} = \frac{\mathcal{E}_c + i\mathcal{E}_s}{\sqrt{2}} = \frac{\mathcal{E}_0}{\sqrt{2}}e^{i\phi_0}.
\end{aligned} \tag{A.4}$$

Figure A.1 shows these parameters on a complex plane. In this way, the electric field of the light is expressed using a vector on the complex plane, which is called a phasor diagram.

The electromagnetic wave as a plane wave is a function depending only on the argument ζ. Therefore, even if only the point of $x = 0$ is considered and let $E(\zeta) \equiv E(t)$, generality is not lost.

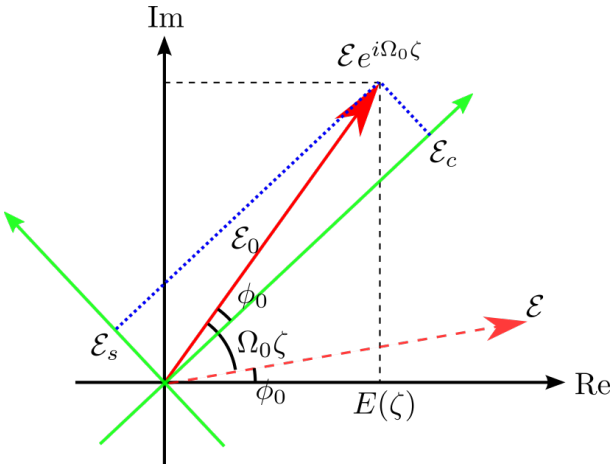

Figure A.1: Parameters in a phasor diagram. The red solid vector represents the light rotating at the frequency Ω_0 and the red dashed vector represents the initial state of the light. The coordinate system represented by the green arrows consisting of quadrature amplitudes turns with the light. From this, it can be considered that the quadrature amplitude is the magnitude of each component in the coordinate system in which the vector representing the light stands still.

A.1.2 Propagation of the light

Then, we consider how each parameter changes due to light propagation. Let the electric fields of the light at two spatially separated points $x_1 = 0$ and $x_2 = L$ be $E^{(0)}(t)$ and $E^{(L)}(t)$, then obviously $E^{(L)}(t) = E^{(0)}(t - L/c)$. Therefore, the complex amplitude $\mathcal{E}$ can be easily denoted as

$$\mathcal{E}^{(L)} = e^{-i\Omega_0 L/c}\mathcal{E}^{(0)}. \tag{A.5}$$

Also, the quadrature amplitude $\boldsymbol{\mathcal{E}} = (\mathcal{E}_c, \mathcal{E}_s)^T$ can be written as ,

$$\boldsymbol{\mathcal{E}}^{(L)} = \begin{pmatrix} \cos\phi_L & \sin\phi_L \\ -\sin\phi_L & \cos\phi_L \end{pmatrix} \begin{pmatrix} \mathcal{E}_c^{(0)} \\ \mathcal{E}_s^{(0)} \end{pmatrix} = \mathbb{R}(-\phi_L)\boldsymbol{\mathcal{E}}^{(0)}, \tag{A.6}$$

where $\phi_L = \Omega_0 L/c$, and $\mathbb{R}(\theta)$ is a rotation matrix in the quadratic plane. Furthermore, consider the case where the propagation distance L is sufficiently shorter than the wavelength λ. In this case, the change in the quadrature amplitude and the complex amplitude can be written as

$$E^{(L)} = (1 - i\phi_L)E^{(0)}, \tag{A.7}$$

$$\begin{aligned} \boldsymbol{\mathcal{E}}^{(L)} &= \begin{pmatrix} 1 & \phi_L \\ -\phi_L & 1 \end{pmatrix} \boldsymbol{\mathcal{E}}^{(0)} \\ &= (I + \delta\mathbb{R}(-\phi_L))\boldsymbol{\mathcal{E}}^{(0)}, \end{aligned} \tag{A.8}$$

where $\delta\mathbb{R}(-\phi_L)$ is a matrix showing how much the quadrature amplitude has changed during propagation from the start point to the end point .

Consider the case where the light whose frequency changes by $\delta\Omega(t)$ around Ω_0 propagates the distance L. The electric fields can be written as

$$E^{(0)}(t) = \frac{\mathcal{E}e^{i(\Omega_0+\delta\Omega(t))t} + \mathcal{E}^* e^{-i(\Omega_0+\delta\Omega(t))t}}{\sqrt{2}}, \tag{A.9}$$

$$E^{(L)}(t) = \frac{\mathcal{E}e^{i(\Omega_0+\delta\Omega(t-L/c))(t-L/c)} + \mathcal{E}^* e^{-i(\Omega_0+\delta\Omega(t-(L/c)))(t-L/c)}}{\sqrt{2}}. \tag{A.10}$$

Here, assuming that the frequency change $\delta\Omega(t)$ is sufficiently slow with respect to the propagation time L/c. Then, $\delta\Omega(t - L/c) \simeq \delta\Omega(t)$, and from Eq. (A.10), $\mathcal{E}^{(L)}(t)$ can be derived as

$$\begin{aligned} \mathcal{E}^{(L)}(t) &= \exp(-i(\Omega_0 + \delta\Omega(t))\frac{L}{c})\mathcal{E}^{(0)}(t) \\ &= \exp\left(-i\Omega_0(1 + \frac{\delta\Omega(t)}{\Omega_0})\frac{L}{c}\right)\mathcal{E}^{(0)}(t). \end{aligned} \tag{A.11}$$

Therefore, the frequency change can be regarded as the propagation of the additional distance of $(\delta\Omega(t)/\Omega_0)L$

A.1.3 Modulation

In this section, we consider how the parameters change when the light is modulated. Consider a light with frequency Ω_0, amplitude $\mathcal{E}_0$, initial phase $\phi_0 = 0$, and modulate this

light. This light before the modulation can be expressed as

$$E_{\mathrm{car}}(t) = \mathcal{E}_0 \cos \Omega_0 t = \mathrm{Re}[\mathcal{E}_0 e^{i\Omega_0 t}]. \tag{A.12}$$

Hereafter this light is called the carrier light. There are two modulations, amplitude modulation and phase modulation. Consider how each modulation is represented.

Amplitude modulation

Let the amplitude-modulated electric field be $E_{\mathrm{AM}}(t)$, which is modulated at a single frequency of ω. Then, the electric field can be written as

$$E_{AM}(t) = \mathcal{E}_0(1 + \epsilon_m \cos(\omega t + \phi_m)) \cos \Omega_0 t, \tag{A.13}$$

where $\Omega_0 \gg \omega$. ϵ_m is called the modulation depth and represents the modulation strength. Typically, $\epsilon_m \ll 1$. By transforming Eq. (A.13), we can write

$$E_{\mathrm{AM}}(t) = \mathrm{Re}[\mathcal{E}_0 e^{-i\Omega_0 t} + \frac{\mathcal{E}_0 \epsilon_m}{2} e^{-i\phi_m} e^{-i(\Omega_0+\omega)t} + \frac{\mathcal{E}_0 \epsilon_m}{2} e^{i\phi_m} e^{-i(\Omega_0-\omega)t}]. \tag{A.14}$$

From this equation, light modulated in intensity has a component that oscillates at the frequency Ω_0 and components oscillating at $\Omega_0 \pm \omega$ that are separated by the modulation frequency around the carrier frequency. These components standing on both sides of the carrier light are called sidebands. A representation of the state of this light by a phasor diagram is shown in Fig. A.2. Since the axes in Fig. A.2 represent quadrature components, the vector representing the carrier light does not rotate. In contrast, each sideband rotates at $\pm\omega$. Each sideband is called upper sideband or lower sideband.

When such a modulation is applied, the complex amplitude and the quadrature amplitude can be written as

$$\mathcal{E}_{\mathrm{AM}}(t) = \frac{\mathcal{E}_0}{\sqrt{2}}(1 + \epsilon_m \cos(\omega t + \phi_m)), \tag{A.15}$$

$$\mathcal{E}_{c,\mathrm{AM}}(t) = \mathcal{E}_0(1 + \epsilon_m \cos(\omega t + \phi_m)), \tag{A.16}$$

$$\mathcal{E}_{s,\mathrm{AM}} = 0. \tag{A.17}$$

When amplitude modulation is applied, the effect appears in the cosine part of the quadrature phase component.

By generalizing the above results, we can get the expression of an amplitude-modulated light by an arbitrary modulation function $A(t) = \int_{-\infty}^{\infty} \frac{d\omega}{2\pi} \tilde{A}(\omega) e^{-i\omega t}$, where $\tilde{A}(\omega)$ is the Fourier transform of $A(t)$. The electrical field of the amplitude-modulated light can be

written as

$$E_{\mathrm{AM}}(t) = \mathrm{Re}\left[\mathcal{E}_0(1+\epsilon_m(t))e^{-i\Omega_0 t}\right]. \tag{A.18}$$

Here, the quadrature amplitude is derived as

$$\mathcal{E}_{c,\mathrm{AM}}(t) = \mathcal{E}_0(1+\epsilon_m \int_{-\infty}^{\infty} \frac{d\omega}{2\pi}\tilde{A}(\omega)e^{-i\omega t}). \tag{A.19}$$

Therefore, the Fourier transform of the quadrature amplitude $\tilde{\mathcal{E}}_{c,\mathrm{AM}}(\omega)$ can be written as

$$\tilde{\mathcal{E}}_{c,\mathrm{AM}}(\omega) = \epsilon_m \mathcal{E}_0 \tilde{A}(\omega), \tag{A.20}$$

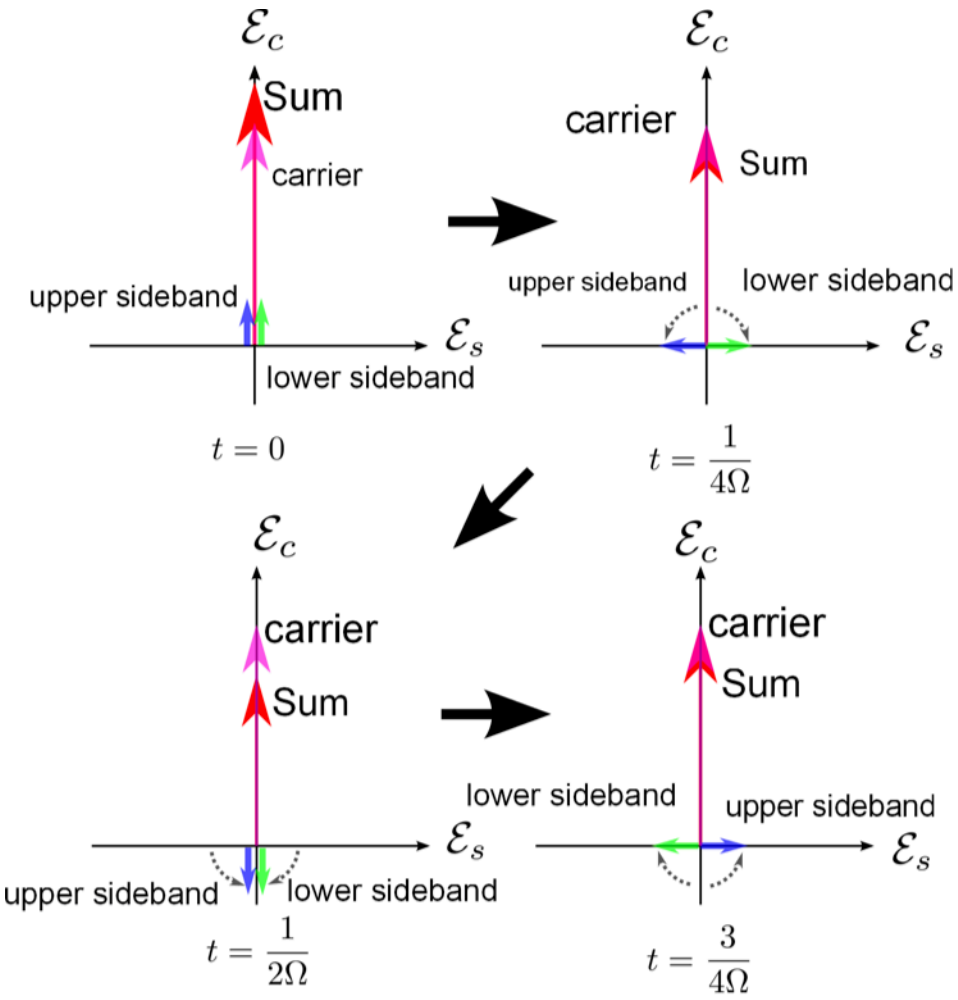

Figure A.2: Schematic view showing the amplitude modulation by a phasor diagram. By the rotation of the sideband, the amplitude modulation is represented.

Phase modulation

Next, phase modulation is considered in the same way. Considering phase modulation at a single frequency ω, an electric field E_{PM} can be written as

$$\begin{aligned} E_{\mathrm{PM}}(t) &= \mathcal{E}_0 \cos(\Omega_0 t + \delta_m \cos(\omega t + \phi_m)) \\ &= \mathrm{Re}[\mathcal{E}_0 e^{i\Omega_0 t} e^{-i\delta_m \cos(\omega t + \phi_m)}], \end{aligned} \tag{A.21}$$

where $\delta_m \ll 1$. Here, $e^{i\delta_m \cos(\omega t + \phi_m)}$ can be expanded with Bessel functions of the k-th-order $J_k(\delta_m)$ as

$$e^{i\delta_m \cos(\omega t + \phi_m)} = \sum_{k=-\infty}^{\infty} i^k J_k(\delta_m) e^{ik(\omega t + \phi_m)}. \tag{A.22}$$

Here

$$J_0(\delta_m) = 1 - \frac{\delta_m^2}{4} + \mathcal{O}(\delta_m^4), \tag{A.23}$$

$$J_1(\delta_m) = \frac{\delta_m}{2} + \mathcal{O}(\delta_m^3), \tag{A.24}$$

$$\text{and} \qquad J_k(\delta_m) = \frac{1}{k!}\left(\frac{\delta_m}{2}\right)^k + \mathcal{O}(\delta_m^k + 2). \tag{A.25}$$

Then Eq. (A.21) can be approximated to the first-order term of δ_m as

$$E_{\mathrm{PM}}(t) \simeq \mathrm{Re}[\mathcal{E}_0 e^{i\Omega_0 t} + i\frac{\delta_m \mathcal{E}_0}{2} e^{i\phi_m} e^{i(\Omega_0 + \omega)t} + i\frac{\delta_m \mathcal{E}_0}{2} e^{-i\phi_m} e^{i(\Omega_0 - \omega)t}]. \tag{A.26}$$

As in the amplitude modulation, it can be seen that the sidebands are established around the carrier frequency Ω_0 even when phase modulation is applied. Figure A.3 shows these phasor diagrams.

The complex amplitude and quadrature amplitude when phase modulation is applied can be written as

$$\mathcal{E}_{\mathrm{PM}}(t) = \frac{\mathcal{E}_0}{\sqrt{2}} e^{i\delta_m \cos(\omega t + \phi_m)}, \tag{A.27}$$

$$\mathcal{E}_{c,\mathrm{PM}}(t) = \mathcal{E}_0 \cos[\delta_m \cos(\omega t + \phi_m)] \simeq \mathcal{E}_0, \tag{A.28}$$

$$\mathcal{E}_{s,\mathrm{PM}}(t) = \mathcal{E}_0 \sin[\delta_m \cos(\omega t + \phi_m)] \simeq \delta_m \mathcal{E}_0 \cos(\omega t + \phi_m). \tag{A.29}$$

It can be seen that the phase modulation appears in the sine component, whereas the amplitude modulation appears in the cosine component of the quadrature amplitude as in Eq. (A.16). From this, the two quadrature components are called amplitude and phase components, respectively.

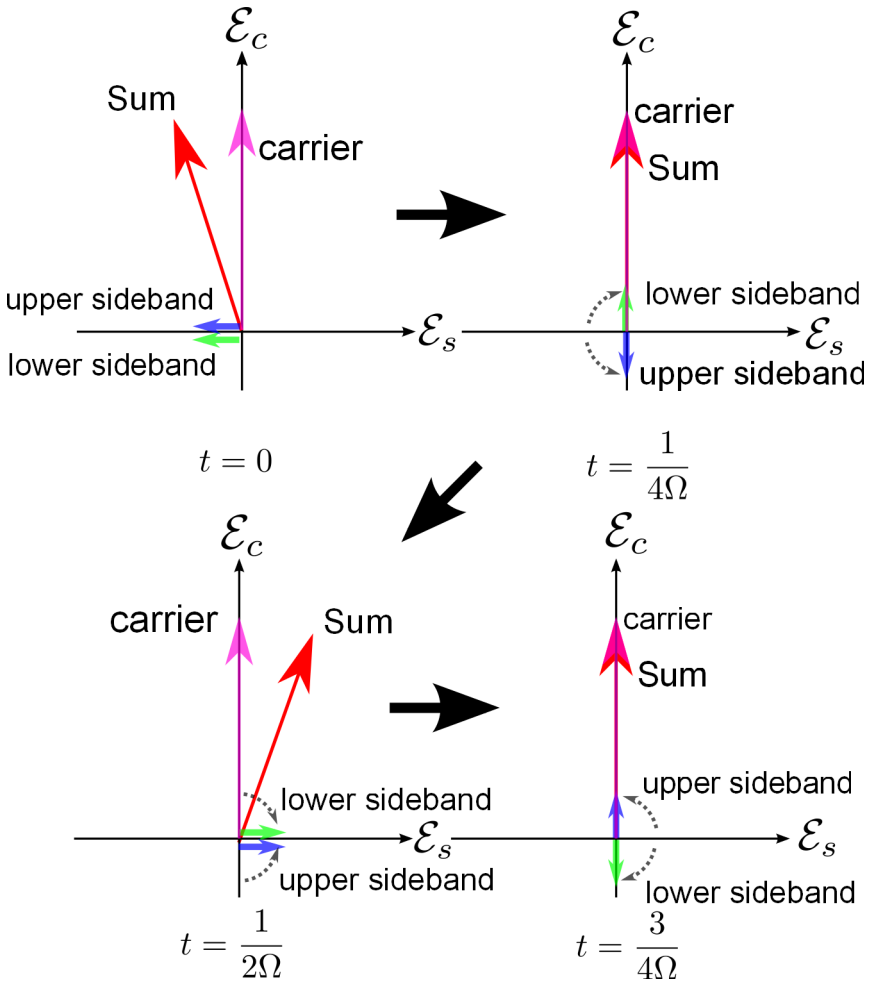

Figure A.3: Schematic view showing phase modulation by phasor diagram. Light fluctuates in the phase direction by the sideband.

We can generalize the above results and obtain the modulated light with an arbitrary modulation function $\Phi(t) = \int_{-\infty}^{\infty} \frac{d\omega}{2\pi} \tilde{\Phi}(\omega) e^{-i\omega t}$

$$E_{\mathrm{PM}}(t) = \mathrm{Re}\left[\mathcal{E}_0 e^{i\delta_m \Phi(t)} e^{-i\Omega_0 t}\right] = \mathrm{Re}\left[\mathcal{E}_0 (1 + i\delta_m \Phi(t)) e^{-i\Omega_0 t}\right]. \tag{A.30}$$

Therefore, the quadrature amplitude is expressed by using the Fourier transform $\Phi(\omega)$ of $\Phi(t)$ as

$$\mathcal{E}_{s,\mathrm{PM}}(t) \simeq \delta_m \mathcal{E}_0 \int_{-\infty}^{\infty} \frac{d\omega}{2\pi} \tilde{\Phi}(\omega) e^{-i\omega t}. \tag{A.31}$$

Therefore, the Fourier transform of the quadrature amplitude $\tilde{\mathcal{E}}_{s,\mathrm{PM}}(\omega)$ can be written as

$$\tilde{\mathcal{E}}_{s,\mathrm{PM}}(\omega) = \delta_m \mathcal{E}_0 \tilde{\Phi}(\omega). \tag{A.32}$$

A.1.4 Noise of the laser light

In this section, we show how noises of the laser source are expressed. In the discussions so far, the laser light has been treated as an ideal single frequency light, but the actual laser light includes intensity fluctuations and frequency fluctuations. We can write such an actual laser electric field using Eq. (A.1) as

$$\begin{aligned} E(t) =&(\mathcal{E}_0 + a_n(t))\cos(\Omega_0 t + \phi_0 + \phi_n(t)) \\ =&(\mathcal{E}_0 + \int_{-\infty}^{\infty}\frac{d\omega}{2\pi}\tilde{a}_n(\omega)e^{-i\omega t})\cos(\Omega_0 t + \phi_0 + \int_{-\infty}^{\infty}\frac{d\omega}{2\pi}\tilde{\phi}_n(\omega)e^{-i\omega t}), \end{aligned} \tag{A.33}$$

where $a_n(t)$ is an intensity noise and $\phi_n(t)$ is a phase noise, and $\tilde{a}(\omega)$ and $\tilde{\phi}(\omega)$ are Fourier components of each noise. Note that a frequency noise $\delta\nu_n(t)$ can be derived from the phase noise as

$$\delta\nu_n(t) = \frac{1}{2\pi}\frac{\partial\phi_n(t)}{\partial t}. \tag{A.34}$$

From Eq. (A.33), the laser intensity and phase noise can be regarded as the amplitude modulation and the phase modulation for the laser light as the carrier light, respectively. In other words, it means that sidebands are generated by the intensity noise and the frequency noise. As we have seen, a quadrature amplitude expression is convenient to express the the modulations. Furthermore, it is easy to calculate the propagation of quadrature amplitude with a matrix calculation. Therefore, the quadrature amplitude expression is the most suitable for considering the laser noise. Hereafter, let noises in the quadrature amplitude expression be $e_c(t), e_s(t)$, respectively. Their Fourier expansion can be written as

$$e_{c,s}(t) = \int_{-\infty}^{\infty}\frac{d\omega}{2\pi}\tilde{e}_{c,s}(\omega)e^{-i\omega t}, \tag{A.35}$$

where $\tilde{e}_{c,s}$ are the Fourier components of $e_{c,s}$. The relationship between $a_n(t), \phi_n(t)$ and $e_c(t), e_s(t)$ can be obtained from Eq. (A.4).

Consider how this laser noise propagates through free space. Regarding propagation of a carrier light, it is the same as shown in Appendix A.1.2. However, a correnction is necessary for the noise sideband, since the frequency is different from the carrier frequency by the sideband frequency ω. The strength of the noise electric field δE_{noise} can be written as

$$\delta E_{\text{noise}}(t) = e_c(t)\cos\Omega_0 t + e_s(t)\sin\Omega_0 t. \tag{A.36}$$

When the carrier light travels a distance L, the change in the intensity of the noise electric field can be derived as

$$\delta E^{(L)}_{\text{noise}}(t) = \delta E^{(0)}_{\text{noise}}(t - L/c). \tag{A.37}$$

From this and Eq. (A.35), propagation of the noise sideband at the sideband frequency ω

can be written as

$$\tilde{\boldsymbol{e}}^{(L)}(\omega) = e^{-i\omega L/c} \begin{pmatrix} \cos\phi_L & \sin\phi_L \\ -\sin\phi_L & \cos\phi_L \end{pmatrix} \tilde{\boldsymbol{e}}^{(0)}(\omega) = e^{-i\omega L/c}\mathbb{R}[-\phi_L]\tilde{\boldsymbol{e}}^{(0)}(\omega). \tag{A.38}$$

Compared with the carrier light, the phase is shifted by $e^{i\omega L/c}$. Therefore, we must compute the phase shift for each frequency component when we consider the propagation of the sidebands.

A.1.5 Reflection from a mirror

Next, we show how the reflection from a mirror can be expressed. Assume an ideal mirror without loss, and define the electric field of an incident light, a reflected light, the reflectance and the transmittance on each surface as shown in Fig. A.4.

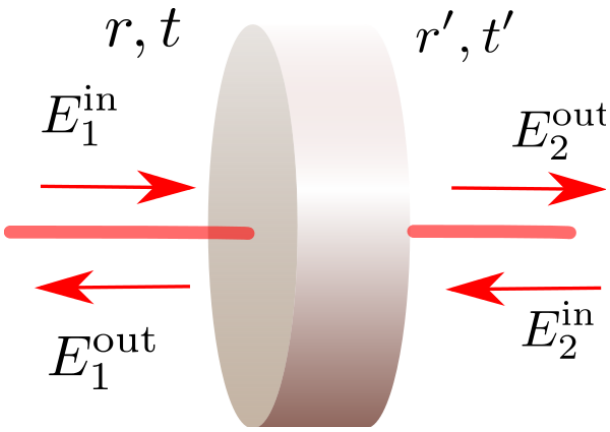

Figure A.4: Schematic view showing the reflection from a mirror. E_1^{in} and E_2^{in} are electric fields of incident beams from the left side and the right side, respectively. E_1^{out} and E_2^{out} are electric fields of outcoming beams from the left side and right side, respectively. r and r' are the reflectances of the left side and the right side, respectively. t and t' are the transmittances of the left side and the right side, respectively.

The relationship between the incident light and the reflected light can be expressed by using a 2×2 matrix as

$$\begin{pmatrix} E_1^{\mathrm{out}} \\ E_2^{\mathrm{out}} \end{pmatrix} = \begin{pmatrix} r & t \\ t & r' \end{pmatrix} \begin{pmatrix} E_1^{\mathrm{in}} \\ E_2^{\mathrm{in}} \end{pmatrix} = M \begin{pmatrix} E_1^{\mathrm{in}} \\ E_2^{\mathrm{in}} \end{pmatrix}. \tag{A.39}$$

We can characterize the mirror by the matrix M. r, t, r', and t' are the complex reflectance and transmittance of the mirror. From the energy conservation, these must satisfy the

following relationships

$$|r| = |r'|,\ |t| = |t'|,\ |r|^2 + |t|^2 = 1,\ r^*t' + r't^* = 0,\ r^*t + r't'^* = 0. \tag{A.40}$$

In order to satisfy Eq. (A.40), the matrix M needs to be unitary. The matrix M satisfying Eq. (A.40) is not uniquely determined and has a degree of freedom. So we will use the following matrix

$$M = \begin{pmatrix} -\sqrt{R} & \sqrt{T} \\ \sqrt{T} & \sqrt{R} \end{pmatrix}, \tag{A.41}$$

where $R = |r|^2$ and $T = |t|^2$ and they are called the power reflectance and the power transmittance, respectively.

Consider how the quadrature phase component changes due to mirror reflection. From a simple calculation, the relationship between the incident light and the reflected light is calculated as

$$\begin{pmatrix} \mathcal{E}_{1c}^{\text{out}} \\ \mathcal{E}_{1s}^{\text{out}} \\ \mathcal{E}_{2c}^{\text{out}} \\ \mathcal{E}_{2s}^{\text{out}} \end{pmatrix} = \begin{pmatrix} \boldsymbol{\mathcal{E}}_1^{\text{out}} \\ \boldsymbol{\mathcal{E}}_2^{\text{out}} \end{pmatrix} = \begin{pmatrix} -\sqrt{R} & 0 & \sqrt{T} & 0 \\ 0 & -\sqrt{R} & 0 & \sqrt{T} \\ \sqrt{T} & 0 & \sqrt{R} & 0 \\ 0 & \sqrt{T} & 0 & \sqrt{R} \end{pmatrix} \begin{pmatrix} \mathcal{E}_{1c}^{\text{in}} \\ \mathcal{E}_{1s}^{\text{in}} \\ \mathcal{E}_{2c}^{\text{in}} \\ \mathcal{E}_{2s}^{\text{in}} \end{pmatrix} = \mathbb{M} \begin{pmatrix} \boldsymbol{\mathcal{E}}_1^{\text{in}} \\ \boldsymbol{\mathcal{E}}_2^{\text{in}} \end{pmatrix}. \tag{A.42}$$

Also, sidebands are reflected in the same way, and frequency components can be written as

$$\begin{pmatrix} \tilde{e}_{1c}^{\text{out}} \\ \tilde{e}_{1s}^{\text{out}} \\ \tilde{e}_{2c}^{\text{out}} \\ \tilde{e}_{2s}^{\text{out}} \end{pmatrix} = \begin{pmatrix} \tilde{\boldsymbol{e}}_1^{\text{out}} \\ \tilde{\boldsymbol{e}}_2^{\text{out}} \end{pmatrix} = \begin{pmatrix} -\sqrt{R} & 0 & \sqrt{T} & 0 \\ 0 & -\sqrt{R} & 0 & \sqrt{T} \\ \sqrt{T} & 0 & \sqrt{R} & 0 \\ 0 & \sqrt{T} & 0 & \sqrt{R} \end{pmatrix} \begin{pmatrix} \tilde{e}_{1c}^{\text{in}} \\ \tilde{e}_{1s}^{\text{in}} \\ \tilde{e}_{2c}^{\text{in}} \\ \tilde{e}_{2s}^{\text{in}} \end{pmatrix} \equiv \mathbb{M} \begin{pmatrix} \tilde{\boldsymbol{e}}_1^{\text{in}} \\ \tilde{\boldsymbol{e}}_2^{\text{in}} \end{pmatrix}. \tag{A.43}$$

Next, when the mirror moves, what kind of change will occur in the reflected light is considered. Consider a case where a lossless mirror with a reflection matrix $\mathbb{M}$ moves as much as $x(t)$ as shown in Fig. A.5. Movement of the mirror is assumed to be sufficiently small compared to the wavelength of the light. The reflected light can be written as

$$\begin{aligned} E_1^{\text{out}}(t) &= -\sqrt{R}E_1^{\text{in}}(t - 2x(t)/c) + \sqrt{T}E_2^{\text{in}}(t), \\ E_2^{\text{out}}(t) &= \sqrt{T}E_1^{\text{in}}(t) + \sqrt{R}E_2^{\text{in}}(t + 2x(t)/c). \end{aligned} \tag{A.44}$$

These equations show that the reflection by the moving mirror can be expressed by a

combination of reflection by the fixed mirror and light propagation. Since $x(t) \ll \lambda$, the response of the carrier light can be written as

$$\begin{pmatrix} \mathcal{E}_1^{\text{out}\prime} \\ \mathcal{E}_2^{\text{out}\prime} \end{pmatrix} = \mathbb{M} \begin{pmatrix} (I + \delta\mathbb{R}[-2\Omega_0\tilde{x}(\omega)/c])\mathcal{E}_1^{\text{in}} \\ (I + \delta\mathbb{R}[2\Omega_0\tilde{x}(\omega)/c])\mathcal{E}_2^{\text{in}} \end{pmatrix} = \mathbb{M} \begin{pmatrix} \mathcal{E}_1^{\text{in}} \\ \mathcal{E}_2^{\text{in}} \end{pmatrix} + \frac{2\Omega_0\sqrt{R}}{c} x(t) \begin{pmatrix} \mathcal{E}_{1s}^{\text{in}} \\ -\mathcal{E}_{1c}^{\text{in}} \\ \mathcal{E}_{2s}^{\text{in}} \\ \mathcal{E}_{2c}^{\text{in}} \end{pmatrix}$$

$$= \begin{pmatrix} \mathcal{E}_1^{\text{out}} \\ \mathcal{E}_2^{\text{out}} \end{pmatrix} + \begin{pmatrix} \boldsymbol{R}_1 \\ \boldsymbol{R}_2 \end{pmatrix} x(t). \tag{A.45}$$

Here, $\boldsymbol{R}_1$ and $\boldsymbol{R}_2$ are coefficients representing the response of the light to mirror movement. From Eq. (A.45), the carrier light is not changed from the reflection by the fixed mirror, but a new sideband is induced by the movement of the mirror. The Fourier transform of $x(t)$ can be written as

$$x(t) = \int_{-\infty}^{\infty} \frac{d\omega}{2\pi} \tilde{x}(\omega) e^{-i\omega t}. \tag{A.46}$$

In the same way, the noise sideband can be derived from Eq. (A.43) as

$$\begin{pmatrix} \tilde{\boldsymbol{e}}_1^{\text{out}}(\Omega) \\ \tilde{\boldsymbol{e}}_2^{\text{out}}(\Omega) \end{pmatrix} = \mathbb{M} \begin{pmatrix} \tilde{\boldsymbol{e}}_1^{\text{in}}(\Omega) \\ \tilde{\boldsymbol{e}}_2^{\text{in}}(\Omega) \end{pmatrix} + \begin{pmatrix} \boldsymbol{R_1} \\ \boldsymbol{R_2} \end{pmatrix} \tilde{x}(\Omega). \tag{A.47}$$

Considering the quadrature amplitude coordinate where the phase component of the carrier light $\mathcal{E}_s$ is 0, we see from a simple calculation that the effect of the moving mirror appears only in the phase component. Therefore, mirror movement appears as the phase modulation.

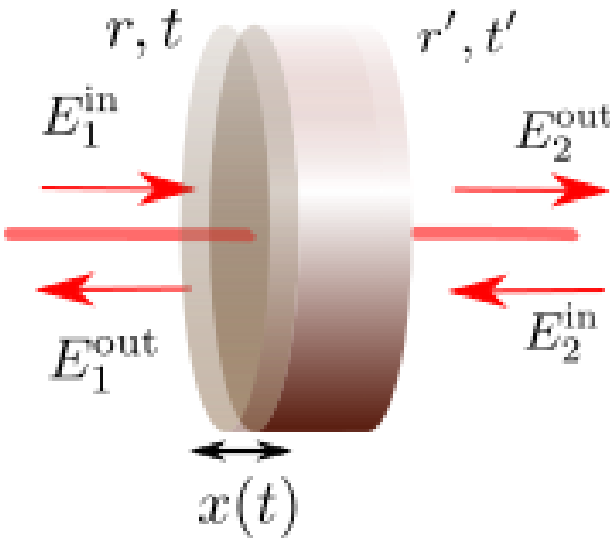

Figure A.5: Reflection on the moving mirror

A.2 Fabry-Perot cavity

We have seen how a light changes in optical elements. Here we consider how the electric field changes in a Fabry-Perot cavity.

A.2.1 Electric field inside of a cavity

First, consider the relationship between the light incident on the Fabry-Perot cavity and the light emitted from the cavity. The two mirrors constituting the cavity are called the front mirror and the end mirror. It is assumed that the front mirror is a fixed mirror and the end mirror is a movable one. Let the length of the cavity be L. Consider that a laser light with frequency Ω_0 and quadrature amplitude $\mathcal{E}_{\text{in}}$ is incident on a cavity. Moreover, assume that the incident light has noises as in Eq. (A.33), and let its Fourier component at frequency ω be $\tilde{\boldsymbol{e}}_{\text{in}}$. Let the quadrature amplitude of the reflected and the incident light of the front mirror inside the cavity be $\mathcal{E}_{\text{F1}}$ and $\mathcal{E}_{\text{F2}}$, the reflected light and the incident light of the end mirror inside the cavity be $\mathcal{E}_{\text{E1}}$ and $\mathcal{E}_{\text{E2}}$, the light reflected from the cavity be $\mathcal{E}_r$, transmitted through the cavity be $\mathcal{E}_{\text{t}}$. The $\tilde{\boldsymbol{e}}_\alpha$ represents the sideband at each point, where α stands for one of F1, F2, E1, E2, r, and t. Let the change of position of the end mirror be $x(t)$, and the light transmittance and reflectance of the front mirror and the end mirror be t_F, r_F, t_E, and r_E. The mirrors are assumed to be lossless. The sign of the reflectance of each mirror surface is set as shown in Fig. A.6. The reflection

matrices $\mathbb{M}_F$ and $\mathbb{M}_E$ of the front mirror and end mirror can be written as

$$\mathbb{M}_F = \begin{pmatrix} -r_F & 0 & t_F & 0 \\ 0 & -r_F & 0 & t_F \\ t_F & 0 & r_F & 0 \\ 0 & t_F & 0 & r_F \end{pmatrix}, \mathbb{M}_E = \begin{pmatrix} r_E & 0 & t_E & 0 \\ 0 & r_E & 0 & t_E \\ t_E & 0 & -r_E & 0 \\ 0 & t_E & 0 & -r_E \end{pmatrix}. \tag{A.48}$$

$\mathcal{E}_{F1}$ is the electric field when $\mathcal{E}_{E1}$ propagates the distance of L. Let the difference between the resonance frequency of the cavity and the laser frequency be Ω. From Eqs. (A.35) and (A.38)

$$\boldsymbol{\mathcal{E}}_{E1}(\Omega) = \mathbb{R}\left[-\frac{\Omega L}{c}\right]\boldsymbol{\mathcal{E}}_{F1}(\Omega), \tag{A.49}$$

$$\tilde{\boldsymbol{e}}^{(\Omega)}_{E1}(\omega) = e^{-i\omega L/c}\mathbb{R}\left[-\frac{\Omega L}{c}\right]\tilde{\boldsymbol{e}}^{(\Omega)}_{F1}(\omega). \tag{A.50}$$

Changes in $\mathcal{E}_{\mathrm{E2}}(\tilde{\boldsymbol{e}}_{\mathrm{E2}})$ to $\mathcal{E}_{\mathrm{F2}}(\tilde{\boldsymbol{e}}_{\mathrm{F2}})$ are the same .

In the cavity, the incident light is reflected by the end mirror. If the end mirror is moving, a new sideband appears as seen in Appendix A.1.5.

Based on the above discussion, we can formulate the equations for the reflection on the end mirror as

$$\begin{pmatrix} \boldsymbol{\mathcal{E}}_{\mathrm{E2}}(\Omega) \\ \boldsymbol{\mathcal{E}}_{\mathrm{t}}(\Omega) \end{pmatrix} = \mathbb{M}_E \begin{pmatrix} \boldsymbol{\mathcal{E}}_{\mathrm{E1}}(\Omega) \\ 0 \end{pmatrix} = \begin{pmatrix} r_E\boldsymbol{\mathcal{E}}_{\mathrm{E1}}(\Omega) \\ t_E\boldsymbol{\mathcal{E}}_{\mathrm{E1}}(\Omega) \end{pmatrix}, \tag{A.51}$$

$$\begin{aligned} \begin{pmatrix} \tilde{\boldsymbol{e}}^{(\Omega)}_{\mathrm{E2}}(\omega) \\ \tilde{\boldsymbol{e}}^{(\Omega)}_{\mathrm{t}}(\omega) \end{pmatrix} &= \mathbb{M}_E \begin{pmatrix} \tilde{\boldsymbol{e}}^{(\Omega)}_{\mathrm{E1}}(\omega) \\ 0 \end{pmatrix} + \begin{pmatrix} \boldsymbol{R}_1 \\ \boldsymbol{R}_2 \end{pmatrix} \tilde{x}(\omega) \\ &= \begin{pmatrix} r_E\tilde{\boldsymbol{e}}^{(\Omega)}_{E1}(\omega) + \boldsymbol{R}_1\tilde{x}(\omega) \\ t_E\tilde{\boldsymbol{e}}^{(\Omega)}_{E1}(\omega) \end{pmatrix}, \end{aligned} \tag{A.52}$$

where $\mathcal{E}$ represents the quadrature amplitude for each carrier light, and

$$\boldsymbol{R}_1 = \frac{2\Omega r_E}{c}\begin{pmatrix} \mathcal{E}_{s,\mathrm{E1}}(\Omega) \\ -\mathcal{E}_{c,\mathrm{E1}}(\Omega) \end{pmatrix}. \tag{A.53}$$

From Eqs. (A.49), (A.50), and (A.52), the electric field incident on the cavity and circu-

lating through the cavity changes as

$$\boldsymbol{\mathcal{E}}_{\mathrm{F2}}(\Omega) = r_E \mathbb{R}\left[-\frac{2\Omega L}{c}\right] \boldsymbol{\mathcal{E}}_{\mathrm{F1}}(\Omega), \tag{A.54}$$

$$\tilde{\boldsymbol{e}}^{(\Omega)}_{\mathrm{F2}}(\omega) = r_E e^{-2i\omega L/c}\mathbb{R}\left[-\frac{2\Omega L}{c}\right] \tilde{\boldsymbol{e}}^{(\Omega)}_{\mathrm{F1}}(\omega) + e^{-i\omega L/c}\mathbb{R}\left[-\frac{\Omega L}{c}\right] \boldsymbol{R}_1 \tilde{x}(\omega). \tag{A.55}$$

The reflection on the front mirror can be written as

$$\begin{pmatrix} \boldsymbol{\mathcal{E}}_{\mathrm{r}}(\Omega) \\ \boldsymbol{\mathcal{E}}_{\mathrm{F1}}(\Omega) \end{pmatrix} = \mathbb{M}_F \begin{pmatrix} \boldsymbol{\mathcal{E}}_{\mathrm{in}}(\Omega) \\ \boldsymbol{\mathcal{E}}_{\mathrm{F2}}(\Omega) \end{pmatrix}, \begin{pmatrix} \tilde{\boldsymbol{e}}^{(\Omega)}_{\mathrm{r}}(\omega) \\ \tilde{\boldsymbol{e}}^{(\Omega)}_{\mathrm{F1}}(\omega) \end{pmatrix} = \mathbb{M}_F \begin{pmatrix} \tilde{\boldsymbol{e}}^{(\Omega)}_{\mathrm{in}}(\omega) \\ \tilde{\boldsymbol{e}}^{(\Omega)}_{\mathrm{F2}}(\omega) \end{pmatrix}. \tag{A.56}$$

From Eqs. (A.54), (A.55), and (A.56), the quadrature amplitude inside the cavity can be derived as

$$\boldsymbol{\mathcal{E}}_{\mathrm{F1}}(\Omega) = \left(1 - r_F r_E \mathbb{R}\left[-\frac{2\Omega L}{c}\right]\right)^{-1} t_F \mathbb{R}\left[-\frac{2\Omega L}{c}\right] \boldsymbol{\mathcal{E}}_{\mathrm{in}}(\Omega) \tag{A.57}$$

$$\begin{aligned} \tilde{\boldsymbol{e}}^{(\Omega)}_{\mathrm{F1}}(\omega) = &\left(1 - r_F r_E e^{-2i\omega L/c}\mathbb{R}\left[-\frac{2\Omega L}{c}\right]\right)^{-1}, \\ &\times \left(t_F e^{-2i\omega L/c}\mathbb{R}\left[-\frac{2\Omega L}{c}\right] \tilde{\boldsymbol{e}}^{(\Omega)}_{\mathrm{in}}(\omega) + r_F e^{-i\omega L/c}\mathbb{R}\left[-\frac{\Omega L}{c}\right] \boldsymbol{R}_1 \tilde{x}(\omega)\right). \end{aligned} \tag{A.58}$$

Figure A.6: Schematic view showing a Fabry-Perot cavity. $\mathcal{E}_{\mathrm{in}}, \mathcal{E}_{\mathrm{r}}$, and $\mathcal{E}_{\mathrm{t}}$ are the electric fields of the incident, the reflected and the transmitted light, respectively. $\mathcal{E}_{\mathrm{F1}}, \mathcal{E}_{\mathrm{F2}}, \mathcal{E}_{\mathrm{E1}}$, and $\mathcal{E}_{\mathrm{E2}}$ are electric fields inside of the cavity.

A.2.2 The reflected and transmitted light in Fabry-Perot cavity

Next, we will consider the reflected light and the transmitted light from a cavity. Let the incident light be $\mathcal{E}_{\rm in} = (E_0, 0)^t$. From Eqs. (A.49), (A.51), (A.56) and (A.57), the reflected light $\mathcal{E}_{\rm r}(\Omega)$ and the transmitted light $\mathcal{E}_{\rm t}(\Omega)$ can be derived as

$$\begin{aligned}\boldsymbol{\mathcal{E}}_{\rm r}(\Omega) &= \left(1 - r_F r_E \mathbb{R}\left[-2\phi\right]\right)^{-1} \left(-r_F + r_E \mathbb{R}\left[-2\phi\right]\right) \mathcal{E}_{\rm in}(\Omega) \\ &= \frac{1}{(1 - r_F r_E)^2 \left\{1 + \left(\frac{2\mathcal{F}}{\pi}\right)^2 \sin^2\phi\right\}} \begin{pmatrix} -r_F(1 + r_E^2) + r_E(1 + r_F^2)\cos 2\phi \\ r_E(r_F^2 - 1)\sin 2\phi \end{pmatrix} E_0,\end{aligned} \tag{A.59}$$

$$\begin{aligned}\boldsymbol{\mathcal{E}}_{\rm t}(\Omega) &= \left(1 - r_F r_E \mathbb{R}\left[-2\phi\right]\right)^{-1} \left(t_F t_E \mathbb{R}\left[-3\phi\right]\right) \mathcal{E}_{\rm in}(\Omega) \\ &= \frac{t_F t_E}{(1 - r_F r_E)^2 \left\{1 + \left(\frac{2\mathcal{F}}{\pi}\right)^2 \sin^2\phi\right\}} \begin{pmatrix} (1 - r_E r_F)\cos\phi \\ (1 + r_E r_F)\sin\phi \end{pmatrix} E_0,\end{aligned} \tag{A.60}$$

where $\phi = \Omega L/c$ and the finesse $\mathcal{F}$ is given by

$$\mathcal{F} = \frac{\pi\sqrt{r_F r_E}}{1 - r_F r_E}. \tag{A.61}$$

From Eqs. (A.59) and (A.60), the reflected power P_r and the transmitted power P_t can be derived as

$$P_r(\Omega) = |\mathcal{E}_r(\Omega)|^2 = \frac{(r_E - r_F)^2 + 4 r_F r_E \sin^2(\Omega L/c)}{(1 - r_F r_E)^2 \left\{1 + (2\mathcal{F}/\pi)^2 \sin^2(\Omega L/c)\right\}}, \tag{A.62}$$

$$P_t(\Omega) = |\mathcal{E}_t(\Omega)|^2 = \frac{(t_F t_E)^2}{(1 - r_F r_E)^2 \left\{1 + (2\mathcal{F}/\pi)^2 \sin^2(\Omega L/c)\right\}}. \tag{A.63}$$

The internal power of the cavity is maximized when the transmitted power reaches a maximum. From Eq. (A.63), when $\Omega = 0$, the transmitted power is maximum. As Ω increases, the transmitted power decreases. Furthermore, when Ω shifts by $\Omega_{\rm FSR} = \pi c/L$, the resonance condition is satisfied again and the transmitted power reaches the maximum again. This frequency separation is called the free spectral range (FSR). When the cavity is on resonance, the transmitted power and the reflected power can be derived as

$$\boldsymbol{\mathcal{E}}_r = \frac{-r_F + r_E}{1 - r_F r_E} \begin{pmatrix} E_0 \\ 0 \end{pmatrix}, \tag{A.64}$$

$$\boldsymbol{\mathcal{E}}_t = \frac{t_F t_E}{1 - r_F r_E} \begin{pmatrix} E_0 \\ 0 \end{pmatrix}. \tag{A.65}$$

From Eq. (A.63), we can calculate the full width at half maximum Ω_{FWHM} of the resonance peak by solving the equation below

$$\frac{1}{1+(2\mathcal{F}/\pi)^2\sin^2(\Omega_{\mathrm{FWHM}}L/c)}=\frac{1}{2}. \tag{A.66}$$

Note $\Omega_{\mathrm{FWHM}}L/c \ll 1$ in general, then Ω_{FWHM} can be written as

$$\Omega_{\mathrm{FWHM}}=\frac{1}{\mathcal{F}}\Omega_{\mathrm{FSR}}. \tag{A.67}$$

$\mathcal{F}$ is called finesse which is the ratio of Ω_{FSR} to Ω_{FWHM}. It is a quantity representing the sharpness of the resonance peak. Figure A.7 shows the reflectance of cavities with finesse of 10 and 100. As shown in Eq. (A.61) finesse is determined by the reflectance of the mirrors of the cavity. A cavity composed of the mirror having the higher reflectance has the higher finesse. Furthermore, from Eq. (A.57), the internal power of higher finesse cavity is higher.

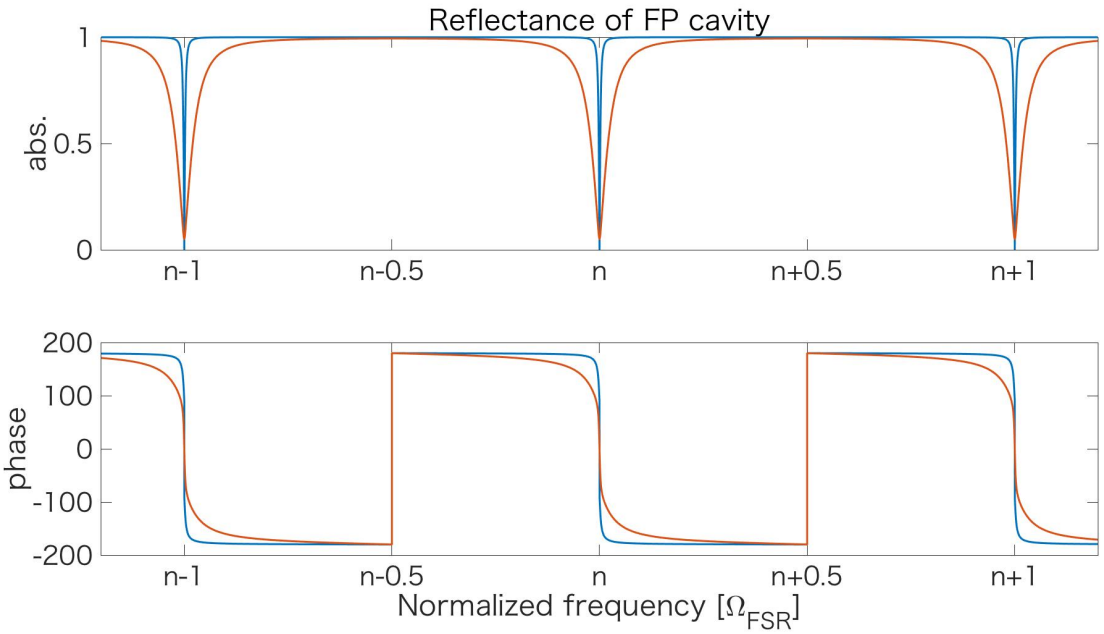

Figure A.7: Plots of the absolute value (upper) and the phase (lower) of the complex reflectance of a Fabry-Perot cavity. Blue curves are for the cavity with finesse of 100 and red curves are for one with finesse of 10. Horizontal axis represents the angular frequency of the laser normalized by Ω_{FSR}, and n is an integer.

A.2.3 Passive filtering of Fabry-Perot cavity

As we have seen, the intensity noise and the frequency noise of laser light can be expressed by using sidebands imposed on the laser light. Here, we show how the noise sideband of a light incident on the cavity changes in an output light.

When $\Omega = n\Omega_{\mathrm{FSR}}$ where n is an integer, the Fourier component of the noise sideband in the outgoing light $\tilde{\boldsymbol{e}}_t(\omega)$ can be obtained from Eq. (A.58) as

$$\tilde{\boldsymbol{e}}_t(\omega) = \frac{t_F t_E e^{-i\omega L/c}\tilde{\boldsymbol{e}}_{\mathrm{in}}(\omega) + r_F t_E e^{-2i\omega L/c}\boldsymbol{R}_1\tilde{x}(\omega)}{1 - r_F r_E e^{-2i\omega L/c}}. \tag{A.68}$$

From Eq. (A.68), we can obtain the frequency response $H_{\mathrm{FP}}^{\mathrm{cav}}(\omega)$ of the sideband amplitude from the incident light to the outgoing light as

$$H_{\mathrm{FP}}^{\mathrm{cav}}(\omega) = \frac{t_F t_E e^{-i\omega L/c}}{1 - r_F r_E e^{-2i\omega L/c}}. \tag{A.69}$$

From Eq. (A.36), the noise on the outgoing light from the cavity can be derived as

$$\begin{aligned}
\delta E_{\mathrm{t,noise}} &= e_{t,c}(t)\cos\Omega_0 t + e_{t,s}(t)\sin\Omega_0 t \\
&= \int_{-\infty}^{\infty}\frac{d\omega}{2\pi}\tilde{e}_{t,c}(\omega)e^{-i\omega t}\cos\Omega_0 t + \int_{-\infty}^{\infty}\frac{d\omega}{2\pi}\tilde{e}_{t,s}(\omega)e^{-i\omega t}\sin\Omega_0 t \\
&= \int_{-\infty}^{\infty}\frac{d\omega}{2\pi}H_{\mathrm{FP}}^{\mathrm{cav}}(\omega)(\tilde{e}_{\mathrm{in},c}(\omega)\sin\Omega_0 t + \tilde{e}_{\mathrm{in},s}(\omega)\cos\Omega_0 t)e^{-i\omega t} \\
&= \int_{-\infty}^{\infty}\frac{d\omega}{2\pi}H_{\mathrm{FP}}^{\mathrm{cav}}(\omega)\tilde{E}_{\mathrm{in,noise}}(\omega)e^{-i\omega t}.
\end{aligned} \tag{A.70}$$

where $\tilde{E}_{\mathrm{in,noise}}(\omega)$ is the Fourier component of the noise on the incident light. Therefore, $H_{\mathrm{FP}}^{\mathrm{cav}}(\omega)$ is the frequency response of the noise from the incident light to the outgoing light from the cavity. When $\omega L/c \ll 1$, that is, $\omega \ll \Omega_{\mathrm{FSR}}$, the absolute value of the frequency response $H_{\mathrm{FP}}^{\mathrm{cav}}(\omega)$ can be obtained as

$$\begin{aligned}
|H_{\mathrm{FP}}^{\mathrm{cav}}(\omega)| &= \frac{t_F t_E}{1 - r_F r_E}\frac{1}{\sqrt{\left\{1 + (2\mathcal{F}/\pi)^2\sin^2(\omega L/c)\right\}}} \\
&\simeq \frac{t_F t_E}{1 - r_F r_E}\frac{1}{\sqrt{1 + ((2\mathcal{F}/\pi)\times(\omega L/c))^2}} \\
&= \frac{t_F t_E}{1 - r_F r_E}\frac{1}{\sqrt{1 + (2\omega/\Omega_{\mathrm{FWHM}})^2}}.
\end{aligned} \tag{A.71}$$

From Eq. (A.71), the Fabry-Perot cavity acts as a first-order low-pass filter with a cutoff frequency $\omega_c = \Omega_{\mathrm{FWHM}}/2$ for the noise sideband. Therefore, the frequency noise and the intensity noise of the light transmitted through the cavity are reduced in the frequency band above the cutoff frequency ω_c. This is because the noise with periods shorter than the storage time of the cavity is averaged in the cavity. The storage time τ can be obtained from the cutoff frequency as

$$\tau = 1/\omega_c. \tag{A.72}$$

The cutoff frequency ω_c is often called a cavity pole frequency.

A.2.4 Application of a Fabry-Perot cavity

The Fabry-Perot cavity is used as a frequency reference because of its frequency selectivity. When the resonance frequency of the cavity is sufficiently stable, the frequency of the laser can be stabilized by controlling the laser frequency to follow the resonance frequency.

As we will see below, the Fabry-Perot cavity also has selectivity for the laser's spatial mode. Therefore, it is possible to clean up the spatial mode of the light by letting the light resonate in and pass through the cavity. A cavity used for such an application is called a mode cleaner.

A beam jitter can be expressed as an intensity fluctuation of the first-order spatial mode. Therefore, the beam jitter can be reduced by passing the light through the cavity and filtering the first-order spatial mode.

A.3 Control of Fabry-Perot cavity

Usually, when using a cavity, the length of the cavity or the input light frequency has to be controlled to maintain the resonance state. As will be described below, it can be seen that changes in the cavity length or the laser frequency are included in the phase component of the reflected light. Therefore, to obtain an error signal, it is necessary to read the phase component. Pound, Drever, Hall, *et al.* have devised a readout technique called the Pound-Drever-Hall method (PDH method) [57]. In this section, we describe the signal extraction for the cavity control by the PDH method.

A.3.1 Frequency response of Fabry-Perot cavity

Before discussing the PDH method, let's see how the reflected light changes when the laser frequency deviates from the resonance frequency or when the cavity length changes.

First, let's consider what signal can be obtained when the cavity length L changes. Assume that the cavity length fluctuates around the resonance. Information on the change in the cavity length is included in the sidebands of the reflected light, in which the Fourier component of the sideband can be derived from Eq. (A.58) as

$$\tilde{\boldsymbol{e}}_r(\omega) = \frac{(-r_F + r_E e^{-2i\omega L/c})\tilde{\boldsymbol{e}}_{\rm in}(\omega) + t_F e^{-i\omega L/c}\boldsymbol{R}_1\tilde{x}(\omega)}{1 - r_F r_E e^{-2i\omega L/c}}. \tag{A.73}$$

Assuming the electric field of the incident light is $\boldsymbol{\mathcal{E}}_{\rm in} = (E_0, 0)^t$, then from Eqs. (A.53) and (A.55)

$$\boldsymbol{R}_1 = \frac{2\Omega r_E}{c}\frac{t_F}{1 - r_F r_E}\begin{pmatrix} 0 \\ \\ -E_0 \end{pmatrix}. \tag{A.74}$$

Therefore, when the cavity length changes, the phase component of the reflected light changes. Assuming that $\omega \ll \Omega_{\rm FSR}$ and $r_F \sim r_E \sim 1$, the frequency response from the cavity length change to the reflected light $H^L_{\rm FP}(\omega)$ can be obtained as

$$H^L_{\rm FP}(\omega) = \frac{e_{r,s}(\omega)}{\tilde{x}(\omega)} = -\frac{2\Omega r_E}{c}\frac{t_F}{1-r_F r_E}\frac{t_F e^{-i\omega L/c}E_0}{1-r_F r_E e^{-2i\omega L/c}} \tag{A.75}$$

$$\simeq \frac{2\Omega}{c}\frac{t_F^2 r_E}{1-r_F r_E}\frac{1-2i\omega L/c}{1-r_F r_E(1-2i\omega L/c)}E_0$$

$$\simeq \frac{E_0}{x_c}H^{\rm cav}_{\rm LP}(\omega), \tag{A.76}$$

where x_c is a length representing a width of the resonance peak,

$$x_c = \frac{\lambda}{2\mathcal{F}}, \tag{A.77}$$

where λ is the wavelength of the light. $H^{\rm cav}_{\rm LP}(\omega)$ is a transfer function of a low pass filter,

$$H^{\rm cav}_{\rm LP}(\omega) = \frac{1}{i\omega/\omega_{\rm c}+1}. \tag{A.78}$$

Next, consider the case where the frequency of the incident light changes. From Appendix A.1.2, when the laser frequency Ω fluctuates around the resonance frequency Ω_0 by $\delta\Omega(\omega)$, it can be regarded as the same as when the cavity length fluctuates with $\frac{\delta\tilde{\Omega}(\omega)}{\Omega}L$. Therefore, if we use the approximation that $\omega \ll \omega_c$, the frequency response from the laser frequency fluctuation to the reflected light can be derived as

$$H^F_{\rm FP}(\omega) = \frac{L}{\Omega}H^L_{\rm FP}(\omega) = \frac{E_0}{\omega_c}H^{\rm cav}_{\rm LP}(\omega). \tag{A.79}$$

A.3.2 Pound Drever Hall method

As we have seen, a signal for controlling a cavity is included in a phase component of the reflected light. To read the phase component, a phase modulation is applied to the incident light with a modulation frequency ω_m and a modulation index δ_m, and a beat signal between sidebands and carrier lights is measured. The incident light can be written from Eq. (A.29) as

$$\boldsymbol{\mathcal{E}}^{\mathbf{tot}}_{\mathbf{in}} = \begin{pmatrix} E_0 \\ 0 \end{pmatrix} + \begin{pmatrix} 0 \\ \delta_m \mathrm{E}_0 \cos\omega_m t \end{pmatrix} = \boldsymbol{\mathcal{E}}_{\rm in} + \boldsymbol{e}_m, \tag{A.80}$$

where $\boldsymbol{\mathcal{E}}_{\rm in}$ is the carrier light and $\boldsymbol{e}_m$ is a sideband of the phase modulation. Note that the incident light also has noise sidebands omitted in Eq. (A.80)

For the sidebands applied for signal extraction, we choose the modulation frequency to satisfy $\omega_m \gg \omega_c$. Therefore, when the carrier light is resonating, the sideband for signal

extraction is not resonant. In this case, almost entirely reflected by the front mirror, and the cavity reflectance for the sideband is approximately r_F. Let the frequency of the incident light fluctuate with $\delta\Omega(t)$ around the resonance frequency Ω_0, and the cavity length fluctuates by $x(t)$ around L.

Fourier transform of the cavity length fluctuation $x(t)$ and the laser frequency fluctuation $\delta\Omega(t)$ can be written as

$$x(t) = \int_{-\infty}^{\infty} \frac{d\omega}{2\pi} \tilde{x}(\omega) e^{-i\omega t}, \tag{A.81}$$

$$\delta\Omega(t) = \int_{-\infty}^{\infty} \frac{d\omega}{2\pi} \delta\tilde{\Omega}(\omega) e^{-i\omega t}. \tag{A.82}$$

From Eqs. (A.64), (A.76), and (A.79), the reflected light $\boldsymbol{\mathcal{E}}_{\mathrm{r}}^{\mathrm{tot}}$ can be obtained as

$$\begin{aligned}
\boldsymbol{\mathcal{E}}_{\mathrm{r}}^{\mathrm{tot}} &= \frac{-r_F + r_E}{1 - r_F r_E} \boldsymbol{\mathcal{E}}_{\mathrm{in}} + \int_{-\infty}^{\infty} \frac{d\omega}{2\pi} \left(H_{\mathrm{FP}}^{\mathrm{L}} \tilde{x}(\omega) + H_{\mathrm{FP}}^{\mathrm{F}} \delta\tilde{\Omega}(\omega) \right) e^{-i\omega t} \begin{pmatrix} 0 \\ 1 \end{pmatrix} + r_F \boldsymbol{e}_m \\
&= \frac{-r_F + r_E}{1 - r_F r_E} \boldsymbol{\mathcal{E}}_{\mathrm{in}} + E_0 \int_{-\infty}^{\infty} \frac{d\omega}{2\pi} \left(\frac{\tilde{x}(\omega)}{x_c} + \frac{\delta\tilde{\Omega}(\omega)}{\omega_c} \right) H_{\mathrm{LP}}^{\mathrm{cav}}(\omega) e^{-i\omega t} \begin{pmatrix} 0 \\ 1 \end{pmatrix} + r_F \boldsymbol{e}_m \\
&= \boldsymbol{\mathcal{E}}_{\mathrm{r}} + \boldsymbol{e}_s + r_F \boldsymbol{e}_m,
\end{aligned} \tag{A.83}$$

where $\boldsymbol{\mathcal{E}}_{\mathrm{r}}$ is the carrier light in the reflected light from the cavity and $\boldsymbol{e}_s$ is a signal sideband. The reflected power P_r^{tot} can be derived as

$$\begin{aligned}
P_r^{\mathrm{tot}} &= \left| \boldsymbol{\mathcal{E}}_{\mathrm{r}}^{\mathrm{tot}} \right|^2 = |\boldsymbol{\mathcal{E}}_{\mathrm{r}}|^2 + |\boldsymbol{e}_s + r_F \boldsymbol{e}_m|^2 \\
&= \left(\frac{-r_F + r_E}{1 - r_F r_E} E_0 \right)^2 + |\boldsymbol{e}_s|^2 + R_F (\delta_m \cos\omega_m t)^2 E_0^2 \\
&\quad + 2\delta_m E_0^2 \cos\omega_m t \int_{-\infty}^{\infty} \frac{d\omega}{2\pi} \left(\frac{\tilde{x}(\omega)}{x_c} + \frac{\delta\tilde{\Omega}(\omega)}{\omega_c} \right) H_{\mathrm{LP}}^{\mathrm{cav}}(\omega) e^{-i\omega t}.
\end{aligned} \tag{A.84}$$

In Eq. (A.84), the first and the second terms are static components, the third term is a component oscillating at the frequency of $2\omega_m$, and the fourth term is a component oscillating at the frequency of ω_m which contains information on the cavity length and the laser frequency. Therefore, to obtain the error signal, the output of the PD detecting the reflected light is demodulated with $\cos\omega_m t$. The demodulated signal P_r^{demod} can be derived as

$$P_r^{\mathrm{demod}} = P_r^{\mathrm{tot}} \cos(\omega_m t) = \delta_m E_0^2 \int_{-\infty}^{\infty} \frac{d\omega}{2\pi} \left(\frac{\tilde{x}(\omega)}{x_c} + \frac{\delta\tilde{\Omega}(\omega)}{\omega_c} \right) H_{\mathrm{LP}}^{\mathrm{cav}}(\omega) e^{-i\omega t} + (\text{AC term}), \tag{A.85}$$

where (AC term) includes component that oscillates at frequency $2\omega_m$. By removing this

oscillation component with a low pass filter, the error signal $\epsilon(t)$ can be obtained. The Fourier component of the error signal can be written as

$$\tilde{\epsilon}(\omega) = \sqrt{2P_0P_s}\left(\frac{\tilde{x}(\omega)}{x_c} + \frac{\delta\tilde{\Omega}(\omega)}{\omega_c}\right) H_{\rm LP}^{\rm cav}(\omega), \tag{A.86}$$

where $P_0 = E_0^2$ is the direct current (DC) power of the incident light, and $P_s = (\delta_m E_0)^2/2$ is the DC power of the modulation sidebands. The reflectivity of the cavity and the error signal are plotted in Fig. A.8. The central signal in the plot corresponds to when the carrier light resonates, and similar signals seen on the left and the right are generated when the lower sideband and the upper sideband resonate, respectively.

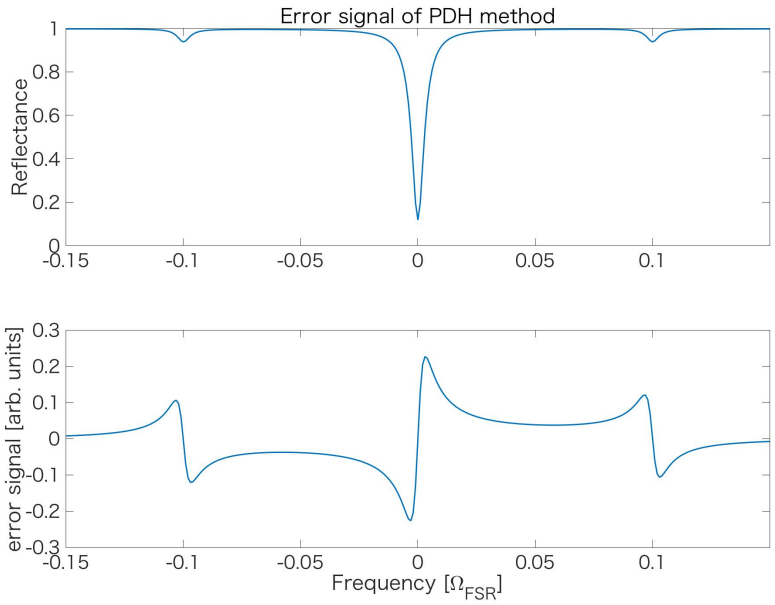

Figure A.8: Plots of the reflectance (upper) and the error signal of a Fabry-Perot cavity by a PDH method (lower). Horizontal axis is the deviation from a resonance frequency in unit of $\Omega_{\rm FSR}$. In this calculation, the modulation frequency is set to $\Omega_{\rm FSR}/10$

A.4 Mode cleaning

Because of the spatial mode selectivity of a cavity, it can be used as a mode cleaner. The nature of this mode cleaning is also used to reduce a beam jitter. In this section, we consider a spatial mode of the light and see how the cavity cleans it.

A.4.1 Spatial mode

Up to here, a laser light has been considered as a one-dimensional ideal plane wave. However, in reality, it is a beam with a transverse spatial profile. The wave equation which the electric field u should satisfy can be written as

$$\Delta u - k^2 u = 0. \tag{A.87}$$

When it is solved using the paraxial approximation [58], we obtain a solution called a Gaussian beam, since its spatial distribution of the intensity in the fundamental mode has a Gaussian distribution. The normalized transverse intensity distribution of a Gaussian beam propagating in the z-axis direction can be written as

$$U_{00}(r,z) = \sqrt{\frac{2}{w(z)^2}} \exp\left(\frac{-r^2}{w(z)^2} - ikz - ik\frac{r^2}{2R(z)} + i\zeta(z)\right), \tag{A.88}$$

where r is the distance from the central axis of the beam and k is the wave number. $w(z)$ is the radius of the beam spot, at which the strength of the electric field is $1/e$ times of the value at the center $r = 0$ where e is Napier's constant. $w(z)$ can be written as

$$w(z)^2 = w_0^2 \left[1 + \left(\frac{\lambda z}{\pi w_0^2}\right)^2\right], \tag{A.89}$$

where λ is the wavelength of the laser light, and $w(z)$ has the minimum value w_0 called waist size at $z = 0$. $R(z)$ represents the radius of curvature of the wavefront and is given by

$$R(z) = z\left[1 + \left(\frac{\pi w_0^2}{\lambda z}\right)^2\right]. \tag{A.90}$$

The beam radius $w(z)$ can be regarded as being proportional to z when $z \gg z_R$, where $z_R = \pi w_0^2/\lambda$. This means that the beam can be regarded as a cone at the region far from the beam waist. The angle between the line $r = w(z)$ and the beam center axis $r = 0$ is called the divergence angle of the beam, and it is given as

$$\alpha_0 = \frac{\lambda}{\pi w_0}. \tag{A.91}$$

$\zeta(z)$ is called the gouy phase and represents the deviation of the phase from the plane

wave e^{-ikz}. It can be written as

$$\zeta(z) = \tan^{-1}\left(\frac{\lambda z}{\pi w_0^2}\right). \tag{A.92}$$

The degrees of freedom necessary to describe a Gaussian beam are only the waist size w_0 and the waist position, in addition to the wave number and the intensity. Therefore, the spatial mode of the laser can be described by the waist size and the waist position. These parameters change when transmitting through a lens or reflected by a curved mirror. Equation (A.87) has a general solution as

$$U_{lm}(x, y, z) = U_l(x, z)U_m(y, z)\exp\{-ikz + i(l + m + 1)\zeta(z)\}, \tag{A.93}$$

where l and m are the orders of mode on the x and y axes, and they represent the number of nodes on each axis. Here,

$$U_l(x, z) = \left(\frac{2}{\pi w(z)^2}\right)^{1/4}\left(\frac{1}{l!2^l}\right)^{1/2} H_l\left(\frac{\sqrt{2}x}{w(z)}\right)\exp\left[-\left(\frac{x}{w(z)}\right)^2 - i\frac{k}{2R(z)}x^2\right], \tag{A.94}$$

where H_l is the lth-order Hermite polynomial. Modes in which the Hermite polynomials represent the intensity distribution of the beam cross-section are called a Hermite Gaussian modes. Equation (A.93) can be rewritten by using the fundamental mode as

$$U_{lm}(x, y, z) = \sqrt{\frac{1}{2^l l! 2^m m!}} H_l\left(\frac{\sqrt{2}x}{w(z)}\right) H_m\left(\frac{\sqrt{2}y}{w(z)}\right)\exp[i(l + m)\zeta(z)]U_{00}(x, y, z)]. \tag{A.95}$$

Hermite Gaussian modes are denoted as TEM_{lm} (transverse electromagnetic) modes by using its orders l and m. Note that in a higher-order TEM_{lm} mode, the phase rotates by an extra amount $(l + m)\zeta(z)$ compared to the TEM_{00} mode. Regarding the TEM_{00}, TEM_{10}, and TEM_{20}, the cross-sections on the zx plane are shown in Figs.A.9, A.10 ,and A.11, respectively.

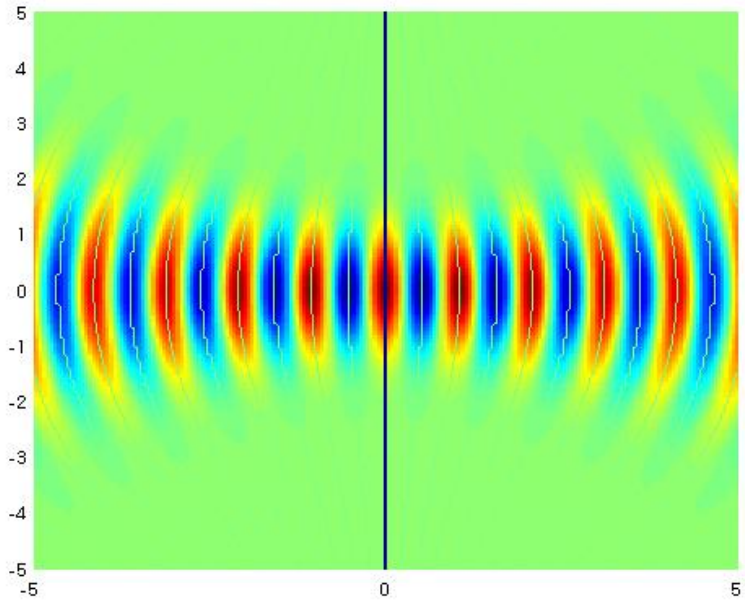

Figure A.9: Cross-section of the amplitude of TEM_{00} mode. The horizontal axis is in unit of the wavelength of the light, and the vertical axis is in unit of the waist size of the beam.

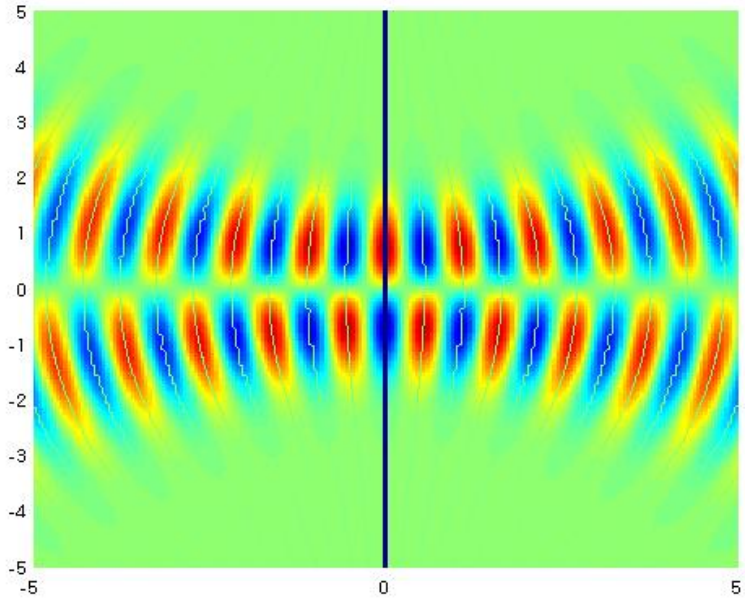

Figure A.10: Cross-section of the amplitude of TEM_{10} mode. The horizontal axis is in unit of the wavelength of the light, and the vertical axis is in unit of the waist size of the beam.

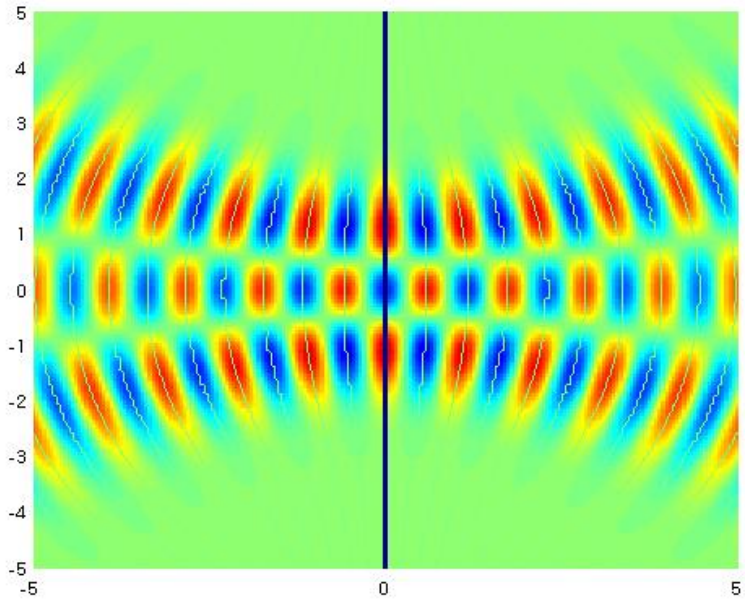

Figure A.11: Cross-section of the amplitude of TEM_{20} mode. The horizontal axis is in unit of the wavelength of the light, and the vertical axis is in unit of the waist size of the beam.

A.4.2 Resonant spatial mode of a Fabry-Perot cavity

When thinking in one dimension, only the frequency was considered in the resonance condition. However, in reality, it is necessary to satisfy the resonance condition also for the spatial mode. For a cavity to resonate, it is necessary for the spatial mode of the incident light to coincide with the wavefront of the light after traveling around the cavity. Here, we use the complex beam parameter q to describe the eigenmode of the cavity. It can be written as

$$q(z) = z + i\frac{\pi w_0^2}{\lambda} = z + iz_R, \tag{A.96}$$

where $z_R = \pi w_0^2/\lambda$ is called the Rayleigh length. This q represents the spatial mode of the beam. Taking the reciprocal of q, then

$$\frac{1}{q(z)} = \frac{1}{R(z)} - i\frac{\lambda}{\pi w^2(z)}. \tag{A.97}$$

Using q, the radius of curvature R of the wavefront and the beam size $w(z)$ can be easily calculated.

Consider the eigenmode of the cavity using the complex beam parameter q. Suppose q changes from q_1 to q_2 when the light is reflected by a mirror or passes through a lens.

This transformation is described in a matrix form as

$$\begin{pmatrix} q_2 \\ 1 \end{pmatrix} = a \begin{pmatrix} A & B \\ C & D \end{pmatrix} \begin{pmatrix} q_1 \\ 1 \end{pmatrix}. \tag{A.98}$$

This can be solved as

$$q_2 = \frac{Aq_1 + B}{Cq_1 + D}. \tag{A.99}$$

This matrix is called an ABCD matrix.

Let us see the ABCD matrix of each optical component or propagation. Firstly considering when light propagates for a distance of L. q_2 can be written as

$$q_2 = L + q_1. \tag{A.100}$$

Therefore, the ABCD matrix can be written as

$$\mathbb{T}_{\mathrm{p}}(L) = \begin{pmatrix} 1 & L \\ 0 & 1 \end{pmatrix}. \tag{A.101}$$

Next, consider the case where the light passes through a lens with a focal length of f. By passing through the lens, the light converts the spherical wavefront with the radius of curvature R_1 into a spherical wavefront with the radius of curvature R_2. The relationship between R_1 and R_2 can be written as [59]

$$\frac{1}{R_2} = \frac{1}{R_1} - \frac{1}{f}. \tag{A.102}$$

Note that the beam size does not change immediately before and after the lens, then from Eq. (A.97)

$$\frac{1}{q_2} = \frac{1}{q_1} - \frac{1}{f} \tag{A.103}$$

$$\therefore q_2 = \frac{q_1}{-q_1/f + 1}. \tag{A.104}$$

Therefore, the ABCD matrix can be written as

$$\mathbb{T}_{\mathrm{lens}}(f) = \begin{pmatrix} 1 & 0 \\ -1/f & 1 \end{pmatrix}. \tag{A.105}$$

Finally consider a reflection by a curved mirror. The reflection from the mirror with the radius of curvature R works in the same way as a lens with focal length $f = R/2$.

Therefore, the ABCD matrix can be written as

$$\mathbb{T}_{\mathrm{mirror}}(R) = \begin{pmatrix} 1 & 0 \\ -2/R & 1 \end{pmatrix}. \tag{A.106}$$

Using these ABCD matrices, the ABCD matrix of travel around a Fabry-Perot cavity with two mirrors of the radii of curvature of R_F, R_E and a cavity length of L can be written as

$$\mathbb{T}_{\mathrm{FP}}(L, R_F, R_E) = \mathbb{T}_{\mathrm{mirror}}(R_F)\mathbb{T}_{\mathrm{p}}(L)\mathbb{T}_{\mathrm{mirror}}(R_E)\mathbb{T}_{\mathrm{p}}(L). \tag{A.107}$$

The eigenmode of the cavity can be obtained by calculating the eigenvector for this matrix $\mathbb{T}_{\mathrm{FP}}(L, R_F, R_E)$.

When the light is incident on the cavity, it is necessary to match the spatial mode of the light with the eigen spatial mode of the cavity. This operation is called mode matching, and lenses or curved mirrors are used to achieve it. The coupling ratio between the incident laser mode and the cavity eigenmode is called the mode matching ratio.

A.4.3 Spatial mode selectivity

A Fabry-Perot cavity also has selectivity for a spatial mode, not only for a frequency. This is because the phase rotation during propagation inside a cavity depends on the order of the mode. This property can be used to clean the spatial mode of the incident light, and a cavity used in this application is called a mode cleaner.

Regarding an eigenmode of the cavity, let the distance from the position of the beam waist to the front mirror and the end mirror be d_F and d_E, respectively. From Eq. (A.92), the rotation of gouy phase between the mirrors can be written as

$$\zeta_0 = \zeta(d_E) + \zeta(d_F). \tag{A.108}$$

From Eq. (A.93), the resonance condition including the higher-order modes can be written as

$$\frac{2L}{\lambda} = m_0 + (l + m + 1)\frac{\zeta_0}{\pi}, \tag{A.109}$$

where m_0 is an integer. Therefore, unless ζ_0/π is an integer, the fundamental mode and the higher-order modes do not satisfy the resonance condition simultaneously. Therefore, when designing a mode cleaner, one must determine the curvatures of the mirrors by considering this point.

A.4.4 Beam jitter reduction

Taking advantage of the mode cleaning properties of a cavity, a beam jitter can be reduced, since the beam jitter is represented by an intensity fluctuation of the first-order mode contained in the beam. The intensity distribution of TEM_{00} can be expanded around $z' = 0$ in the coordinate system (x', y', z'), which is shifted by δx in the x-axis direction [60] as

$$U_{00}(x, y, z)_{z'=0} \simeq U_{00}(x', y', 0) + \left(\frac{\delta x}{w_0}\right) U_{10}(x', y', 0). \tag{A.110}$$

Also, the TEM_{00} mode can be expanded in the coordinate system rotated with the angle of $\delta\theta$ around the y axis as

$$U_{00}(x, y, z)|_{z'=0} \simeq U_{00}(x', y', 0) + i\left(\frac{\delta\theta}{\alpha_0}\right) U_{10}(x', y', 0) \tag{A.111}$$

Figure A.12 shows the intensity distributions of TEM_{00} and TEM_{10}, i.e., U_{00}, U_{10} and their linear combination $U_{00} + (\delta x/w)U_{10}$ on the x-axis. The TEM_{00} translated in the x-axis direction is represented by a linear combination of TEM_{00} and TEM_{10}. Therefore, the beam jitter is expressed by the intensity fluctuations of the first-order modes. The cavity has the spatial mode selectivity, so the first-order mode is filtered by the cavity, that is, the beam jitter can be reduced by passing through a mode cleaner.

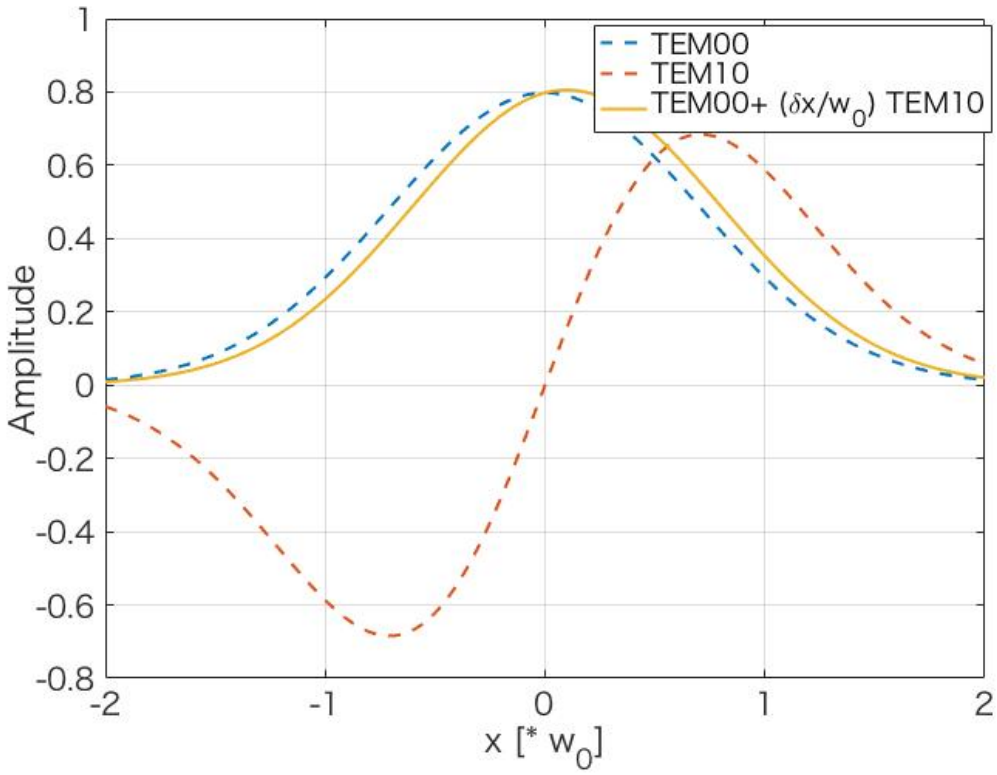

Figure A.12: Plot of the cross-section of amplitudes of TEM_{00}, TEM_{10} and their linear combination. Blue dashed line is the plot of U_{00} and red dashed line is that of U_{10}. Yellow solid line is the plot of $U_{00} + (\delta x/w)U_{10}$. The linear combination is the shifted TEM_{00} mode.

A.5 Noise Source in frequency stabilization

When a cavity is used as a frequency reference, a fluctuation in the cavity length causes the noise for the frequency stabilization. Also, a quantum fluctuation of the light, a light intensity fluctuation, etc. can be noise sources. In this section, we will consider each type of noise.

A.5.1 Shot noise

The shot noise occurs when the light is detected by a PD. Its amplitude spectral density (ASD) can be written as follows using the DC current I_{DC} of the PD.

$$\delta I_{\mathrm{shot}}(\omega) = \sqrt{2eI_{\mathrm{DC}}}, \tag{A.112}$$

where e is the elementary charge. When the DC laser power P_{DC} is incident on the PD, the generated current can be written as

$$I_{\mathrm{DC}} = \frac{e\eta P_{\mathrm{DC}}}{\hbar\Omega_0}, \tag{A.113}$$

where $\hbar$ is the reduced Planck constant, η is the quantum efficiency of the PD, and Ω is the laser frequency. Therefore, Eq. (A.112) can be rewritten as

$$\delta P_{\mathrm{shot}}(\omega) = \sqrt{\frac{2\hbar\Omega_0}{\eta}P_{\mathrm{DC}}}. \tag{A.114}$$

The ASD of the shot noise occurring when the reflected light is detected on the PD is

$$\delta P_{\mathrm{shot}} = \sqrt{\frac{2\hbar\Omega_0}{\eta}P_{\mathrm{DC}}^{\mathrm{PDH}}}, \tag{A.115}$$

where $P_{\mathrm{DC}}^{\mathrm{PDH}}$ is the laser power incident on the PD at resonance. From Eq. (A.84), it can be written as

$$\begin{aligned} P_{\mathrm{DC}}^{\mathrm{PDH}} &= \left(\frac{-r_F + r_E}{1 - r_F r_E}E_0\right)^2 + \frac{(\delta_m E_0)^2}{2} \\ &= R_{\mathrm{FP}}P_0 + P_s, \end{aligned} \tag{A.116}$$

where R_{FP} is the power reflectance of the cavity, P_0 and P_s are the power of the carrier light and the sideband in the reflected light, respectively. If $P_{\mathrm{DC}}^{\mathrm{PDH}}$ is demodulated with

$\cos\omega_m t$,

$$\begin{aligned}\delta P_{\rm shot}^{\rm demod} &= \cos\omega_m t \int_{-\infty}^{\infty} \frac{d\omega}{2\pi}\delta P_{\rm shot} e^{-i\omega t} \\ &= \int_{-\infty}^{\infty} \frac{d\omega}{2\pi}\delta P_{\rm shot} e^{-i\omega t}\frac{e^{-i\omega_m t}+e^{i\omega_m t}}{2} \\ &= \int_{-\infty}^{\infty} \frac{d\omega}{2\pi}\delta P_{\rm shot} e^{-i\omega t}. \end{aligned} \tag{A.117}$$

Then, the ASD of frequency fluctuation due to the shot noise can be written as

$$\begin{aligned}\delta\nu(\omega)_{\rm shot} &= \frac{1}{2\pi}\frac{\delta P_{\rm shot}}{\tilde{\epsilon}/\delta\Omega} \\ &= \frac{\sqrt{hc^3}}{8\pi}\sqrt{\frac{1}{\eta}}\sqrt{\frac{R_{\rm FP}}{P_s}+\frac{1}{P_0}}\sqrt{\frac{1}{\lambda}}\frac{1}{\mathcal{F}}\frac{1}{L}\frac{1}{H_{\rm LP}^{\rm cav}(\omega)}, \end{aligned} \tag{A.118}$$

where h is the Plank constant, c is the speed of light, λ is the wavelength of the laser, $\mathcal{F}$ and L are finesse and the length of the cavity, respectively.

A.5.2 Residual amplitude modulation noise

When amplitude fluctuations are present in the incident light at the modulation frequency ω_m, an intensity component of the carrier light rides on the error signal when demodulated, resulting in a control noise. There are many sources of the residual amplitude modulation (RAM). For instance, when the polarization axis of an EOM deviates from the polarization axis of the incident light, the EOM also modulates the intensity of the light. Scattered light can also be a RAM source. Here, we consider RAM noise.

Let the amplitude modulation index be $\epsilon_m(t)$. From Eq. (A.16), Eq. (A.80) can be rewritten using the new sideband $\boldsymbol{e}_{\rm RAM}$ as

$$\begin{aligned}\boldsymbol{\mathcal{E}}_{\mathbf{in}}^{\mathbf{tot}} &= \boldsymbol{\mathcal{E}}_{\rm in} + \boldsymbol{e}_m + \boldsymbol{e}_{\rm RAM} \\ &= \boldsymbol{\mathcal{E}}_{\rm in} + \boldsymbol{e}_m + \begin{pmatrix} \epsilon_m(t)\cos(\omega_m t) \\ \\ \delta_m\epsilon_m(t)\cos^2(\omega_m t)\end{pmatrix} E_0. \end{aligned} \tag{A.119}$$

Then, we can obtain the reflected light intensity. Here,

$$2\boldsymbol{\mathcal{E}}_{\rm r}\cdot\boldsymbol{e}_{\rm RAM} = 2\frac{-r_F+r_E}{1-r_F r_E}P_0\epsilon_m(t) \tag{A.120}$$

$$\begin{aligned}2\tilde{\boldsymbol{e}}_m\cdot\boldsymbol{e}_{\rm RAM} &= 2\delta_m^2 P_0\epsilon_m(t)\cos^3(\omega_m t) \\ &= \frac{3}{4}\delta_m^2 P_0\epsilon_m(t) + (\text{AC term}). \end{aligned} \tag{A.121}$$

A new term $\delta P_{\rm RAM}$ oscillating at the frequency ω_m is added to Eq. (A.84). It can be

written as

$$\delta P_{\mathrm{RAM}} = \left(2\frac{-r_F + r_E}{1 - r_F r_E} - \frac{3 r_E \delta_m^2 \epsilon_m(t)}{4} \right) P_0 \epsilon_m(t) \cos \omega_m t. \tag{A.122}$$

If r_F and $r_E \sim 1$, by the demodulation with $\cos(\omega_m t)$ we obtain the demodulated signal as

$$\begin{aligned} \delta P_{\mathrm{RAM}}^{\mathrm{demod}} &= \left(\frac{-r_F + r_E}{1 - r_F r_E} + \frac{3 r_E \delta_m^2}{8} \right) P_0 \epsilon_m(t) \\ &\simeq \frac{3\delta_m^2 \epsilon_m(t)}{8} P_0 \end{aligned} \tag{A.123}$$

Therefore、the RAM noise can be written as

$$\begin{aligned} \delta\nu(\omega)_{\mathrm{RAM}} &= \frac{1}{2\pi} \frac{\delta P_{\mathrm{RAM}}^{\mathrm{demod}}}{\tilde{\epsilon}/\delta\Omega} \\ &= \frac{3}{16} \nu_{\mathrm{FSR}} \frac{1}{\mathcal{F}} \delta_m \tilde{\epsilon}_m(\omega) \frac{1}{H_{\mathrm{LP}}^{\mathrm{cav}}}, \end{aligned} \tag{A.124}$$

where $\tilde{\epsilon}_m(\omega)$ is the Fourier component of RAM.

A.5.3 Residual gas noise

When gas exists in the optical path inside the cavity, the refractive index changes due to molecular motion of gas. This causes a change in the optical path length and the effective cavity length. Therefore, residual gas generates a noise. The change in the optical path length due to the residual gas is expressed by the following equation [61, 55].

$$\delta l_{\mathrm{gas}} = \frac{1}{4\pi} \frac{8\sqrt{2}}{\sqrt{\pi}} \frac{(n_0 - 1)^2}{(A_0/V_0) u_0 \sqrt{l\lambda}} \left(\frac{p}{p_0} \right) \left(\frac{T_0}{T} \right), \tag{A.125}$$

where n_0 is the refractive index of the gas, $A_0 = 6.02 \times 10^{23}$ is the Avogadro's number, u_0 is the average speed of the molecule, $V_0 = 2.24 \times 10^{-2}$ m^3 is the volume of gas with the amount of 1 mol under the standard state, $p_0 = 1$ atm is the standard pressure, $T_0 = 273.15$ K is the standard temperature, l is the cavity length, and λ is the wave length of the laser.

A.5.4 Seismic noise

A fluctuation of the cavity length due to seismic motion also generates a noise. When the mirrors constituting the cavity are independent of each other, the relative vibration spectrum of the mirror is simply the fluctuation of the cavity length. In the case of a rigid cavity whose mirrors are fixed on a spacer, if acceleration is applied to the cavity due to the ground vibration, the elastic modes are excited, and the cavity length fluctuates. The

fluctuation spectrum of the cavity length due to the ground vibration can be written as

$$\delta l_{\rm acc}(\omega) = ALa(\omega), \tag{A.126}$$

where $a(\omega)$ is the spectrum of the acceleration of the seismic motion, L is the cavity length, and A is the coupling constant between the acceleration and the length fluctuation.

A.5.5 Other noise

In the case of a rigid cavity, the spacer expands or shrinks due to temperature changes, and the cavity length is changed. This also generates noise, and it is a very slow noise due to the thermal inertia of the spacer. Usually, a temperature sensor and a heater are attached to the cavity, and this noise is reduced by locally controlling the temperature.

A thermal noise is also a fundamental noise source. The thermal noise is generally due to the thermal motion of mirror substrate, mirror coatings, suspensions suspending the mirrors or the spacer.

Furthermore, an electric noise of circuits used for control can also be a noise.

B Fundamentals of the control theory

In this section, we briefly explain the fundamentals of the control theory. As a simplest system, consider a negative feedback system consisting of a plant that measures a controlled variable x, an actuator, and a servo filter. H, A, and F represent the frequency response of the plant, the actuator, and the servo filter, respectavely. The block diagram of this system is shown in Fig.B.1. δx represents a disturbance. It is the purpose of the feedback control to keep the controlled variable x at 0 by the feedback when the controlled variable x changes by the disturbance δx. In the case of an FSS, a controlled variable x is a difference between a laser frequency and a resonance frequency of a cavity, while a plant is the cavity. The disturbance δx corresponds to the cavity length change and the frequency fluctuation of the laser, while the actuator A to a laser frequency actuator or a cavity length actuator. An output $V_{\rm err}$ of the plant H is called an error signal, and a servo filter output $V_{\rm fb}$ is called as a control signal or a feedback signal. In the negative feedback system, the control signal is fed back with the sign reversed.

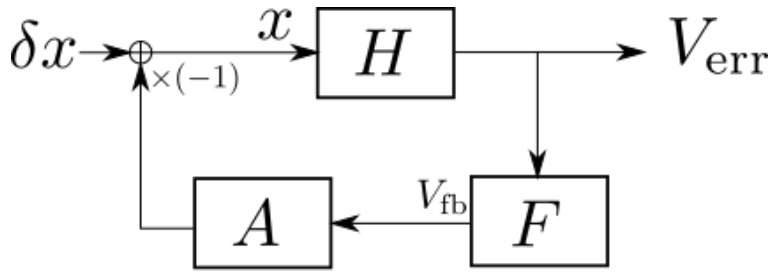

Figure B.1: Block diagram of the simple feedback system. H, A, and F are transfer functions of the plant, actuator and servo filter, respectively. $V_{\rm err}$ is an error signal and $V_{\rm fb}$ is a feedback signal.

The transfer function from the disturbance δx to the error signal $V_{\rm err}$ can be calculated as

$$\begin{aligned} V_{\rm err} &= H(\delta x - AFV_{\rm err}), \\ \therefore V_{\rm err} &= \frac{H\delta x}{1+G}, \end{aligned} \tag{B.1}$$

where $G = HAF$ is called an open loop gain (OLG) or open loop transfer function. If $|G| \gg 1$, then

$$\begin{aligned} x &= \frac{\delta x}{1+G} \\ &\simeq \frac{\delta x}{G}. \end{aligned} \tag{B.2}$$

On the other hand, in the case of $|G| \ll 1$, Eq.B.2 can be written as $x \simeq \delta x$. If $|G|$ is

greater than 1, the disturbance is suppressed to $1/|G|$, and if $|G|$ is less than 1, nothing is controlled. Therefore, a system which has larger OLG can suppress the controlled variable x more efficiently. The frequency f_{UGF} at which $|G| = 1$ is called as a unity gain frequency (UGF).

Next, consider the stability of the feedback system. For example, considering a positive feedback system in which the control signal is fed back with the same sign, the disturbance will be amplified and the controlled variable x will diverge. Such a system is called an unstable system. Howling of a microphone is an example of an unstable feedback system. As a criterion of identifying the stability of the system, there is a criterion using poles of the system, the Nyquist stability criterion using a vector locus on the complex plane of an OLG [62], and the Routh-Hurwitz stability criterion using coefficients of a polynomial of a denominator of an OLG [63]. Here, a pole is a complex frequency at which the denominator of the transfer function is 0, while a complex frequency at which the numerator is 0 is called a zero. We often use the Nyquist stability criterion, which will be explained below.

Now we assume that all of the poles of the OLG do not have a positive real part. This assumption is equivalent to that the open loop system itself is a stable system, and if a feedback system includes only stable actuators, plants and servo filters, this assumption is automatically satisfied. Consider the vector locus of an OLG increasing the frequency from $-\infty$ to $+\infty$ (this is called the Nyquist diagram). If the Nyquist diagram makes no encirclements around the point (-1,0), the system is stable. In Fig.B.2, a Nyquist diagram Γ_1 of an OLG with one pole at $\omega = -1$, and a Nyquist diagram Γ_2 of an OLG with three poles at $\omega = -1$. The gain at $\omega = 0$ is 10 for both. From this Nyquist diagram, we can see that the feedback system with Γ_1 is stable and the other with Γ_2 is unstable.

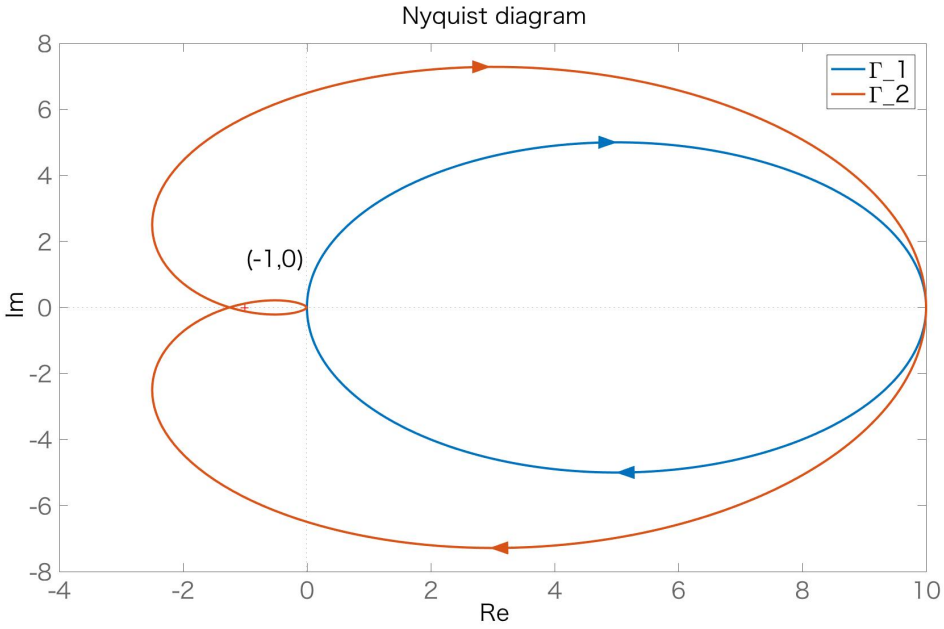

Figure B.2: Nyquist diagram. Γ_1 is the Nyquist plot of the OLG $G_1 = 10/(i\omega+1)$ and Γ_2 is the Nyquist plot of the OLG $G_2 = 10/(i\omega+1)^3$. Γ_2 is the Nyquist plot of the unstable system.

When discussing how a system is stable based on the Nyquist stability criterion, we can judge the stability of the system by how far the Nyquist diagram is from the point (-1, 0). Therefore, the system becomes unstable if the phase θ_{UGF} of an OLG at a UGF is delayed by $-180°$. Thus, the stability can be discussed with a phase margin $\theta_{\mathrm{PM}} = \pi + \theta_{\mathrm{UGF}}$. The system is stable when the phase margin is positive, and unstable when it is negative. Similarly, the system is stable, if the absolute value of an OLG $|G_{\mathrm{c}}|$ is less than 1 at the frequency where the phase is delayed by 180°. A gain margin $G_{\mathrm{GM}} = -20\log|G_{\mathrm{c}}|$ can also be used for discussing the stability. A system with a small phase margin and a gain margin will easily become unstable when the system changes by an external disturbance.

A Bode diagram is useful for this determination. The Bode diagram is a plot of an absolute value and a phase of a transfer function. The Bode diagram visualize an UGF, allowing us to intuitively estimate a phase margin and a gain margin. The UGF can be estimated by reading off the frequency at which the gain crosses 0 dB, and the phase margin can be estimated by checking the phase at that frequency. The Bode diagrams of OLGs G_1 and G_2 which are the same as these in Fig.B.2 are shown in Fig.B.3. Each phase margin can be estimated as $\theta_{\mathrm{PM}}|_{\Gamma_1} = 180 - \theta_{\mathrm{UGF},1} = 95°$ and $\theta_{\mathrm{PM}}|_{\Gamma_2} = 180 - \theta_{\mathrm{UGF},2} = -7°$, and again we can see Γ_2 is unstable.

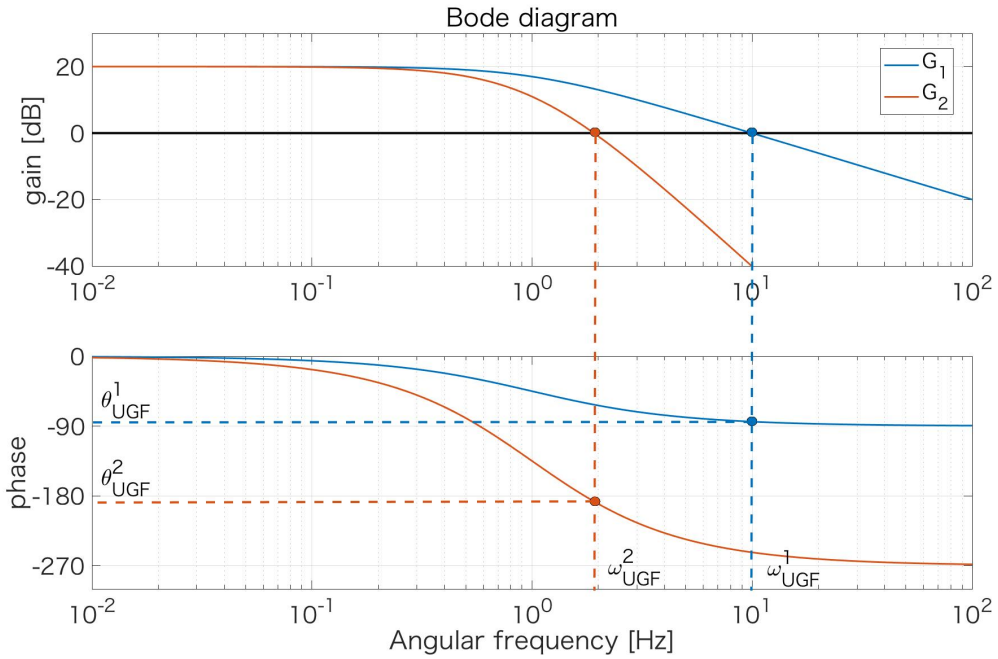

Figure B.3: Bode diagrams of the OLG $G_1 = 10/(i\omega + 1)$ and of the OLG $G_2 = 10/(i\omega + 1)^3$. $\theta_{\mathrm{UGF},1} = -85°$ and $\theta_{\mathrm{UGF},2} = -187°$ are the phases at the UGF.

Finally, consider a system with two actuators as shown in Fig.B.4, where A_1 and A_2 are the actuator responses, F_1 and F_2 are the transfer function of the servo filters. Then, a transfer function from the disturbance δx to the error signal V_{err} can be calculated as

$$V_{\mathrm{err}} = \frac{H\delta x}{1 + G_1 + G_2}, \tag{B.3}$$

where $G_1 = HA_1F_1$ and $G_2 = HA_2F_2$. To discuss the stability in this system, we should consider not only the phase margin and the gain margin of an OLG of the whole system $G_{\mathrm{tot}} = G_1 + G_2$, but also a phase difference between the two OLGs at the frequency where $|G_1| = |G_2|$. This frequency is called a cross over frequency. When the phase difference between the two OLGs at a cross over frequency is 180 °, then, $G_{\mathrm{tot}} = 0$. Namely, the system is not under control at the cross over frequency. Therefore, the control loop should be designed so that the phase difference at the cross over frequency is not close to 180°.

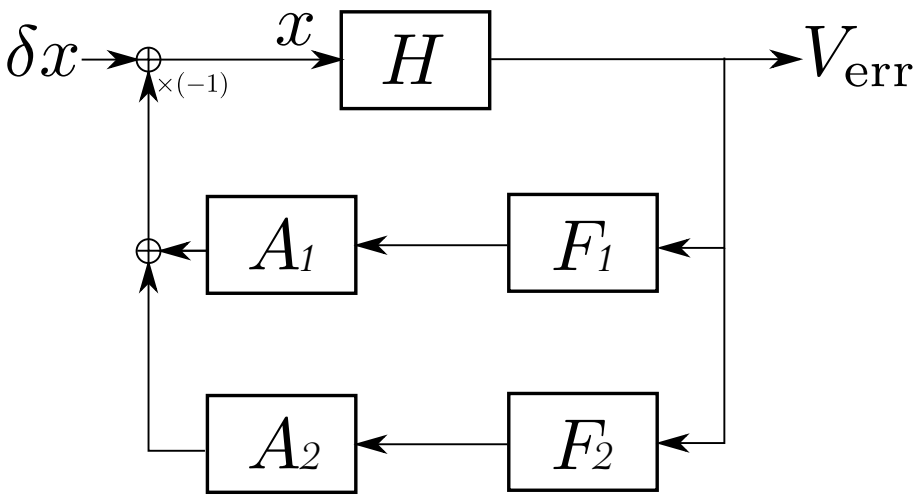

Figure B.4: Block diagram of the system with two actuators

References

[1] A. Einstein, Annalen der Physik **354**, pp 769–822.
Die grundlage der allgemeinen relativitätstheorie.

[2] J. H. Taylor, J. M. Weisberg, Astrophys. J. **345**, pp 434–450 (1989).
Further experimental tests of relativistic gravity using the binary pulsar PSR 1913 + 16.

[3] B. P. Abbott *et al.*, Phys. Rev. Lett. **116**, 061102 (2016).
Observation of Gravitational Waves from a Binary Black Hole Merger.

[4] J. Weber, Phys. Rev. **117**, pp 306–313 (1960).
Detection and Generation of Gravitational Waves.

[5] K. Kawabe. PhD thesis, The university of Tokyo (1998).
Development of a 3-meter fabry-perot-michelson interferometer for gravitational wave detection.

[6] J. Mizuno *et al.*, Phys. Lett. A **175**, pp 273–276 (1993).
Resonant sideband extraction: a new configuration for interferometric gravitational wave detectors.

[7] H. B. Callen, T. A. Welton, Phys. Rev. **83**, pp 34–40 (1951).
Irreversibility and Generalized Noise.

[8] P. R. Saulson, Phys. Rev. D **42**, pp 2437–2445 (1990).
Thermal noise in mechanical experiments.

[9] W. J. Startin, M. A. Beilby, P. R. Saulson, Rev. Sci. Instrum. **69**, pp 3681–3689 (1998).
Mechanical quality factors of fused silica resonators.

[10] T. Uchiyama *et al.*, Phys. Lett. A **261**, pp 5–11 (1999).
Mechanical quality factor of a cryogenic sapphire test mass for gravitational wave detectors.

[11] P. Amico *et al.*, Nucl. Instrum. Methods Phys. Res. A **518**, pp 240–243 (2004).
Thermal noise reduction for present and future gravitational wave detectors.

[12] V. B. Braginsky, F. Y. Khalili, Rev. Mod. Phys. **68**, pp 1–11 (1996).
Quantum nondemolition measurements: the route from toys to tools.

[13] J. Aasi *et al.*, Nat. Photonics **7**, pp 613–619 (2013).
Enhanced sensitivity of the LIGO gravitational wave detector by using squeezed states of light.

[14] K. Riles, Prog. Part. Nucl. Phys. **68**, pp 1–54 (2013).
Gravitational waves: Sources, detectors and searches.

[15] M. Maggiore. Oxford University Press, Oxford, 1 edition, (2007).
Gravitational Waves: Volume 1: Theory and Experiments.

[16] C. D. Ott, Class. Quantum Grav. **26**, 063001 (2009).
The gravitational-wave signature of core-collapse supernovae.

[17] T. L. Smith, M. Kamionkowski, A. Cooray, Phys. Rev. D **73**, 023504 (2006).
Direct detection of the inflationary gravitational-wave background.

[18] B. P. Abbott *et al.*, Phys. Rev. Lett. **116**, 241103 (2016).
GW151226: Observation of Gravitational Waves from a 22-Solar-Mass Binary Black Hole Coalescence.

[19] B. P. Abbott *et al.*, Phys. Rev. Lett. **118**, 221101 (2017).
GW170104: Observation of a 50-Solar-Mass Binary Black Hole Coalescence at Redshift 0.2.

[20] B. P. Abbott *et al.*, Phys. Rev. Lett. **119**, 141101 (2017).
GW170814: A Three-Detector Observation of Gravitational Waves from a Binary Black Hole Coalescence.

[21] B. P. Abbott *et al.*, Phys. Rev. Lett. **119**, 161101 (2017).
GW170817: Observation of Gravitational Waves from a Binary Neutron Star Inspiral.

[22] B. P. Abbott *et al.*, The Astrophysical Journal Letters **851**, L35 (2017).
Gw170608: Observation of a 19 solar-mass binary black hole coalescence.

[23] B. P. Abbott *et al.*, Astrophys. J. **848**, L13 (2017).
Gravitational Waves and Gamma-Rays from a Binary Neutron Star Merger: GW170817 and GRB 170817a.

[24] B. P. Abbott *et al.*, Rep. Prog. Phys. **72**, 076901 (2009).
LIGO: the Laser Interferometer Gravitational-Wave Observatory.

[25] J. R. Smith, f. t. L. S. Collaboration, Class. Quantum Grav. **26**, 114013 (2009).
The path to the enhanced and advanced LIGO gravitational-wave detectors, arXiv: 0902.0381.

[26] R. L. Ward *et al.*, Class. Quantum Grav. **25**, 114030 (2008).
dc readout experiment at the Caltech 40m prototype interferometer.

[27] The LIGO Scientific Collaboration, Class. Quantum Grav. **32**, 074001 (2015).
Advanced LIGO.

[28] F. Matichard *et al.*, Class. Quantum Grav. **32**, 185003 (2015).
Seismic isolation of advanced ligo: Review of strategy, instrumentation and performance.

[29] T. Accadia et al., J. Instrum. **7**, P03012 (2012).
Virgo: a laser interferometer to detect gravitational waves.

[30] F. Acernese *et al.*, Class. Quantum Grav. **32**, 024001 (2015).
Advanced Virgo: a second-generation interferometric gravitational wave detector.

[31] B. P. Abbott *et al.*, Living Reviews in Relativity **21**, 3 (2018).
Prospects for observing and localizing gravitational-wave transients with advanced ligo, advanced virgo and kagra.

[32] H. Grote, t. L. S. Collaboration, Class. Quantum Grav. **27**, 084003 (2010).
The GEO 600 status.

[33] R. L. Ward *et al.*, Class. Quantum Grav. **25**, 114030 (2008).
dc readout experiment at the caltech 40m prototype interferometer.

[34] K. Arai, T. Collaboration, Class. Quantum Grav. **19**, 1843 (2002).
Sensing and controls for power-recycling of tama300.

[35] T. Uchiyama *et al.*, Phys. Rev. Lett. **108**, 141101 (2012).
Reduction of Thermal Fluctuations in a Cryogenic Laser Interferometric Gravitational Wave Detector.

[36] M. Colpi, A. Sesana. In An Overview of Gravitational Waves, pp 43–140 (2016).
Gravitational Wave Sources in the Era of Multi-Band Gravitational Wave Astronomy.

[37] K. Izumi. PhD thesis, The university of Tokyo (2012).
Multi-color interferometry for lock acquisition of laser interferometric gravitational-wave detectors.

[38] J. Veitch *et al.*, Phys. Rev. D **85**, (2012).
Estimating parameters of coalescing compact binaries with proposed advanced detector networks.

[39] B. P. Abbott *et al.*, Living Rev. Relativ. **21**, 3 (2018).
Prospects for observing and localizing gravitational-wave transients with Advanced LIGO, Advanced Virgo and KAGRA.

[40] K. Yamamoto *et al.* Technical report, JGW-T1000218-v1, ICRR, (2010).
Measurement of seismic motion at Large-scale Cryogenic Gravitational wave Telescope project site.

[41] T. Akutsu *et al.*, PTEP **2018**, 013F01 (2018).
Construction of kagra: an underground gravitational-wave observatory.

[42] T. Sekiguchi. PhD thesis, The university of Tokyo (2016).
A study of low frequency vibration isolation system for large scale gravitational wave detectors.

[43] K. R *et al.*, J. Phys.: Conf. Ser. **716**, 012017 (2016).
Status of the cryogenic payload system for the KAGRA detector.

[44] D. R *et al.*, Class. Quantum Grav. **31**, 045001 (2014).
Cryogenic and room temperature strength of sapphire jointed by hydroxide-catalysis bonding.

[45] T. J. Kane, R. L. Byer, Opt. Lett. **10**, 65 (1985).
Monolithic, unidirectional single-mode Nd:YAG ring laser.

[46] R. Nishiuchi. Master's thesis, The University of Tokyo (2015).
Juryokuha kenshutsuki kagra you koushuturyoku laser kougen no anteika system no kaihatsu.

[47] M. Xue, S. Pan, Y. Zhao, J. Light. Technol. **32**, pp 3317–3323 (2014).
Optical Single-Sideband Modulation Based on a Dual-Drive MZM and a 120 #x00b0; Hybrid Coupler.

[48] O. V. Palashov *et al.*, J. Opt. Soc. Am. B, JOSAB **29**, pp 1784–1792 (2012).
High-vacuum-compatible high-power Faraday isolators for gravitational-wave interferometers.

[49] J. G. Rollins, Rev. Sci. Instrum. **87**, 094502 (2016).
Distributed state machine supervision for long-baseline gravitational-wave detectors.

[50] R. Takahashi *et al.*, Rev. Sci. Instrum. **73**, pp 2428–2433 (2002).
Vacuum-compatible vibration isolation stack for an interferometric gravitational wave detector TAMA300.

[51] K. Arai. Master's thesis, The University of Tokyo (1996).
Kisenchou 300 m laser kanshoukeigatajuryokuha kenshutuki no tameno kenka system no kaihatsu.

[52] E. A. Donley *et al.*, Rev. Sci. Instrum. **76**, 063112 (2005).
Double-pass acousto-optic modulator system.

[53] B. Willke *et al.*, Opt. Lett. **25**, 1019 (2000).
Frequency stabilization of a monolithic Nd:YAG ring laser by controlling the power of the laser-diode pump source, arXiv: physics/0005015.

[54] J. Millo *et al.*, Phys. Rev. A **79**, (2009).
Ultrastable lasers based on vibration insensitive cavities.

[55] D. hoemaker *et al.*, Phys. Rev. D **38**, pp 423–432 (1988).
Noise behavior of the Garching 30-meter prototype gravitational-wave detector.

[56] T. Ushiba. PhD thesis, The university of Tokyo (2015).
Laser frequency stabilization with a cryogenic optical cavity.

[57] R. W. P. Drever *et al.*, Appl. Phys. B **31**, pp 97–105 (1983).
Laser phase and frequency stabilization using an optical resonator.

[58] H. Kogelnik, T. Li, Proc. IEEE **54**, pp 1312–1329 (1966).
Laser beams and resonators.

[59] S. A. Self, Appl. Opt. **22**, 658 (1983).
Focusing of spherical Gaussian beams.

[60] T. Tochikubo. PhD thesis, The university of Tokyo (1999).
Development of a 300-m fabry-perot cavity with automatic alignment.

[61] M. Ohashi, N. Mio. Technical report, (1992).
Interferometer handbook.

[62] H. Nyquist, Bell Syst. Tech. J. **11**, pp 126–147 (1932).
Regeneration theory.

[63] Edward John Routh. Macmillan and co., (1877).
A Treatise on the Stability of a Given State of Motion, Particularly Steady Motion: Particularly ...

Acknowledgement

The KAGRA project is a huge project and not an experiment that can be done without the cooperation of many people. Thanks to the many people who supported me, I enjoyed even tough works at the Kamioka mine, which is a very harsh place for not only an experiment but also everyday life. I would like to express my gratitude here.

First of all, I would like to thank the supervisors. It is no exaggeration to say that Prof. Kawamura who instructed me from the time of master's degree formed the foundation of my physics. Since starting experiments in Kamioka, we have done various exercises not only for experiments but also for making a better life in Kamioka. I would like to express my gratitude to him for taking care of not only studying but also private life. Also, Prof Ohashi, the current supervisor, gained tremendous cooperation in writing the Ph.D. thesis. Although I had a lot of worries, thanks to the warm guidance of Prof. Ohashi, finally I could write a doctoral thesis.

I would also like to thank all the co-researchers. Keiko Kokeyama got a lot of cooperation while experimenting. Sometimes I was very encouraged to have the experiment helped even on holidays and late evenings where students cannot enter just by ourselves. Yuta Michimura pointed out the experimental direction at just the right timing, and it was extremely helpful. Tomotada Akutsu gave me many advice and assistance in various ways and gained significant cooperation in experimental savings. Eiichi Hirose has reminded me of a big goal that tends to forget merely by doing daily experiments and has given me opportunities to think about what kind of way to go as a researcher many times. Kazuhiro Yamamoto gave me very useful comments and advice every time there was a conference and presentation. Osamu Miyakawa is also the one who always cared about our experiments. Furthermore, KAGRA's digital system essential for installation work would not have been able to move without him.

Also, I would like to tell big thanks to Rick Savage who is working LIGO Hanford site. Since visiting LIGO Hanford site in 2016 and carrying out experiments together, we cooperated with many things. We could not manufacture the PMC without him, and this thesis would not have been completed without his help.

I would like to express my heartfelt appreciation to the students of Toyama University who assisted me with my experiments. I could not thank enough to Kagawa Tomohiro who came to Kashiwa almost for half a year and helped the experiment even he was the students at Toyama University. It was a great pleasure to have worked together at the hardest time of launching the Laser room. Also, I would like to thank Kambara Shogo who gave me great help installing the IMC which is fun and hard time. I also want to thank Yutaro Enomoto and Koji Nagano who are the member of the Kawamura lab. They maintained the IMC and kept stable control while I was going to LIGO. In addition to cooperating with the experiment at various timings, it became a big help.

Also, I would also like to thank the staff of the Kamioka office. Especially Kyoichi Takayama and Mihoko Okinaka supported us from the time we started working in Kamioka. Life in Kamioka would not have happened without them.

Finally, I would like to give an enormous thankfulness to my family who supported me for my life.